



<https://theses.gla.ac.uk/8593/>

Papersenos, George F. (1983) *The analysis of the transwall passive solar system*. PhD thesis.

This is a digitised version of the original print thesis.

Copyright and moral rights for this work are retained by the author

A copy can be downloaded for personal non-commercial research or study, without prior permission or charge

This work cannot be reproduced or quoted extensively from without first obtaining permission in writing from the author

The content must not be changed in any way or sold commercially in any format or medium without the formal permission of the author

When referring to this work, full bibliographic details including the author, title, awarding institution and date of the thesis must be given

Enlighten:Theses  
<http://theses.gla.ac.uk/>  
theses@gla.ac.uk

THE ANALYSIS OF THE TRANSWALL  
PASSIVE SOLAR SYSTEM.

by

GEORGE F. PAPARSENOS

Ph.D. Thesis

MECHANICAL ENGINEERING DEPARTMENT  
GLASGOW UNIVERSITY

JULY 1983.



ProQuest Number: 10662393

All rights reserved

INFORMATION TO ALL USERS

The quality of this reproduction is dependent upon the quality of the copy submitted.

In the unlikely event that the author did not send a complete manuscript and there are missing pages, these will be noted. Also, if material had to be removed, a note will indicate the deletion.



ProQuest 10662393

Published by ProQuest LLC (2017). Copyright of the Dissertation is held by the Author.

All rights reserved.

This work is protected against unauthorized copying under Title 17, United States Code  
Microform Edition © ProQuest LLC.

ProQuest LLC.  
789 East Eisenhower Parkway  
P.O. Box 1346  
Ann Arbor, MI 48106 – 1346

Thesis  
6901  
copy 2



DEDICATED TO

Fanourios and Ecaterini, my parents

Achilleas and Alexandros, my brothers.

## ACKNOWLEDGEMENTS

The author wishes to thank Dr. S.K. Nisbet, who supervised the present work for his continual guidance and encouragement, and the Department of Mechanical Engineering, Glasgow University, for making laboratory facilities available for the present work.

Thanks are also due to:

Prof. B.F. Scott, Mr. W. Carson and Mr. W.W. Mackie for their advice and help on certain aspects of this work.

Mr. R. Kleizer for his assistance in making the experimental rig and in taking measurements.

The Greek Foundation of State Scholarships and the Faculty of Engineering, Glasgow University, for financial support.

# CONTENTS

	Page
SUMMARY	I
DEFINITIONS	III
NOMENACLATURE	IV
 INTRODUCTION	 1
 CHAPTER 1	
CALCULATION OF THE TRANSMITTED, REFLECTED AND LOCALLY ABSORBED RADIATION OF A TRANSWALL SYSTEM ELEMENT	
Introduction	7
1.1 The 1-dimensional ray-tracing technique for an infinite number of internal reflections.	10
1.2 The 3-dimensional ray-tracing technique.	16
1.3 Application of the 1-dimensional ray-tracing technique to a transwall system element.	20
1.3.1 Direct radiation-Discussion of the results.	23
1.3.2 Diffuse radiation from the sky.	32
1.3.2a Calculation of the incident diffuse radiation coming from the sky.	34
1.3.2b Discussion of the results.	39
1.3.3 Diffuse radiation from the ground.	41
1.4 The 3-dimensional ray-tracing technique in the case of a transwall module with one outside glass plate.	46
 CHAPTER 2	
THERMAL MODELLING OF A TRANSWALL PASSIVE SOLAR SYSTEM.	
Introduction	59
2.1 Radiation falling on an unobscured external plane surface.	62
2.1.1 Solar radiation.	62
2.1.2 Longwave radiation.	64
2.2 The distribution of solar radiation entering an enclosure.	66
2.3 The distribution of solar radiation among the passive element and the internal surfaces of the test-box.	73
2.4 Analytical modelling of a passive solar system.	93
2.5 Thermal modelling of passive solar systems using a small test-box.	104
2.6 Application of the analytical modelling of a passive solar system in the case of the small test-box	113

2.6.1	The measured input data.	117
2.6.2	The completion of the input data.	119
2.6.3	Test-box measurements and analytical model results.	124
CHAPTER 3	NUMERICAL FLOW PREDICTION AND EFFECTIVE CONDUCTIVITY OF THE TRANSWALL FLUID.	
Introduction		141
3.1	Modelling the phenomenon of the natural convection of a fluid induced by the absorption of radiation.	143
3.1.1	Assumptions.	143
3.1.2	Governing differential equations.	144
3.1.3	The discretization of the system of differential equations.	146
3.1.4	The coupling of conduction and convection regions.	150
3.1.5	The complete difference equations for the transwall module.	152
3.1.6	The solution of the set of the difference equations.	156
3.2	Effective conductivity.	160
3.2.1	The definition.	160
3.2.2	Effective conductivity at a control volume boundary at which there is no production or storage of energy.	161
3.2.3	Effective conductivity at the interface of two control volumes without convection across it.	163
3.2.4	Examples of numerical prediction of the effective conductivity in the case of various transwall modules.	163
3.3	Examples of the numerical prediction of the velocity, pressure and temperature field.	184
3.4	Measurements of temperature and velocity.	191
3.4.1	The transwall module.	191
3.4.2	The supporting system.	191
3.4.3	The solar simulator.	196
3.4.4	Temperature measurements.	202
3.4.5	Velocity measurements.	214

## APPENDICES

A	A closed formula example of the 1-dimensional ray-tracing technique with infinite number of internal reflections.	234
B	Exit point of a radiation vector from a control volume.	239
C	Calculation of the vectors of the reflected and transmitted radiation in the case of specular reflection and refraction.	242
D	Optical properties-refractive index and extinction coefficient-of clear float glass and Antisun glass, grey 41/60.	245
E	Extinction coefficient of various dyes and gelling agents.	248
F	Calculation of the spectral composition of the components of solar radiation.	251
G	Approximate calculation of the view factor of two polygons sited on two different planes.	257
H	Calculation of the projection point on a plane.	262
I	Calculation of the intersection polygon of two coplanar convex polygons.	264
J	Calculation of mass-flux $(Gx)_{x+}$ and water vapour mass concentration $m_{w,p}$	266
K	Example of a closed air-gap discontinuity.	268
L	Application of the method of distribution of solar radiation among the surfaces of a typical glasshouse enclosure.	270
M	A numerical example of the importance of the relative magnitude of all the coefficients APC, APi, BPC of the set of the discretization equations, $APC * \phi_p = \sum_i (APi * \phi_i) + BPC$ on the convergence of the line-by-line iterative solution.	275

N	Comparison of 1-dimensional ray-tracing techniques with infinite and finite number of internal reflections.	278
O	The computer listing of the tridiagonal algorithm.	279
P	Optimization of solar simulators.	280
	REFERENCES	285



## SUMMARY

The thesis presents analytical and experimental methods of studying various aspects of the optical and thermal performance of a transwall passive solar system. Some of these methods are applicable to other solar systems.

Two ray-tracing techniques, 1-dimensional and 3-dimensional, are presented for an accurate calculation of the optical properties of a transwall module with its outside glass plate(s). These techniques calculate not only the reflected, absorbed or transmitted fractions of the incident radiation but also the spectrum of the transmitted radiation. This information is required for a better assessment of the transwall system as an illuminating source and as a thermal system. Both techniques are applied to a particular transwall module with one outside glass plate and the importance of various features of the incident solar radiation (such as spectrum, angular variation, polarization, etc.) are discussed. The difficulties associated with the nature of the diffuse solar radiation coming from the sky, or the ground, are overcome by employing a discretization method in which the continuous diffuse radiation is divided into discrete pencils of radiation.

An analytical thermal model of a passive solar system is presented and its verification is established by using a test-box containing a full size transwall module. The outcome of this verification is satisfactory given the uncertainties of the optical and thermal properties of the various elements of the test-box. The success of the analytical modelling depends on accounting for the 3-dimensional solar radiation field outside and inside the passive solar system. The methods developed, accompanied by the two ray-tracing techniques, allow for an accurate distribution of the total incident radiation among the semitransparent elements and the external and internal surfaces of any passive system. The method of distributing the solar radiation among the internal surfaces of an enclosure is applied to the convex parallelepiped enclosure of the test-box and, as additional example of the method, also applied to the non-convex enclosure of a typical glasshouse with E-W transwalls.

The phenomenon of the natural convection of a fluid inside a transwall module induced by the absorption of radiation is predicted by a numerical method, first introduced by Patankar. Examples of

the temperature, pressure and velocity fields of three transwall modules filled with distilled water under the irradiance conditions of 400 to 500 W/m<sup>2</sup> are presented. By introducing the effective conductivity concept the complicated phenomenon of the fluid convection inside the module is simplified to a conduction phenomenon. This is also necessary for the long term-days or months - analytical modelling of the total transwall passive system because the numerical prediction of the former phenomenon requires an excessive amount of computer time. The calculation of the effective conductivity is obtained by employing an analytical approach which makes use of the data collected from the application of the numerical method, mentioned above. Values of the ratio of the effective conductivity to the conductivity of the still water are calculated at two interfaces inside the water of four different transwall modules. Measurements of the temperature and the velocity at certain points in a small transwall module irradiated by a solar simulator have been performed to support some of the numerical predictions.

## Definitions

transwall module: the annealed glass rectangular container filled with a liquid.

transwall (system) element: the transwall module or the assembly of the modules with one or more outside glass (or plastic) plates.

transwall system: the transwall element with the enclosure of which the element is part.

angle of incidence: the angle between the vector of the incident radiation on a surface and the vector normal to that surface. For opaque surfaces the direction of the surface vector is always from the thick to the light medium. The surface is lit only if the angle of incidence is greater than  $90^\circ$ . The conventional definition requires the angle of incidence to be smaller than  $90^\circ$ .

# NOMENACLATURE

a	solar altitude angle, coefficient of general differential equation
$a_o$	extinction coefficient ( $m^{-1}$ ) due to solved dye
$a_s$	solar azimuth angle, extinction coefficient ( $m^{-1}$ ) of solvent
$a_w$	wall azimuth angle
A	area
$c_p$	constant pressure specific heat capacity
$c_v$	constant volume specific heat capacity
C	dye concentration (mol of dye/Kg of solvent)
D	dimension of control volume
$g = 9.81$	$m/s^2$
$\vec{G}$	mass-flux vector
Gr	Grashof number
h	heat transfer coefficient, specific enthalpy
$h_{fg}$	latent heat
$h_s$	solar hour angle
H	height
$\vec{i}$	unit vector
i	angle of incidence
$\vec{j}$	unit vector
$\vec{k}$	unit vector
l	hydraulic diameter
L	thickness, distance
m	mass concentration of air-vapour mixture
Mnu	number of anisotropy
n	number
N	number
Nu	Nusselt number
P	pressure
$\vec{P}$	vector normal to surface
$P_o$	degree of polarization
q	heat or radiation flux per unit area
Q	heat flux
t	optical path, time
T	temperature
u	component of velocity vector along the x-axis
U	conductance

$v$  component of velocity vector along the y-axis  
 $V$  volume, wind velocity  
 $\vec{V}$  velocity vector, direct radiation vector  
 $w$  component of velocity vector along the z-axis  
 $W$  width  
 $W^*$  strength of solution (Kg of dye/Kg of solvent)  
 $x$  normal, along the x-direction  
 $X$  along the X-direction, X coordinate  
 $Y$  along the Y-direction, Y coordinate  
 $Z$  along the Z-direction, Z coordinate

#### Greek letters

$\theta^\circ$  tilt  
 $\delta_s$  declination angle  
 $\Delta$  finite difference  
 $\epsilon$  extinction coefficient (Kg of solvent/mol of dye\*m)  
 $\lambda$  thermal conductivity  
 $\lambda_{ef}$  effective conductivity  
 $\lambda^*$  wavelength of radiation  
 $\lambda_b^*$  wavelength band of radiation  
 $\mu$  first coefficient of viscosity  
 $\mu'$  second coefficient of viscosity  
 $\nu$  kinematic viscosity  
 $\rho$  density, reflectance, reflectivity  
 $\epsilon = 5.6697 \cdot 10^{-8} \text{ W/m}^2 \cdot \text{K}^4$

#### Subscripts

$a$  dry air  
 $at$  atmospheric  
 $Ai$  face  $i$  of control volume  $A$   
 $b$  backward direction  
 $cond$  pure conduction  
 $d$  diffuse  
 $D$  direct  
 $f$  forward direction  
 $g$  passive solar element  
 $gr$  ground  
 $h$  on a horizontal surface  
 $i$  surface, passive system element

L at node L  
p at node P  
x+ at the part x+ of the surface  
w water vapour  
 $\phi$  dependent on  $\phi$

Superscript

o at time t

## **Introduction**

## INTRODUCTION

A transwall passive solar system combines some of the characteristics of two basic passive solar systems the "direct gain" and the "thermal storage wall" system. In a direct gain system solar energy enters windows and is absorbed and stored by the floor, the ceiling and the walls. In a thermal storage wall system the solar energy is collected by a massive dark-surfaced storage wall placed behind glass. The heat reaches the inside room by conduction through the storage wall and, in some designs, by air circulation through vents at the top and bottom of the wall (Trombe wall).

The transwall passive solar system consists of an assembly of visually semi-transparent modules stacked vertically in a wooden or metal support frame, and placed behind a glazed area, as shown in Fig. 1.

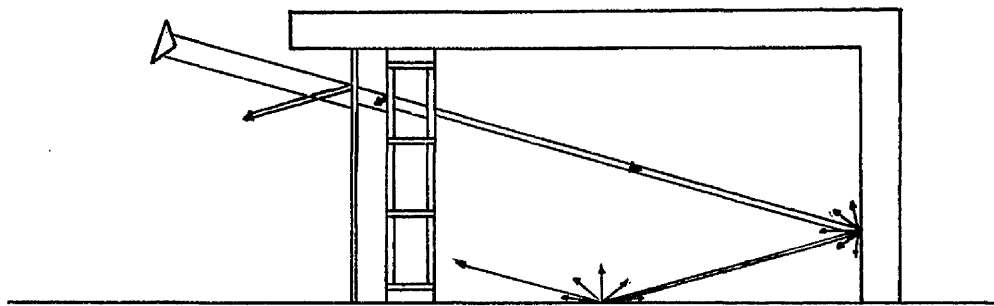


Fig. 1

### Transwall passive solar system

Transwall modules usually have the form of annealed glass rectangular containers, filled with a high thermal capacity liquid, generally based on water. Part of the incident radiation of the transwall system is reflected back, part is absorbed and stored by the outer glazing, the glass structure and the liquid of the module, part is absorbed by the surface of the support frame and a final part of the transmitted radiation into the interior is absorbed by the floor, the ceiling and the walls. Because the front surface of the transwall assembly does not reach the relatively high temperatures of the thermal storage wall vents at the top and bottom of the transwall assembly are not an important feature of the system.

The transwall passive solar system overcomes some of the disadvantages frequently experienced in both the direct gain and the thermal storage wall systems. It admits light to the interior space, allows the occupants to see out through the window with negligible



visual distortion (the face glass plates of the module deflect slightly because of the hydrostatic pressure) and reduces weight and space requirements relative to the conventional concrete storage wall. It also reduces glare, photodegradation, air temperature fluctuations and some radiant temperature comfort problems associated with some direct gain systems. Analytical and experimental results have shown that the transwall system thermal performance is equal to or better than the two other passive solar systems (1),(2),(5).

The aim of the present work was to provide analytical and experimental methods of studying aspects of the optical and thermal performance of a transwall passive solar system. The methods and techniques, developed in this work allow an accurate distribution of the total incident radiation to the various elements and external and internal surfaces of the transwall system. The effective conductivity inside various transwall modules is calculated by adopting an analytical approach based on the numerical modelling of the phenomenon of the natural convection of a fluid induced by the absorption of radiation. This analysis is necessary for the analytical thermal modelling of a transwall passive solar system, presented in this thesis. This analytical modelling is verified by using a small test-box containing a full size transwall module. The test-box constructed at the Mechanical Engineering Research Annexe (M.E.R.A.), Glasgow University, can be used for the thermal modelling of various passive solar systems.

#### The transwall module and system design - A review

Most of the research concerning transwall systems has been undertaken by the A.M.E.S. laboratory - USDOE, Iowa State University, U.S.A., the results of which have been presented in References (1), (2), (3), (4), (5), (6) and (7). The analytical results are based on 1-dimensional thermal network models of the thermal performance of the passive systems. Experimental evidence has been collected from measurements in test-rooms, on the south-facing side of which are various passive solar systems.

The transwall module suggested by A.M.E.S. (4), (5) is a rectangular water filled container fabricated from 6.4mm thick annealed plate glass using General Electric RTV108 silicone adhesive sealant to bond butt joints. Its outer dimensions are:

58 cm width , 38 cm height and 14 cm thickness. To enhance the module's solar radiation absorptance a standard 3.2 mm thick grey tinted glass plate is mounted with silicone adhesive parallel to the large face plates at the centre of the module. The construction of the modules is in accordance with standard aquarium technique. The top of the module is closed by a glass plate, bonded on to the module and having two 2 cm diameter holes for filling and emptying. These holes are closed with open cell foam filters to reduce water contamination by air-born particles. An absolutely sealed system does not appear to be economically practical although it has the advantage of maintaining water quality. The first transwall modules in A.M.E.S. were made from acrylic plastic but they were abandoned because of reliability problems.

The increase in the absorptance of the module by using an extra absorber plate is scarcely cost effective since the absorber plate cost is roughly half that of the rest of the module. This is one of the reasons for the current examination of transwall modules in A.M.E.S. (8), in which the absorber plate is transferred from the centre to form the interior facing module wall. The use of dye, diluted into the water, e.g. acid green B, methyl orange, copper chloride (their extinction coefficients are given in Appendix E ) seems to be a more cost effective way of increasing the absorptance of the transwall module. However uncertainties in the dye reliability in respect to its optical and thermal properties over a long period of time, e.g. years, have to be resolved first. Burke, et al. (9), (10) suggest ways of studying the stability of optical and thermal properties of solar irradiated solutions of dyes. Under normal thermal and irradiance conditions the abovementioned three dyes did not show any apparent change in their optical properties by using them in the transwall modules tested in M.E.R.A, Glasgow University, for a period of about two years.

Preliminary analytical results by Fuchs, et al (1), showed that a transwall module with inhibited water convection ( $Nu=1$ )<sup>+</sup> gives a better thermal performance than a transwall module with free water convection ( $Nu=20$ ). Experiments by Hull, et al. (3) suggest that horizontal convective heat transfer

+ Nu is the Nusselt number.

is suppressed somewhat because of vertical temperature stratification. They estimated the actual Nu value by varying the transwall conductances in their 1-dimensional thermal network model to fit the experimental data. They found that  $Nu=2.5$  and concluded that relatively low Nu values could exist for transwall modules without resorting to inhibiting the water convection by baffles or by the addition of gelling agents. Certainly, Hull, et al. (3) expressed cautiousness about generalizing their results on convection within the transwall. Indeed, in this thesis a main target was to establish values of effective conductivity inside different aspect ratio (height-to-thickness) transwall modules. The results for a continuous radiation input of about 400 to 500  $W/m^2$  showed a high effective conductivity which is compatible with a Nu value of 20 and not that of Hull's 2.5. Anyway, the use of baffles to inhibit the water convection should be considered a rather difficult and uneconomical solution. The use of gelling agents may provide a better solution. Two different types of gelling agents have been tried in M.E.R.A. Courtoulds Courlose F1000G and Celanese Celacol HA7 150000S, the former being the better for clarity. (The extinction coefficient of two solutions of the first gel are given in Appendix E ). However the long chain molecules appeared to "contract" over several weeks leaving the upper regions clear and the lower regions opaque. Solutions stronger than the 0.5% (Kg of agent/Kg of water) tested might avoid this problem but at the expense of visual clarity. Long term tests are continuing. On the other hand, these gelling agents seemed to enhance the growth of micro-organisms.

Analytical results (4), (5) suggest a great improvement in the thermal performance of the transwall systems with modules having their outside surface treated with heat-mirror coating. The importance of these coatings is almost comparable to that of providing insulation at night but is less than that of double glazing. At present, the thermal performance of the transwall system with heat-mirror coating modules is under test in A.M.E.S. (8). Hull et al. (3) also studied analytically the importance of various design parameters on the thermal performance of a transwall system.

These design parameters are: the collector area to building load ratio, the thickness of the water layer, the transmittance of the absorber plate and the amount of internal thermal mass. According to his analysis good thermal performance can be obtained while still allowing substantial design flexibility especially in respect to the thickness of the water layer and the plate absorptivity (nominal values used, 15.2 cm and 0.8, respectively). The values are based on the Nu value of 2.5 and this introduces uncertainty.

Problems which usually arise in transwall modules include water evaporation, air bubbles, algae growth and suspended precipitates of minerals: (a) To prevent evaporation a thin layer of low vapour pressure liquid which floats on and seals the top water surface from the air can be used. Mercer et al. (5) suggests fluosilicone oil because it does not only have a low vapour pressure but it is also compatible with the silicone bonding adhesive - a common adhesive for fish-tanks works - and it is not biologically active. (b) Small air-bubbles attach to the interior glass surfaces during or shortly after filling the module. The bubbles combine into larger ones and float to the surface in a matter of few days. The suggestion by Mercer et al. (5) to accelerate the elimination of these bubbles in a matter of few hours by using heat lamps is rather expensive and not justified by the bubbles effect on the thermal and optical performance. (c) The algae and precipitates problem of A.M.E.S. has not been experienced in the transwall modules of M.E.R.A. using an acid green B solution of water. It is suggested (5) that the problem can be controlled by tracing the water with 100 ppm  $\text{CuSO}_4$  and 150 ppm disodium ethylenediamine tetracetate (EDTA).

Although the preliminary experimental verification of the 1-dimensional models with the test-rooms can be considered satisfactory (3), there are reasons that support the use of more elaborate analytical models for some of the elements of the passive solar system or the system itself, e.g. the models presented in this thesis. The analysis and experiments presented in this thesis show that the velocity and temperature fields - and therefore the heat transfer - in a transwall module are 3-dimensional with complex circulation patterns. The 1-dimensional

approach, while saving on computing time, cannot by its limitations represent the actual phenomenon in various transwalls with any degree of accuracy. The experimental evidence of test-rooms (2), (5) shows that a transwall system has much more favourable mean radiant temperatures for thermal comfort than its competing systems of direct gain and thermal storage wall for the whole year thermal performance of these systems. A 1-dimensional model cannot match the 3-dimensional nature of the radiation field in the room behind the transwall module, which is a major factor in determining the radiation distribution and fails to calculate accurately the corresponding comfort level.

## **Chapter 1**

CALCULATION OF THE TRANSMITTED, REFLECTED AND LOCALLY  
ABSORBED RADIATION OF A TRANSWALL SYSTEM ELEMENT.

## Introduction.

A 3-dimensional ray-tracing technique is presented (section 1.2) for the accurate calculation of the optical properties of a system - total transmittance, total reflectance and the local rate of radiation absorption. The computational procedure is simplified without incurring any serious penalty in accuracy if the optical system can be considered as 1-dimensional. This is a common assumption in most solar applications where 1) the least dimension of the 3-dimensional optical system is very small in relation to the two other dimensions and 2) the incident radiation falls on one or both of its large and opposite sides ( $L \ll W$ ,  $L \ll H$ , Fig. 1.1). These sides are usually parallel to each other.

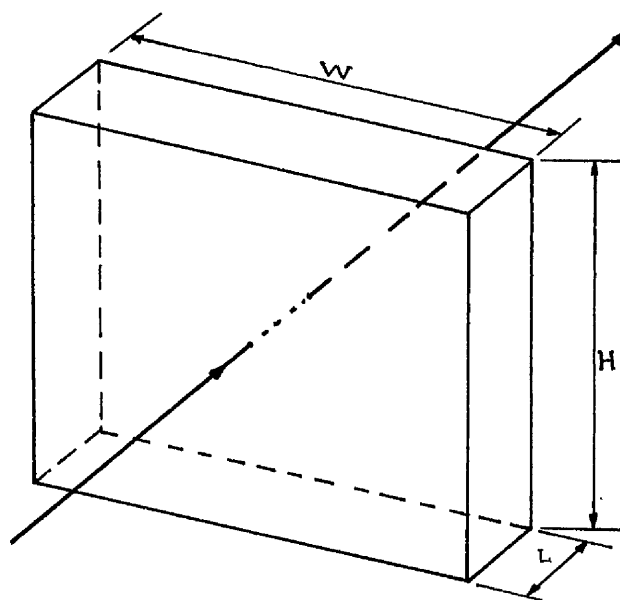


Fig. 1.1

The assumption of a 1-dimensional optical system permits the calculation of the relevant properties by employing an approach where only the transmission of the radiation along the optical path from one large side to the other is taken into account and edge effects and other factors, e.g. frame, are neglected. Furthermore, this assumption reduces drastically the required computational effort, especially in the case of the diffuse solar radiation. The approach presented in the thesis (section 1.1) is believed to be a new form of the ray-tracing technique accounting for an infinite number of internal

reflections.

Both techniques can calculate the spectrum of the transmitted radiation. This information is important to assess the transwall system element as an illuminating source.

The 1-dimensional ray-tracing technique is applied to a particular transwall module with one outside glass plate and the importance of various features of the incident solar radiation are discussed (section 1.3). These features are:

- 1) Angular variation of direct solar radiation.
- 2) Anisotropy and polarization of the diffuse solar radiation from the sky and the ground and
- 3) The spectrum and polarization effects within the transwall element.

The discussion reveals that

- 1) The radiation absorbed by each of the three glass plates of this particular system is a high proportion of the incident radiation and should not be neglected in any thermal analysis. This is an important consideration because, for example, it may influence the location of coatings on glass surfaces required to reduce the heat losses.
- 2) For both direct and diffuse incident radiation their spectral composition is an important factor in determining the values of total transmittance, spectral composition of the transmitted radiation and the absorptance of the liquid.
- 3) Accounting for the degree of polarization of the incident diffuse radiation and the change in the degree within the optical system are not justified by the better accuracy in the calculated optical properties. In addition the required computational time is double.
- 4) For the particular vertical transwall system element neglecting the cosine effect of the diffuse radiation leads to very different optical values.

The difficulties associated with the nature of the diffuse radiation from the sky, e.g. anisotropy, nonuniform degree of polarization, are overcome by employing a method (section 1.3.2a) in which the continuous sky diffuse radiation is divided into discrete pencils of radiation all over the sky dome. The method also allows the calculation of the so-called 'number of anisotropy',  $M_{nu}$ . This is a measure of the importance of accounting for the anisotropy of sky diffuse radiation. The same discretization method is used in the case of the diffuse radiation from the ground by introducing the concept of an imaginary sky dome. This dome is the half hemisphere underneath the horizon (section 1.3.3).

In section 1.4 the 3-dimensional ray-tracing technique is applied



to the same transwall module with one outside glass plate for 5 different cases of direct solar radiation of air-mass 2. The effect of the edges and other factors is evident but small. Accounting for the degree of polarization within the optical system is again not justified by the better accuracy of the calculated optical values. It is interesting that the 3-dimensional ray-tracing technique predicts smaller values of total transmittance than the 1-dimensional ray-tracing technique.

1.1 THE 1-DIMENSIONAL RAY-TRACING TECHNIQUE FOR  
AN INFINITE NUMBER OF INTERNAL REFLECTIONS.

A 1-dimensional optical system generally consists of a series of parallel sub-systems (layers) whose optical properties are generally different (Fig. 1.2).

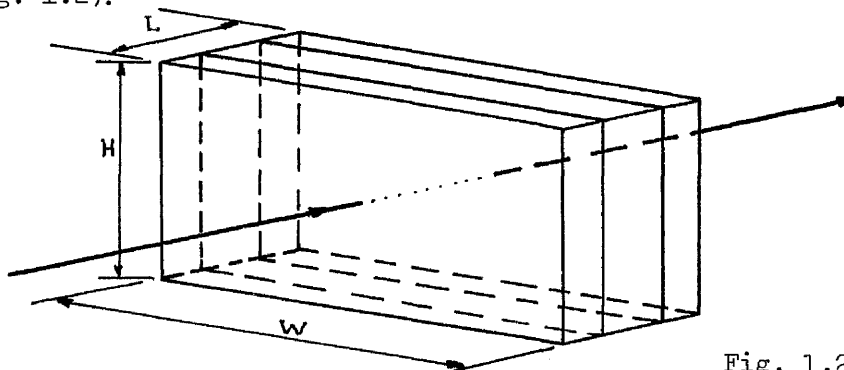


Fig. 1.2

In the following analysis a new form of the ray-tracing technique for an infinite number of internal reflections is used. This allows the derivation of algebraic relations from which recurrence relations are obtained to calculate the total reflectance, transmittance, absorptance and the absorptance of each individual sub-system. These recurrence relations are ideally suited for use in a digital computer program.

The ray-tracing technique, first introduced by Stokes (11), has usually been used to calculate the total transmittance, reflectance and absorptance of a multi-layer system in its alternate forms of accounting for a finite (12) or infinite number of internal reflections (13), (14), (15). The former has more commonly been used to calculate the absorptance of each layer of a multi-layer system.

Belov (16) developed his own method for the calculation of the hemispherical monochromatic reflectance, transmittance and absorptance of a multi-layered coating and a stack of layers of absorbing and scattering materials with diffuse interfaces.

Siegel (17) adapted the "net radiation method" for enclosures with opaque surfaces to a multi-layer system, and obtained total transmittance and reflectance of this system. In his method a set of  $2N$  simultaneous equations is written for computer solution of an  $N$ -layer system. Shurcliff (18) applied a similar matrix method to the case of non-absorbing layers. Wigegysundera (19) extended the "net radiation method" and obtained a recurrence relation for the calculation of the absorptance of each layer of a multi-layer system.

Edwards (20), employing the "embedding technique", gave a similar computational algorithm that calculates the absorptance of each element

in an absorber-coverglass array.

The basic concept of the new technique is that every optical system can be supposed to consist of a series of two elementary optical subsystems:

1. The boundary surface of two different optical materials A and B.
2. The optically uniform transparent, or semitransparent material G between two boundary surfaces which are not included in this elementary subsystem.

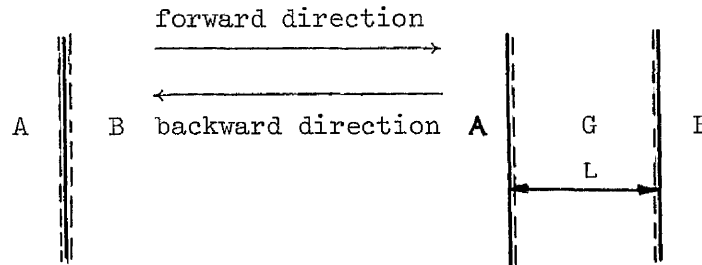


Fig. 1.3

Each of these two elementary subsystems is assigned the three optical properties of reflectivity, absorptivity and transmissivity for each of the two opposite directions of the incident radiation (see Fig. 1.3). The values of these properties can be understood to be spectral or monochromatic values appropriate to each component of polarization at the angle of incidence of interest, or to the extent that polarization and spectral effects may be neglected they may be regarded as total-grey directional values. The reflectivity of the elementary subsystem 2 is always zero because it excludes surfaces.

A typical example of a system consisting of three elementary subsystems is presented in Appendix A, where relations for the calculation of their properties are given as well.

In the above definition of the two elementary subsystems it is assumed that the elementary subsystem 2 is thick in comparison to the wavelengths of incident radiation ( $L \gg \lambda$ ) and hence it is not necessary to consider wave interference effects. As far as a thin film is concerned ( $L \approx \lambda$ ) this is considered to be an elementary subsystem 1 with absorptivity for both directions of the incident radiation different from zero. The case of zero absorptivity is that of a pure interface of two different transparent or semitransparent materials A and B (Fig. 1.3).

Another basic feature of the new technique is the introduction of different optical properties of the optical system for the two opposite directions of the incident radiation. For example, this is evident in the case of total reflection. Therefore, at the beginning, the forward and backward direction of the incoming

radiation to the system should be defined. Then the forward and backward directions for each subsystem will be those of the main system. In the following relations the subscripts f and b imply the forward and backward direction of the incoming radiation, respectively.

Derivation of the algebraic relations.

For an optical system M, we define:

$$\text{reflectance } re_f(M) \quad re_b(M)$$

$$\text{absorptance } ab_f(M) \quad ab_b(M)$$

$$\text{transmittance } tr_f(M) \quad tr_b(M)$$

Because of the conservation of energy for the system M,

$$re_f(M) + tr_f(M) + ab_f(M) = 1 \quad (1.1)$$

$$re_b(M) + tr_b(M) + ab_b(M) = 1 \quad (1.2)$$

For an optical system (M+N) consisting of the two optical systems M and N where the direction from system M to system N is the forward direction, we define:

$$\text{total reflectance } \rho_f(M+N) \quad \rho_b(M+N)$$

$$\text{total absorptance } \alpha_f(M+N) \quad \alpha_b(M+N)$$

$$\text{total transmittance } \tau_f(M+N) \quad \tau_b(M+N)$$

$$\text{absorptance of system M}^+ \quad \alpha_{Mf}(M+N) \quad \alpha_{Mb}(M+N)$$

$$\text{absorptance of system N}^+ \quad \alpha_{Nf}(M+N) \quad \alpha_{Nb}(M+N)$$

Because of the conservation of energy for the system (M+N),

$$\rho_f(M+N) + \tau_f(M+N) + \alpha_f(M+N) = 1 \quad (1.3)$$

$$\rho_b(M+N) + \tau_b(M+N) + \alpha_b(M+N) = 1 \quad (1.4)$$

$$\alpha_f(M+N) = \alpha_{Mf}(M+N) + \alpha_{Nf}(M+N) \quad (1.5)$$

$$\alpha_b(M+N) = \alpha_{Mb}(M+N) + \alpha_{Nb}(M+N) \quad (1.6)$$

A continued tracing of the radiation (see for example, Fig. 1.4) gives the following relations for the system (M+N):

Total reflectance, forward direction

$$\begin{aligned} \rho_f(M+N) &= re_f(M) + \\ &\quad tr_f(M) * re_f(N) * tr_b(M) + \\ &\quad tr_f(M) * re_f(N) * re_b(M) * re_f(N) * tr_b(M) + \dots \Rightarrow \\ \rho_f(M+N) &= re_f(M) + tr_f(M) * re_f(N) * tr_b(M) * \left( \frac{1}{1 - re_b(M) * re_f(N)} \right) \end{aligned} \quad (1.7)$$

+fraction of the incident radiation on optical system (M+N)  
absorbed by the individual system M or N

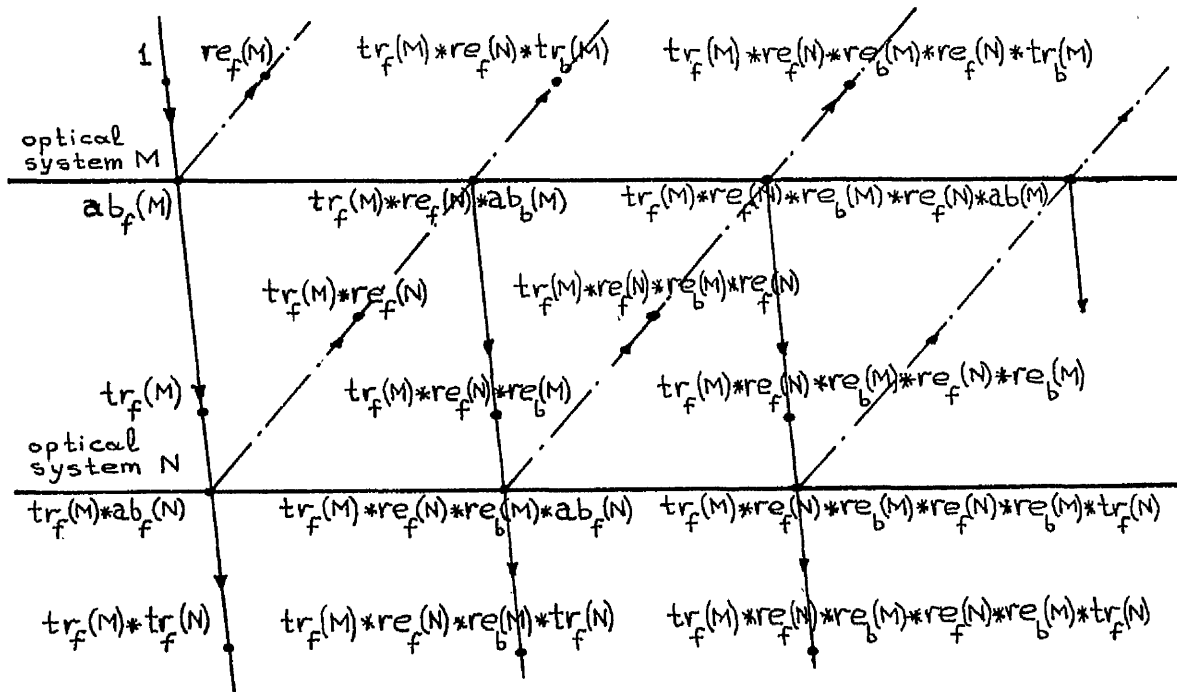


Fig. 1.4.

Similarly, total reflectance, backward direction,

$$\rho_b(M+N) = re_b(N) + tr_b(N) * re_b(M) * tr_f(N) * \left( \frac{1}{1 - re_f(N) * re_b(M)} \right) \quad (1.8)$$

Total transmittance, forward direction,

$$\begin{aligned} \tau_f(M+N) &= tr_f(M) * tr_f(N) + \\ &\quad tr_f(M) * re_f(N) * re_b(M) * tr_f(N) + \\ &\quad tr_f(M) * re_f(N) * re_b(M) * re_f(N) * re_b(M) * tr_f(N) + \dots \Rightarrow \\ \tau_f(M+N) &= tr_f(M) * tr_f(N) * \left( \frac{1}{1 - re_f(N) * re_b(M)} \right) \end{aligned} \quad (1.9)$$

Similarly, total transmittance, backward direction,

$$\tau_b(M+N) = tr_b(N) * tr_b(M) * \left( \frac{1}{1 - re_b(M) * re_f(N)} \right) \quad (1.10)$$

Absorbance of system M, forward direction,

$$\begin{aligned} \alpha_{Mf}(M+N) &= ab_f(M) + \\ &\quad tr_f(M) * re_f(N) * ab_b(M) + \\ &\quad tr_f(M) * re_f(N) * re_b(M) * re_f(N) * ab_b(M) + \dots \Rightarrow \\ \alpha_{Mf}(M+N) &= ab_f(M) + tr_f(M) * re_f(N) * ab_b(M) * \left( \frac{1}{1 - re_b(M) * re_f(N)} \right) \end{aligned} \quad (1.11)$$

Absorbance of system N, forward direction,

$$\begin{aligned} \alpha_{Nf}(M+N) &= tr_f(M) * ab_f(N) + \\ &\quad tr_f(M) * re_f(N) * re_b(M) * ab_f(N) + \dots \Rightarrow \\ \alpha_{Nf}(M+N) &= tr_f(M) * ab_f(N) * \left( \frac{1}{1 - re_f(N) * re_b(M)} \right) \end{aligned} \quad (1.12)$$

Similarly, absorptance of system M, backward direction,

$$\alpha_{Mb}(M+N) = \text{tr}_b(N) * \text{ab}_b(M) * \left\{ \frac{1}{1 - \text{re}_b(M) * \text{re}_f(N)} \right\} \quad (1.13)$$

and, absorptance of system N, backward direction,

$$\alpha_{Nb}(M+N) = \text{ab}_b(N) + \text{tr}_b(N) * \text{re}_b(M) * \text{ab}_f(N) * \left\{ \frac{1}{1 - \text{re}_f(N) * \text{re}_b(M)} \right\} \quad (1.14)$$

The relations (1.1) to (1.14) are the basis for recurrence relations that are suited for use in a digital computer program. These are finally used to calculate the total reflectance, absorptance and transmittance and the absorptance of each individual layer of a multi-layer system.

#### Derivation of the recurrence relations.

The system is made of  $N^*$  layers and the forward direction of the incoming radiation is the one from layer 1 to layer  $N^*$

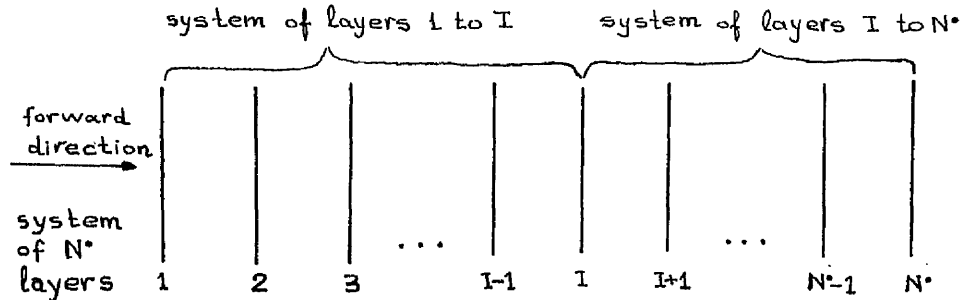


Fig. 1.5

We define:

for the individual layer  $i$ ,

reflectivity	$F_f(i)$ for forward	$F_b(i)$ for backward
transmissivity	$Y_f(i)$ direction	$Y_b(i)$ direction

for the system made of layers from 1 to  $I$

reflectance	$FR_f(I)$ for forward	$FR_b(I)$ for backward
transmittance	$YR_f(I)$ direction	$YR_b(I)$ direction

fraction of incident radiation on the total system of $N^*$ layers absorbed by the system of layers 1 to $I$	$AR_b(I)$
--	-----------

for the system made of layers from  $I$  to  $N^*$

reflectance	$FT_f(I)$ for forward	$FT_b(I)$ for backward
transmittance	$YT_f(I)$ direction	$YT_b(I)$ direction

fraction of incident radiation on the total system of $N^*$ layers absorbed by the system of layers $I$ to $N^*$	$AT_f(I)$
--	-----------

Finally, the absorptance<sup>+</sup> of the individual layer  $i$  of the multi-

layer system of  $N^*$  layers is  $AS_f(i)$  for forward direction and  $AS_b(i)$

for backward direction.

The recurrence relations are:

$$\begin{aligned} FT_f(N^*) &= F_f(N^*) \\ YT_f(N^*) &= Y_f(N^*) \\ FT_b(N^*) &= F_b(N^*) \\ YT_b(N^*) &= Y_b(N^*) \end{aligned} \quad \text{for } i = N^*$$

<sup>+</sup> fraction of the incident radiation on the system of  $N^*$  layers absorbed by the individual layer  $i$

$$\begin{aligned} FT_f(i) &= F_f(i) + Y_f(i) * FT_f(i+1) * Y_b(i) / (1 - F_b(i) * FT_f(i+1)) \\ YT_f(i) &= Y_f(i) * YT_f(i+1) / (1 - F_b(i) * FT_f(i+1)) \\ FT_b(i) &= FT_b(i+1) + YT_b(i+1) * F_b(i) * YT_f(i+1) / (1 - F_b(i) * FT_f(i+1)) \\ YT_b(i) &= YT_b(i+1) * Y_b(i) / (1 - F_b(i) * FT_f(i+1)) \end{aligned}$$

for i from N-1 to 1

$$\begin{aligned} FR_f(1) &= F_f(1) \\ YT_f(1) &= Y_f(1) \\ FR_b(1) &= F_b(1) \\ YR_b(1) &= Y_b(1) \end{aligned}$$

for i = 1

and,

$$\begin{aligned} FR_f(i) &= FR_f(i-1) + YR_f(i-1) * F_f(i) * YR_b(i-1) / (1 - FR_b(i-1) * F_f(i)) \\ FR_f(i) &= YR_f(i-1) * Y_b(i) / (1 - FR_b(i-1) * F_f(i)) \\ FR_b(i) &= F_b(i) + Y_b(i) * FR_b(i-1) * Y_f(i) / (1 - FR_b(i-1) * F_b(i)) \\ YR_b(i) &= Y_b(i) * YR_b(i-1) / (1 - FR_b(i-1) * F_f(i)) \end{aligned}$$

for i from 2 to N\*

$$AR_b(i) = YT_b(i+1) * (1 - FR_b(i) - YR_b(i)) / (1 - FR_b(i) * FT_f(i+1))$$

for i from 1 to N-1

and,

$$AR_b(N^*) = 1 - FR_b(N^*) - YR_b(N^*)$$

for i = N\*

$$AT_f(i) = YR_f(i-1) * (1 - FT_f(i) - YT_f(i)) / (1 - FT_f(i) * FR_b(i-1))$$

for i from N\* to 2

and,

$$AT_f(1) = 1 - FT_f(1) - YT_f(1)$$

for i = 1

$$AS_f(N^*) = AT_f(N^*)$$

for i = N\*

$$AS_f(i) = AT_f(i) - AT_f(i+1)$$

for i from N-1 to 1

$$AS_b(1) = AR_b(1)$$

for i = 1

$$AS_b(i) = AR_b(i) - AR_b(i-1)$$

for i from 2 to N\*

A closed-formula example is given in Appendix A. The example stresses the fact that an optical system may behave differently for opposite direction incident radiation, not only in respect to the total reflectance as is usually shown by other techniques, but in respect to the total transmittance as well (in the case of occurrence of total reflection).

## 1.2 THE 3-DIMENSIONAL RAY-TRACING TECHNIQUE

The transmittance equations for glass covers of flat plate solar collectors given by Gillette et. al.(21) can be considered as an approach to handle a multi-dimensional optical system. In their approach the solar vector angular variations are taken into account under certain assumptions.

The present technique has the following basic characteristics:

1. Small control volumes are constructed which fill the domain of the optical system and a space surrounding the optical system. The aim is to calculate the rate of radiation absorption at every control volume and every boundary between two control volumes. Furthermore, the radiation that escapes from, or is absorbed at, a part or the whole outer boundary of the space which surrounds the optical system, is also calculated. See Fig. 1.6.
2. If external radiation, falling on the outer boundary of the space is volumetrically uniform, then it is approximated by discrete pencils of radiation.

The number, type and size of the control volumes and the number of the pencils of radiation and their points of incidence are determined after a compromise between a reasonable accuracy and computational effort has been made. They strongly depend on the specific characteristics of the optical system. It should be remembered that, generally, the larger the

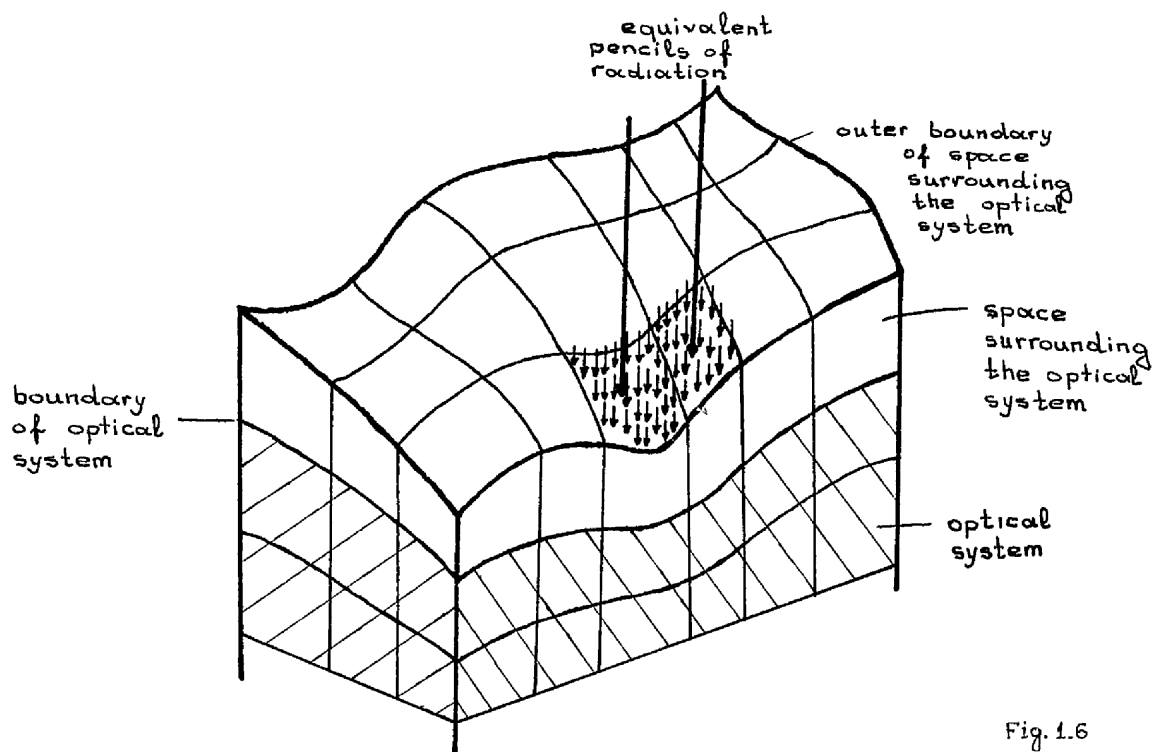
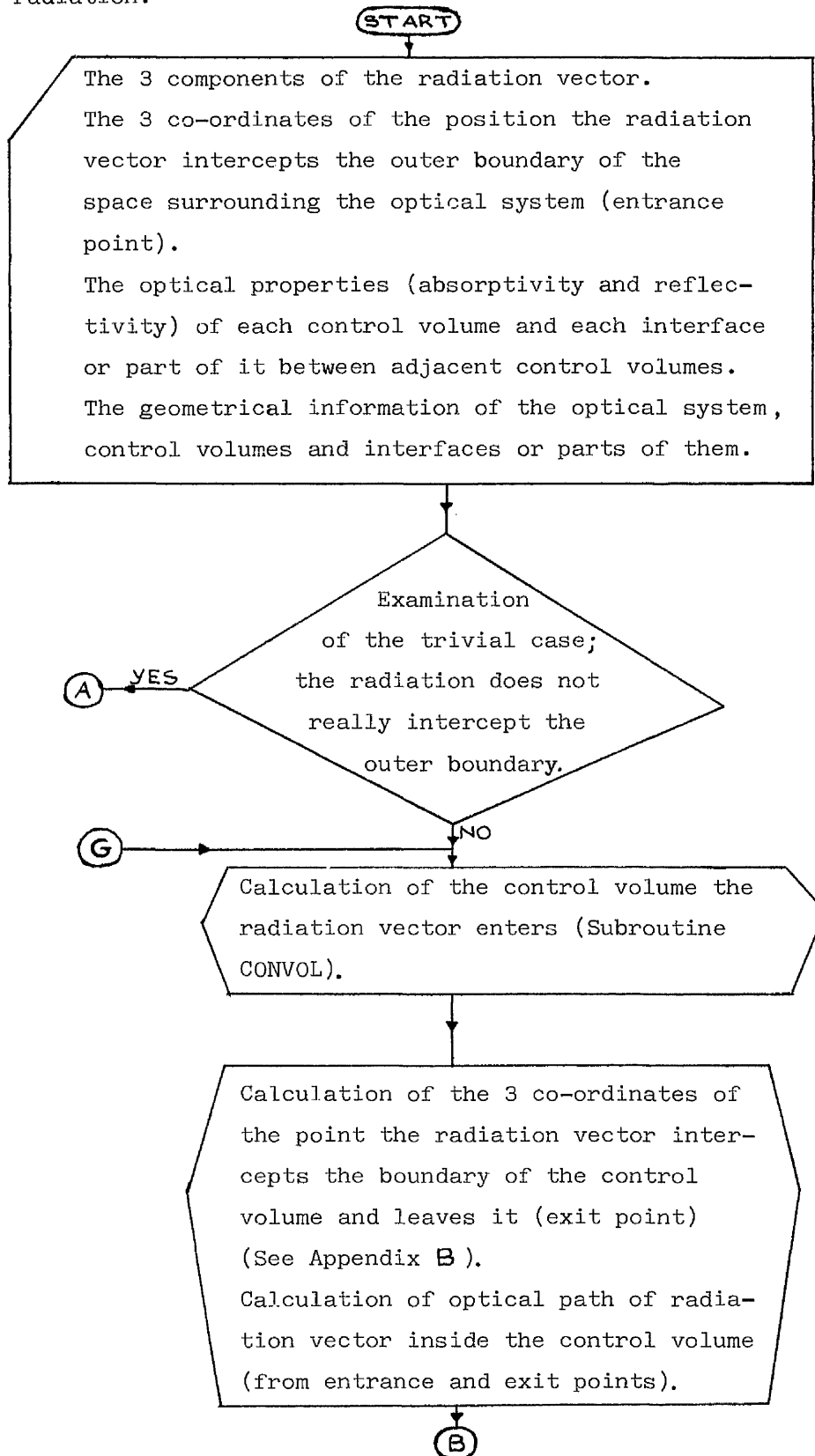


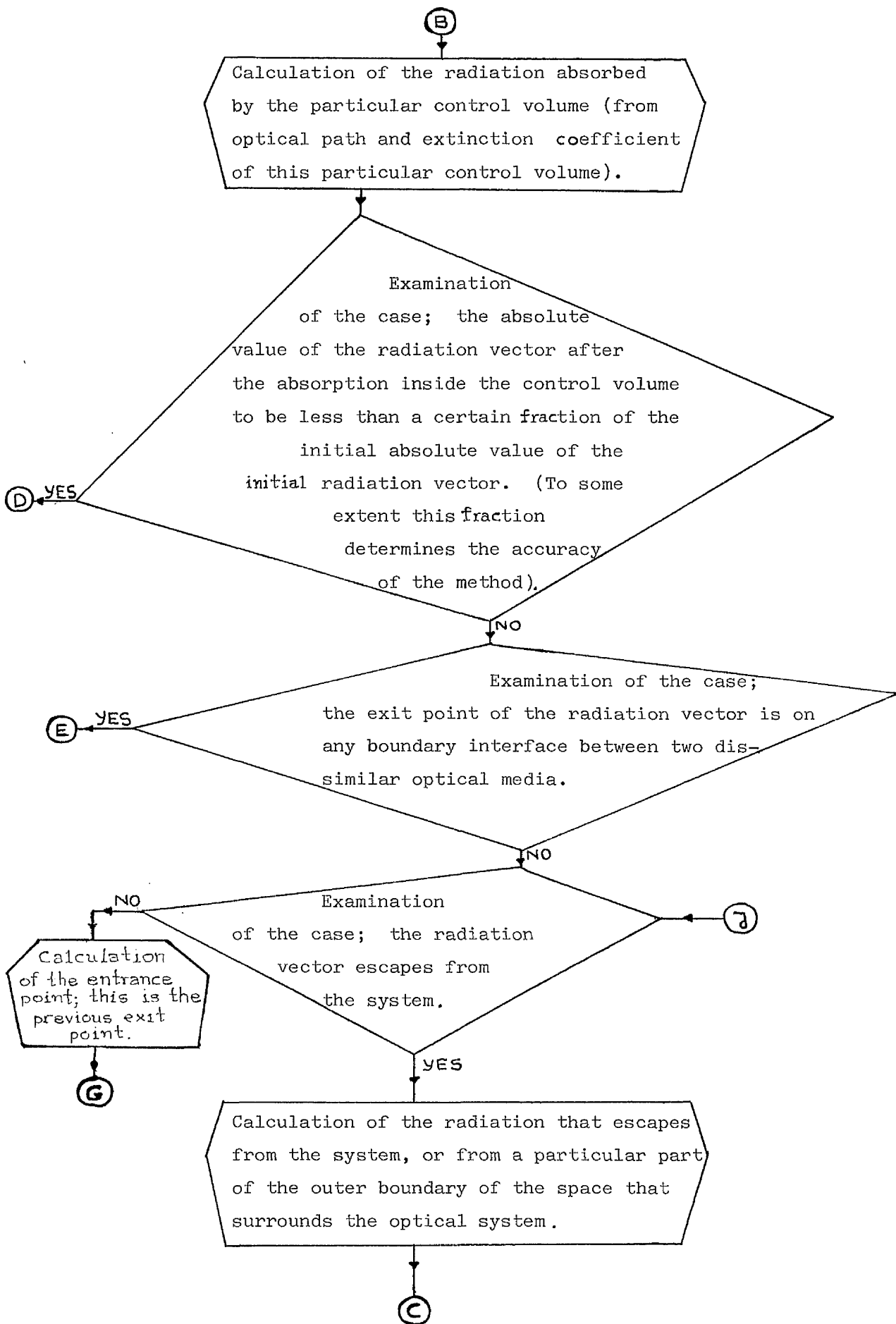
Fig. 1.6

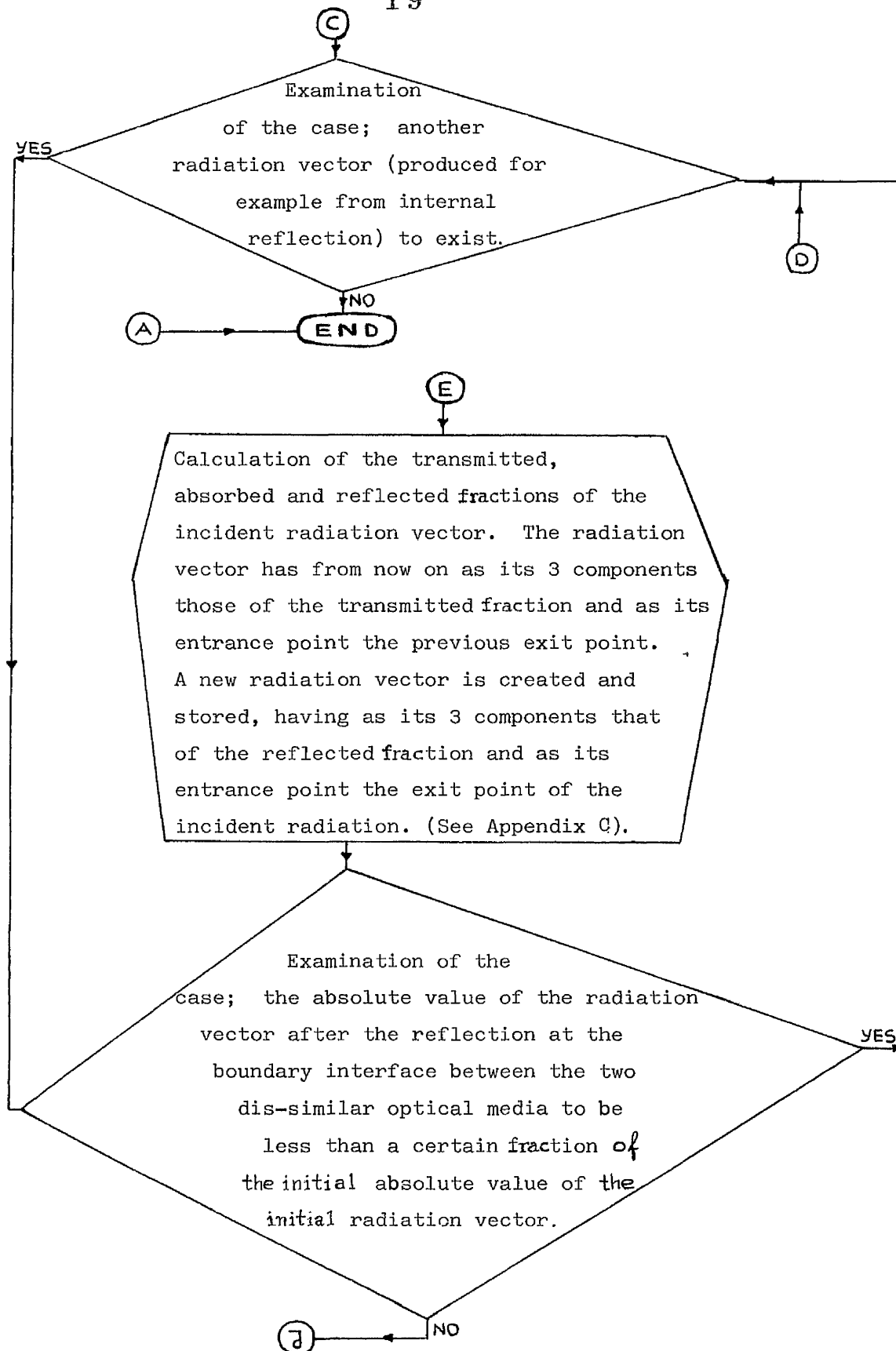


number of control volumes and the pencils of radiation, the better the accuracy but the larger the computational effort.

The following flow-chart illustrates the basic steps taken in the 3-dimensional optical system ray-tracing technique, for each pencil of radiation.







The optical properties of each control volume and each interface between two adjacent control volumes can be understood to be spectral or monochromatic values or they can be regarded as total gray values.

### 1.3 APPLICATION OF THE 1-DIMENSIONAL RAY-TRACING TECHNIQUE TO A TRANSWALL SYSTEM ELEMENT.

The importance of the following are examined:

- 1) Angular variation in direct solar radiation.
- 2) Anisotropy and polarization of the diffuse solar radiation from the sky and the ground.
- 3) The spectrum and polarization effects within the transwall system element.

The present analysis concerns a module made of 6mm thickness annealed glass. This module of 0.15 m(thickness), 1.12 m (width) and 0.61m (height) internal dimensions, was a part of a solar passive test-box constructed at the M.E.R.A., University of Glasgow. The module contained a weak solution of acid green B in water (strength of solution,  $W^* = 9.164 \times 10^{-9}$  Kg of acid green B/Kg water). The outside glass plate, in front of the module, was 4mm thickness annealed glass. The properties of clear float glass from Pilkington have been used for those of annealed glass in the present analysis. More details of the module and the test box are given in section 2.5.

In Fig. 1.7 a part of the cross section view of the transwall module and its outside glass plate is shown. Only the cross section is actually of significance in this present 1-dimensional ray-tracing technique. The direction from the outside glass plate to the module is defined as the forward direction of the incoming radiation.

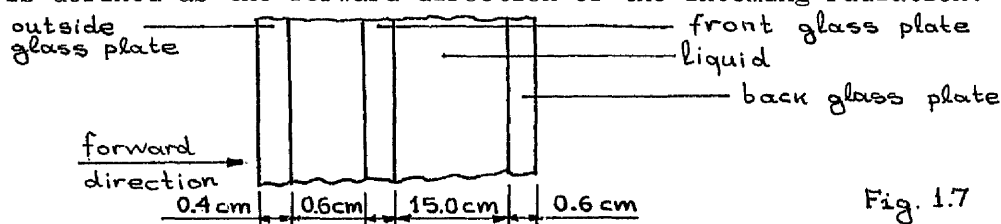


Fig. 1.7

The optical properties (refractive index and extinction coefficient) of clear float glass made by Pilkington, water and acid green B averaged over 8 different wavelength bands are given in Table 1.1. (see also Appendix D). In the same table, the extinction coefficient of Antisun glass, grey 41/60 made by Pilkington, a possible candidate for the middle absorbing glass of a transwall module, is also included. The actual extinction coefficient,  $K$ , of the solution to be used in the Bouguer's law relation for the calculation of the absorptance or transmittance of the particular solution over a certain optical path ( $e^{-K \cdot t}$ ,  $t$  = optical path) depends on the concentration of dye C and the wavelength  $\lambda^*$  of radiation. For a liquid solution in which a particular concentration of dye is responsible for the optical attenuation through the liquid, an extinction coefficient  $\epsilon$  can be

defined which depends only on the type of dye and the wavelength of radiation, but not on the concentration  $C$  of the dye in solution (22). In this case, the Beer-Lambert relation can be used.

$$K(\lambda^*, C) = \epsilon(\lambda^*) * C + a_s(\lambda^*) \quad (1.15)$$

where  $a_s(\lambda)$  is the extinction coefficient due to the solvent. The same relation is used for averaged values over wavelength band,  $\lambda_b^*$ ,

$$K(\lambda_b^*, C) = \epsilon(\lambda_b^*) * C + a_s(\lambda_b^*) \quad (1.16)$$

(See in Appendix E, the extinction coefficient of various dyes).

In Table 1.2 the averaged solar radiation at 8 wavelength bands, is given as part of the solar radiation over the whole spectrum for 5 different spectra of solar radiation. See Appendix F for the calculation of the spectral composition of the components of solar radiation. The calculation of the optical properties of each optical system is performed separately for each of the 8 wavelength bands, using the averaged values of Tables 1.1 and 1.2. This certainly leads to an approximation; but it is a convenient compromise between accuracy of the calculated values and computational effort. Hull (34) used 40 equal wavelength bands between the wavelengths of 0.3125 and 1.3125 for both direct and diffuse radiation.

These 8 particular wavelength bands were mainly chosen on the basis that knowledge of 1) the radiation at the four main portions of the spectrum (ultra-violet, visible, near infrared, infrared) is generally useful for every solar thermal system, 2) the transmitted radiation through a glazing or transwall system in the visible portion of spectrum is necessary to assess the effectiveness of the glazing or transwall system as a lighting source of a building during the day-time.

In Appendix L (Table L3), the averaged solar radiation at 8 different wavelength bands, appropriate now for research in green-houses (35) is given as part of the solar radiation over the whole spectrum for 5 different spectra of solar radiation. This Appendix also gives (Table L4) the refractive index and extinction coefficient of clear float glass from Pilkington and water, averaged at these 8 new wavelength bands.

A comparison of 1-dimensional ray-tracing techniques with an infinite and a finite number of internal reflection for this particular optical system is given in Appendix N.

Table 1.1

Averaged optical properties of water, clear float glass, Antisun glass and acid green B.

wavelength band ( $\mu\text{m}$ )	refractive index of water	extinction coefficient of water ( $\text{m}^{-1}$ )	extinction coefficient of acid green B (Kg of water/ mol dye * m)	refractive index of clear float glass	extinction coefficient of clear float glass ( $\text{m}^{-1}$ )	extinction coefficient of Antisun glass ( $\text{m}^{-1}$ )
0.3 + 0.35	1.346	$4.428 \times 10^{-2}$	$1.898 \times 10^{+6}$	1.511	540.41	8146.54
0.35 + 0.4	1.341	$1.773 \times 10^{-2}$	$1.463 \times 10^{+6}$	1.514	20.59	153.67
0.4 + 0.6	1.335	$1.483 \times 10^{-2}$	$4.644 \times 10^{+5}$	1.514	8.88	125.35
0.6 + 0.75	1.331	$3.895 \times 10^{-1}$	$1.038 \times 10^{+6}$	1.511	21.83	108.35
0.75 + 0.9	1.329	$2.583 \times 10^0$	$6.869 \times 10^{+5}$	1.512	44.55	125.42
0.9 + 1.2	1.326	$7.106 \times 10^1$	$1.575 \times 10^{+5}$	1.511	55.24	157.95
1.2 + 2.1	1.315	$7.114 \times 10^3$	$6.362 \times 10^{+5}$	1.513	33.43	101.56
2.1 + 4.1	1.332	$2.0 \times 10^6$	-	1.510	244.79	2000.00

Table 1.2

Fractional average solar radiation (total radiation = 1.0)

wavelength band ( $\mu\text{m}$ )	Air Mass, Mr			
	1	2	4	7
0.3 + 0.35	0.014	0.006	0.001	0.000
0.35 + 0.4	0.034	0.022	0.010	0.003
0.4 + 0.6	0.298	0.279	0.234	0.170
0.6 + 0.75	0.203	0.215	0.236	0.247
0.75 + 0.9	0.128	0.142	0.150	0.169
0.9 + 1.2	0.143	0.146	0.151	0.159
1.2 + 2.1	0.144	0.150	0.173	0.199
2.1 + 4.1	0.036	0.040	0.045	0.053
				0.000
				0.001
				0.120
				0.245
				0.184
				0.164
				0.223
				0.063
				ultra-violet
				»
				visible
				»
				near infrared
				»
				infrared
				»

+ data: References (26) and (27).

### 1.3.1 Direct radiation - Discussion of the results

#### Total Reflectance

This is an important factor not only of the optical system itself but of the thermal system, because it is an indirect measure of the energy available.

The angular variation of the total reflectance of the transwall element for incoming radiation from both directions is the typical one met in glazing systems (Fig. 1.8, Tables 1.3 to 1.6). The total reflectance is almost constant until about  $45^\circ$  angle of incidence, after which it becomes progressively higher as the angle of incidence increases. The rate of increase of total reflectance is smaller in the case of the transwall element with backward direction of the incoming radiation (compare, as an example, Tables 1.3 and 1.5) until about  $80^\circ$  angle of incidence, when it becomes larger. As was expected, the total reflectance of the transwall element with backward direction of the incoming radiation is smaller than that with forward. The difference is about 3% of the total incoming radiation at  $0^\circ$  angle of incidence and rises to about 9% of the total incoming radiation at about  $80^\circ$  angle of incidence (compare for example Tables 1.3 and 1.5).

The spectral composition of the incoming radiation is not an important factor in determining the total reflectance for its both directions. Spectral compositions of the incoming radiation of air-mass 1, 2, 4, 7 and 10 were examined. This is shown in Fig. 1.8 and Tables 1.3 and 1.4. A 1% difference in values of total reflectance for the same angle of incidence but different air-mass is small relative to uncertainties in determining the total incident radiation.

For the same reason accounting for the effect of the polarization of radiation on its way through the optical system is not justified by the better accuracy of the calculated total reflectance. In addition the required computational time is doubled. The maximum difference in values of total reflectance attributable to the polarization of radiation occurs in the region of  $70^\circ$  angle of incidence and is about 3 ÷ 4 % of the incident radiation. It should be mentioned here that accounting for the polarization always gives smaller optical values. (See, for example, Tables 1.3 and 1.6).

Total transmittance - Spectral composition of the transmitted radiation.

The results are exactly the same for both directions of the incoming radiation, forward or backward, because there is no chance of total reflection occurrence in the system, as it can be seen from the analysis of page 237 of Appendix A.

The total transmittance of the transwall element is almost constant for angles of incidence from  $0^{\circ}$  to about  $20^{\circ}$ . Then it becomes progressively lower and as the angle of incidence increases with a higher rate of change after  $50^{\circ}$  angle of incidence (Fig. 1.9 and Tables 1.3 to 1.6). The spectral composition of the transmitted radiation changes much less than the value of the total transmittance with the increase of angle of incidence, practically after  $25^{\circ}$  angle of incidence. This change of the spectral composition actually favours the visible fraction of the transmitted radiation that always is the main fraction (more than 80% of the transmitted radiation). This means that there is a potential of about 20% of the transmitted radiation that can be absorbed further by the transwall system without any effect on the quality of the transwall element as a lighting source. It should be mentioned that the visible fraction of air-mass 1 is 50.1% and of air-mass 10 36.5% of the total solar radiation.

The spectral composition of the incident radiation is quite important in determining both the total transmittance of the system and the spectral composition of the transmitted radiation, as Fig. 1.9 and Tables 1.3 to 1.6 show. The difference in values of total transmittance for air-mass 1 and 10 spectral compositions is about 11% of the incident radiation for angles of incidence from  $0^{\circ}$  to about  $60^{\circ}$ . This difference becomes progressively smaller as the angle of incidence increases to  $90^{\circ}$  when the total transmittance becomes virtually zero. The large difference in the spectral composition of the transmitted radiation for different air-mass spectra of incident radiation remains unchanged, for every angle of incidence, as Tables 1.3 and 1.4 show.

Taking into account polarization is not justified by the resulting slight increase in accuracy, for both total transmittance and spectral composition of the transmitted radiation. Note (for example Tables 1.3 and 1.6) that the inclusion of polarization leads to a slightly higher total transmittance.



## Absorptance of individual layers

### Glass plates

The absorptance<sup>+</sup> of the outside glass plate and the front glass plate increases as the angle of incidence increases until about 70° angle of incidence for the former and about 45° angle of incidence for the latter, after which it starts decreasing rapidly. The rate of change of absorptance<sup>+</sup> is always higher in the case of the outside glass plate. The absorptance<sup>+</sup> of the back glass plate remains almost constant until about 20° angle of incidence and then it steadily decreases as the angle of incidence increases.<sup>++</sup> (Fig. 1.10 and Tables 1.3 to 1.6).

The spectral composition of the incident radiation is not an important factor in determining the absorptance of the glass plates. The highest difference in values of absorptance for different air-mass spectra occurs in the case of the outside glass plate. This difference does not exceed 3% of the incident radiation for the two rather extreme cases of calculating the absorptance for air-mass 1 and 10.

Again the increased complexity of incorporating polarization into the analysis is not justified by the small increase in the accuracy of the absorptance.

### Liquid layer

The absorptance of the liquid becomes progressively lower with increasing incident angle. The rate of this change is near zero until a critical angle of incidence after which the rate increases rapidly. The critical angle is 20° for the transwall element with forward incoming radiation and 45° for the transwall element with backward incoming radiation. The effect is demonstrated in Fig. 1.11 and Tables 1.3 to 1.6. The same holds for the individual sub-layers of the liquid layer.

The spectral composition of the incident radiation is quite important in determining the absorptance of the liquid for both directions of the incoming radiation, and angle of incidence smaller than about 65° (Fig. 1.11 and Tables 1.3 to 1.4). For example, at 0° angle of incidence the difference of absorptance of the liquid for air-mass 1 and air-mass 10 is about 7.5% of the incident radiation for forward direction and about 9.7% of the incident radiation for backward direction.

Again, taking into account the polarization of radiation in its way through the optical systems is not justified by the better accuracy of the calculated absorptance as Tables 1.3, 1.6 show. The reasons are the same as in the case of total reflectance.

+for forward direction of the incoming radiation.  
++ For backward direction, similar but inverse behaviour of the absorptance of the three glass plates occurs.

Table 1.3

Total reflectance and transmittance of the transwall element. Absorptance of each layer of the element and spectral composition of the transmitted radiation for incident direct radiation of Air-Mass 1. Account taken of polarization. Forward direction of incoming radiation. % of incident radiation.

Angle of incidence +	Total reflectance	Total transmittance	Spectral composition of the transmitted radiation (%)								Absorptance of outside glass	Absorptance of front glass	Absorptance of 1st layer of liquid, 1.2cm	Absorptance of 2nd layer of liquid, 12.6cm	Absorptance of 3rd layer of liquid, 1.2cm	Absorptance of liquid	Absorptance of back glass
0°	11.3	38.8	.300 + .350 $\mu$ m	.350 + .400 $\mu$ m	.400 + .600 $\mu$ m	.600 + .750 $\mu$ m	.750 + .900 $\mu$ m	.900 + 1.20 $\mu$ m	1.20 + 2.10 $\mu$ m	2.10 + 4.10 $\mu$ m	13.5	12.0	13.8	5.8	0.2	19.8	4.5
15°	11.3	38.6	0.0	5.3	56.1	29.3	9.2	0.0	0.0	0.0	13.7	12.1	13.8	5.8	0.2	19.8	4.5
30°	11.4	37.9	0.0	5.3	56.8	29.2	8.7	0.0	0.0	0.0	14.2	12.4	13.6	5.7	0.2	19.5	4.6
45°	12.6	36.3	0.0	5.3	57.6	28.9	8.2	0.0	0.0	0.0	14.9	12.7	13.2	5.4	0.2	18.8	4.7
60°	18.4	31.9	0.0	5.3	58.6	28.6	7.4	0.0	0.0	0.0	15.8	12.3	11.9	4.9	0.2	17.0	4.6
75°	41.9	18.5	0.0	5.2	60.0	27.8	6.5	0.0	0.0	0.0	16.3	8.7	7.7	3.2	0.2	11.1	3.6
89.5°	95.9	0.0	0.0	2.8	83.3	12.6	1.3	0.0	0.0	0.0	3.7	0.2	0.0	0.0	0.0	0.0	0.1

+ conventionally defined

Table 1.4

Total reflectance and transmittance of the transwall element. Absorptance of each layer of the element and spectral composition of the transmitted radiation for incident direct radiation of Air-Mass 10. Account taken of polarization. Forward direction of incoming radiation. % of incident radiation.

Angle of incidence +	Total reflectance	Total transmittance	spectral composition of the transmitted radiation (%)										Absorptance of outside glass	Absorptance of front glass	Absorptance of 1st layer of liquid, 1.2cm	Absorptance of 2nd layer of liquid, 12.6cm	Absorptance of 3rd layer of liquid, 1.2cm	Total absorptance of liquid	Absorptance of back glass
			0.30 + 0.35 μm	0.35 + 0.40 μm	0.40 + 0.60 μm	0.60 + 0.75 μm	0.75 + 0.90 μm	0.90 + 1.20 μm	1.20 + 2.10 μm	2.10 + 4.10 μm									
0°	10.5	27.7	0.0	0.2	31.7	49.6	18.6	0.0	0.0	0.0	15.8	14.4	19.7	7.3	0.3	27.3	4.3		
15°	10.5	27.5	0.0	0.2	31.8	49.6	18.4	0.0	0.0	0.0	16.0	14.5	19.6	7.2	0.3	27.1	4.3		
30°	10.6	26.8	0.0	0.2	32.3	49.7	17.8	0.0	0.0	0.0	16.6	14.8	19.4	7.2	0.3	26.9	4.4		
45°	11.7	25.4	0.0	0.2	33.1	49.9	16.8	0.0	0.0	0.0	17.5	15.1	18.7	6.8	0.3	25.8	4.4		
60°	17.4	22.0	0.0	0.2	34.3	50.0	15.4	0.0	0.0	0.0	18.6	14.5	16.8	6.0	0.3	23.1	4.2		
75°	40.1	12.5	0.0	0.2	36.2	49.7	13.8	0.0	0.0	0.0	19.2	10.1	10.8	4.0	0.2	15.0	3.2		
89.5°	95.7	0.0	0.0	0.2	66.2	30.0	3.6	0.0	0.0	0.0	4.0	0.1	0.1	0.0	0.0	0.1	0.1		

+ conventionally defined

Table 1.5

Total reflectance and transmittance of the transwall element. Absorptance of each layer of the element and spectral composition of the transmitted radiation for incident direct radiation of Air-Mass 1. Account taken of polarization. Backward direction of incoming radiation. % of incident radiation

Angle of incidence +	Total reflectance	Total transmittance	spectral composition of the transmitted radiation (%)										Absorptance of 1st layer of liquid, 1.2cm	Absorptance of 2nd layer of liquid, 12.6cm	Absorptance of 3rd layer of liquid, 1.2cm	Absorptance of liquid	Absorptance of back glass
			0.30 + 0.35 $\mu\text{m}$	0.35 + 0.40 $\mu\text{m}$	0.40 + 0.60 $\mu\text{m}$	0.60 + 0.75 $\mu\text{m}$	0.75 + 0.90 $\mu\text{m}$	0.90 + 1.20 $\mu\text{m}$	1.20 + 2.10 $\mu\text{m}$	2.10 + 4.10 $\mu\text{m}$	Absorptance of outside glass	Absorptance of front glass					
0°	8.5	38.8	0.0	5.3	56.1	29.3	9.2	0.0	0.0	0.0	2.9	5.7	0.4	7.7	18.0	26.1	17.9
15°	8.5	28.6	0.0	5.3	56.3	29.3	9.1	0.0	0.0	0.0	2.9	5.8	0.4	7.7	18.0	26.1	18.1
30°	8.6	37.9	0.0	5.3	56.8	29.2	8.7	0.0	0.0	0.0	3.0	5.9	0.4	7.6	18.0	26.0	18.7
45°	9.5	36.3	0.0	5.3	57.6	28.9	8.2	0.0	0.0	0.0	3.1	6.1	0.4	7.5	17.8	25.7	19.5
60°	14.2	31.9	0.0	5.3	58.8	28.6	7.4	0.0	0.0	0.0	3.0	6.4	0.4	6.9	17.0	24.3	20.1
75°	33.9	18.5	0.0	5.2	60.6	27.8	6.5	0.0	0.0	0.0	2.3	6.7	0.4	6.0	14.0	20.4	18.3
89.5°	95.3	0.0	0.0	2.8	83.3	12.6	1.3	0.0	0.0	0.0	0.1	1.1	0.0	0.5	0.9	1.4	1.9

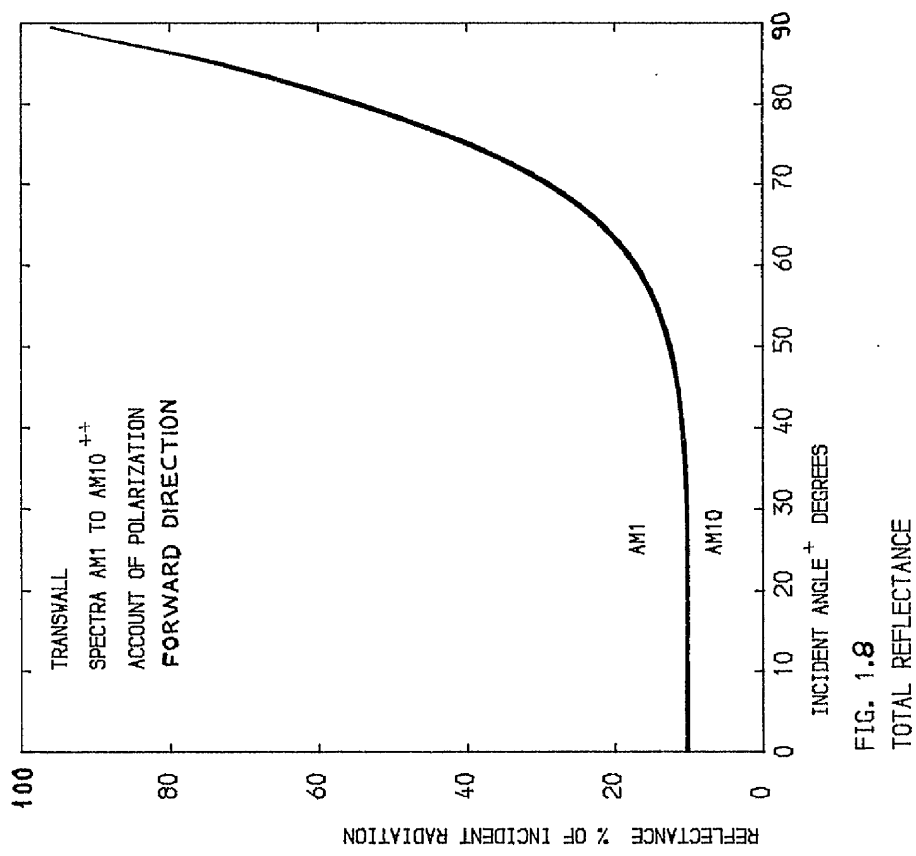
+ conventionally defined

Table 1.6

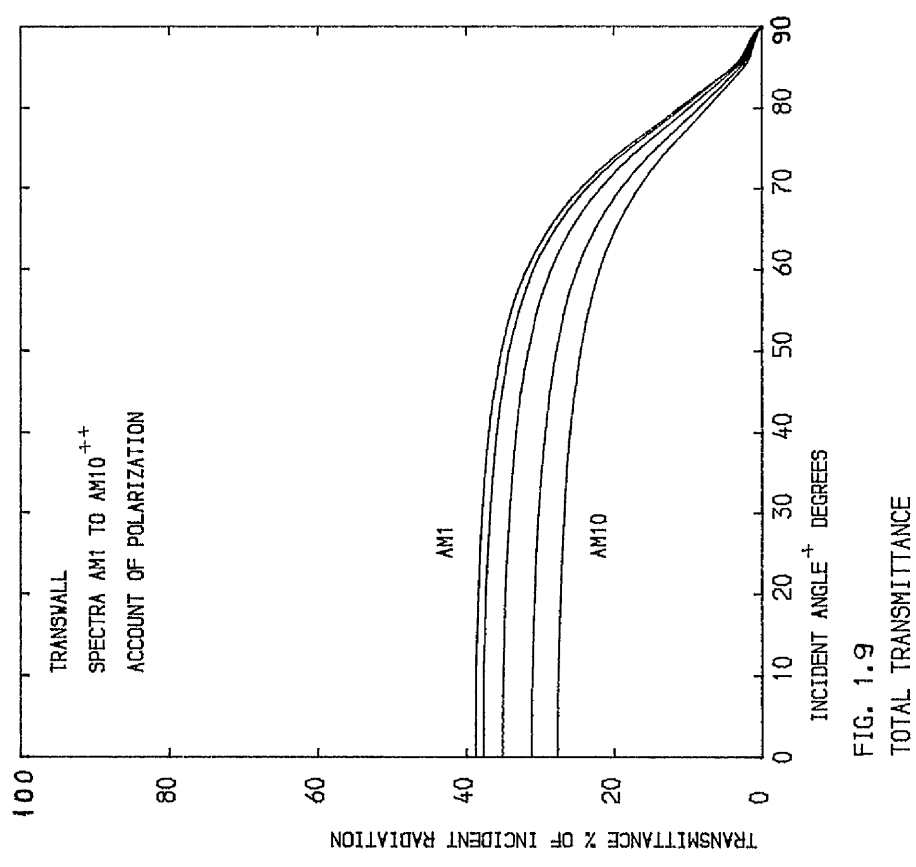
Total reflectance and transmittance of the transwall element. Absorptance of each layer of the element and spectral composition of the transmitted radiation for incident direct radiation of Air-Mass 1. Polarization is not taken into account. Forward direction of incoming radiation. % of incident radiation.

Angle of incidence <sup>+</sup>	Total reflectance	Total transmittance	spectral composition of the transmitted radiation (%)								Absorptance of outside glass	Absorptance of front glass	Absorptance of 1st layer of liquid, 1.2cm	Absorptance of 2nd layer of liquid, 12.6cm	Absorptance of 3rd layer of liquid, 1.2cm	Absorptance of liquid	Absorptance of back glass
0°	11.3	38.8	0.30 + 0.35 μm	0.35 + 0.40 μm	0.40 + 0.60 μm	0.60 + 0.75 μm	0.75 + 0.90 μm	0.90 + 1.20 μm	1.20 + 2.10 μm	2.10 + 4.1 μm	13.5	12.0	13.8	5.8	0.2	19.8	4.5
15°	11.3	38.6	0.0	5.3	56.3	29.3	9.1	0.0	0.0	0.0	13.7	12.1	13.8	5.8	0.2	19.8	4.5
30°	11.5	37.8	0.0	5.3	56.8	29.2	8.7	0.0	0.0	0.0	14.2	12.4	13.6	5.7	0.2	19.5	4.6
45°	13.4	35.7	0.0	5.3	57.6	29.0	8.2	0.0	0.0	0.0	15.0	12.6	13.1	5.3	0.2	18.6	4.7
60°	21.4	29.9	0.0	5.3	58.7	28.6	7.4	0.0	0.0	0.0	16.0	11.9	11.5	4.6	0.2	16.3	4.5
75°	45.4	16.1	0.0	5.2	61.0	27.5	6.3	0.0	0.0	0.0	16.7	8.2	7.0	3.1	0.2	10.3	3.4
89.5°	95.8	0.0	0.0	2.7	84.5	11.7	1.1	0.0	0.0	0.0	3.8	0.2	0.0	0.0	0.0	0.0	0.1

+ conventionally defined



+ conventionally defined  
++ AM = air mass



+ conventionally defined  
++ AM = air mass

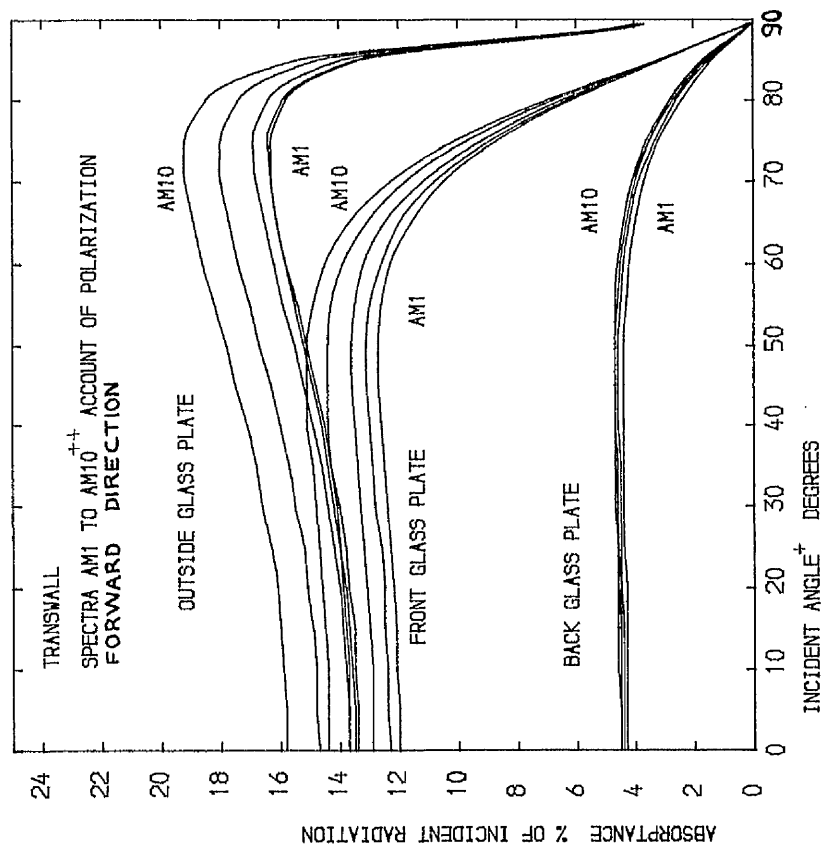


FIG. 1.10  
ABSORPTANCE OF GLASS PLATES

+ conventionally defined  
++ AM = air mass

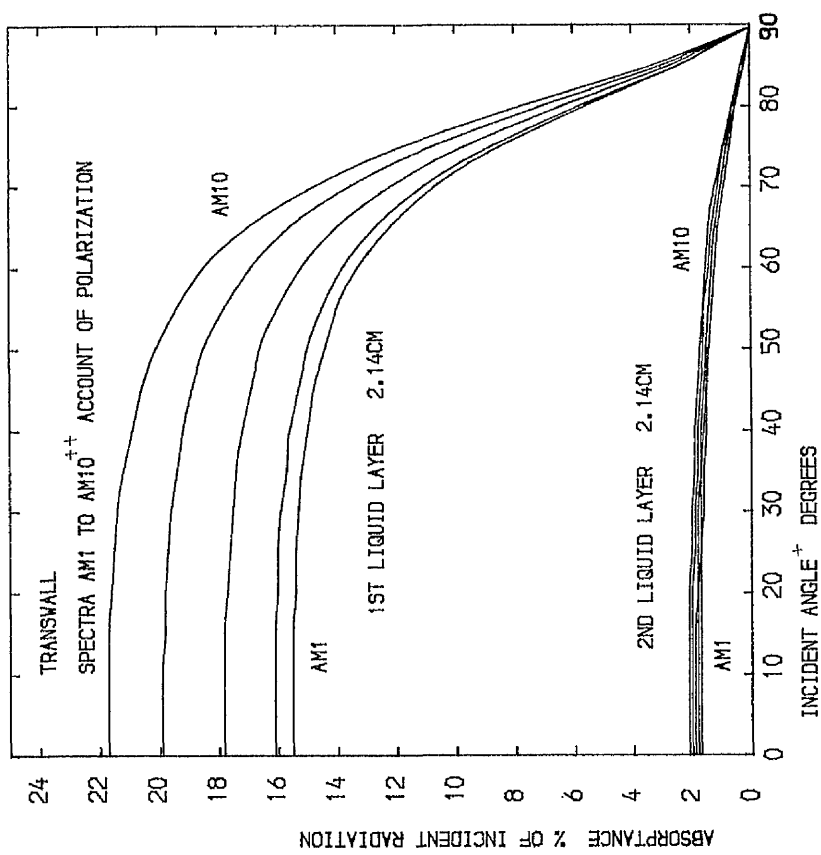


FIG. 1.11  
ABSORPTANCE OF TWO LIQUID LAYERS

FORWARD DIRECTION

+ conventionally defined  
++ AM = air mass





there was information available. These two types of radiation are for a cloudless sky and solar altitude angle of  $39^\circ$  and for a cloudy sky with solid stratocumulus clouds and solar altitude angle of  $48^\circ$ . The distribution (relative) of these two types of sky diffuse radiation over the sky dome are given in figure forms, in (36). Simplified tabular forms of these distributions are given in Tables 1.7, 1.8.

Table 1.7

Relative distribution of diffuse radiation over the sky dome for a cloudless sky, for solar altitude angle of  $39^\circ$

$T_1$	$90^\circ$	$120^\circ$ or $60^\circ$	$150^\circ$ or $30^\circ$	$180^\circ$ or $0^\circ$	$210^\circ$ or $330^\circ$	$240^\circ$ or $300^\circ$	$270^\circ$
$t_1$							
$0^\circ$	0.8	0.8	0.8	0.7	0.6	0.8	1.0
$15^\circ$	0.5	0.7	0.6	0.4	0.4	0.7	1.3
$30^\circ$	0.3	0.5	0.4	0.4	0.4	0.6	1.3
$45^\circ$	0.5	0.6	0.7	0.4	0.4	0.6	1.2
$60^\circ$	0.9	0.9	0.9	0.5	0.4	0.6	0.8
$75^\circ$	0.9	0.9	0.9	0.8	0.7	0.8	0.9
$90^\circ$	1.0	1.0	1.0	1.0	1.0	1.0	1.0

Note: The angles  $t_1$  and  $T_1$  are the two spherical coordinates of a sky point corresponding to a cartesian system OXYZ (Fig. 1.12) in which the directions of axes OX, OY and OZ are the west-east, south-north and earth-zenith directions respectively.

Table 1.8

Relative distribution of diffuse solar radiation over the sky dome, for solid stratocumulus clouds, for a solar altitude angle of  $48^\circ$

$T_1$	$90^\circ$	$135^\circ$ or $45^\circ$	$180^\circ$ or $0^\circ$	$225^\circ$ or $315^\circ$	$270^\circ$
$t_1$					
$0^\circ$	0.8	0.8	0.8	0.4	0.6
$15^\circ$	0.6	0.2	0.2	0.3	0.4
$30^\circ$	0.3	0.4	0.4	0.5	1.0
$45^\circ$	0.4	0.6	0.6	0.8	1.3
$60^\circ$	0.6	0.7	0.8	0.9	1.3
$75^\circ$	0.8	0.8	0.9	1.0	1.2
$90^\circ$	1.0	1.0	1.0	1.0	1.0

Note: The angles  $t_1$  and  $T_1$  are the two spherical coordinates of a sky point corresponding to a cartesian system OXYZ (Fig. 1.12) in which the directions of axes OX, OY and OZ are the west-east, south-north and earth-zenith directions respectively.



$$X_P = X'_P$$

$$Y_P = Y'_P * \cos(-t') - Z'_P * \sin(-t')$$

$$Z_P = Y'_P * \sin(-t') + Z'_P * \cos(-t')$$

Because of relation (1.17) and (1.18),

$$X_P = \cos(T)$$

$$Y_P = \sin(T) * \cos(-t')$$

$$Z_P = \sin(T) * \sin(-t')$$

The surface A with vector  $\vec{P}_A$  receives radiation only from that part of the sky dome, for which:

$$0 \ll t' \ll (180^\circ - \theta^\circ)$$

The components of vector  $\vec{P}_A$  are:

$$X_A = \cos(90^\circ) * \cos(\theta^\circ + 90^\circ)$$

$$Y_A = \sin(90^\circ) * \cos(\theta^\circ + 90^\circ)$$

$$Z_A = \sin(\theta^\circ + 90^\circ)$$

or  $X_A = 0$

$$Y_A = -\sin(\theta^\circ)$$

$$Z_A = \cos(\theta^\circ)$$

So, the angle of incidence  $i$  of the intensity vector  $\vec{I}_p$  and surface A, or the angle between the vectors  $\vec{I}_p$  and  $\vec{P}_A$  is:

$$i = \cos^{-1}[-(X_P * X_A + Y_P * Y_A + Z_P * Z_A)]$$

$$\text{or } i = \cos^{-1}[(+\sin(T) * \cos(t') * \sin(\theta^\circ) + \sin(T) * \sin(t') * \cos(\theta^\circ))]$$

If  $I_p$  is the absolute value of vector  $\vec{I}_p$  then the contribution of point P of the sky with intensity vector  $\vec{I}_p$  to the diffuse radiation flux per unit solid angle in the direction OP, received by surface A, is given by the relation<sup>+</sup>:

$$\Delta q_p = -I_p * \cos(i)$$

So, the total diffuse radiation flux coming from the sky dome  $\Omega$  and received by the surface is:

$$q = \int_{\Omega} \Delta q_p * d\omega \quad (1.19)$$

The relation (1.19) is approximated by the relation (1.20):

$$q \approx \sum_{p=1}^N \Delta q_p * \Delta\omega \quad (1.20)$$

that means that the whole sky dome is separated into N equal small areas  $\Delta A'_p$ , each being assigned an intensity vector  $\vec{I}_p$ , passing through its centre.

It is known that

$$\Delta\omega = \Delta A'_p / r^2$$

where  $r$  is the sky dome imaginary radius.

So equation (1.20) takes the form:

+ The negative sign is explained by the fact that  $i > 90^\circ$ .

$$q \approx \sum_{p=1}^N (-I_p * \cos(i) * \Delta A'_p / r^2)$$

$$q \approx (\sum_{p=1}^N (-I_p * \cos(i))) * (\Delta A'_p / r^2)$$

If  $I_p^*$  is the relative value of the intensity  $I_p$  against a normal value  $I_o$ ,

$$I_p^* = I_p / I_o$$

then,

$$q \approx (\sum_{p=1}^N (-I_p^* * \cos(i))) * (I_o * \Delta A'_p / r^2)$$

As far as the calculation of the optical properties of a system is concerned the effect of each term  $I_p^* * \cos(i)$  on the particular property is separately determined and then all these  $N$  effects are properly averaged to give the value of the property for the particular sky conditions (subroutines ANN, ANNI, RENE). Tables 1.7 and 1.8 give actual values of  $I_p^*$  for the two types of anisotropic sky diffuse radiation. For these tables, the values of angles  $t_1$  and  $T_1$  are related to the Fig. 1.12 with the direction of axis OX being the west-east direction and the direction of axis OY being the south-north direction.

The ratio, Mnu, of the radiation flux received by a surface for anisotropic sky diffuse radiation to the flux for an assumed isotropic sky radiation is given by the following relation:

$$Mnu = \frac{\sum_{p=1}^N (I_p^* * \cos(i))}{(\sum_{p=1}^N \cos(i))}$$

We called this ratio the number of anisotropy. The number of anisotropy is a measure of the importance of accounting for the anisotropy of the sky diffuse radiation.

Tables 1.9, 1.10 give values of Mnu, for south-facing and north facing surfaces, corresponding to the nonisotropic sky conditions of Tables 1.7 and 1.8, respectively, as functions of surface tilt,  $\theta^\circ$ . Linear interpolation (subroutine TAIN) is used for those points P of sky dome that do not have the exact values of angles  $T_1$  and  $t_1$  of the first row and first column, respectively, of Tables 1.7 and 1.8.

Table 1.9

Number of anisotropy of sky,  $M_{nu}$ ,  
for south and north facing  
surfaces. Sky conditions of  
Table 1.7.

tilt	South-facing surface	North-facing surface
0°	0.623	0.623
5	0.627	0.620
10	0.632	0.617
15	0.637	0.615
20	0.642	0.614
25	0.648	0.613
30	0.652	0.613
35	0.657	0.614
40	0.661	0.615
45	0.665	0.616
50	0.668	0.618
55	0.671	0.619
60	0.674	0.621
65	0.678	0.622
70	0.682	0.623
75	0.687	0.623
80	0.693	0.623
85	0.699	0.622
90	0.707	0.622

Table 1.10

Number of anisotropy of sky,  $M_{nu}$ ,  
for south and north facing surfaces.  
Sky conditions of Table 1.8.

tilt	South-facing surface	North-facing surface
0°	0.635	0.635
5	0.640	0.630
10	0.645	0.624
15	0.650	0.617
20	0.655	0.610
25	0.659	0.601
30	0.661	0.592
35	0.663	0.583
40	0.663	0.573
45	0.662	0.563
50	0.660	0.554
55	0.656	0.545
60	0.652	0.536
65	0.646	0.528
70	0.640	0.521
75	0.632	0.514
80	0.624	0.508
85	0.615	0.503
90	0.605	0.499

---

Note. Because  $M_{nu} < 1$ , an assumption of isotropic diffuse radiation for these two anisotropic sky conditions, actually over-estimates the diffuse radiation received by an optical system.  $(M_{nu})_{South} > (M_{nu})_{North}$ , that means south facing surfaces receive more diffuse radiation than north-facing surfaces.

### Accounting for the polarization of sky diffuse solar radiation

Apart from the intensity, its angular distribution over the sky dome, discussed just earlier, and the spectral composition, discussed in Appendix F, the main fourth characteristic of the sky diffuse radiation is its polarization. The radiation from the sun is unpolarised, that is, its waves vibrate in all directions at right angles to the line of sight. The sun radiation, travelling through the earth's atmosphere, is scattered by molecules and other particles that are small with respect to the wavelength of radiation, so that at each point in the sky its waves tend to vibrate in a specific direction.

The pattern of polarization in the sky varies with the position of the sun or, more exactly, with the orientation of the plane of a triangle, formed by the sun, the observer (point O in Fig. 1.12) and the specific point observed on sky. At any point of the sky dome the direction of polarization is always perpendicular to the plane of such a triangle. By disregarding a few exceptions and applying this general rule to all points in the sky the entire pattern of polarization can be determined for any given position of the sun.

Computer programs have been developed elsewhere, that specify both the direction and the degree of polarization for all points in the sky, for different atmospheric conditions and for spectral wavelengths ranging from the infrared to the ultraviolet (36),(38).

In the present analysis, the effect of polarization of sky diffuse radiation on the optical properties of the transwall is estimated with the following, somewhat arbitrary but relatively simple method:

Each intensity vector  $\vec{I}_p$  on the sky dome is assigned the same degree of polarization. The degree of polarization  $P_o$  is defined by the following relation:

$$P_o = (I_{\perp} - I_{\parallel}) / (I_{\perp} + I_{\parallel})$$

where,

$I_{\perp}$ , the component of intensity perpendicular to the plane of incidence

$I_{\parallel}$ , the component of intensity parallel to the plane of incidence

It is obvious that:  $I_p = I_{\perp} + I_{\parallel}$

For unpolarized radiation,  $I_{\perp} = I_{\parallel}$  and  $P_o = 0$

The whole procedure is actually that described previously in pages 32 to 36. The only difference here is that the two components

of polarization  $I_{\perp}$ ,  $I_{\parallel}$  are not equal as previously, but have been assigned magnitudes relative to the specified degree of polarization. In such a case, the computational procedure is applied twice for each component of polarization in its path through the optical system.

### 1.3.2b Discussion of the results

Only the transwall element in vertical position is examined at present. The system faces south.

#### Total reflectance

There is a large difference in total reflectance between the isotropic incident diffuse radiation and the three other types of sky diffuse radiation. This difference is about 19% of the incident diffuse radiation. The isotropic incident diffuse radiation actually overestimates the total reflectance. The difference in total reflectance between the isotropic sky radiation type and the two unisotropic sky radiation types is rather small, not exceeding 3% of the incident diffuse radiation. These can be shown in Table 1.11.

The equivalent angle of incidence of direct radiation that gives the same total reflectance with the diffuse radiation is about  $60^{\circ} + 63^{\circ}$ , for the first three types of diffuse radiation, and about  $72^{\circ} + 75^{\circ}$  for the 4th type of isotropic incident diffuse radiation, for both directions of incoming radiation.

The spectral composition of the incident diffuse radiation is not so important in determining the value of total reflectance as Tables 1.12 and 1.13 show.

The total reflectance, according to Table 1.14, constructed using methodology of pp. 38-39, shows a higher dependence on the degree of polarization than on the spectral composition of the incident diffuse radiation. Hull (34) used an averaged 20% degree of polarization for the whole sky. What is suggested is a more accurate approach on the calculation of the effect of sky diffuse radiation on the optical properties of an optical system, incorporating the degree and direction of polarization for all points in the sky.

#### Total transmittance

Again, there is a significant difference in total transmittance between the isotropic incident diffuse radiation and the three other types of sky diffuse radiation. This difference is about 9-10% of the incident diffuse radiation. The isotropic diffuse radiation actually underestimates the total transmittance of the transwall element. The difference in total transmittance between the isotropic sky radiation

type and the two anisotropic sky radiation types is small, less than 2% of the incident diffuse radiation, as Table 1.11 shows. As far as the spectral composition of the transmitted radiation is concerned, this is almost identical for the first 3 types of sky radiation and is slightly different in the case of isotropic incident diffuse radiation (Table 1.11).

The total transmittance changes a lot for different spectra of diffuse radiation. The difference between the total transmittance of air-mass 1 and air-mass 10 spectra of incident diffuse radiation is about 10% of the incident diffuse radiation. Quite different is the spectral composition of the transmitted radiation for different spectra of the incident diffuse radiation, although the total percentage of the visible part remains almost constant (Table 1.12).

The polarization of the incident diffuse radiation does not seem to be important in estimating the total transmittance of the transwall element. Especially the spectral composition of the transmitted radiation is almost identical for different degrees of polarization.

#### Absorptance of the various glass plates

The type, the spectrum and the polarization of the incident diffuse radiation are not important factors in determining the value of absorptance of the various glass plates. The difference that appears in the Tables 1.11, 1.12, 1.13 and 1.14 can be considered little in comparison with the uncertainties in estimating the type, the spectrum, the polarization and the value itself of the incident diffuse radiation.

#### Absorptance of the liquid

A rather large difference has been found in the absorptance of the liquid between the isotropic incident diffuse radiation and the three other types of sky diffuse radiation. This difference is 4.5 to 5% of the incident diffuse radiation for the transwall element. The difference in absorptance between the isotropic sky radiation and the two anisotropic sky radiation types is almost zero as Table 1.11 shows.

The spectral composition of the incident diffuse radiation is important as Tables 1.12 and 1.13 show for forward and backward, respectively, incoming radiation. The difference in absorptance of the liquid between air-mass 1 spectrum and air-mass 10 spectrum of incident diffuse radiation is about 6 to 9% of the incident radiation.



The polarization of the diffuse radiation does not seem to play any important role in determining the value of the absorptance of the liquid according to Table 1.14.

### 1.3.3 Diffuse radiation from the ground

One part of the diffuse radiation falling on an optical system comes from the diffusely reflected direct and diffuse radiation that falls on the ground. There is a dearth of knowledge on the relative magnitude of the intensity in all directions of this diffuse radiation from the ground and every assumption is rather speculative.

The optical properties of the transwall element can be calculated for any type of incident diffuse radiation from the ground by adopting the analysis of section 1.3.2a concerning the incident diffuse radiation from the sky. In this case the introduction of the concept of an imaginary sky dome is necessary. This imaginary sky dome from which the radiation is supposed to come is the other half of the real sky sphere, the half underneath the horizon (Fig. 1.12 and 1.14). There are two other differences in the analysis: (1) the surface A with vector  $\vec{P}_A$  (Fig. 1.14) receives radiation only from that part of the imaginary sky dome, for which  $0 \leq t_g \leq \theta^0$ . (Instead of angle  $t$ , the angle  $t_g$  is used in the present case, Fig. 1.14) and (2) the angle of incidence  $i_{gr}$  of vector of intensity  $\vec{I}_{Pg}$  of point  $P_g$  of imaginary sky dome and vector  $\vec{P}_A$  is:

$$i_{gr} = \cos^{-1} [(+ \sin(T) * \cos(t_g) * \sin(\theta^0) - \sin(T) * \sin(t_g) * \cos(\theta^0))]$$

### Discussion of the results

What has been discussed for the diffuse radiation from the sky in the case of the transwall element in the vertical position applies to the diffuse radiation from the ground. However, the uncertainty over the spectrum of the diffuse radiation from the ground is much higher.

Table 1.11

Total reflectance and transmittance of the transwall element. Absorptance of each layer of the element and spectral composition of the transmitted radiation for sky diffuse radiation of air-mass 2, equally polarized. Transwall in vertical position, account taken of polarization. % of incident radiation.

	isotropic incident radiation	isotropic sky radiation	anisotropic sky radiation clear sky	anisotropic sky radiation cloudy sky	anisotropic sky radiation without cosine effect clear sky	anisotropic sky radiation without cosine effect cloudy sky
Reflectance	38.2	20.7	18.3	20.6	34.5	37.4
Transmittance	22.0	30.7	32.3	30.7	24.0	22.3
0.30 ÷ 0.35 $\mu\text{m}$	0.0	0.0	0.0	0.0	0.0	0.0
0.35 ÷ 0.4 $\mu\text{m}$	3.3	3.5	3.5	3.5	3.4	3.4
0.4 ÷ 0.6 $\mu\text{m}$	60.1	56.4	56.0	56.5	59.4	59.9
0.6 ÷ 0.75 $\mu\text{m}$	29.1	31.2	31.3	31.2	29.4	29.2
0.75 ÷ 0.9 $\mu\text{m}$	7.5	8.9	9.2	8.9	7.8	7.5
0.9 ÷ 1.2 $\mu\text{m}$	0.0	0.0	0.0	0.0	0.0	0.0
1.2 ÷ 2.1 $\mu\text{m}$	0.0	0.0	0.0	0.0	0.0	0.0
2.1 ÷ 4.1 $\mu\text{m}$	0.0	0.0	0.0	0.0	0.0	0.0
Absorpt. of outside glass	14.3	14.9	14.7	15.0	14.2	14.3
Absorpt. of front glass	9.1	11.8	12.0	11.8	9.6	9.3
Absorpt. of liquid	13.0	17.5	18.1	17.5	14.0	13.1
Absorpt. of back glass	3.5	4.4	4.4	4.4	3.7	3.6

position  
composition  
spectral  
transmission  
(%)

Table 1.12

Total reflectance and transmittance of the transwall element.

Absorptance of each layer and spectral composition of the transmitted radiation for isotropic sky diffuse radiation of air-mass 1, 2, 4, 7 and 10, equally polarized. Transwall in vertical position, account taken of polarization, forward direction.

% of incident radiation	Air-mass					spectral composition of transmitted radiation(%)
	1	2	4	7	10	
reflectance	20.8	20.7	20.5	20.1	19.7	
transmittance	31.7	30.7	28.5	25.1	22.1	
0.3 ÷ 0.35 $\mu\text{m}$	0.0	0.0	0.0	0.0	0.0	
0.35 ÷ 0.4 $\mu\text{m}$	5.3	3.5	1.7	0.6	0.2	
0.4 ÷ 0.6 $\mu\text{m}$	58.4	56.4	51.2	42.4	34.0	
0.6 ÷ 0.75 $\mu\text{m}$	28.5	31.2	37.0	44.1	49.7	
0.75 ÷ 0.9 $\mu\text{m}$	7.8	8.9	10.1	13.0	16.1	
0.9 ÷ 1.2 $\mu\text{m}$	0.0	0.0	0.0	0.0	0.0	
1.2 ÷ 2.1 $\mu\text{m}$	0.0	0.0	0.0	0.0	0.0	
2.1 ÷ 4.1 $\mu\text{m}$	0.0	0.0	0.0	0.0	0.0	
Absorpt. of outside glass	15.0	14.9	15.3	16.5	17.6	
Absorpt. of front glass	11.5	11.8	12.3	13.0	13.6	
Absorpt. of liquid	16.7	17.5	19.2	21.1	23.0	
Absorpt. of back glass	4.3	4.4	4.3	4.2	4.0	

Table 1.13

Total reflectance and transmittance of the transwall element.

Absorptance of each layer and spectral composition of the transmitted radiation for isotropic sky diffuse radiation of air-mass 1, 2, 4, 7 and 10, equally polarized. Transwall in vertical position, backward direction of incoming radiation, account taken of polarization.

% of incident radiation.

	Air-mass				
	1	2	4	7	10
reflectance	16.6	16.4	16.0	15.3	14.7
transmittance	31.7	30.7	28.5	25.1	22.1
0.3 ÷ 0.35 $\mu\text{m}$	0.0	0.0	0.0	0.0	0.0
0.35 ÷ 0.4 $\mu\text{m}$	5.3	3.5	1.7	0.6	0.2
0.4 ÷ 0.6 $\mu\text{m}$	58.4	56.4	51.2	42.4	34.0
0.6 ÷ 0.75 $\mu\text{m}$	28.5	31.2	37.0	44.1	49.7
0.75 ÷ 0.9 $\mu\text{m}$	7.8	8.9	10.1	13.0	16.1
0.9 ÷ 1.2 $\mu\text{m}$	0.0	0.0	0.0	0.0	0.0
1.2 ÷ 2.1 $\mu\text{m}$	0.0	0.0	0.0	0.0	0.0
2.1 ÷ 4.1 $\mu\text{m}$	0.0	0.0	0.0	0.0	0.0
Absorptance outside glass	2.8	2.8	2.8	2.7	2.6
Absorptance front glass	6.1	6.2	6.1	6.0	5.8
Absorptance liquid	24.0	25.1	27.4	30.3	32.8
Absorptance back glass	18.8	18.8	19.3	20.6	21.9

spectral composition  
of transmitted  
radiation(%)

Table 1.14

Total reflectance and transmittance of the transwall element. Absorptance of each individual layer and spectral composition of the transmitted radiation for isotropic sky diffuse radiation of air-mass 2, unequally polarized. Transwall in vertical position, account taken of polarization. Values are given also for backward direction.

	Degree of polarization								
	-20%	back- ward	0%	back- ward	20%	back- ward	40%	back- ward	
Reflectance	18.5	14.6	20.7	16.4	22.9	18.2	25.1	19.9	spectral composition of transmitted radiation(%)
transmittance	31.9	31.9	30.7	30.7	29.5	29.5	28.3	28.3	
0.30 ÷ 0.35 $\mu\text{m}$	0.0	0.0	0.0	0.0	0.0	0.0	0.0	0.0	
0.35 ÷ 0.40 $\mu\text{m}$	3.5	3.5	3.5	3.5	3.5	3.5	3.5	3.5	
0.40 ÷ 0.60 $\mu\text{m}$	56.3	56.3	56.4	56.4	56.5	56.5	56.6	56.6	
0.60 ÷ 0.75 $\mu\text{m}$	31.2	31.2	31.2	31.2	31.1	31.1	31.0	31.0	
0.75 ÷ 0.90 $\mu\text{m}$	8.9	8.9	8.9	8.9	8.9	8.9	8.8	8.8	
0.90 ÷ 1.20 $\mu\text{m}$	0.0	0.0	0.0	0.0	0.0	0.0	0.0	0.0	
1.20 ÷ 2.10 $\mu\text{m}$	0.0	0.0	0.0	0.0	0.0	0.0	0.0	0.0	
2.10 ÷ 4.10 $\mu\text{m}$	0.0	0.0	0.0	0.0	0.0	0.0	0.0	0.0	
absorptance of outside glass	14.9	2.9	14.9	2.8	14.9	2.8	14.9	2.7	
absorptance of front glass	12.1	6.2	11.8	6.2	11.4	6.2	11.1	6.2	
absorptance of 1st liquid layer, 1.2 cm	12.5	0.4	12.2	0.4	11.7	0.4	11.4	0.4	
absorptance of 2nd liquid layer, 12.6 cm	5.2	7.6	5.1	7.4	4.9	7.4	4.8	7.3	
absorptance of 3rd liquid layer, 1.2 cm	0.2	17.5	0.2	17.3	0.2	17.0	0.2	16.8	
absorptance of liquid	17.9	25.5	17.5	25.1	16.8	24.8	16.4	24.5	
absorptance of back glass	4.5	19.0	4.4	18.8	4.2	18.6	4.1	18.4	

Note: the values are percentages of incident radiation.

#### 1.4 THE 3-DIMENSIONAL RAY-TRACING TECHNIQUE IN THE CASE OF A TRANSWALL MODULE WITH ONE OUTSIDE GLASS PLATE.

The 3-dimensional ray-tracing technique is applied to the transwall element, examined earlier in the application of the 1-dimensional technique for an infinite number of internal reflections.

Basic features and dimensions of the transwall element, important for the 1-dimensional technique, have already been given in section 1.3. In the present section, pages 47 to 49, additional information is given which is necessary for the 3-dimensional technique. This additional information itself shows the complexity of the 3-dimensional technique versus the 1-dimensional technique.

The radiation absorbed by each control volume is given in pages 51 to 58 for 5 different cases. For each case, the 3 components of the direct radiation vector and the angle of incidence of the vector with surface BB (See Fig. 1.17) are given in Table 1.15. The spectrum of incident direct radiation is that of air-mass 2.

Table 1.15

Direct radiation vector components

Case → component ↓	1	2	3	4	5
$V_x$	1.0	0.9848078	0.9396926	0.9396926	0.7660444
$V_y$	0.0	0.0	0.2418448	0.0	0.4545195
$V_z$	0.0	0.1736482	0.2418448	0.3420201	0.4545195
Angle of incidence <sup>+</sup> →	0°	10°	20°	20°	40°

The incident radiation only passes through a part of the outer boundary of the space surrounding the optical system, that is the surface with  $X = 0$  (BB, at Fig. 1.17).

The control volumes and areas are generally unequal. The discrete pencils of the incoming radiation are not distributed uniformly over the whole surface BB. The energy, corresponding to each area, is distributed in the form of 16 equal pencils of radiation at 16 points over the whole control area according to Fig. 1.16.

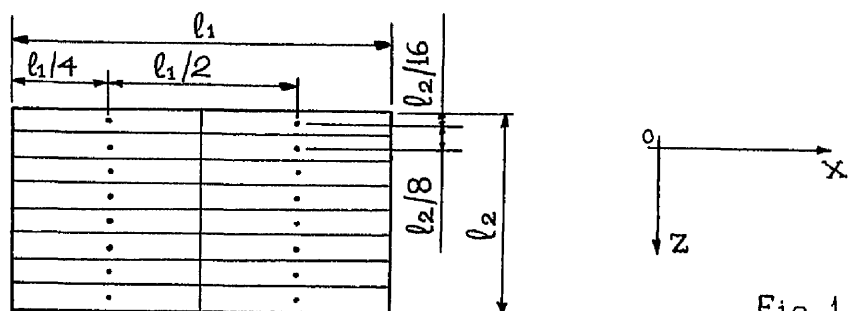
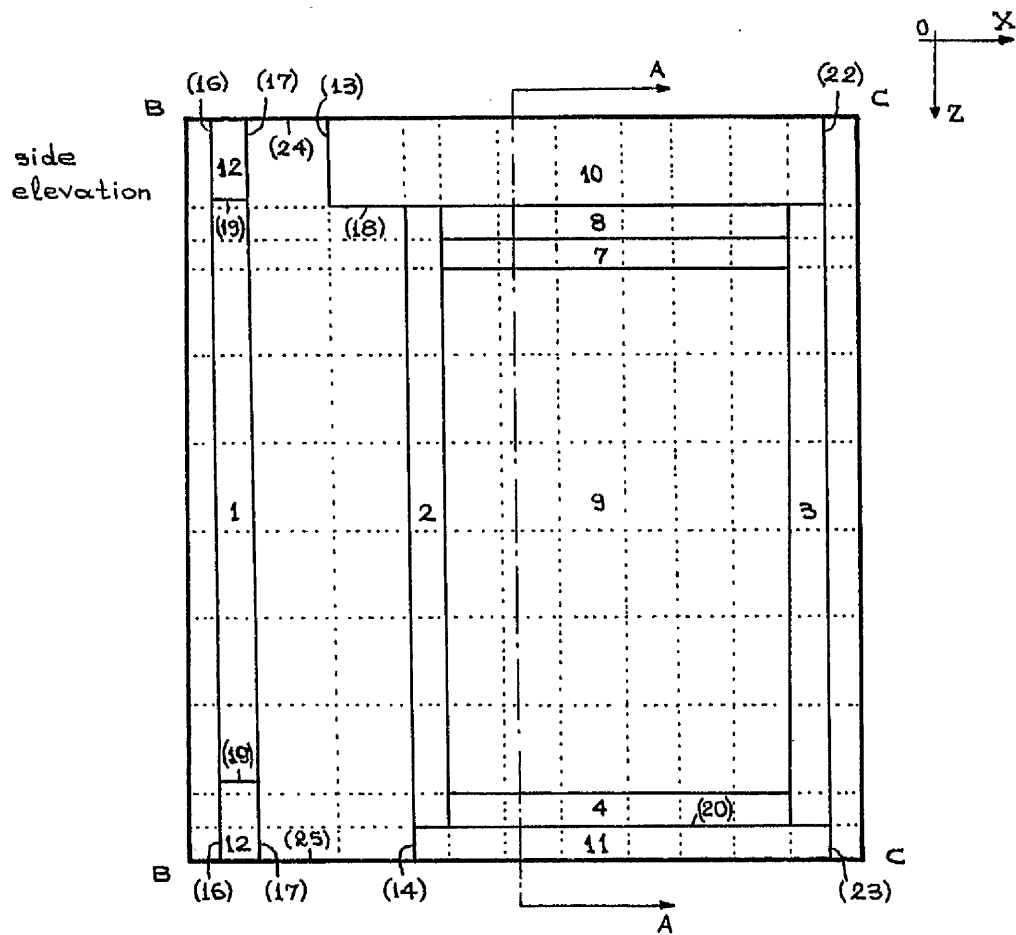


Fig. 1.16

<sup>+</sup> conventionally defined.



section AA

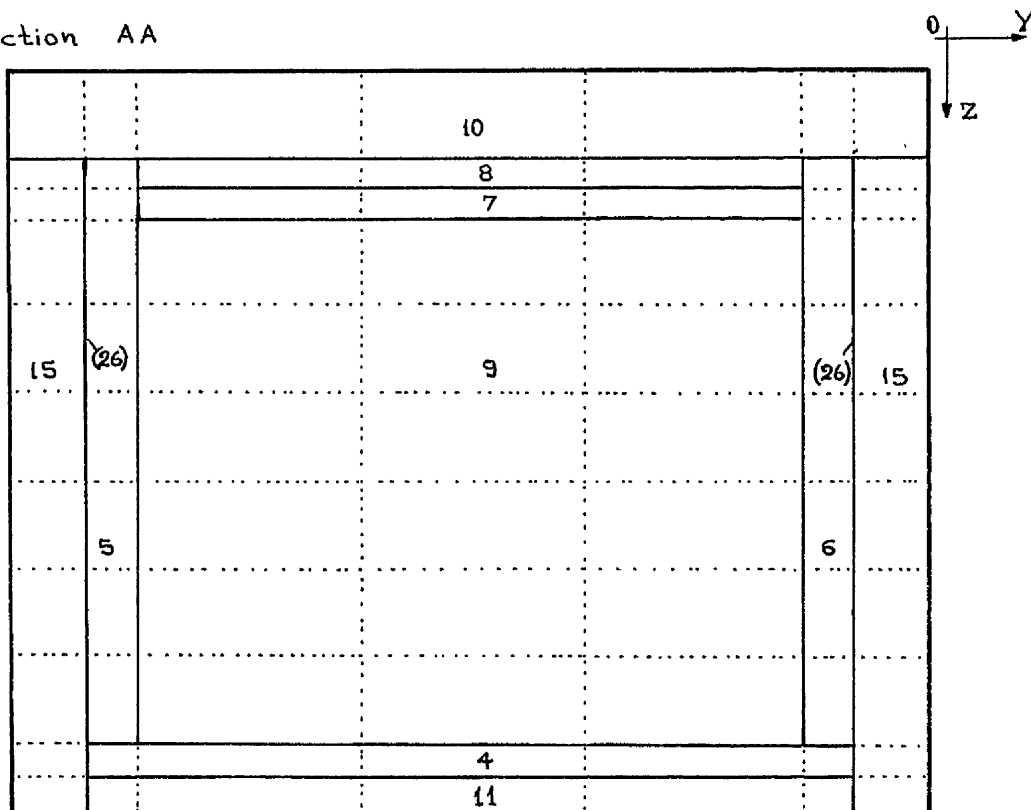


Fig. 1.17

Description of the transwall element components and surfaces

(A number inside brackets implies surface)

- 1 outside glass plate (0.004m x 1.251m x 0.640m)
- 2 front glass plate (0.006m x 1.132m x 0.598m)
- 3 back glass plate (0.006m x 1.132m x 0.598m)
- 4 base glass plate of transwall module (0.150m x 1.132m x 0.006m)
- 5, 6 side glass plates of transwall module (0.150m x 0.006 x 0.592m)
- 7 oil layer (0.150m x 1.120m x 0.010m)
- 8 air layer (0.150m x 1.120m x 0.015m)
- 9 Liquid (0.150m x 1.120m x 0.567m)
- 10 insulation cover, non-transparent (0.195m x 1.260m x 0.072m)
- 11 insulation base, non-transparent (0.162m x 1.132m x 0.055m)
- 12 outside glass plate frame, non-transparent,  
(0.004m x 1.260m x 0.021m) and (0.004m x 1.260m x 0.064m) and  
2 x (0.004m x 0.0045m x 0.640m)
- (16) outside surface of 12, (1.260m x 0.021m),  
(1.260m x 0.064m) and 2 x (0.0045m x 0.640m)  
absorpt. = 0.80
- (17) inside surface of 12, (1.260m x 0.021m), (1.260m x 0.064m)  
and 2 x (0.0045m x 0.640m) absorpt. = 0.80
- (19) internal surface of 12, 2 x (0.004m x 1.251m) and  
2 x (0.004m x 0.640m) absorpt. = 0.20
- (24) top surface, opaque, (0.0323m x 1.260m)  
absorpt. = 0.80
- (25) bottom surface, opaque, (0.0653m x 1.260m)  
absorpt. = 0.80
- (13) front surface of 10, (1.260m x 0.072m)  
absorpt. = 0.20
- (18) external bottom surface of 10, (0.033m x 1.260m)  
absorpt. = 0.80
- (21) internal bottom surface of 10, (0.162m x 1.260m)  
absorpt. = 0.20
- (22) back surface of 10, (1.260m x 0.072m)  
absorpt. = 0.20
- (14) front surface of 11, (1.132m x 0.055m)  
absorpt. = 0.80
- (20) top surface of 11, (0.162m x 1.132m)  
absorpt. = 0.20
- (23) back surface of 11, (1.132m x 0.055m)  
absorpt. = 0.20



- (26) side surfaces 2 x(0.162m x 0.598m)  
absorpt. = 0.20
- 15 side insulation, non-transparent  
2 x(0.162m x 0.064m x 0.653m)
- (27) front surfaces of 15 2 x(0.064m x 0.653m)  
absorpt. = 0.20
- (28) back surfaces of 15 2 x(0.064m x 0.653m)  
absorpt. = 0.20

Table 1.16

Dimensions of control volumes DX, DY and DZ along the X, Y and Z axis respectively

Number of control volume, NX	along X axis m	Number of control volume, NY	Along Y axis m	Number of control volume, NZ	Along Z axis m
1	0.001	1	0.064	1	0.072
2	0.004	2	0.006	2	0.015
3	0.0323	3	0.370	3	0.010
4	0.033	4	0.380	4	0.080
5	0.006	5	0.370	5	0.095
6	0.012	6	0.006	6	0.1085
7	0.030	7	0.064	7	0.1085
8	0.033			8	0.095
9	0.033			9	0.080
10	0.030			10	0.006
11	0.012			11	0.055
12	0.006				
13	0.0001				

In all cases, the incident radiation is  $388 \text{ W/m}^2$  and the results are given in mW of energy absorbed by each control volume. In Table 1.17 a comparison can be made between the 1-dimensional technique and the 5 cases of the 3-dimensional technique. Values obtained without taking into account the polarization of the radiation in its way through the system are also given for the 3rd and 5th case. Total transmittance and absorptance are referred to the radiation falling only on the glass part of the front surface of the whole system.

It should be stressed again that the success of the technique depends very much on the number and type of control volumes and the distribution of incident radiation over the outer boundary (or part of it). However, from pages 51 to 58 it is quite clear that the control volumes with the higher Z co-ordinate and for the 3rd and 5th case with the higher Y co-ordinate absorb much more radiation.

Table 1.17

Comparison between the 1-dimensional and 3-dimensional technique. % of incident radiation.

	Total reflectance	Total transmittance	Total absorptance
1-D, $0^\circ$ angle of incidence	11.2	37.7	51.1
3-D, 1st case	12.4	33.7	47.8
1-D, $10^\circ$ angle of incidence	11.2	37.6	51.2
3-D, 2nd case	12.4	33.5	48.5
1-D, $20^\circ$ angle of incidence	11.2	37.4	51.4
3-D, 3rd case	12.4	33.1	47.8
3-D, 3rd case no account of polarization	12.4	32.7	48.4
3-D, 4th case	12.4	32.7	48.5
1-D, $40^\circ$ angle of incidence	11.9	35.9	52.2
3-D, 5th case	12.9	31.8	50.1
3-D, 5th case no account of polarization	12.4	31.6	50.6

Table 1.18

3-dimensional ray-tracing technique case 1 (see Table 1.15)

NZ	NY	NX→	2	5	6	7	8	9	10	11	12
↓	↓										
1	1		193	0	0	0	0	0	0	0	0
	2		17	0	0	0	0	0	0	0	0
	3		1120	0	0	0	0	0	0	0	0
	4		1151	0	0	0	0	0	0	0	0
	5		1120	0	0	0	0	0	0	0	0
	6		17	0	0	0	0	0	0	0	0
	7		193	0	0	0	0	0	0	0	0
2	1		52	0	0	0	0	0	0	0	0
	2		4	3	5	7	2	1	0	0	0
	3		289	291	0	0	0	0	0	0	194
	4		297	299	0	0	0	0	0	0	199
	5		289	291	0	0	0	0	0	0	194
	6		4	3	5	7	2	1	0	0	0
	7		52	0	0	0	0	0	0	0	0
3	1		35	0	0	0	0	0	0	0	0
	2		2	2	3	4	1	0	0	0	0
	3		184	179	957	0	0	0	0	0	0
	4		189	184	983	0	0	0	0	0	0
	5		184	179	957	0	0	0	0	0	0
	6		2	2	3	4	1	0	0	0	0
	7		35	0	0	0	0	0	0	0	0
4	1		286	0	0	0	0	0	0	0	0
	2		22	23	31	41	20	9	5	1	0
	3		1498	1467	1702	424	137	95	78	30	538
	4		1539	1507	1748	435	141	97	80	30	552
	5		1498	1467	1702	424	137	95	78	30	538
	6		22	23	31	41	20	9	5	1	0
	7		286	0	0	0	0	0	0	0	0
5	1		340	0	0	0	0	0	0	0	0
	2		28	27	37	49	24	11	6	1	0
	3		1779	1742	2022	503	163	113	92	35	639
	4		1828	1789	2077	517	167	116	95	36	656
	5		1779	1742	2022	503	163	113	92	35	639
	6		28	27	37	49	24	11	6	1	0
	7		340	0	0	0	0	0	0	0	0
6	1		389	0	0	0	0	0	0	0	0
	2		32	32	42	56	27	13	7	2	1
	3		2032	1990	2310	575	186	129	106	40	729
	4		2087	2044	2372	591	191	132	109	42	749
	5		2032	1990	2310	575	186	129	106	40	729
	6		32	31	42	56	27	13	7	2	1
	7		389	0	0	0	0	0	0	0	0
7	1		389	0	0	0	0	0	0	0	0
	2		32	31	42	56	27	13	7	2	1
	3		2032	1990	2310	575	186	129	106	40	729
	4		2087	2044	2372	591	191	132	109	42	749
	5		2032	1990	2310	575	186	129	106	40	729
	6		32	31	42	56	27	13	7	2	1
	7		389	0	0	0	0	0	0	0	0

Table 1.18 (contd.)

3-dimensional ray-tracing technique case 1 (see Table 1.15)

NZ	NY	NX→	2	5	6	7	8	9	10	11	12
↓	↓										
8	1		340	0	0	0	0	0	0	0	0
	2		28	27	37	49	24	11	6	1	0
	3		1779	1742	2022	503	163	113	92	35	639
	4		1828	1789	2077	517	167	116	95	36	656
	5		1779	1742	2022	503	163	113	92	35	639
	6		28	27	37	49	24	11	6	1	0
	7		340	0	0	0	0	0	0	0	0
9	1		286	0	0	0	0	0	0	0	0
	2		22	23	31	41	20	9	5	1	0
	3		1498	1467	1702	424	137	95	78	30	538
	4		1539	1507	1748	435	141	97	80	30	552
	5		1498	1467	1702	424	137	95	78	30	538
	6		22	23	31	41	20	9	5	1	0
	7		286	0	0	0	0	0	0	0	0
10	1		0	0	0	0	0	0	0	0	0
	2		0	0	0	0	0	0	0	0	0
	3		0	0	0	0	0	0	0	0	0
	4		0	0	0	0	0	0	0	0	0
	5		0	0	0	0	0	0	0	0	0
	6		0	0	0	0	0	0	0	0	0
	7		0	0	0	0	0	0	0	0	0

See note of page 58.

Table 1.19

3-dimensional ray-tracing technique case 2 (see Table 1.15)

NZ	NY	NX→	2	5	6	7	8	9	10	11	12
↓	↓										
1	1		207	0	0	0	0	0	0	0	0
	2		18	0	0	0	0	0	0	0	0
	3		1205	0	0	0	0	0	0	0	0
	4		1237	0	0	0	0	0	0	0	0
	5		1205	0	0	0	0	0	0	0	0
	6		18	0	0	0	0	0	0	0	0
	7		207	0	0	0	0	0	0	0	0
2	1		54	0	0	0	0	0	0	0	0
	2		5	4	5	6	2	1	0	0	0
	3		277	302	0	0	0	0	0	0	70
	4		285	310	0	0	0	0	0	0	72
	5		277	302	0	0	0	0	0	0	70
	6		4	4	5	6	2	1	0	0	0
	7		54	0	0	0	0	0	0	0	0
3	1		35	0	0	0	0	0	0	0	0
	2		2	2	3	4	1	0	0	0	0
	3		184	179	1022	188	537	11	0	0	0
	4		189	184	1051	193	552	11	0	0	0
	5		184	179	1022	188	537	11	0	0	0
	6		2	2	3	4	1	0	0	0	0
	7		35	0	0	0	0	0	0	0	0

Table 1.19 (contd.)

3-dimensional ray-tracing technique case 2 (see Table 1.15)

NZ	NY	NX→	2	5	6	7	8	9	10	11	12
↓	↓										
4	1		316	0	0	0	0	0	0	0	0
	2		22	22	30	40	19	8	4	1	0
	3		1508	1468	1728	425	126	82	68	26	485
	4		1549	1508	1774	437	130	84	69	28	498
	5		1508	1468	1728	425	126	82	68	26	485
	6		22	22	30	40	19	8	4	1	0
	7		316	0	0	0	0	0	0	0	0
5	1		379	0	0	0	0	0	0	0	0
	2		27	27	36	48	24	11	5	1	0
	3		1791	1728	2022	497	169	111	89	34	658
	4		1840	1775	2077	510	174	114	91	35	676
	5		1791	1728	2022	497	169	111	89	34	658
	6		27	27	36	48	24	11	5	1	0
	7		379	0	0	0	0	0	0	0	0
6	1		444	0	0	0	0	0	0	0	0
	2		32	31	41	55	27	13	7	2	0
	3		2060	1977	2313	571	184	137	102	39	750
	4		2115	2031	2375	587	189	141	105	40	770
	5		2060	1977	2313	571	184	137	102	39	750
	6		32	31	41	55	27	13	7	2	0
	7		444	0	0	0	0	0	0	0	0
7	1		437	0	0	0	0	0	0	0	0
	2		32	31	42	55	27	13	7	2	1
	3		2050	2010	2350	579	186	129	106	40	772
	4		2105	2064	2414	595	191	132	108	41	792
	5		2050	2010	2350	579	186	129	106	40	772
	6		32	31	42	55	27	13	7	2	1
	7		437	0	0	0	0	0	0	0	0
8	1		374	0	0	0	0	0	0	0	0
	2		27	28	37	49	24	11	5	2	0
	3		1785	1791	2095	515	165	104	96	36	697
	4		1833	1840	2152	529	170	170	98	37	716
	5		1785	1791	2095	515	165	104	96	36	697
	6		27	28	37	49	24	11	5	2	0
	7		374	0	0	0	0	0	0	0	0
9	1		324	0	0	0	0	0	0	0	0
	2		22	23	31	42	19	9	5	1	0
	3		1515	1512	1768	436	135	101	85	33	618
	4		1556	1552	1816	448	139	104	88	34	634
	5		1515	1512	1768	436	135	101	85	33	618
	6		22	23	31	42	19	9	5	1	0
	7		324	0	0	0	0	0	0	0	0
10	1		0	0	0	0	0	0	0	0	0
	2		0	2	3	4	2	1	0	0	0
	3		0	184	250	272	252	148	69	21	14
	4		0	189	257	279	253	152	71	21	15
	5		0	184	250	272	252	148	69	21	14
	6		0	2	3	4	2	1	0	0	0
	7		0	0	0	0	0	0	0	0	0

See note of page 58.

Table 1.20

3-dimensional ray-tracing technique case 3 (see Table 1.15)

NZ	NY	NX→	2	5	6	7	8	9	10	11	12
1	1		193	0	0	0	0	0	0	0	0
	2		14	0	0	0	0	0	0	0	0
	3		1137	0	0	0	0	0	0	0	0
	4		1164	0	0	0	0	0	0	0	0
	5		1133	0	0	0	0	0	0	0	0
	6		14	0	0	0	0	0	0	0	0
	7		181	0	0	0	0	0	0	0	0
2	1		49	0	0	0	0	0	0	0	0
	2		4	0	0	0	0	0	0	0	0
	3		293	226	0	0	0	0	0	0	10
	4		300	226	0	0	0	0	0	0	10
	5		292	220	0	0	0	0	0	0	10
	6		4	0	0	0	0	0	0	0	0
	7		48	0	0	0	0	0	0	0	0
3	1		31	0	0	0	0	0	0	0	0
	2		2	0	0	0	0	0	0	0	0
	3		176	167	1099	555	0	0	1	0	0
	4		177	169	1102	561	0	0	1	0	0
	5		172	165	1073	546	0	0	1	0	0
	6		2	0	0	0	0	0	0	0	0
	7		32	0	0	0	0	0	0	0	0
4	1		270	0	0	0	0	0	0	0	0
	2		24	0	0	0	0	0	0	0	0
	3		1497	1515	1741	378	120	75	60	23	397
	4		1508	1516	1742	380	121	75	60	23	397
	5		1468	1476	1696	370	118	73	59	22	386
	6		21	0	0	0	0	0	0	0	0
	7		273	0	0	0	0	0	0	0	0
5	1		324	0	0	0	0	0	0	0	0
	2		31	0	0	0	0	0	0	0	0
	3		1787	1705	1997	513	151	116	88	33	685
	4		1793	1701	1993	513	152	116	88	33	672
	5		1746	1656	1940	500	148	113	85	32	655
	6		26	0	0	0	0	0	0	0	0
	7		331	0	0	0	0	0	0	0	0
6	1		366	0	0	0	0	0	0	0	0
	2		35	0	0	0	0	0	0	0	0
	3		2027	1948	2060	572	178	123	110	40	728
	4		2038	1946	2256	571	179	122	110	40	725
	5		1984	1894	2196	556	174	119	107	39	706
	6		30	0	0	0	0	0	0	0	0
	7		374	0	0	0	0	0	0	0	0
7	1		367	0	0	0	0	0	0	0	0
	2		36	0	0	0	0	0	0	0	0
	3		2032	1982	2298	562	180	126	104	40	762
	4		2041	1978	2294	562	181	126	104	40	759
	5		1987	1926	2234	546	176	123	101	39	739
	6		30	0	0	0	0	0	0	0	0
	7		375	0	0	0	0	0	0	0	0

Table 1.20 (contd.)

3-dimensional ray-tracing technique case 3 (see Table 1.15)

NZ	NY	NX→	2	5	6	7	8	9	10	11	12
↓	↓										
8	1		323	0	0	0	0	0	0	0	0
	2		32	0	0	0	0	0	0	0	0
	3		1784	1767	2050	481	160	115	85	34	701
	4		1790	1764	2046	481	160	114	85	34	699
	5		1743	1717	1992	468	156	111	83	33	681
	6		26	0	0	0	0	0	0	0	0
	7		330	0	0	0	0	0	0	0	0
9	1		268	0	0	0	0	0	0	0	0
	2		25	0	0	0	0	0	0	0	0
	3		1489	1490	1714	407	143	94	86	33	599
	4		1499	1489	1712	406	144	94	86	33	597
	5		1459	1450	1667	396	140	92	84	33	581
	6		21	0	0	0	0	0	0	0	0
	7		273	0	0	0	0	0	0	0	0
10	1		0	0	0	0	0	0	0	0	0
	2		0	0	0	0	0	0	0	0	0
	3		0	8	63	192	75	194	87	21	49
	4		0	5	60	190	72	194	85	21	49
	5		0	5	59	185	70	189	83	20	48
	6		0	0	0	0	0	0	0	0	0
	7		0	0	0	0	0	0	0	0	0

See note of page 58.

Table 1.21

3-dimensional ray-tracing technique case 4 (see Table 1.15)

NZ	NY	NX→	2	5	6	7	8	9	10	11	12
↓	↓										
1	1		191	0	0	0	0	0	0	0	0
	2		16	0	0	0	0	0	0	0	0
	3		1112	0	0	0	0	0	0	0	0
	4		1142	0	0	0	0	0	0	0	0
	5		1112	0	0	0	0	0	0	0	0
	6		16	0	0	0	0	0	0	0	0
	7		191	0	0	0	0	0	0	0	0
2	1		51	0	0	0	0	0	0	0	0
	2		4	2	0	0	0	0	0	0	0
	3		296	121	0	0	0	0	0	0	0
	4		304	124	0	0	0	0	0	0	0
	5		296	121	0	0	0	0	0	0	0
	6		4	2	0	0	0	0	0	0	0
	7		51	0	0	0	0	0	0	0	0
3	1		29	0	0	0	0	0	0	0	0
	2		2	2	5	5	1	0	0	0	0
	3		169	168	1470	0	0	0	0	0	0
	4		173	173	1510	0	0	0	0	0	0
	5		169	168	1470	0	0	0	0	0	0
	6		2	2	5	5	1	0	0	0	0
	7		29	0	0	0	0	0	0	0	0

Table 1.21 (contd.)

3-dimensional ray-tracing technique case 4 (see Table 1.15 )

NZ	NY	NX→	2	5	6	7	8	9	10	11	12
↓	↓										
4	1		304	0	0	0	0	0	0	0	0
	2		21	21	30	38	17	7	4	1	0
	3		1474	1401	1646	386	113	68	53	18	341
	4		1514	1439	1691	396	116	70	54	18	350
	5		1474	1401	1646	386	113	68	53	18	341
	6		21	21	30	38	17	7	4	1	0
	7		304	0	0	0	0	0	0	0	0
5	1		373	0	0	0	0	0	0	0	0
	2		27	25	33	46	22	10	5	1	0
	3		1744	1621	1880	475	151	111	86	35	664
	4		1791	1665	1931	488	155	115	88	36	682
	5		1744	1621	1880	475	151	111	86	35	664
	6		27	25	33	46	22	10	5	1	0
	7		373	0	0	0	0	0	0	0	0
6	1		419	0	0	0	0	0	0	0	0
	2		31	33	40	51	26	12	6	2	1
	3		1983	2102	2380	530	182	117	106	37	695
	4		2036	2156	2444	544	187	120	109	38	714
	5		1983	2102	2380	530	182	117	106	37	695
	6		31	33	40	51	26	12	6	2	1
	7		419	0	0	0	0	0	0	0	0
7	1		423	0	0	0	0	0	0	0	0
	2		31	30	40	53	26	12	6	2	0
	3		1987	1926	2234	546	176	123	101	39	739
	4		2041	1978	2294	562	181	126	104	40	759
	5		1987	1926	2234	546	176	123	101	39	739
	6		31	30	40	53	26	12	6	2	0
	7		423	0	0	0	0	0	0	0	0
8	1		374	0	0	0	0	0	0	0	0
	2		27	23	35	48	22	10	5	1	0
	3		1745	1510	1809	495	148	113	83	35	691
	4		1792	1550	1858	508	152	116	86	36	710
	5		1745	1510	1809	495	148	113	83	35	691
	6		27	23	35	48	22	10	5	1	0
	7		374	0	0	0	0	0	0	0	0
9	1		307	0	0	0	0	0	0	0	0
	2		21	23	31	39	20	10	5	1	0
	3		1460	1484	1721	408	135	91	82	30	580
	4		1500	1524	1768	419	139	93	84	30	595
	5		1460	1484	1721	408	135	91	82	30	580
	6		21	23	31	39	20	10	5	1	0
	7		307	0	0	0	0	0	0	0	0
10	1		0	0	0	0	0	0	0	0	0
	2		0	2	3	5	2	1	0	0	0
	3		0	176	223	389	253	295	199	94	27
	4		0	180	229	400	260	304	204	97	28
	5		0	176	223	389	253	295	199	94	27
	6		0	2	3	5	2	1	0	0	0
	7		0	0	0	0	0	0	0	0	0

See note of page 58.



Table 1.22

3-dimensional ray-tracing technique case 5 (see Table 1.15)

NZ	NY	NX→	2	5	6	7	8	9	10	11	12
1	1		148	0	0	0	0	0	0	0	0
	2		10	0	0	0	0	0	0	0	0
	3		923	0	0	0	0	0	0	0	0
	4		936	0	0	0	0	0	0	0	0
	5		911	0	0	0	0	0	0	0	0
	6		10	0	0	0	0	0	0	0	0
	7		151	0	0	0	0	0	0	0	0
2	1		38	0	0	0	0	0	0	0	0
	2		2	0	0	0	0	0	0	0	0
	3		248	105	0	0	0	0	0	0	0
	4		250	98	0	0	0	0	0	0	0
	5		243	95	0	0	0	0	0	0	0
	6		2	0	0	0	0	0	0	0	0
	7		39	0	0	0	0	0	0	0	0
3	1		25	0	0	0	0	0	0	0	0
	2		1	0	0	0	0	0	0	0	0
	3		150	209	1587	0	0	0	0	0	0
	4		154	193	1467	0	0	0	0	0	0
	5		150	188	1429	0	0	0	0	0	0
	6		1	0	0	0	0	0	0	0	0
	7		26	0	0	0	0	0	0	0	0
4	1		209	0	0	0	0	0	0	0	0
	2		25	0	0	0	0	0	0	0	0
	3		1295	1220	1394	308	86	53	37	11	217
	4		1309	1132	1291	287	81	49	35	11	208
	5		1274	1101	1257	279	79	48	33	10	204
	6		16	0	0	3	2	0	7	3	0
	7		215	0	0	0	0	0	0	0	0
5	1		245	0	0	0	0	0	0	0	0
	2		32	0	0	0	0	0	0	0	0
	3		1522	1637	1798	407	130	96	81	30	575
	4		1535	1513	1660	377	122	90	75	28	538
	5		1495	1473	1617	367	118	88	73	27	525
	6		19	0	0	7	10	0	0	0	0
	7		254	0	0	0	0	0	0	0	0
6	1		280	0	0	0	0	0	0	0	0
	2		37	0	0	0	0	0	0	0	0
	3		1749	1711	1974	470	154	110	90	36	688
	4		1761	1581	1822	435	145	103	84	34	644
	5		1715	1539	1774	422	141	101	82	33	629
	6		22	0	0	8	12	0	0	0	0
	7		291	0	0	0	0	0	0	0	0
7	1		280	0	0	0	0	0	0	0	0
	2		37	0	0	0	0	0	0	0	0
	3		1746	1762	1984	471	151	110	92	35	667
	4		1759	1628	1831	436	142	103	86	32	624
	5		1713	1585	1783	423	138	101	84	32	609
	6		22	0	0	8	12	0	0	0	0
	7		291	0	0	0	0	0	0	0	0

Table 1.22 (contd.)

3-dimensional ray-tracing technique							case 5 (see Table 1.15)				
NZ	NY	NX→	2	5	6	7	8	9	10	11	12
8	↓	1	245	0	0	0	0	0	0	0	0
		2	32	0	0	0	0	0	0	0	0
		3	1524	1593	1747	413	129	97	82	29	564
		4	1537	1473	1613	382	121	90	77	27	528
		5	1497	1434	1570	371	118	88	75	27	515
		6	19	0	0	7	11	0	0	0	0
		7	254	0	0	0	0	0	0	0	0
9		1	206	0	0	0	0	0	0	0	0
		2	25	0	0	0	0	0	0	0	0
		3	1283	1204	1403	352	115	84	70	27	557
		4	1294	1111	1295	327	108	79	66	26	522
		5	1260	1082	1261	317	105	77	64	25	509
		6	15	0	0	6	10	0	0	0	0
		7	214	0	0	0	0	0	0	0	0
10		1	0	0	0	0	0	0	0	0	0
		2	0	0	0	0	0	0	0	0	0
		3	0	157	203	398	339	303	245	115	19
		4	0	146	188	368	318	284	230	108	18
		5	0	142	183	357	309	277	224	105	17
		6	0	0	0	0	1	0	0	0	0
		7	0	0	0	0	0	0	0	0	0

**Note:**

The control volumes with NX=1, 3, 4, 13 and with NZ=11 absorb zero radiation.

The values are in mW.

## **Chapter 2**

## CHAPTER 2

## THERMAL MODELLING OF A TRANSWALL PASSIVE SOLAR SYSTEM

## Introduction.

The thermal modelling of a passive solar system by an analytical model and by a small test-box is presented in section 2.4 and 2.5, respectively. Although continuous improvement of computers will tend to favour analytical modelling of passive solar systems, there are certain disadvantages in their use. When an accurate simulation of the long term thermal performance of a system is needed, analytical models, especially of multi-room passive solar systems, tend to become complex and very computer-time consuming. Further there are physical phenomena that take place in buildings, or some peculiarities of the site, such as an irregular south-facing slope or nearby trees, that have not yet been studied enough to establish worthwhile simulation procedures. This explains why there is always a need for thermal modelling by using test-rooms (4), (55). Apart from the test rooms' obvious advantage of the experimental study of the physical phenomena on site, they are expensive and rather inflexible. The thermal modelling of passive solar systems with small test-boxes, described by Grimmer (52), (53), and Lee (54), reduces the problems of cost and inflexibility but introduces the difficult problem of the simultaneous scaling down of many physical phenomena which occur in real buildings. Nevertheless, the arguments presented by Grimmer (52) were sufficiently attractive to construct a test-box to allow the study of real transwall modules or other passive solar systems elements under real outside conditions. The theoretical approach which was followed for the construction of the test-box is presented in section 2.5. This approach has certain differences from that suggested by Grimmer (52), which is also presented in the same section.

The experimental thermal behaviour of the test-box has been computer simulated using solar, wind and ambient temperature data inputs. The computer simulation has been based on the analytical model of the passive solar system. This first verification of the analytical modelling in the case of the small test-box can be considered satisfactory taking into account the uncertainties relating to various weather parameters and the optical and thermal properties of the various elements of the test-box. (Section 2.6).

The basic characteristic of the analytical model is the separation of the whole passive system into a finite number of control volumes, each one represented by a node. The temperature of each node is calculated by discretization of the energy equation over each control

volume and time interval  $\Delta t$ . The control volumes are divided into groups in such a way that the nodes of each group lie on a particular line. These lines start and finish at ambient temperature apart from one line that may finish at ground temperature. This is important because it allows not only for the easy treatment of complicated shapes of passive systems in 3-dimensions but also for the use of the line-by-line iterative solution of the discretized energy equations. Thus, the equations of each group of control volumes belonging to a particular line are solved separately. Problems in using this line-by-line procedure that might arise because of discontinuity between convection and conduction regions are overcome easily by the introduction of a new formulation of the heat fluxes at the interface of the conduction and convection regions (section 3.1.4). Solving the discretized equations along the lines from ambient to ambient temperature or from ambient to ground temperature is important because any information along the line is transmitted at once to the whole domain and the convergence of the procedure seems to be faster. This is believed to be an advantage of the present analytical modelling of complicated passive solar systems in respect to other finite difference methods (30) (44). The present method uses semi-empirical relations to calculate mass fluxes and some of the heat fluxes at internal, external surfaces, air cavities, transwall modules etc. Most of these relations are non-linear but are easily incorporated in the method, whereas the other main category of methods - response factor techniques - is challenged when non-linear processes have to be approximated (28) (30).

The success of the analytical modelling depends on accounting for the 3-dimensional solar radiation field outside and inside the passive solar system (sections 2.1 and 2.2.). The methods developed, accompanied by the techniques of chapter 1, allow for an accurate distribution of the total incident radiation among the various elements and surfaces of the passive system.

The method of distributing the solar radiation among the various internal surfaces of an enclosure (section 2.2) is applied to the 'convex' parallelepiped enclosure of the test-box (section 2.3). The analysis of the results showed that the distribution of the total incident radiation among the various elements and internal surfaces of the passive system depends on the type of the passive system element, the proportional composition of solar radiation into direct and diffuse, the spectrum of radiation and the optical properties of the internal

surfaces. For the particular transwall system enclosure, solar radiation and optical properties of the internal surfaces the effect of change in the depth of the parallelepiped was not significant. The application also shows that the common assumption that all the solar radiation entering the enclosure is absorbed by its opaque surfaces may in fact lead to substantial errors, especially in the case of direct systems. The applicability of the method to very complicated enclosures is shown in the example of a typical glasshouse (greenhouse) with E-W transwalls presented in Appendix L.

## 2.1. RADIATION FALLING ON AN UNOBSURED EXTERNAL PLANE SURFACE.

The radiation falling on an external surface consists mainly of solar radiation ( $0.3\mu\text{m} < \lambda < 4.1\mu\text{m}$ ) and longwave radiation ( $\lambda > 4.1\mu\text{m}$ )

### 2.1.1 Solar Radiation

It consists of three components:

Direct radiation

Diffuse radiation from the sky

and reflected radiation from the ground or nearby buildings.

#### Direct Radiation

The direct radiation received by the external surface is

$$q_D = -\text{RAD} * \cos(i) \quad (\text{W/m}^2)$$

where RAD is the absolute value of the direct radiation vector,  $\vec{V}$ .

The calculation of the angle of incidence  $i$  presented here is different from the conventional one of cumbersome relations (as in (14) or (15)). The components of vector  $\vec{P}$  normal to the surface are first calculated and then the components of the direct radiation vector  $\vec{V}$ . The reference co-ordinate system is O.SEZ, shown in Fig. 2.1. If the external surface is transparent or semi-transparent to the incident direct radiation, the knowledge of the components of the direct radiation vector may be of value for a successive analysis, for example the distribution of solar radiation among the surfaces of an enclosure. This analysis can be applied to other non-plane external surfaces, each point of which is given with its associated vector  $\vec{P}$ .

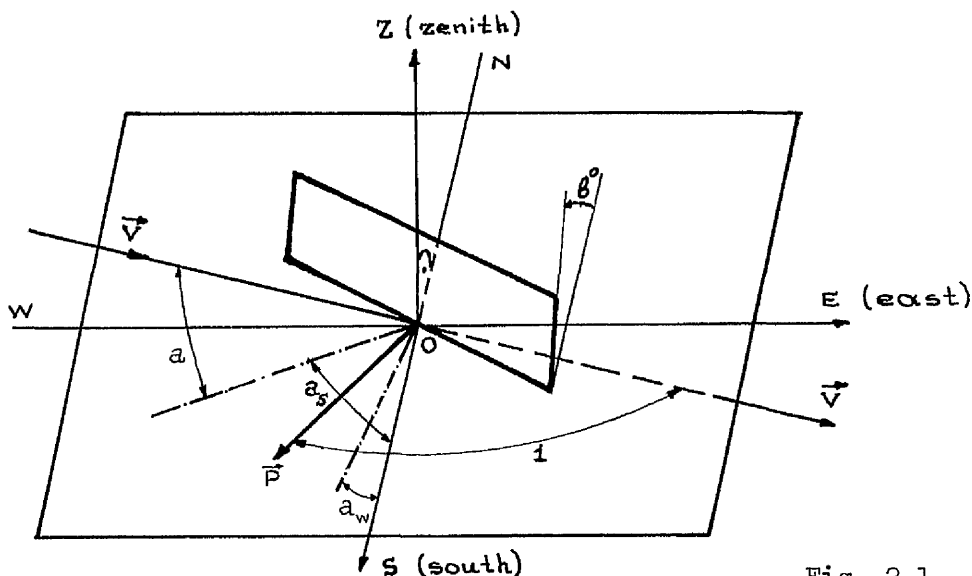


Fig. 2.1

The three components of vector  $\vec{P}$  are :

$$P_x = \sin(\beta^\circ) * \cos(a_w) \quad (2.1)$$

$$P_y = \sin(\beta^\circ) * \sin(a_w) \quad (2.2)$$

$$P_z = \cos(\beta^\circ) \quad (2.3)$$

The three components of the direct radiation  $\vec{V}$  are:

$$V_x = -\cos(a_s) * \cos(a) \quad (2.4)$$

$$V_y = -\sin(a_s) * \cos(a) \quad (2.5)$$

$$V_z = -\sin(a) \quad (2.6)$$

where the angles  $\beta^\circ$ ,  $a_w$ ,  $a$  and  $a_s$  are defined

in Fig. 2.1

$\beta^\circ$  is the surface tilt angle measured from the horizon

$a_w$  is the wall azimuth angle measured from the axis OS ( $a_w > 0$ ,

for east of south,  $a_w < 0$  for west of south)

$a$  is the solar altitude angle, calculated from relation F2 of Appendix F

$a_s$  is the solar azimuth angle measured from the axis OS ( $a_s > 0$ , for east of south,  $a_s < 0$ , for west of south)

$$a_s = (\cos(\delta_s) * \sin(h_s)) / \cos(a)$$

where the declination angle  $\delta_s$  and solar hour angle  $h_s$  are defined on page F3 of Appendix F. So the angle of incidence  $i$  is the angle between the vectors  $\vec{P}$  and  $\vec{V}$ . This means,

$$i = \cos^{-1}[V_x * P_x + V_y * P_y + V_z * P_z]$$

If  $i < 90^\circ$ , the external surface is not lit by the direct radiation.

#### Diffuse radiation from the sky.

$$q_d = DIF_h * \cos^2(\beta^\circ/2) * Mnu(\beta^\circ, a_w) / Mnu(0^\circ) \quad (W/m^2)$$

where,  $DIF_h$  is the diffuse sky radiation received by a horizontal surface in  $W/m^2$ .

$Mnu(\beta^\circ, a_w)$ ,  $Mnu(0^\circ)$  are the numbers of anisotropy (section 1.3.2a) for  $\beta^\circ$  tilt and  $a_w$  wall azimuth angle and  $0^\circ$  tilt, respectively.

#### Diffuse radiation from the ground.

Assuming a uniform intensity of the diffusely reflected radiation from the ground,

$$q_{grd} = f * \rho_{gr} * RAD_h * \sin^2(\beta^\circ/2) + \rho_{gr} * DIF_h * \sin^2(\beta^\circ/2) \quad (W/m^2)$$

where  $RAD_h$  is the direct solar radiation falling on a horizontal surface (in  $W/m^2$ ).



$$RAD_h = RAD * \sin(a)$$

The reflected part of the direct radiation falling on the ground is macroscopically considered to consist of two fractions; a diffusely reflected fraction,  $f$ , and a specularly reflected fraction,  $1-f$ .

$\rho_{gr}$  is the ground reflectance for solar radiation.

Direct radiation specularly reflected from the ground.

$$q_{grD} = -(1-f) * \rho_{gr} * RAD_h * \cos(i_{gr}) \quad (W/m^2)$$

where  $i_{gr}$  is the angle between the normal surface vector  $\vec{P}$  and the vector  $\vec{c}$  of the direct radiation specularly reflected from the ground.

The calculation of the components  $c_x, c_y, c_z$  of the vector  $\vec{c}$  is given in Appendix C.

$$i_{gr} = \cos^{-1}[c_x * P_x + c_y * P_y + c_z * P_z]$$

If  $i_{gr} < 90^\circ$ , the external surface is not lit by the direct radiation specularly reflected from the ground.

The Euler relations are used for calculation of the components  $V'_x, V'_y, V'_z$  of the direct radiation vector  $\vec{V}$  in a new system of co-ordinates  $O'S'E'Z'$ . Similarly these relations are used for the components  $c'_x, c'_y, c'_z$  of the vector  $\vec{c}$  of the direct radiation specularly reflected from the ground. This new system comes from the O.SEZ system of Fig. 2.1 after an angle  $\delta$  rotation around the vector  $\vec{\delta} = \delta_x * \vec{i} + \delta_y * \vec{j} + \delta_z * \vec{k}$ , where  $\vec{i}, \vec{j}$  and  $\vec{k}$  are the unit vectors of axes OS, OE and OZ respectively:

$$V'_x = (\cos(\delta) + \delta_x^2 * (1-\cos(\delta))) * V_x + (\delta_z * \sin(\delta) + \delta_x * \delta_y * (1-\cos(\delta))) * V_y + (-\delta_y * \sin(\delta) + \delta_x * \delta_z * (1-\cos(\delta))) * V_z$$

$$V'_y = (-\delta_z * \sin(\delta) + \delta_x * \delta_y * (1-\cos(\delta))) * V_x + (\cos(\delta) + \delta_y^2 * (1-\cos(\delta))) * V_y + (\delta_x * \sin(\delta) + \delta_y * \delta_z * (1-\cos(\delta))) * V_z$$

$$V'_z = (\delta_y * \sin(\delta) + \delta_x * \delta_z * (1-\cos(\delta))) * V_x + (-\delta_x * \sin(\delta) + \delta_y * \delta_z * (1-\cos(\delta))) * V_y + (\cos(\delta) + \delta_z^2 * (1-\cos(\delta))) * V_z$$

### 2.1.2 Longwave radiation

An external surface receives longwave radiation from the atmosphere and the ground or nearby buildings.

Assuming a uniform intensity, the longwave atmospheric radiation received by the external surface is:

$$q_{at} = \cos^2(\beta^0/2) * e_{at} * \epsilon * (T_{amb})^4 \quad (W/m^2)$$

where  $\epsilon = 5.6698 \times 10^{-8} \text{ W/m}^2 * K^4$

$T_{amb}$ , is the atmospheric ground level dry bulb temperature in kelvins.

$e_{at}$ , is the emittance of atmosphere. According to

Reference (29), the emittance  $e_{at}$  is related to the ground level dew point temperature. Table 2.1 from Reference (29) gives this relation.

Table 2.1

Sky emittance vs dew point temperature ( $^{\circ}\text{C}$ )

Dew point temper.	Sky emittance	Dew point temper.	Sky emittance
-28.9	0.68	1.1	0.79
-23.3	0.71	4.4	0.82
-17.8	0.73	10.0	0.84
-12.2	0.76	15.6	0.86
- 6.7	0.77	21.1	0.88

The longwave radiation from the ground, if buildings or similar surfaces are neglected, under the assumptions of uniform intensity radiation and uniform ground temperature,  $T_{gr}$ , is:

$$q_{gr} = \sin^2 (\beta/2) * e_{gr} * \sigma * (T_{gr})^4 \quad (\text{W/m}^2)$$

where  $e_{gr}$  is the emittance of ground.

$T_{gr}$  (in kelvins)

The previous analysis has been incorporated into two main computer programs WAL1 and WAL2. The air-mass  $M_r$  of the incident radiation is also calculated in program WAL2, in accordance with the analysis presented in Appendix F. A major feature of these programs is that they allow the calculation of the total radiation falling on the complete external surface of a multi-surface system. The analysis is general and applicable to solar systems with different shapes and unobscured external surfaces under various conditions of solar radiation and climatic variations.

## 2.2 THE DISTRIBUTION OF SOLAR RADIATION ENTERING AN ENCLOSURE

The present method distributes the solar radiation which enters an enclosure into radiation absorbed by each opaque internal surface, radiation absorbed by each layer of the semi-transparent parts of the enclosure and radiation reflected out through the transparent or semi-transparent parts of the enclosure.

The method can be applied to every enclosure where internal surfaces are planar polygons. The enclosure should be of convex character in the case of direct solar radiation and specular reflection from one or more of its internal surfaces, otherwise it should be separated into smaller convex enclosures to each of which the method will be applied successively.

Three typical convex enclosures are shown in Fig. 2.2, Fig. 2.3 and Fig. 2.4. In Fig. 2.3 and 2.5 the two convex sub-enclosures of two typical non-convex enclosures are also shown.

Fig. 2.2 gives the elevation section of the solar passive test box used to assess the thermal performance of a transwall module. This enclosure is made of eight internal rectangles. The two side internal surfaces 2 and 3 are not shown. The surface 6 is the internal surface of the transwall module. The solar radiation enters (or leaves) the enclosure through the transwall (surface 6).

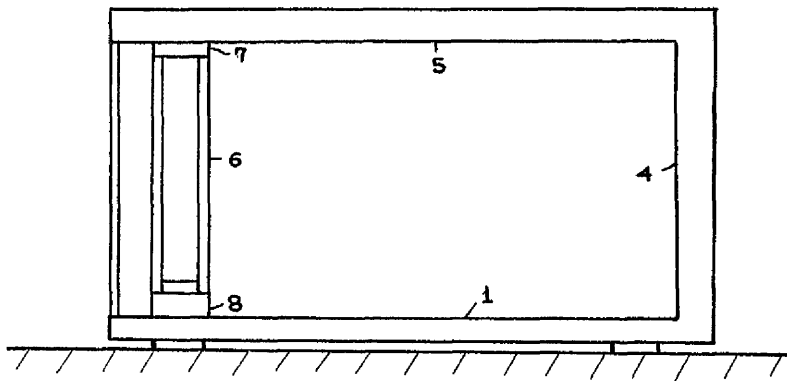


Fig. 2.2

Fig. 2.3 shows two inclined rectangular glass plates representing part of the roof of a conventional glasshouse, shown in the same figure.

The internal surfaces 4 and 5 of the particular enclosure are actually the external surfaces of the glass plates 8 and 7 of the glasshouse. The internal surfaces 1 (rectangle), 2 and 3 (triangles) are actually imaginary. The solar radiation enters (or leaves) the enclosure through every internal surface. The enclosure of Fig. 2.3 can represent another case, that of a flat plate solar collector with its flat reflector (for augmentation of the received solar insolation).

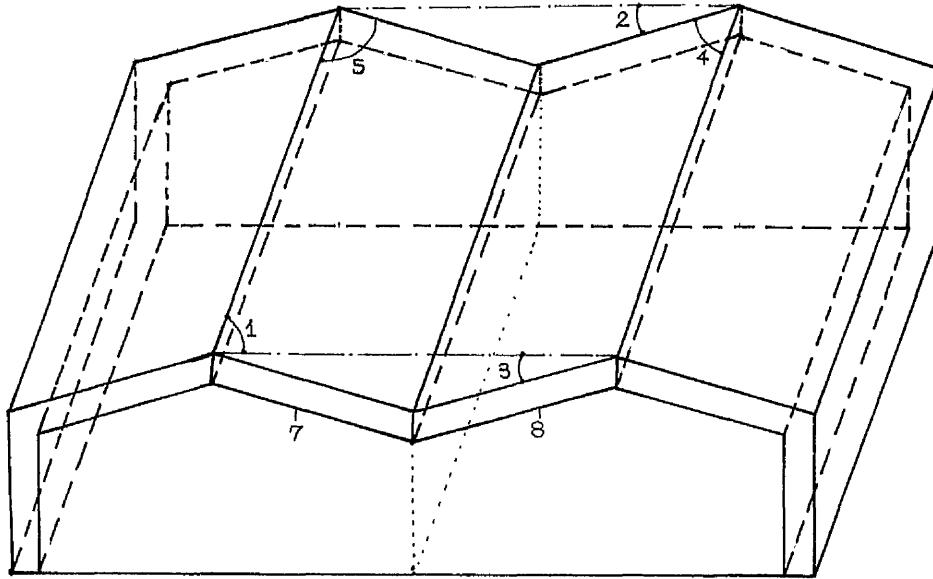


Fig. 2.3

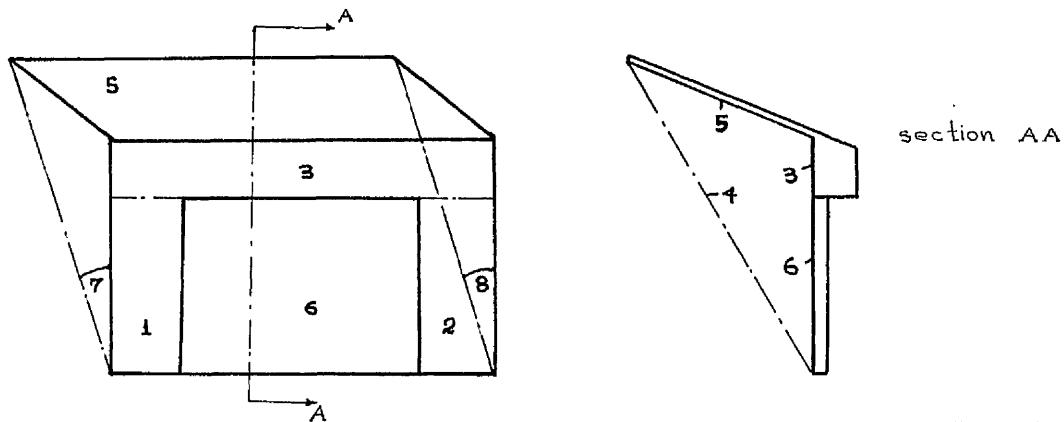


Fig. 2.4

Fig. 2.4 shows the general case of a receiver and an overhang. Surface 6 is the receiver (for example the external surface of a glass plate) and surface 5 is the lower surface of the overhang. The surfaces 1, 2 and 3 are the remaining surfaces of the wall surrounding the receiver. The surfaces 4, 7 and 8 are also imaginary. The solar radiation enters (or leaves) this particular enclosure through the surfaces 4, 7 and 8. A more careful examination of the enclosures of Fig. 2.3 and Fig. 2.4 shows that both enclosures are basically similar to each other.

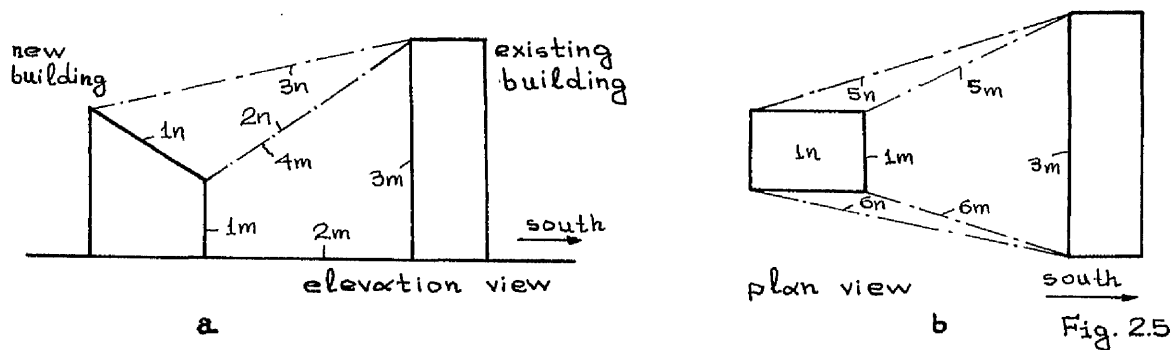


Fig. 2.5a and 2.5b show the plan and elevation view of an existing building and a proposed solar extension. The indices m and n distinguish the two different sub-enclosures.

In the case of enclosures similar to that of Fig. 2.2 Cockroft (30) and Eriksson (44) assume that all the solar radiation entering the radiated enclosure is trapped inside the enclosure. Cockroft (30) actually assumes that all of the direct component and half of the diffuse component of solar radiation is absorbed by the floor (surface 1 in Fig. 2.2) and one sixth of the diffuse component by each of the side walls adjacent to the window wall and by the wall opposite the window wall. On the other hand, Eriksson (44) mentions (but does not present any information or methodology) that the direct radiation is distributed to the internal surfaces of the test box under investigation according to the angle of incidence and the illuminated area. As far as the diffuse radiation is concerned, he assumes a uniform distribution to all internal surfaces. Similar assumptions of a somewhat arbitrary character are also made by Johnson (45). Lebens (39) presents a simplified approach to the distribution of direct solar radiation to the internal surfaces of a solar heated room. However his approach is restricted to collection apertures facing due south at either equinox.

The problem of modelling the three-dimensional movement of the sun around and inside a building, which is of prime significance for dynamically modelled direct gain and transwall passive solar systems, is overcome by the present method. In addition to this, the present method calculates accurately the proportion of solar energy being back reflected out through the window(s). It can also be extended to calculate daylight factor, the effect of sunlight on the lighting of a particular building and the associated possible sky and sun glare.

Calculation procedures for enclosures similar to those of Fig. 2.3 can be found in (15), of Fig. 2.4 in (14), (15), (40), (41), (43) and of Fig. 2.5 in (14).

### The method

The basic assumption of the method is that the reflected radiation from each internal surface of the enclosure consists macroscopically of two fractions; one specularly reflected and the other diffusely reflected in an isotropic way. Thus, for each internal surface two optical properties should be assigned: The first one is simply the specular fraction of the total reflected radiation. The second one is the reflectance of the surface, which is referred to the total reflection, specular and diffuse. If the surface is opaque, its absorptance is calculated easily. In the case of a surface belonging to a semi-transparent, or transparent, optical system an effective or overall absorptance can be used, which incorporates the absorptance of the individual layer(s) and total transmittance of the system. There is no difficulty in taking into account the effects of polarization, spectrum and direction of radiation into the values of reflectance and absorptance, or effective absorptance of any surface. The reflectance of an imaginary surface is always zero.

The radiation entering the enclosure can be split into direct and diffuse, and each type is handled separately. However, in both cases we need to know the polygon of entrance.

In the case of direct radiation, the polygon of entrance is separated into triangles. Each triangle, successively, is projected on every plane of the individual internal surfaces along the vector of radiation,  $\vec{V}$ . This means that the components of the vector of the entering radiation should also be known. The projection point  $W(W_x, W_y, W_z)$  of the point  $S(S_x, S_y, S_z)$  along the vector  $\vec{V}(V_x, V_y, V_z)$  on a plane passing through a point  $A(a_x, a_y, a_z)$  and being perpendicular to the vector  $\vec{P}(P_x, P_y, P_z)$  is given by subroutine PROJ and is described in Appendix H. The individual internal surface is lit by the entering radiation only if the polygon of the surface and the projected triangle on the plane of the surface have an intersection polygon. The calculation of the intersection polygon (if any) of two coplanar convex polygons is described in Appendix I. In such a case, the intersection polygon area AR is calculated using the subroutine AREA. This allows for the calculation of the radiation RABS absorbed by the internal surfaces according to the relation:

$$RABS = -AVSO * \cos(\text{ANIN}) * AR * (1.0 - \text{REFL}) \quad (2.7)$$

(RABS in watts)

and the radiation reflected diffusely RRD, and specularly RRS, according to the following relations:

$$RRD = -AVSO \cdot \cos (ANIN) \cdot AR \cdot REFL \cdot (1.0 - APER) \quad (2.8)$$

(RRD, in watts)

$$RRS = AVSO \cdot REFL \cdot APER \quad (2.9)$$

(RRS in  $W/m^2$ )

where  $AVSO$  ( $W/m^2$ ), is the intensity of the entering radiation.

$ANIN$ , is the angle between the vectors  $\vec{V}$  of the direct solar radiation and  $\vec{P}$  of the plane of the internal surface.

$$ANIN = \cos^{-1} [ \vec{V} \cdot \vec{P} ] \quad (2.10)$$

The conventionally defined angle of incidence  $ANO$ , is given by the relation:

$$ANO = 180^\circ - ANIN \quad (2.11)$$

The negative sign of relations (2.7) and (2.8) is explained by the fact that  $ANIN$  is always greater than  $90^\circ$ , otherwise the internal surface could not be lit by the entering radiation.

$REFL$ , is the reflectance of the internal surface (at the angle of incidence  $ANO$ ).

$APER$ , is the specular fraction of the reflected radiation.

The components of vector  $\vec{R}$  ( $R_x, R_y, R_z$ ) of the specularly reflected radiation are calculated according to the analysis of Appendix C. The associated intensity of this vector  $\vec{R}$  is  $RRS$  (in  $W/m^2$ ).

The above described procedure for the direct radiation entering the enclosure is now applied to each intersection polygon produced by the projection of the entrance polygon, with its associated vector  $\vec{R}(R_x, R_y, R_z)$  (instead of the vector  $\vec{V}(V_x, V_y, V_z)$  of the entrance polygon). This is carried on until the power  $AVAU$  carried by the direct radiation is less than a specified value,  $AVAU_0$ .

$$AVAU = -RRS \cdot \cos (ANIN) \cdot AR \quad (2.12)$$

For example, the value  $AVAU_0 = 4$  watts has been chosen in the numerical example of the test box given later in the next section.

The distribution of the diffuse radiation entering the enclosure through the entrance polygon or the diffusely reflected part of the direct radiation among the various internal surfaces (polygons) of the enclosure is based on the analysis presented in Appendix G. The subroutine ZEYS. SURNI, mentioned in Appendix G, calculates not only the view factor  $FMWi$  from the entrance polygon (or the intersection polygon) towards an internal surface  $i$ , but it also calculates the average angle of incidence  $ANGi$  of the radiation falling on this internal surface  $i$ . This permits the calculation of the reflectance  $REFLi$  of the internal surface  $i$ . Thus, if  $RRD$  is the diffuse radiation entering the enclosure, or the diffusely reflected part of the direct radiation, then the radiation  $RABi$ , absorbed and the radiation  $REFi$

reflected by the surface  $i$ , are given by the relations 2.13 and 2.14 respectively

$$RAB_i = RRD * FMW_i * (1.0 - REFL_i) \quad (2.13)$$

( $RAB_i$ , in watts)

$$REF_i = RRD * FMW_i * REFL_i^+ \quad (2.14)$$

( $REF_i$ , in watts)

Having accomplished this for each intersection polygon on the condition that  $RRD$  is greater than a specified value  $AVAU_o$  (mentioned above), there is still a remaining diffuse radiation  $REF_i$ , leaving each internal surface  $i$  for distribution among the other internal surfaces. However, the remainder of the total radiation has also to be distributed. This arises from the radiation that was excluded from the distribution process of direct and diffuse radiation, mentioned above, because of the constraints:

$$AVAU > AVAU_o \quad \text{and} \quad RRD > AVAU_o \quad (2.15)$$

The remainder contributes in an arbitrary way to the increase of the individual values of diffuse radiation  $REF_i$  (that leaves the surface  $i$ ). The distribution of diffuse radiation  $REF_i$  among the other internal surfaces of the enclosure is achieved using the appropriate net radiation method of radiative heat transfer, described in (42)<sup>+</sup>. The calculation again of the appropriate view factors and average angle of incidence (for the calculation of the corresponding reflectance) is accomplished by the subroutine ZEYS.SURNI of Appendix G.

A reference should be made here to the difficulty of multi-layer semi-transparent optical systems in respect to their character as diffusely or specularly reflecting surfaces when subjected to diffuse radiation. Apart from the reflected radiation coming from the first interface of the multi-layer system (relative to the enclosure) the remaining reflected radiation comes actually from one or more interfaces after one or more internal reflections inside the multi-layer system. This creates so much difficulty in adopting these systems as pure specularly reflecting surfaces that, for reasons of simplicity, the present analysis assumes that these optical systems behave as diffusely reflecting surfaces when subject to diffuse radiation.

It is also assumed in this method, that the flux of direct radiation entering an enclosure, after passing through a semi-transparent multi-layer optical system, is uniform all over the area of the entrance or intersection polygon. Additionally, the calculation of the entrance or intersection polygon is based only on the first interface of the semi-transparent multi-layer system relative to the enclosure (that is

<sup>+</sup>For simplicity reasons, every surface of the enclosure is assumed to behave as totally diffuse surface when subjected to diffuse radiation.



one of the internal surfaces of the enclosure). Without this assumption, refraction and reflection effects on the other interfaces of the system become too cumbersome for their limited effect on accuracy. It should also be added that when a direct or diffuse component of solar radiation inside the enclosure falls on an internal surface which belongs to a semi-transparent system, the equations 2.7 and 2.13 are not used. Instead, the non-reflected energy is separated into that transmitted through the whole system and that absorbed by each individual layer.

2.3 THE DISTRIBUTION OF SOLAR RADIATION AMONG  
THE PASSIVE ELEMENT AND THE INTERNAL SURFACES  
OF THE TEST BOX.

The whole or part of one of the sides of the parallelepiped enclosure of the test box is the internal surface of a passive solar system element. In the present application, the vector normal to this element is always on the horizontal plane facing south at an angle of  $\phi$  east from the north-south axis. A comparison is made between the solar radiation distribution of two passive solar systems; a 4mm clear float glass direct system and a transwall system with one module and one glass plate in front of it, described in section 1.4. Two variations are considered for each system; the system element covers the whole south facing side (case 1) and it covers 82% of this side (case 2). Fig.2.6 shows these systems. For the transwall system of case 2, the importance of the following factors concerning the distribution of solar radiation among the element and the internal surfaces have also been examined:

1. the composition of solar radiation into direct and diffuse
2. the spectrum of radiation
3. the reflectance of the internal opaque surfaces
4. the depth of the parallelepiped enclosure.

The two other dimensions of the enclosures remain constant:

width = 1.090m

height = 0.725m

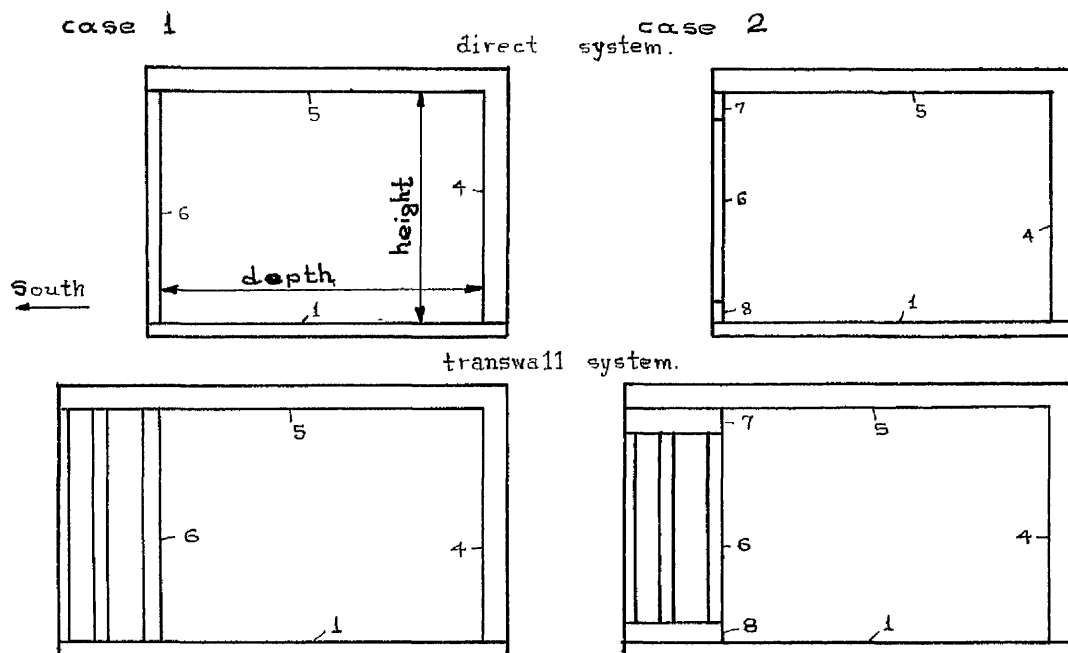


Fig. 2.6

Elevation view of the direct and transwall systems.

The analysis is referred to sea level site,  $56^{\circ}\text{N}$  latitude, standard temperature and pressure. It has been assumed that

- 1) both direct and diffuse radiation falls on an unobscured infinite ground which reflects them diffusely back with a reflectance of 0.82.
- 2) the diffuse radiation from the sky and the ground (or rather from the imaginary sky dome according to the analysis of section 1.3.3) are isotropic.
- 3) both direct and diffuse radiation inside and outside the enclosure have the same air-mass spectrum. Although the analysis of chapter 1 could allow for the calculation of the spectrum of the transmitted radiation into the enclosure, there were two reasons not to abandon this assumption of identical spectra; the dearth of knowledge of the spectral reflectivity of the opaque surfaces of the enclosure; and computational simplification.
- 4) the specular fraction of the reflected radiation of each surface is that given by Table 2.2.

Radiation measurements were not taken inside the test box. But the reasonable match of measured and predicted temperatures given by the analytical model of the test box (section 2.7) implies some verification of the method of distribution of solar radiation.

Table 2.2

Reflectance (REFL) and specularly reflected fraction (APER) of solar radiation of the internal surfaces of the parallelepiped enclosure.

Surface ↓	angle of incidence <sup>+</sup> →	Table 2.2a		Table 2.2b	
		$0^{\circ} \div 80^{\circ}$	$90^{\circ}$	$0^{\circ} \div 80^{\circ}$	$90^{\circ}$
1 (floor)	REFL	0.250	1.000	0.800	1.000
	APER	0.800	0.800	0.800	0.800
2 (west side)	REFL	0.720	1.000	0.960	1.000
	APER	0.500	0.500	0.500	0.500
3 (east side)	REFL	0.720	1.000	0.960	1.000
	APER	0.500	0.500	0.500	0.500
4 (north side)	REFL	0.720	1.000	0.960	1.000
	APER	0.500	0.500	0.500	0.500
5 (ceiling)	REFL	0.720	1.000	0.960	1.000
	APER	0.500	0.500	0.500	0.500
7 (high south side)	REFL	0.720	1.000	0.960	1.000
	APER	0.800	0.800	0.800	0.800
8 (low south side)	REFL	0.100	1.000	0.800	1.000
	APER	0.500	0.500	0.500	0.500

<sup>+</sup> conventionally defined.

Comparison between the distribution of solar radiation of the direct and the transwall systems.

The comparison is referred to the first of January. Estimated values of direct(intensity) and diffuse on a horizontal surface solar radiation are given in Table 2.3. From these values the composition of the direct and diffuse radiation received by the external surface of the passive system element is calculated (see Table 2.4). The radiation spectrum assumed is that of air-mass 2, chosen to provide a comparison with an analysis detailed subsequently in this section. This assumption will introduce a small error, according to the predicted values of air-mass, given in Table 2.4, fifth column.

The reflectance of each of the five (or seven) internal opaque surfaces of the parallelepiped enclosure as function of the angle of incidence is given in Table 2.2a. The reflectance of the remaining glass surface 6 is given in the first row of Table 2.5 and 2.6 for the 4mm glass plate and the transwall system element, respectively. The other optical properties of these two passive solar system elements are also given in these tables. The 1-dimensional ray-tracing technique of section 1.1 has been used for their calculation.

Conclusion.

The difference between the direct and the transwall systems is shown in Fig. 2.7 and 2.8.

The total reflected radiation out of the direct system is 7 to 11% of the total incident radiation larger than the equivalent from the transwall system. This coupled with the fact that the radiation absorbed by the outside glass plate of the transwall system is less than that absorbed by the single glass plate of the direct system, gives a strong indication on the better effectiveness of transwall systems in collecting solar energy compared with direct solar systems.

The "first strike" values (small capital letters in figures) have been calculated without taking into account internal reflections inside the enclosure. This is equivalent to the assumption that all the solar radiation entering the enclosure is totally absorbed by the opaque surfaces. It is apparent from Fig. 2.7 and 2.8 that this common assumption may in fact lead to substantial errors, especially in the case of direct systems. For example the difference between final values and first strike values of reflected radiation could be as large as 20% of the total incident

radiation.

The radiation absorbed by the various internal surfaces of the enclosure with the direct solar system is much larger than that absorbed by the corresponding surfaces of the transwall solar system. This difference can be about 9 to 15% of the incident radiation in the case of the floor surface (internal surface 1), about 2 to 10% of the incident radiation in the case of side walls and the wall opposite to the south facing side of the enclosure (internal surfaces, 2, 3 and 4 respectively). This fact reveals the tendency of direct solar systems to overheat under certain conditions. The diurnal variations of the absorbed radiation by the various internal surfaces are again larger in the case of the enclosure with the direct solar system. This variation can be as much as 10% in the case of floor and 15% of the total incident radiation in the case of side walls for the direct system enclosures. These variations are about half of the above-mentioned in the case of the transwall system enclosure.

The effect of composition of solar radiation  
into direct and diffuse.

This effect is shown in Fig. 2.9 . This figure is related to Tables 2.7 and 2.8 which give the composition of the direct and diffuse radiation received by the external surface of the transwall system element on the second and third of April, 1982. These tables have been constructed from measured data given in graphic form in Fig. 2.10.

Conclusion

The difference between the final values and the first strike values is evident, especially in the case of reflected radiation back out of the system and the absorbed radiation by the liquid and back glass plate of the transwall module.

The increase in the diffuse component of solar radiation leads to a more balanced distribution of the radiation inside the enclosure. This means a difference in absorbed radiation by the floor of the order of about 5% of the total incident radiation between the enclosure of second and third of April, for the same angle of incidence. More unequal distribution can be seen in the case of the enclosure on the first of January (Fig. 2.8 ) where the direct solar radiation component is the main one (85% of total incident radiation). In such a case the direction of direct solar radiation vector is quite important in determining the distribution of the solar radiation inside the enclosure.

### The effect of radiation spectrum.

The example is referred to the first of January. The effect is shown in Fig. 2.11. The assumption of air-mass 7 spectrum is closer to the predicted values than the initial assumption of air-mass 2 (from Table 2.4). The optical properties of the transwall system element for air-mass 7 are given in Table 2.9, constructed according to the 1-dimensional ray-tracing technique of section 1.1.

#### Conclusion.

The change from air-mass 2 to air-mass 7 spectrum produces a decrease in the totally reflected radiation and the absorbed radiation by the back glass plate and the opaque surfaces of the enclosure. This decrease may account for 1.5% of the total incident radiation. An increase of a similar order is experienced for the absorbed radiation by the two front glass plates and as much as 5% for the liquid.

### The effect of the reflectance of the opaque surfaces.

This effect is shown in Fig. 2.12, 2.13 and 2.14 which are referred to the first of January and the second and third of April, respectively.

#### Conclusion.

The change of the reflectance of the internal surfaces results in an increase in the totally reflected radiation amounting to about 6% of the total incident radiation in the present example. The increase in the radiation absorbed by the various glass plates and liquid layer varies up to 4% and 5.5% respectively. The decrease in absorbed radiation in the case of the floor surface can be as much as about 10% of the total incident radiation. Only the radiation absorbed by surface 8 has increased because of the very high increase of the radiation falling on it.

### The effect of change in the box depth.

This effect is shown in Tables 2.10, 2.11 and 2.12, which are referred to the first of January, and the second and third of April, respectively, for the test-box with internal surfaces of low reflectance (Table 2.2a).

#### Conclusion.

There is no significant difference (i.e. order of 1% of the total incident radiation) between corresponding values in every table, apart from the absorbed radiation by surface 1 (floor) on the first of January (Table 2.10). In this case the difference is higher but does not exceed 5% of the total incident radiation. The same order of difference (1%) between all the corresponding values has also been found for the test-box with internal surfaces of high reflectance (Table 2.2b).

Table 2.3

Direct (intensity) and diffuse on a horizontal surface solar radiation.  
1st of January.

Solar time	9	10	11	12	13	14	15
Direct solar radiation W/m <sup>2</sup>	135	265	360	500	416	312	175
Diffuse solar radiation on horizontal surface W/m <sup>2</sup>	12	30	40	46	42	32	10

Table 2.4

Test Box Example. Solar radiation (watts) received by the passive  
1st January system element.

Solar Time	Direct Radiation % of total	Diffuse Radiation % of total	Angle of incidence degrees	Predicted Air-Mass of direct radiation
9	89.2	10.8	36.6	19.6
10	85.7	14.3	24.5	8.0
11	85.0	15.0	14.0	5.7
12	85.8	14.2	11.7	5.2
13	85.3	14.7	20.5	5.7
14	85.6	14.4	32.4	8.0
15	91.3	8.7	44.8	19.6

Table 2.5

Optical properties of 4mm clear float glass

Direct radiation - AM2 spectrum

Angle of incidence	0°	20°	40°	60°	80°	90°
reflectance	0.071	0.071	0.079	0.138	0.495	1.000
transmittance	0.802	0.799	0.784	0.715	0.368	0.000
absorptance	0.127	0.130	0.137	0.147	0.137	0.000

Isotropic sky diffuse radiation on vertical surface - AM2 spectrum

reflectance	transmittance	absorptance
0.160	0.702	0.138

Note: AM2 = Air Mass

Table 2.6

Optical properties of transwall system element.

Direct radiation - AM2

Angle of → incidence	0°	20°	40°	60°	80°	90°
Backward direction						
reflectance	0.084	0.083	0.088	0.140	0.473	1.000
transmittance	0.377	0.374	0.359	0.309	0.108	0.000
absorptance of outside glass	0.030	0.030	0.031	0.030	0.018	0.000
absorptance of front glass	0.058	0.058	0.061	0.064	0.064	0.000
absorptance of 1st liquid layer	0.004	0.004	0.004	0.004	0.004	0.000
absorptance of 2nd liquid layer	0.082	0.081	0.080	0.074	0.056	0.000
absorptance of 3rd liquid layer	0.188	0.187	0.186	0.177	0.119	0.000
absorptance of back glass	0.177	0.183	0.191	0.202	0.158	0.000
Forward direction						
reflectance	0.112	0.112	0.119	0.183	0.565	1.000
transmittance	0.377	0.374	0.359	0.309	0.108	0.000
absorptance of outside glass	0.134	0.137	0.145	0.158	0.159	0.000
absorptance of front glass	0.123	0.125	0.130	0.125	0.063	0.000
absorptance of 1st liquid layer	0.143	0.142	0.139	0.123	0.053	0.000
absorptance of 2nd liquid layer	0.062	0.062	0.058	0.051	0.024	0.000
absorptance of 3rd liquid layer	0.003	0.003	0.003	0.003	0.001	0.000
absorptance of back glass	0.046	0.045	0.047	0.046	0.027	0.000

Isotropic sky diffuse radiation on a vertical surface - AM2 spectrum

	reflectance	transmittance	absorptance of outside glass	absorptance of front glass	absorptance of 1st liquid layer	absorptance of 2nd liquid layer	absorptance of 3rd liquid layer	absorptance of back glass
Backward direction	0.164	0.307	0.028	0.062	0.004	0.074	0.173	0.188
Forward direction	0.207	0.307	0.149	0.118	0.122	0.051	0.002	0.044

Note: AM2 = Air-Mass 2

1st liquid layer = 1.2 cm

2nd liquid layer = 12.6cm

3rd liquid layer = 1.2 cm



# TRANSWALL SYSTEM

# DIRECT SYSTEM

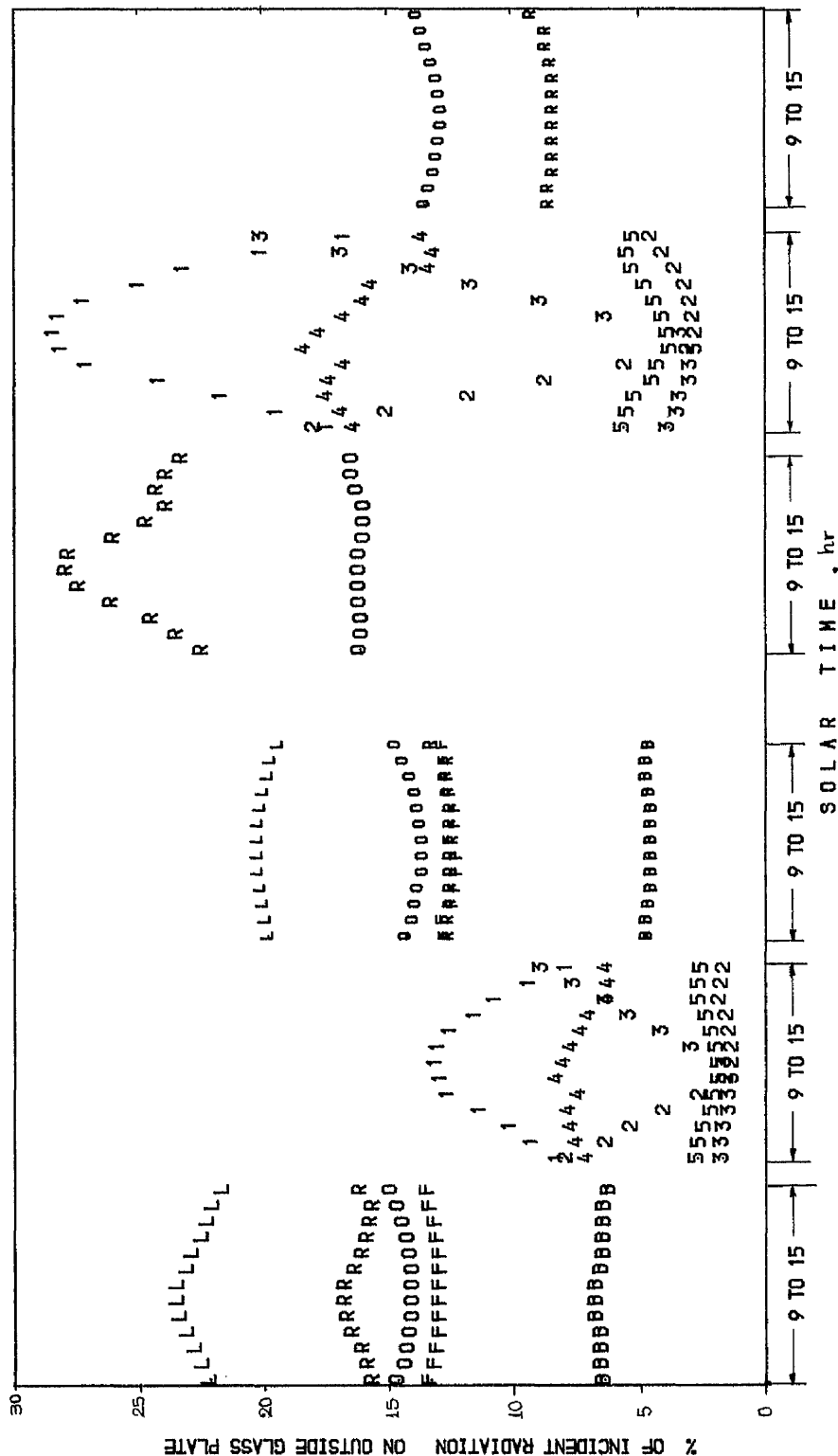


FIG. 2.7

TEST BOX. TOTAL COVER. 4°E ANGLE FROM NORTH-SOUTH AXIS. AIR-MASS 2 SPECTRUM.

1ST JAN. 0.853M DEPTH. REFLECTANCE OF THE INTERNAL OPAQUE SURFACES ACCORDING TO TABLE 2.2a.

# TRANSWALL SYSTEM

# DIRECT SYSTEM

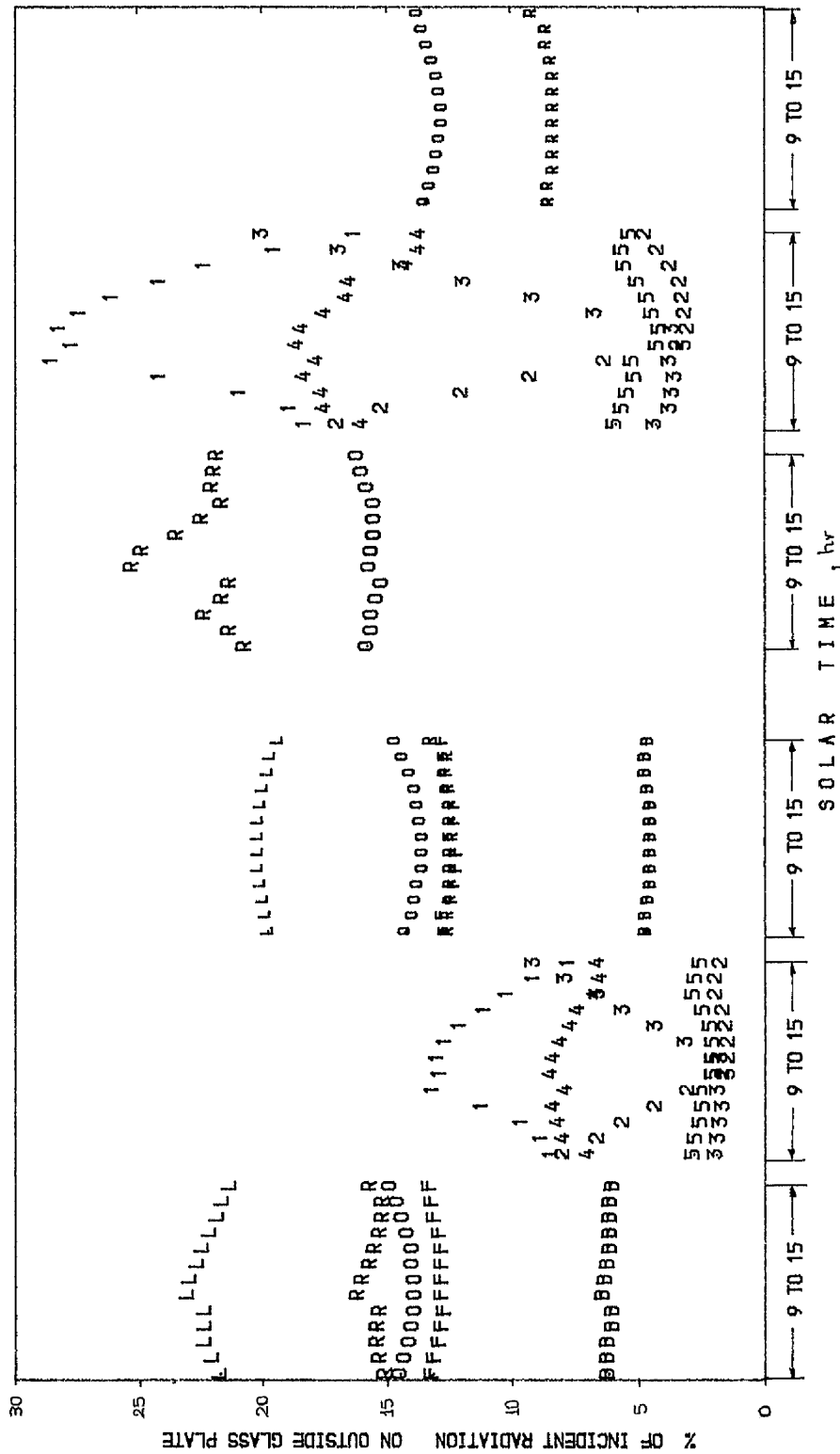


FIG. 2.8

TEST BOX. PARTIAL COVER. 4° E ANGLE FROM NORTH-SOUTH AXIS.

AIR-MASS 2 SPECTRUM.

1ST JAN. 0.853M DEPTH. REFLECTANCE OF THE INTERNAL OPAQUE SURFACES ACCORDING TO TABLE 2.2a.

## TRANSWALL SYSTEM

ABSORPTANCE OF SURFACE 7 ~0.2 %

ABSORPTANCE OF SURFACE 8 FROM 0.5 TO 0.8 %

## DIRECT SYSTEM

ABSORPTANCE OF SURFACE 7 FROM 0.3 TO 0.5 %

ABSORPTANCE OF SURFACE 8 FROM 0.9 TO 1.8 %

The % implies % of incident radiation on outside glass plate.

2ND APRIL

TRANSWALL SYSTEM

3RD APRIL

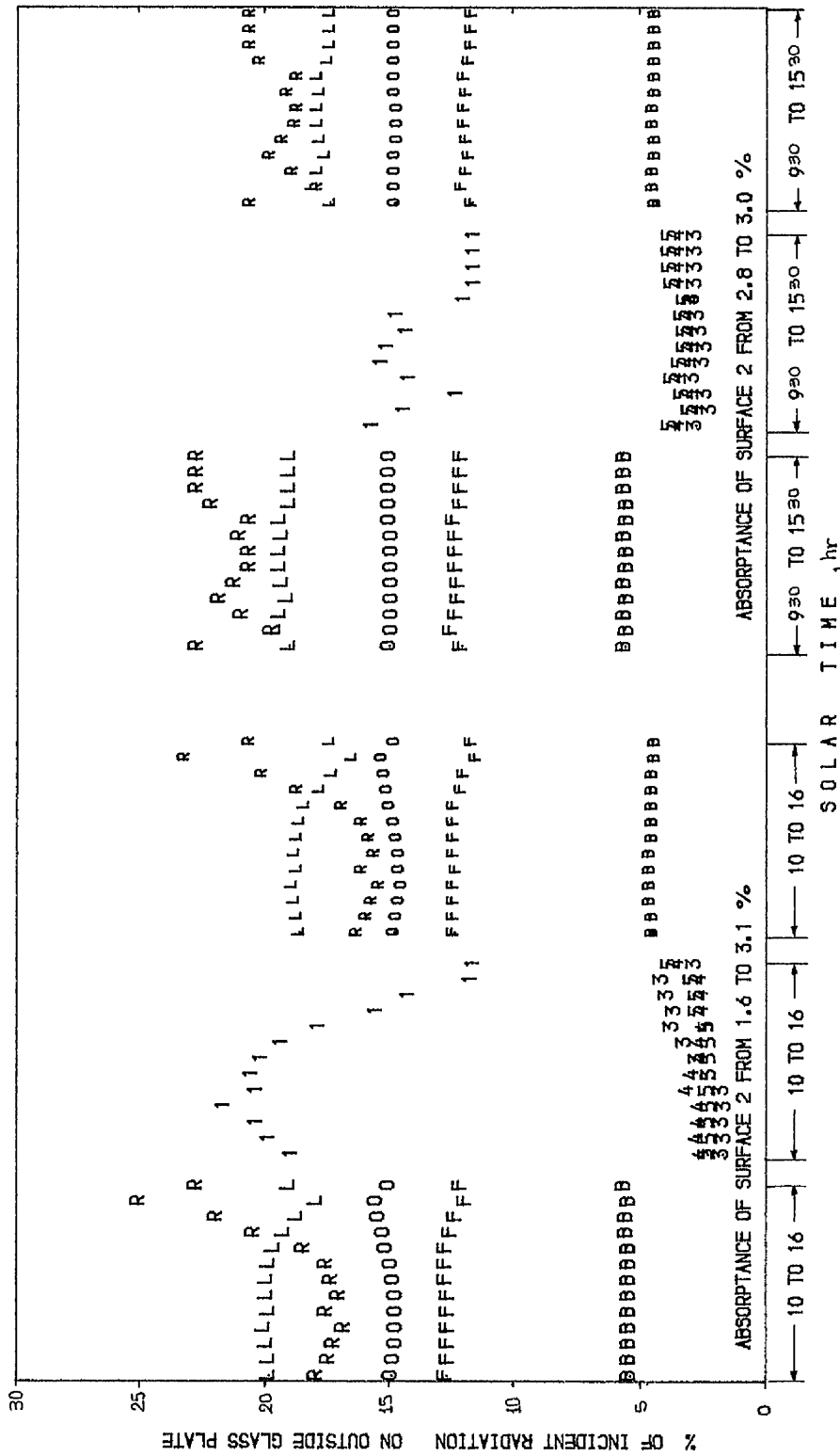


FIG. 2.9.

TEST BOX. PARTIAL COVER. 4° E ANGLE FROM NORTH-SOUTH AXIS.

0.853M DEPTH. REFLECTANCE OF THE INTERNAL OPAQUE SURFACES ACCORDING TO TABLE 2.2a.

Table 2.7

Test box example. Solar radiation (watts) received by the passive  
2nd April system element.  
 Air-mass 2 spectrum of radiation

Solar Time	Direct Radiation % of total	Diffuse Radiation % of total	Angle of incidence degrees	Predicted Air-Mass of direct radiation
10	54.2	45.8	45.4	1.8
11	55.8	44.2	40.0	1.6
12	51.0	49.2	39.2	1.6
13	57.8	42.2	43.2	1.6
14	55.8	44.2	51.0	1.8
15	44.6	55.4	61.1	2.1
16	0.0	100.0	72.4	2.8

Table 2.8

Test box example. Solar radiation (watts) received by the passive  
3rd April system element.  
 Air-Mass 2 spectrum

Solar Time	Direct Radiation % of total	Diffuse Radiation % of total	Angle of incidence degrees	Predicted Air-Mass of direct radiation
9	0.0	100.0	54.5	2.1
10	34.6	65.4	45.9	1.8
11	8.7	91.3	40.4	1.6
12	20.9	79.1	39.6	1.6
13	18.7	81.3	43.6	1.6
14	6.7	93.3	51.3	1.8
15	0.0	100.0	61.3	2.1
16	0.0	100.0	72.7	2.8

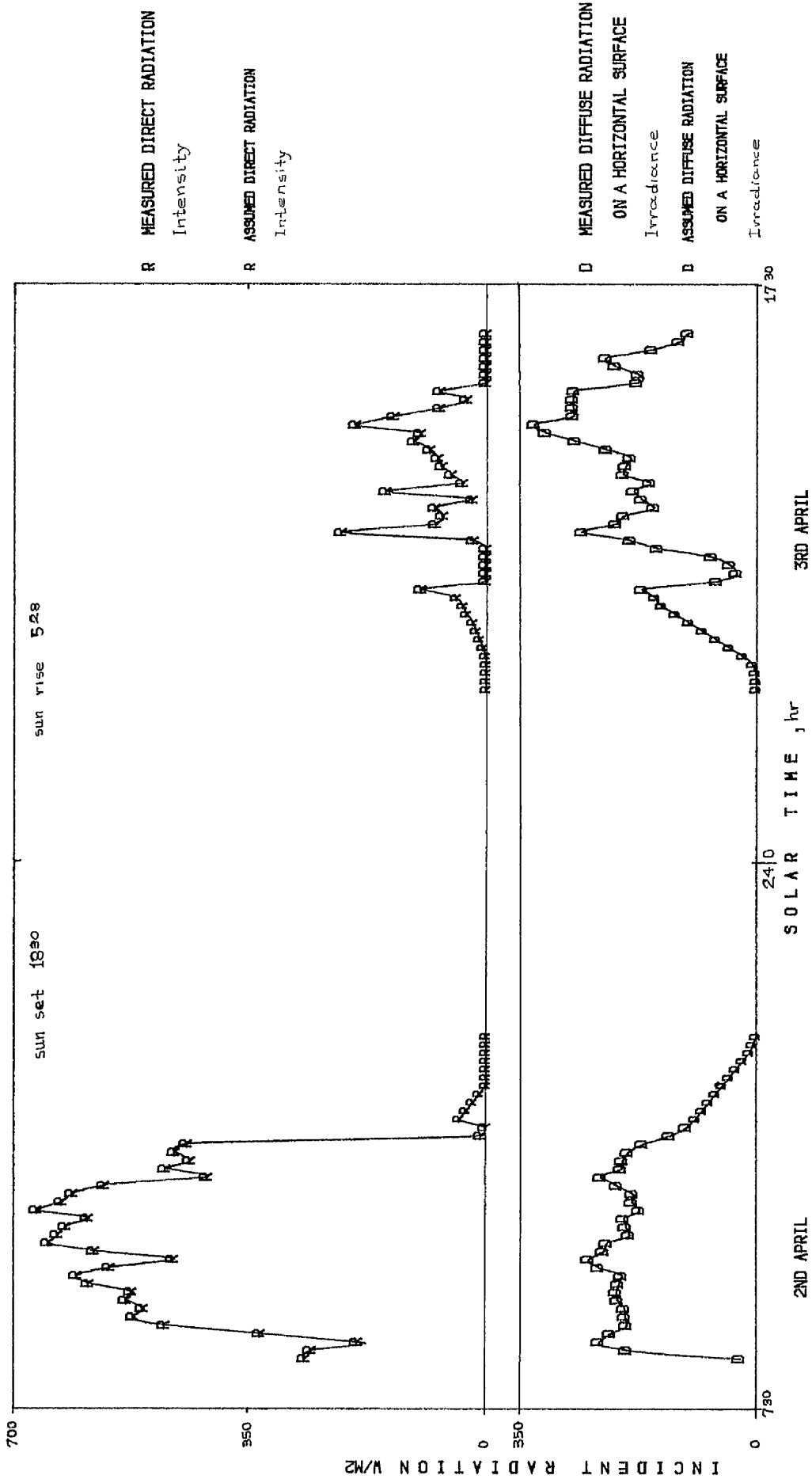


FIG.2.10  
SOLAR RADIATION

# AIR-MASS 2 SPECTRUM      TRANSWALL SYSTEM      AIR-MASS 7 SPECTRUM

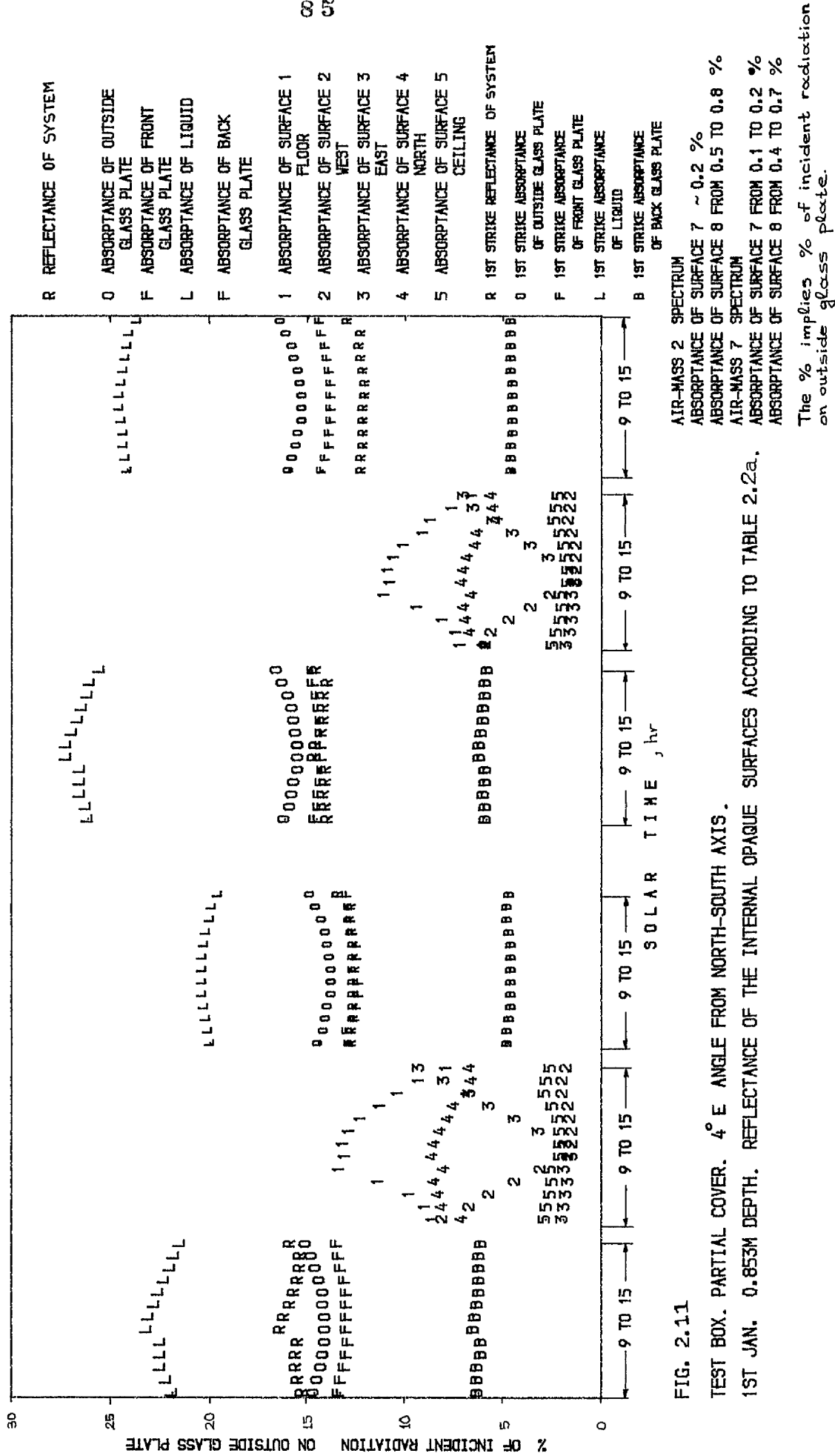


FIG. 2.11

TEST BOX. PARTIAL COVER. 4° E ANGLE FROM NORTH-SOUTH AXIS.

1ST JAN. 0.853M DEPTH. REFLECTANCE OF THE INTERNAL OPAQUE SURFACES ACCORDING TO TABLE 2.2a.

The % implies % of incident radiation on outside glass plate.

Table 2.9

Optical properties of transwall system element.

Direct radiation - AM7

Angle of incidence →	0°	20°	40°	60°	80°	90°
Backward direction						
reflectance	0.075	0.075	0.080	0.129	0.452	1.000
transmittance	0.312	0.308	0.294	0.252	0.086	0.000
absorptance of outside glass	0.029	0.029	0.030	0.028	0.017	0.000
absorptance of front glass	0.056	0.057	0.059	0.062	0.060	0.000
absorptance of 1 <sup>st</sup> liquid layer	0.004	0.004	0.004	0.004	0.004	0.000
absorptance of 2 <sup>nd</sup> liquid layer	0.093	0.092	0.089	0.084	0.062	0.000
absorptance of 3 <sup>rd</sup> liquid layer	0.234	0.234	0.232	0.220	0.147	0.000
absorptance of back glass	0.197	0.201	0.212	0.221	0.172	0.000
Forward direction						
reflectance	0.108	0.107	0.114	0.176	0.553	1.000
transmittance	0.312	0.308	0.294	0.252	0.085	0.000
absorptance of outside glass	0.147	0.152	0.160	0.174	0.174	0.000
absorptance of front glass	0.137	0.139	0.144	0.139	0.068	0.000
absorptance of 1 <sup>st</sup> liquid layer	0.180	0.178	0.174	0.154	0.065	0.000
absorptance of 2 <sup>nd</sup> liquid layer	0.069	0.068	0.066	0.058	0.026	0.000
absorptance of 3 <sup>rd</sup> liquid layer	0.003	0.003	0.003	0.003	0.002	0.000
absorptance of back glass	0.044	0.045	0.045	0.044	0.026	0.000

Isotropic sky diffuse radiation on a vertical surface - AM7 spectrum

	reflectance	transmittance	absorptance of outside glass	absorptance of front glass	absorptance of 1 <sup>st</sup> liquid layer	absorptance of 2 <sup>nd</sup> liquid layer	absorptance of 3 <sup>rd</sup> liquid layer	absorptance of back glass
Backward direction	0.153	0.251	0.027	0.060	0.004	0.084	0.215	0.206
Forward direction	0.201	0.251	0.165	0.130	0.151	0.057	0.003	0.042

Note: AM7 = Air-Mass 7

1<sup>st</sup> liquid layer = 1.2cm2<sup>nd</sup> liquid layer = 12.6 cm3<sup>rd</sup> liquid layer = 1.2 cm

LOW REFLECTANCE-TABLE 2.2a

TRANSWALL SYSTEM

HIGH REFLECTANCE-TABLE 2.2b

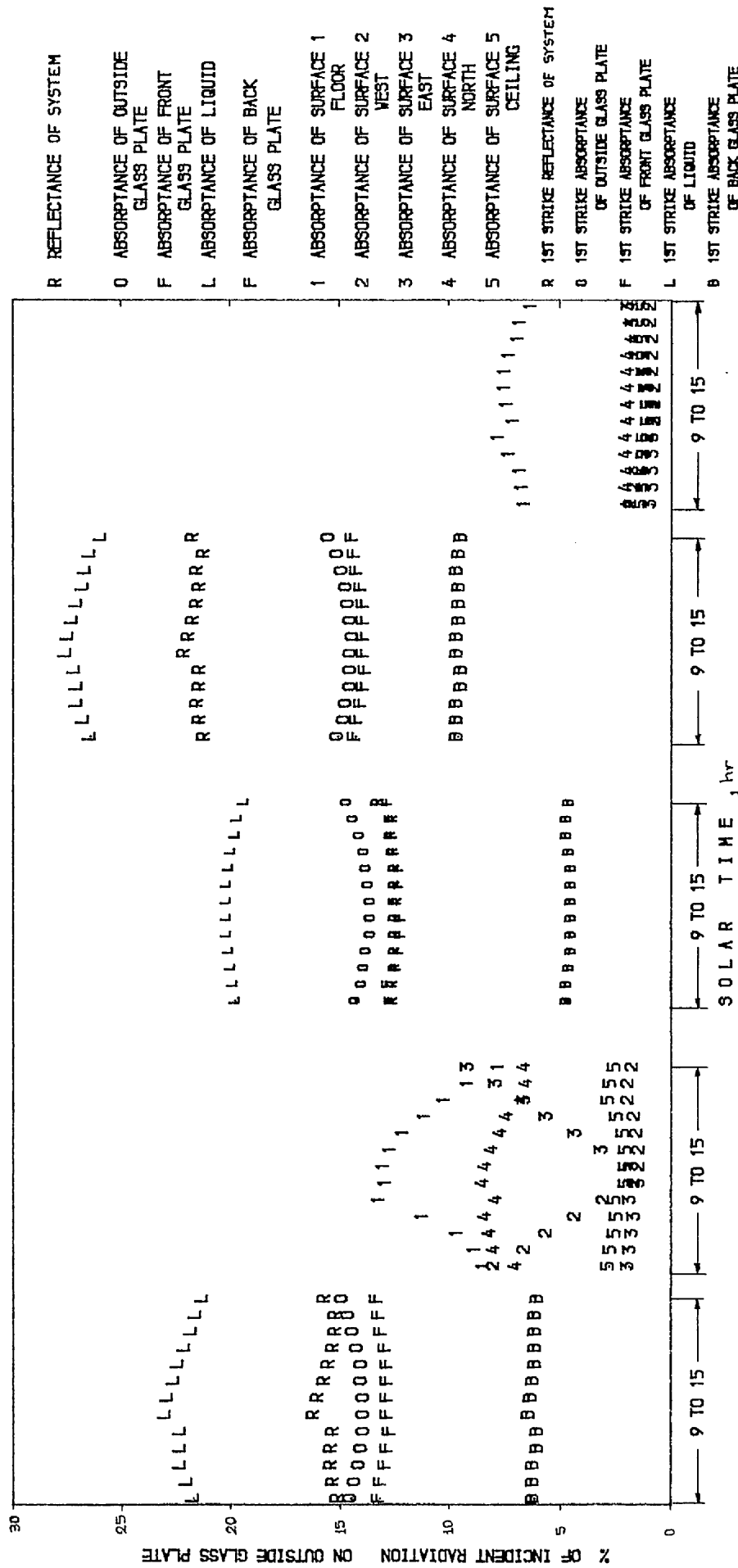


FIG. 2.12

TEST BOX, PARTIAL COVER. 4° E ANGLE FROM NORTH-SOUTH AXIS.

1ST JAN. 0.853M DEPTH.

LOW REFLECTANCE-TABLE 2.2a

ABSORPTANCE OF SURFACE 7 ~ 0.2 %

ABSORPTANCE OF SURFACE 8 FROM 0.5 TO 0.8 %

HIGH REFLECTANCE-TABLE 2.2b

ABSORPTANCE OF SURFACE 7 ~ 0.1 %

ABSORPTANCE OF SURFACE 8 FROM 0.4 TO 0.5 %

The % implies % of incident radiation on the outside glass plate.



LOW REFLECTANCE-TABLE 2.2a

TRANSWALL SYSTEM

HIGH REFLECTANCE-TABLE 2.2b

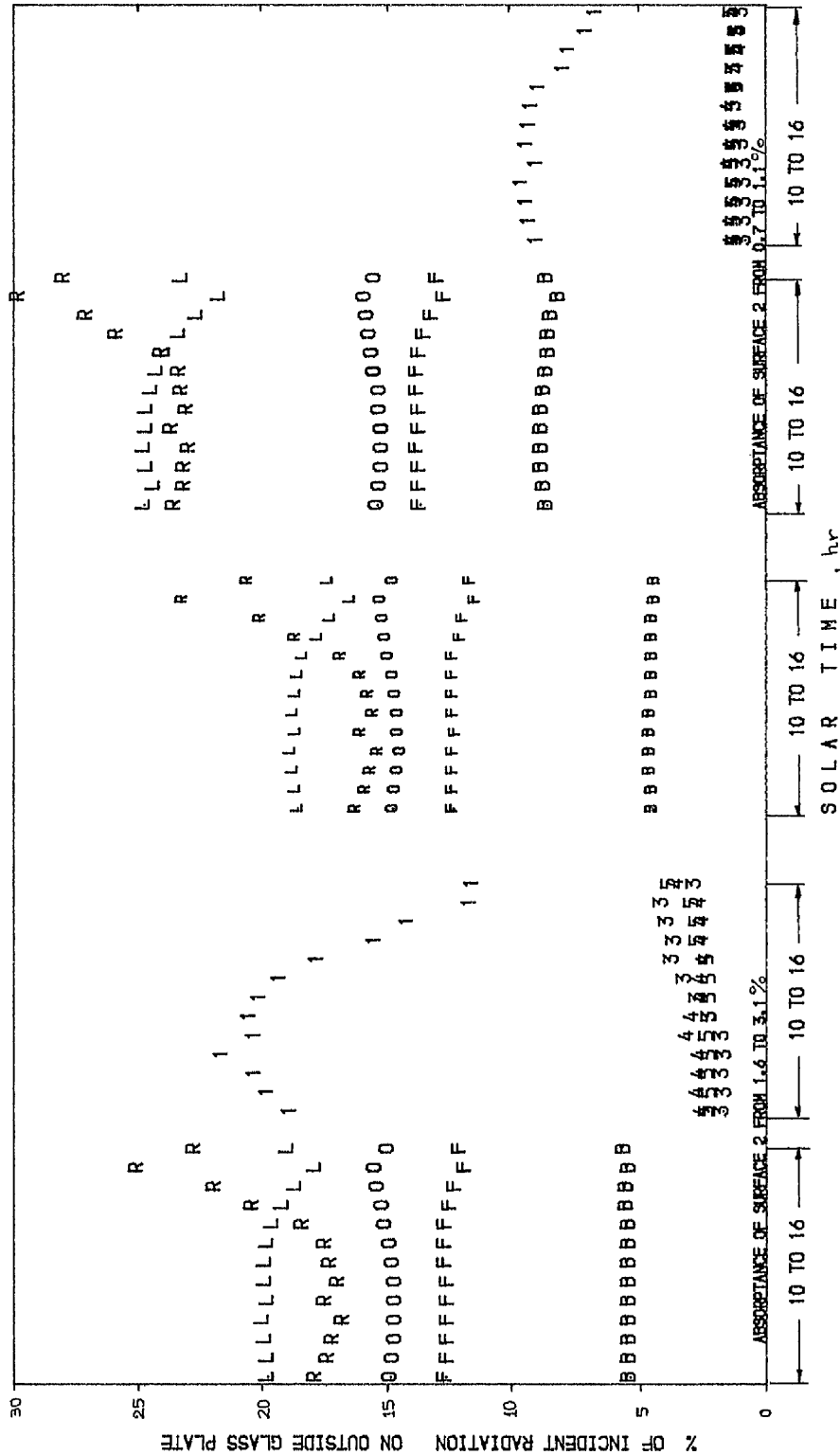


FIG. 2.13

TEST BOX, PARTIAL COVER. 4° E ANGLE FROM NORTH-SOUTH AXIS.  
2ND APRIL. 0.853M DEPTH.

LOW REFLECTANCE-TABLE 2.2a.

ABSORPTANCE OF SURFACE 7 FROM 0.1 TO 0.2 %  
ABSORPTANCE OF SURFACE 8 FROM 0.3 TO 0.4 %  
HIGH REFLECTANCE-TABLE 2.2b  
ABSORPTANCE OF SURFACE 7 ~ 0.1 %  
ABSORPTANCE OF SURFACE 8 FROM 0.3 TO 0.4 %

The % implies % of incident radiation on the outside glass plate.

LOW REFLECTANCE-TABLE 2.2a.

TRANSWALL SYSTEM

HIGH REFLECTANCE-TABLE 2.2b

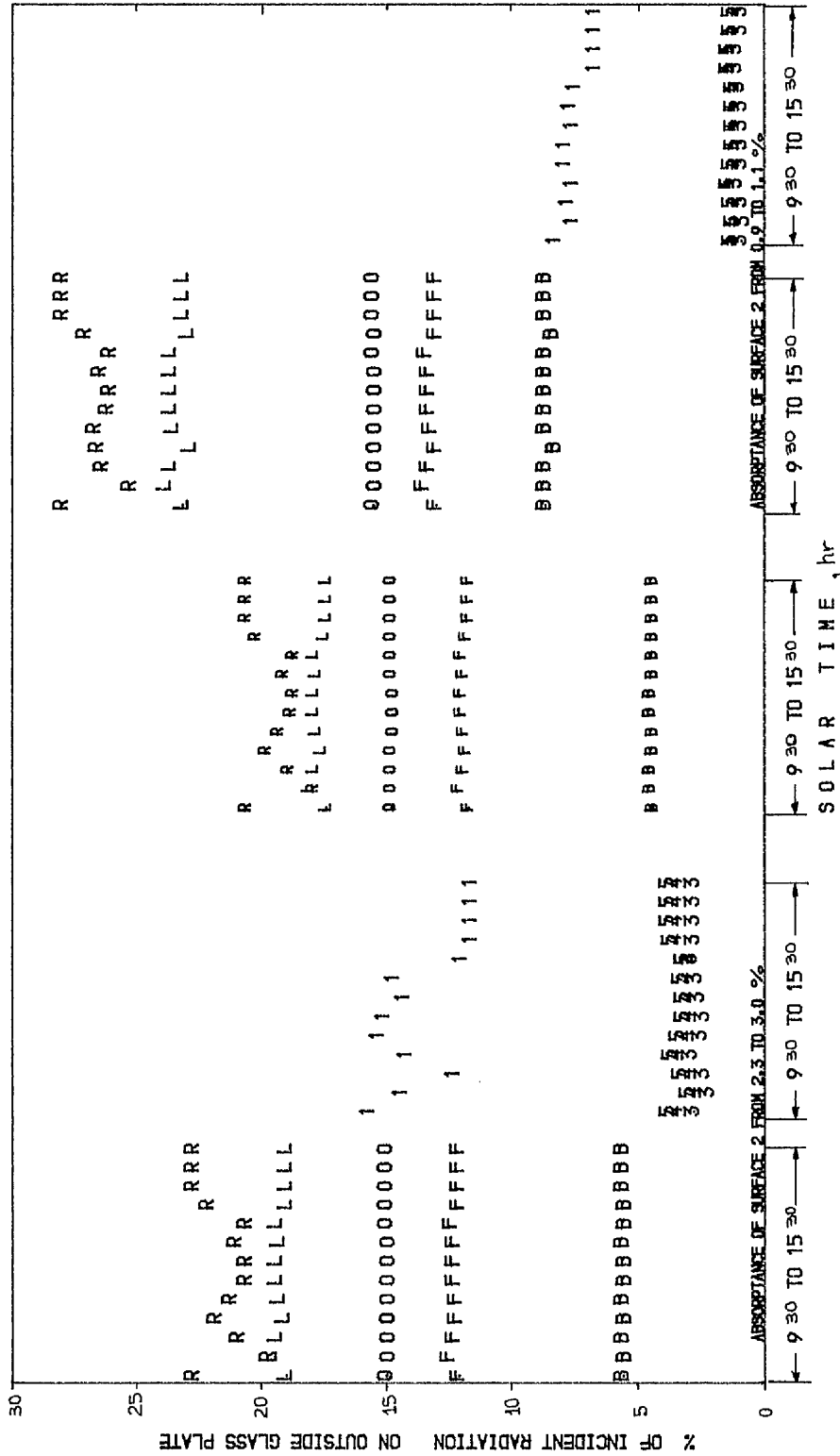


FIG. 2.14

TEST BOX. PARTIAL COVER. 4° E ANGLE FROM NORTH-SOUTH AXIS.

3RD APRIL. 0.853M DEPTH.

LOW REFLECTANCE-TABLE 2.2a.

ABSORPTANCE OF SURFACE 7 FROM 0.2 TO 0.3 %

ABSORPTANCE OF SURFACE 8 FROM 0.3 TO 0.4 %

HIGH REFLECTANCE-TABLE 2.2b

ABSORPTANCE OF SURFACE 7 FROM 0.1 TO 0.2 %

ABSORPTANCE OF SURFACE 8 ~ 0.4 %

The % implies % of incident radiation on the outside glass plate.

Table 2.10

Test box example. Transwall. Partial cover. 1st January. Air-Mass 2 spectrum of radiation.  
 Reflectance of the internal surfaces according to Table 2.2a.

Solar time	Reflected radiation	Absorbed radiation by outside glass	Absorbed radiation by front glass	Absorbed radiation by liquid	Absorbed radiation by back glass	Absorbed radiation by internal surfaces							
						1	2	3	4	5	7	8	
11	14.4	13.9	12.6	21.6	5.4	17.0	3.4	1.9	6.4	2.6	0.1	0.6	
12	14.6	13.9	12.7	21.9	5.6	18.0	1.7	2.0	7.0	2.3	0.1	0.3	
13	14.4	14.0	12.7	21.6	5.5	15.6	1.8	5.3	5.9	2.5	0.1	0.4	
14	14.6	14.4	13.0	21.3	5.7	11.9	2.0	8.3	5.5	2.8	0.1	0.3	
15	15.3	15.0	13.3	21.0	5.7	9.1	2.4	10.5	4.4	2.8	0.2	0.3	
11	15.4	14.0	12.8	22.4	6.0	13.3	3.0	1.8	7.9	2.5	0.2	0.6	
12	16.1	14.0	12.9	23.0	6.3	13.1	1.4	1.7	8.4	2.0	0.2	0.8	
13	15.6	14.1	12.9	22.5	6.1	12.2	1.5	4.3	7.7	2.1	0.2	0.8	
14	15.3	14.5	13.2	21.9	6.1	10.3	1.9	6.6	6.7	2.8	0.2	0.5	
0.853m depth	15	15.8	15.0	13.4	21.4	6.0	7.8	1.7	9.2	6.6	2.5	0.2	0.4

Note: the values are percentages of total incident radiation on the outside glass plate.

Table 2.11

Test box example. Transwall. Partial cover. 2nd April. Air-Mass 2 spectrum of radiation. Reflectance of the internal surfaces according to Table 2.2a.

Solar time	Reflected radiation	Absorbed radiation by outside glass	Absorbed radiation by front glass	Absorbed radiation by liquid	Absorbed radiation by back glass	Radiation absorbed by the internal surfaces							
						1	2	3	4	5	7	8	
1.250m depth													
11	16.9	14.8	12.7	19.7	5.2	21.2	2.6	1.8	2.0	2.8	0.1	0.2	
12	17.3	14.8	12.6	19.6	5.2	21.4	1.9	1.9	2.1	2.9	0.1	0.2	
13	17.1	14.9	12.7	19.7	5.2	21.1	1.7	3.0	1.7	2.7	0.1	0.2	
14	18.2	15.2	12.7	19.4	5.2	18.6	1.9	4.1	1.5	2.6	0.1	0.2	
15	21.6	15.5	12.3	19.5	5.3	15.4	2.2	4.1	1.8	3.0	0.1	0.3	
0.853m depth													
11	17.3	14.8	12.7	20.0	5.4	20.4	2.4	1.7	2.6	2.3	0.1	0.3	
12	17.6	14.8	12.7	19.9	5.4	20.4	1.7	1.7	3.1	2.3	0.1	0.3	
13	17.4	14.9	12.8	20.0	5.4	20.2	1.6	2.7	2.5	2.2	0.1	0.3	
14	18.5	15.2	12.8	19.7	5.4	17.9	1.7	3.7	2.4	2.3	0.1	0.3	
15	22.0	15.5	12.4	18.8	5.3	14.3	2.0	3.9	2.5	2.7	0.2	0.4	

Note: The values are percentages of total incident radiation on the outside glass plate.

Table 2.12

Test box example. Transwall. Partial cover. 3rd April. Air-mass 2 spectrum of radiation.  
 Reflectance of the internal surfaces according to Table 2.2a.

Solar time	Reflected radiation	Absorbed radiation by outside glass	Absorbed radiation by front glass	Absorbed radiation by liquid	Absorbed radiation by back glass	Radiation absorbed by internal surfaces							
						1	2	3	4	5	7	8	
1.250m depth													
11	21.4	15.0	12.2	18.9	5.2	13.8	3.1	3.1	2.5	4.1	0.3	0.4	
12	20.3	14.9	12.3	19.1	5.3	16.7	2.6	2.6	2.1	3.6	0.1	0.3	
13	20.7	15.0	12.3	19.1	5.3	15.7	2.7	3.0	2.2	3.7	0.1	0.3	
14	21.8	15.1	12.1	18.8	5.3	13.6	3.1	3.1	2.5	4.1	0.3	0.3	
15	22.3	15.0	12.1	18.6	5.3	13.2	3.1	3.1	2.4	4.2	0.1	0.3	
0.853m depth													
11	21.9	15.0	12.3	19.2	5.5	12.4	2.9	2.9	3.5	3.7	0.4	0.5	
12	20.7	15.0	12.4	19.5	5.5	15.4	2.4	2.4	3.0	3.2	0.2	0.4	
13	21.1	15.0	12.4	19.4	5.6	14.4	2.4	2.7	3.1	3.3	0.2	0.4	
14	22.2	15.1	12.2	19.1	5.5	12.1	2.8	2.8	3.5	3.7	0.3	0.4	
15	22.8	15.1	12.2	19.1	5.6	11.7	2.8	2.8	3.5	3.8	0.2	0.4	

Note: The values are percentages of total incident radiation on the outside glass plate.

## 2.4 ANALYTICAL MODELLING OF A PASSIVE SOLAR SYSTEM

The present mathematical analysis has been developed to model the thermal performance of a passive solar system and, in general, of a building.

Its basic characteristic is the separation of the whole passive system into a finite number,  $M$ , of control volumes, each one represented by a node, generally at the geometrical middle of the control volume. The temperature of each node is to be calculated. The temperatures and the heat and mass fluxes at the interfaces of the control volumes are to be calculated as well. The control volumes are divided into groups in such a way that the nodes of each group lie on a particular line. These lines start and finish at ambient temperature apart from one line that may finish at ground temperature (see an example in Fig. 2.15)

The number of the lines that pass through a node is determined by the number of the faces of its control volume normal to which heat fluxes are considered to exist. If  $K$  is the number of these faces then the number of lines  $\ell^*$  is:

$$\ell^* = K/2 \quad \text{if } K \text{ is even integer} \quad (2.16)$$

$$\ell^* = (K+1)/2 \quad \text{if } K \text{ is odd integer} \quad (2.17)$$

For example in the case of a wall for which 1-dimensional heat transfer normal to it is considered there is only one line normal to the wall passing through all the nodes. Even in some 2-dimensional or 3-dimensional heat transfer cases the number of the lines can be kept small if we express the heat transfer as 1-dimensional but account for the edge effects. This is a common practice in heat transfer analysis in buildings.

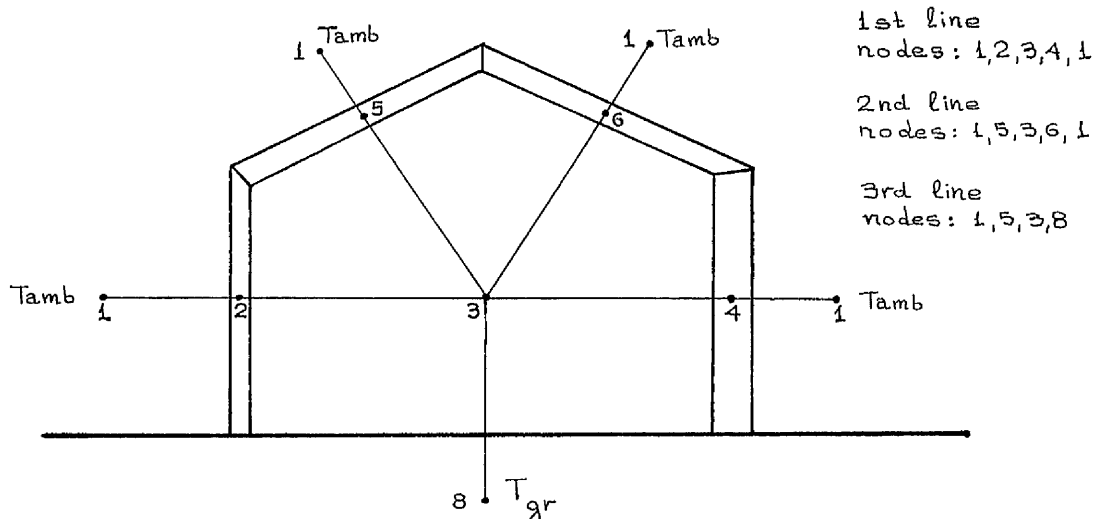


Fig. 2.15

The objective of the construction of these lines of nodes is not only to treat easily complicated shapes of passive systems in 3-dimensions but also to make use of the line-by-line iterative solution of the discretized energy equations. This is achieved by considering only the discretized energy equations of the control volumes the nodes of which belong to one line. We assume that the values of temperature for the nodes of this particular line are unknowns. All the heat fluxes along the other lines and the mass fluxes are considered known. We simply use the best estimates. Then it is easy to see that we can solve only for the unknown temperatures of the particular line. The best way is to use the tri-diagonal algorithm (see Appendix 0). In this manner we traverse along all lines, then using the resulting solution as our best estimate repeat the process until convergence.

Problems in using this line-by-line procedure that might arise because of discontinuity between convection and conduction regions are overcome easily by the introduction of a new formulation of the heat fluxes at the interface of the conduction and convection regions (section 3.1.4).

After the construction of the lines of the nodes, the three main steps which should be followed are:

- I. The integration of the energy equation.
- II. The construction of the complete difference equation.
- III. The solution of the system of difference equations.

I. The first step concerns the integration of the energy equation, appropriate to the particular control volume, over the control volume and the time interval  $\Delta t$ . From known values of temperature  $T^0$  at time  $t$ , the values  $T$  at the next instant  $t+\Delta t$  will be calculated. The superscript 0 is used to denote the values at time  $t$ , while its absence implies values at  $t+\Delta t$ . The general form of the energy equation is

$$\frac{\partial(\rho c_v T)}{\partial t} + \text{div}(\vec{G} c_p T) = \text{div}(\lambda \text{grad} T) + S \quad (\text{in W/m}^3) \quad (2.18)$$

unsteady term + convection term = diffusion term + source term

where,  $T$  is the temperature of the node of the control volume.

$\rho$  is the density of the material of the control volume.

$c_v, c_p$  are the constant volume and constant pressure specific heat of the material of the control volume.

$\vec{G}$  is the mass flux vector.

$$\vec{G} = \rho * \vec{V} \quad (2.19)$$

$\vec{V} = u \vec{i} + v \vec{j} + w \vec{k}$ , is the velocity vector.  $\vec{i}$ ,  $\vec{j}$ ,  $\vec{k}$ , are the unit vectors along the three axes of a cartesian co-ordinate system. For pure conduction, the convection term is not included in equation (2.18).

$\lambda$  is the thermal conductivity of the material of the control volume.

$S$  is the source term, for example absorbed solar power per unit volume by the control volume, power per unit volume produced inside the control volume by an auxiliary heater, and so on.

The equation (2.18) does not include terms arising from mass-concentration gradients, for example due to the condensation on or evaporation from the (internal) surfaces of a control volume filled with moist air.

The assumptions and the methodology on which the integration of the various terms of the energy equation is based are discussed in section 3.1.3. Fig. 2.16 shows a typical control volume  $P$ . The subscript  $p$  is used to denote the values of the variables at node  $P$ . Similarly, the subscript  $x+$  denotes these values at a part of the external surface of the control volume, i.e. this part is area  $A_x$ , normal to the  $x$  direction.

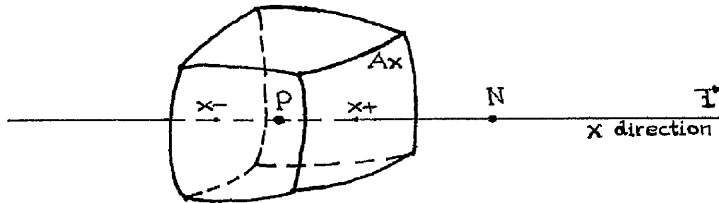


Fig. 2.16

The finite representation of the terms of the energy equation for the control volume  $P$  are:

1. The unsteady term:

$$(\rho_p * c_{v,p} * T_p - \rho_p^o * c_{v,p}^o * T_p^o) * \Delta V / \Delta t \quad (2.20)$$

where  $\Delta V$  is the volume of the control volume

$\Delta t$  is the time interval.

2. The source term:

Throughout this thesis, the absorbed radiation  $\epsilon'$ , as a fraction of the total incident radiation  $I_{tot}$  (in watts), is given for all the control volumes of various multi-layer systems. Thus, the finite representation  $S_p$  of the source term  $S$  is:

$$S_p = \epsilon'_p * (I_{tot} + I_{tot}^o) / 2 \quad (2.21)$$



For other source terms their finite difference representation  $S_p$  is calculated in a straightforward manner when the actual expression of the source term  $S$  is known.

3. The convection term at the part of surface  $x+$  :

$$G_{p,x+} = (G_x)_{x+} * c_{p,x+} * T_{x+} * A_x \quad (2.22)$$

"the convection flux"

where  $(G_x)_{x+}$  is the mass flux component normal to the part of surface  $x+$ .

$$(G_x)_{x+} = \vec{G} \cdot \vec{i} \quad (2.23)$$

where  $\vec{i}$  is the unit vector along the  $x$  direction.

4. The diffusion term at the part of surface  $x+$  :

$$Q_{p,x+} = \lambda_{x+} * (T_{x+} - T_p) * A_x / \Delta L_{x+} \quad (2.24)$$

"the diffusion flux"

where  $\Delta L_{x+}$  is the distance along the  $x$  direction between the node  $P$  and surface  $x+$

The final finite representation of the convection and diffusion flux depends on the expression of the temperature  $T_{x+}$  at the surface  $x+$ . This expression is discussed later in this section.

The present analytical modelling of a passive solar system does not employ a sophisticated approach to calculate the mass flux components  $(G_x)_{x+}$  and the internal and external convective heat transfer by, for example, incorporating the Navier-Stokes equations. This would increase enormously the computing time. Instead semi-empirical relations are used to calculate the mass-flux component  $(G_x)_{x+}$  and the heat transfer coefficients  $h_{x+}$  at internal, external surfaces, air cavities, transwall modules, etc.

The mass-flux component at the surface  $x+$  of the control volume,  $(G_x)_{x+}$ , is mechanically or naturally induced. Extensive coverage is given for both infiltration and ventilation cases in ASHRAE-Handbook-1977-Fundamentals, chapter 21 (18) and in Cockroft's thesis (30). The calculation of the thermocirculation in a Trombe-wall passive solar system is given by Duffie et al. (15), from fitting experimental data.

By introducing the heat transfer coefficient  $h_{x+}$  concept the diffusion flux takes the form:

$$Q_{p,x+} = h_{x+} * A_x * (T_{x+} - T_p) \quad (2.25)$$

The calculation of the heat transfer coefficient  $h_{x+}$ :

1. Pure conduction:

$$h_{x+} = \lambda_{x+} / \Delta L_{x+} \quad (2.26)$$

## 2. Internal surfaces:

The following relations are based on results by Min et al. (46):

### 2a. Heat flow at a vertical surface,

$$h_{x+} = 1.87 * (T_{x+} - T_p)^{0.32 * \ell - 0.05} \quad (2.27) \text{ (in W/m}^2 * K)$$

where  $\ell$  is the height in m of the surface

### 2b. Downward heat flow at a ceiling or floor,

$$h_{x+} = 0.203 * (T_{x+} - T_p)^{0.25 * \ell - 0.24} \quad (2.28) \text{ (in W/m}^2 * K)$$

where  $\ell$  is the hydraulic diameter in m

$$\ell = 4 * A / P \quad (2.29)$$

where A is the area of the surface, in  $m^2$

P is the surface perimeter in m

### 2c. Upward heat flow at a floor or ceiling

$$h_{x+} = 2.42 * (T_{x+} - T_p)^{0.31 * \ell - 0.008} \quad (2.30) \text{ (in W/m}^2 * K)$$

where  $\ell$  is again the hydraulic diameter in m.

This simplified approach in calculating the heat transfer at internal surfaces does not take into account the vertical temperature stratification that usually exists inside heated rooms. A non-stratification assumption not only changes the relative magnitude of the heat fluxes, but it also changes mass fluxes, e.g. due to thermocirculation in a Trombe-wall system. A specific temperature difference  $\Delta T$ , because of stratification, can be determined for each space, filled with air, at the beginning of the computing program in the input data. Then the quantity  $\Delta T/2$  is added to the temperature of the node of the air filled space and this new temperature, instead of the node temperature, is used in the calculation of the heat flux at the ceiling. Similarly, the same quantity  $\Delta T/2$  is subtracted from the temperature of the node of the air filled space and this new temperature is used in the calculation of the heat flux at the floor, or the air thermocirculation at a Trombe-wall system.

## 3. External surfaces:

The discussion presented in (12), (14), (15), (30) shows that the calculation of wind-induced heat transfer coefficients of external surfaces is not well established. Effects of wind direction, surface roughness, turbulence, transition from laminar to turbulent flow have yet to be studied. However, this is also related to the calculation of the external air pressure distribution on the building surfaces, an important factor for the air flow calculations-prediction of the air-mass fluxes  $(Gx)_{x+}$  (30).

Finally, the following procedure for the heat transfer coefficient at external surfaces is suggested:

$$h_{x+} = \text{maximum of } (h_1, h_2) \quad (2.31) \text{ (in W/m}^2 * K)$$

$$\text{where } h_1 = 1.42 * (T_{x+} - T_p)^{0.25} * \sin(\theta)^{0.25} * l^{-0.25} \quad (2.32) \text{ (in W/m}^2\text{*K)}$$

if  $10^4 < Gr < 10^9$  (laminar flow)

$$\text{or } h_1 = 0.95 * (T_{x+} - T_p)^{0.33} * \sin(\theta)^{0.33} \quad (2.33) \text{ (in W/m}^2\text{*K)}$$

if  $10^9 < Gr$  (turbulent flow)

where  $T_p$  is the ambient temperature in  $^{\circ}\text{C}$

$\theta$  is the angle of surface from the horizontal, in degrees (=tilt).

$l$  is the length of the surface in m.

The Grashof number  $Gr$  is:

$$Gr = (\beta_t * g * \sin(\theta) * l^3 * (T_{x+} - T_p)) / \nu^2 \quad (2.34)$$

$$\text{where } \beta_t = 2 / (T_{x+} + T_p) \quad (2.35)$$

assuming the air as an ideal gas. The temperature in relation (2.35) should be in kelvins.

$$h_2 = 8.6 * V^{0.6} * l_b^{-0.4} \quad (2.36) \text{ (in W/m}^2\text{*K)}$$

where  $V$  is the wind velocity in m/s

$$\text{and } l_b = (HV)^{1/3} \quad (2.37) \text{ (in m)}$$

$HV$  is the house volume in  $\text{m}^3$

4. Air-gap:

4a. The heat temperature coefficient  $h_{x+}$  between the air and each of the two surfaces of an open air-gap is discussed in (14), (15) and (49).

4b. The relations of the coefficient between the two parallel surfaces of a closed air-gap are given in Appendix K.

5. At the interface between two water control volumes of a transwall module:

The coefficient is calculated indirectly from the effective conductivity  $\lambda_{ef}$  at the interface, the calculation of which is presented in section 3.2 for various transwall modules and typical irradiance conditions.

III. The second step concerns the construction of the complete difference equation of each control volume.

The expressions of the convection and diffusion fluxes (2.22) and (2.25) are not the final finite difference representations used for the construction of the complete difference equation of the control volume  $P$ . Only the difference in the temperature of the nodes of the control volume  $P$  and its adjacent volumes should appear explicitly in the final representation. This is achieved by the appropriate expression of the temperature of the external surface of the control volume, for example the temperature  $T_{x+}$  at the surface  $x+$

of Fig. 2.16. An unsuccessful expression of  $T_{x+}$  may produce instability problems because of physical unrealism.

When there is convection normal to the external surface and no production or storage of energy at it the final expression of the convection and diffusion fluxes without the explicit appearance of the value of  $T_{x+}$  are obtained by employing the hybrid scheme (see also section 3.1.3).

When there is no convection normal to the external surface the final expression of the diffusion flux is obtained by accounting for the energy balance at the surface (section 3.1.4). According to this method the expression of the diffusion flux  $Q_{p,x+}$  depends on the quantity  $q_i$  (defined by the relation 3.22 of section 3.1.4). Because it has been assumed at the beginning of the present section that no condensation or evaporation happens at the (internal) surfaces of the control volumes filled with moist air, the quantity  $q_i$  represents the absorbed radiation flux minus the emitted flux from the particular interface (in  $W/m^2$ ). For external surfaces of a passive solar system the irradiance part of the quantity  $q_i$  is calculated in section 2.1. For internal surfaces the solar part of the quantity  $q_i$  ( $0.3\mu m < \lambda < 4.1\mu m$ ) is calculated from the method of section 2.2. The longwave part ( $\lambda > 4.1\mu m$ ) is calculated from the net radiation method presented by Eckert et al. in (42), assuming that the whole enclosure is made of grey, diffusely reflecting (internal) surfaces. The computing program ZEYS.NET has been developed for this purpose. For each surface, its emissivity, its temperature and its view factor from the surface to another surface of the enclosure should be known. Apart from the view factor of a pair of parallel or perpendicular surfaces that can be calculated from less cumbersome relations, every view factor of two polygons sited on two different planes can be approximately calculated by the method presented in Appendix G.

When the finite-difference representation of all the terms of the energy differential equation (2.18) has been worked out, the general difference equation can be obtained in the following form:

$$A_p * T_p = \sum_{n=1}^{N_p} (A_{pn} * T_{pn}) + B \quad (2.39)$$

where,  $A_p$ ,  $A_{pn}$  and  $B$  are coefficients.  $T_p$  denotes the temperature of the node of the control volume  $P$  and  $T_{pn}$  the temperature of the node of its  $n^{th}$  adjacent control volume with unknown temperature. There are  $N_p$  control volumes adjacent to control volume  $P$  with unknown temperature.

The values of  $T_p$  and  $T_{bn}$  correspond to time  $t+\Delta t$ . The terms  $A_p^0 * T_p^0$  at time  $t$  and terms  $A_{bn} * T_{bn}$  at time  $t+\Delta t$  with known temperature  $T_{bn}$  have been absorbed in  $B$ . The known temperatures  $T_{bn}$  are generally the ambient or ground temperature.

III. The third step concerns the solution of the system of the  $M$  difference equations of the  $M$  different control volumes of the whole passive system.

Equation (2.39) gives the general form of these equations, with coefficient  $A_p$  and  $A_{bn}, n=1, \dots, N_p$  generally dependent on the temperatures  $T_p$  and  $T_{bn}, n=1, \dots, N_p$ . This non-linearity is handled by an iteration procedure in which the coefficients are recalculated in every iteration cycle. This is actually the line-by-line procedure, outlined in section 3.1.5. All the grid lines start and finish at ambient temperature apart from one line that may finish at ground temperature (See Fig. 2.15). This is significant because any information along the line, for example information concerning the boundaries and such quantities as  $q_i$ , is transmitted at once to the whole domain and the convergence of the procedure seems to be faster.

The calculation of the coefficients  $A_p$  and  $A_{bn}$  generally requires the solution of other auxiliary equations or systems of equations. For example, these auxiliary equations may be referred to the thermal properties of the material of the control volumes or to the energy balance at the control volumes interfaces  $x+$  (section 3.1.4). A typical auxiliary system of equations is the one calculating the mass-flux component at the surface of a control volume,  $(G_x)_{x+}$ .

The solution of the system of equations (2.39), accompanied with the auxiliary set of equations, provides the values of the temperature at every node and at every interface of the control volumes and the values of the heat fluxes at every interface at the time  $t+\Delta t$ . If mass flux exists the values of pressure  $P_{p,water}$  vapour and dry air mass concentrations  $m_{w,p}$ ,  $m_{a,p}$ , mixture density  $\rho_p$  and mass fluxes  $(G_x)_{x+}$  at the interfaces of the control volumes are also provided for the time  $t+\Delta t$ . The solution procedure proceeds by the cyclic repetition of the following steps:

- (i) Provide initial estimates of the values of temperature of the nodes of the  $M$  control volumes and of the values of

- temperature  $T_i$  of those interfaces with values of the quantities  $h_{Ai}$ ,  $h_{Bi}$  and  $q_i$  (of relations (3.29), (3.30), (3.22) of section 3.1.4) dependent on the temperature of the interface  $T_i$ .
- (ii) Calculate the values of all the quantities  $h_{Ai}$ ,  $h_{Bi}$ ,  $q_i$  and  $S_p$ .
  - (iii) If there is no mass-flux normal to the interface of any of the control volumes calculate the values of density  $\rho_p$  and constant volume specific heat capacity  $c_{v,p}$  at the node of every control volume. Auxiliary equations may be needed. If mass-flux normal to the interface of a control volume exists follow the procedure outlined in Appendix J from steps (1) to (9) and calculate the values of pressure  $P_p$ , water vapour and dry air mass concentrations  $m_{w,p}$ ,  $m_{a,p}$  the mixture density  $\rho_p$ , the mixture heat capacity  $c_{v,p}$ , the mass flux  $(Gx)_{x+}$  and the heat capacity  $c_{px+}$  at the interface of this control volume.
  - (iv) Solve the M difference equations of the form of relation (2.39) and calculate the values of temperature of the nodes of the M control volumes.
  - (v) Calculate the values of temperature  $T_i$  of those interfaces with values of the quantities  $h_{Ai}$ ,  $h_{Bi}$  and  $q_i$  dependent on the temperature  $T_i$ . This is described in section 3.1.4.
  - (vi) Regard the new values of temperature of nodes and interfaces as improved estimates and return to step (ii) unless the degree of convergence is satisfactory. In such a case go to (vii).
  - (vii) Calculate the heat fluxes  $\vec{Q}\vec{A}$  and  $\vec{Q}\vec{B}$  from relations (3.29), (3.30) of section 3.1.4 and the remaining temperatures of the interfaces  $T_i$  (if this is required) from the relation (3.29) of the same section. Calculate the absorbed energy by each control volume from a relation such as the relation (2.21), during the time interval  $\Delta t$  (if this is required). Calculate the radiant exchange of an object inside a control volume filled with air, with the internal surfaces of the control volume. The radiant exchange should include the solar energy effect as well (if any). (section 2.2). This radiant exchange can be expressed in the form of a specific index, as mean radiant temperature or globe

temperature (if this is required)

- (viii) For all or some of the air filled control volumes, compare the dry bulb temperature  $T_p$ , the water vapour mass concentration  $m_{w,p}$  and the radiant exchange or an appropriate combination of these three quantities with corresponding minima and maxima. The minima and maxima are determined for a specific purpose, e.g. comfort conditions (chapters 8,9 and 10 of the ASHRAE Handbook of Fundamentals (28)). The present analysis does not calculate the air-movement inside a control volume, sometimes an important factor in choosing the appropriate combination of the three quantities and their maxima and minima. An indirect way, through the mass-fluxes at the interfaces  $(Gx)_{x+}$ , has to be developed if the complicated and computer time-consuming solution of, for example, the Navier-Stokes equations had to be avoided. The procedure developed by Wray (50) for assessing thermal comfort in passive solar heated buildings should be mentioned here, being better than those suggested by Cockroft (30), Ohanessian (51) and Fuchs (1). In this procedure the thermal comfort is determined as function not only of dry bulb and mean radiant temperatures but also of activity level, clothing insulation, relative humidity, ratio of surface area of clothed body to surface area of nude body and convective heat transfer coefficient from clothing surface to air (and thus of air-movement).

The abovementioned comparisons are important because they will determine the change or the inclusion/exclusion of some terms in the finite difference equations (2.39) and (J3) and (J5) of Appendix J, for the next time interval  $\Delta t$ .

For example, the switching on of a heater inside a control volume will add another source term apart from  $S_p$  of equation (2.21). The activation of a heating or cooling mechanical ventilating system will produce new mass-flux components  $(Gx)_{x+}$  at a certain surface  $x+$ . Different mass-flux components will be produced naturally by opening a window (ventilation rather than infiltration). In this case the conduction terms, referred to the particular interface  $x+$ , should be excluded. The switching on or off of a humidifier or dehumidifier will change the right part of

equation (J5) of Appendix J.

The last part of (vii)<sup>th</sup> step (calculation of the radiant exchange of an object inside a control volume filled with air) and (viii)<sup>th</sup> step can be performed not at the end of every time interval  $\Delta t$ , but at the end of a multi- $\Delta t$  time interval, if the response to certain values of temperature  $T_p$ , mass concentration of water vapour,  $m_{w,p}$  and radiation exchange is not automated.

All finite difference equations have been constructed in such a way (fully-implicit formulation, hybrid schemes) that the stability criterion is never violated. The stability criterion, for example in the case of equation (2.39), required the coefficients  $A_p$  and  $A_{bn}$ ,  $n = 1, \dots, N_p$  to be always positive. However, divergence of the solution procedure (i) to (vi) can result from the changes in the coefficients in the difference equations from one iteration cycle to the next. Therefore, it is sometimes necessary to employ some form of under-relaxation in order to prevent any divergence, especially when the time interval  $\Delta t$  is rather large. Using moderate time steps is a simple way of achieving under-relaxation.



## 2.5 THERMAL MODELLING OF PASSIVE SOLAR SYSTEMS USING A SMALL TEST-BOX

### Description of the passive solar systems test box

The test box is shown in photographs 1 and 2 and Fig. 2.17. The one side of the test box is a full size transwall module of 1.132m x 0.162m x 0.635m external dimensions (A in Fig. 2.17) with one 4mm annealed glass plate in front of it (B in Fig. 2.17).

The module is a simple rectangular container, made of 6mm annealed glass. Its section and part of the plan section with the cover removed is shown in Fig. 2.18. Polystyrene sheets (C in Fig. 2.18) protect the module base taking some of the weight. The aluminium-alloy lid of the module (A in Fig. 2.18) with two screw-clamps (B in Fig. 2.18) is necessary to prevent the top face plates from moving apart due to hydrostatic pressure.

A second module of 1.14m x 0.17m x 0.63m external dimensions has also been used in M.E.R.A., Glasgow University (Fig. 2.19). This is made of 10mm annealed glass in accordance with the well-established fish-tank construction technique. Provision has been made for the location of a removable central absorbing plate halfway between the two face plates. This absorbing plate, made of 4mm Antisun glass, grey, 41/60 (from Pilkington Ltd.) is supported by pairs of vertical strips cemented to each side of the module. The section of this module and a part of the plan section are shown in Fig. 2.19. Its lid (not shown in the figure) is made of perspex. The hydrostatic deflection of the face plates produces negligible visual distortion.

In both modules the lid reduces the water evaporation and contamination. Each module lid has a hole for insertion of a hose for filling. The modules can be emptied either by using a small pump or a simple siphon.

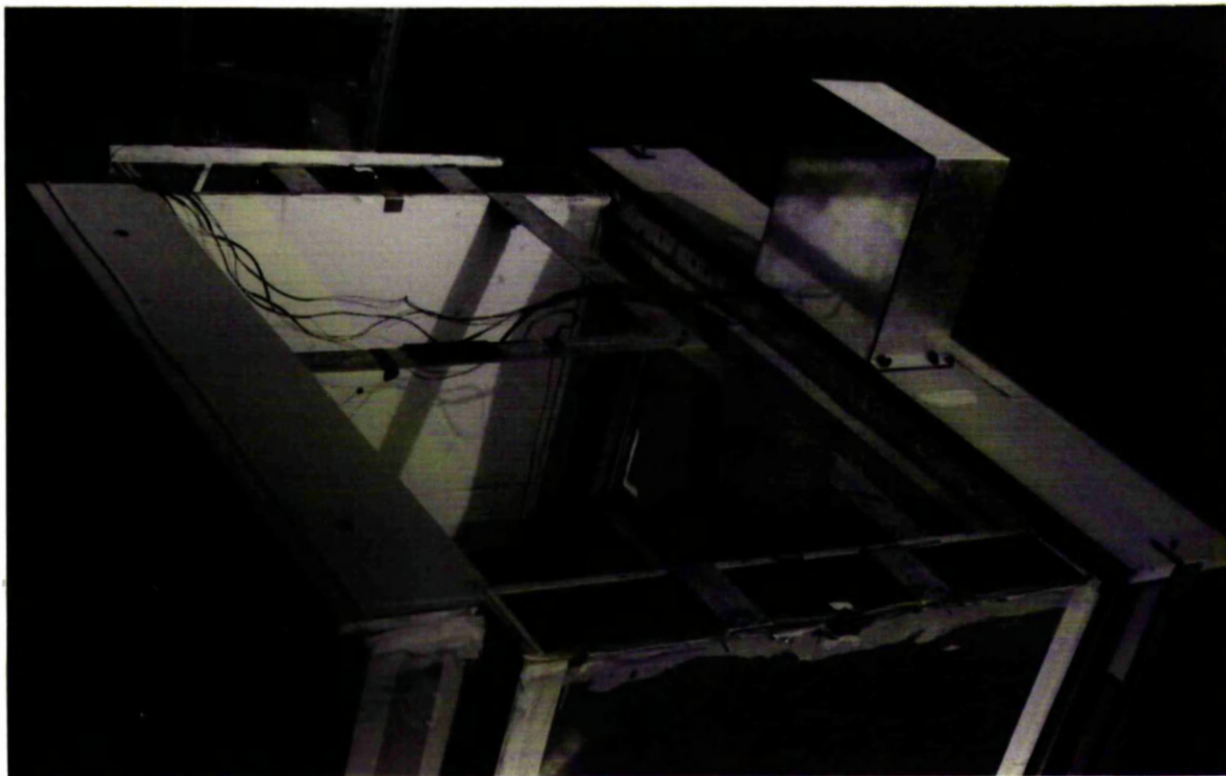
The solar absorptance of the first module was enhanced by diluting a small quantity of acid green B. Evaporation was prevented by using an oil film. Further details concerning the first module, the strength of its solution and the outside glass plate are given in sections 1.3 and 1.4.

The three other sides of the test box are made of three aluminium-alloy tanks (C, D and E in Fig. 2.17) filled with water and insulated, with a polystyrene sheet facing the interior of the test-box (K in Fig. 2.17). In Fig. 2.20 the dimensions of the cross sections of the three tanks are given.



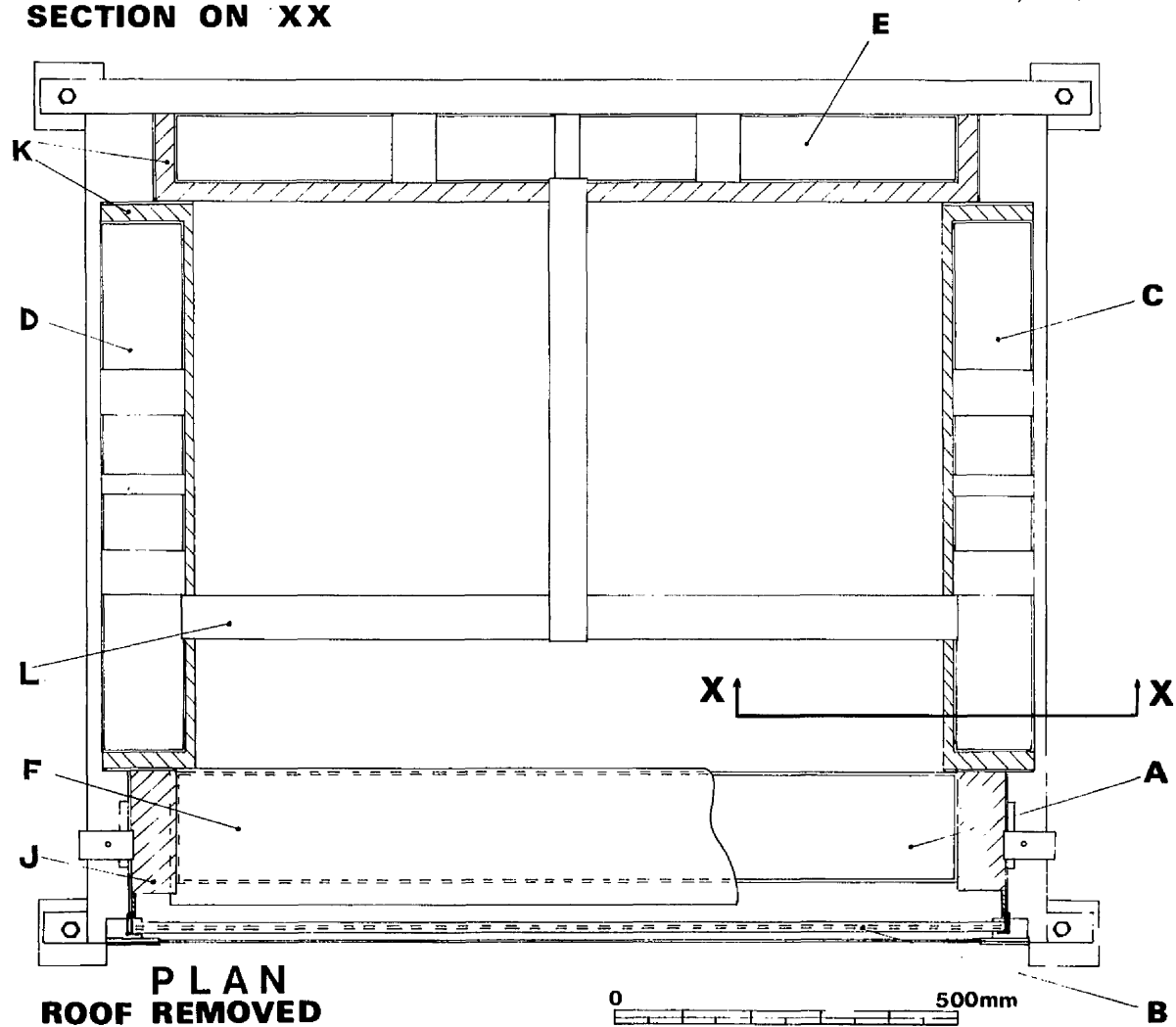
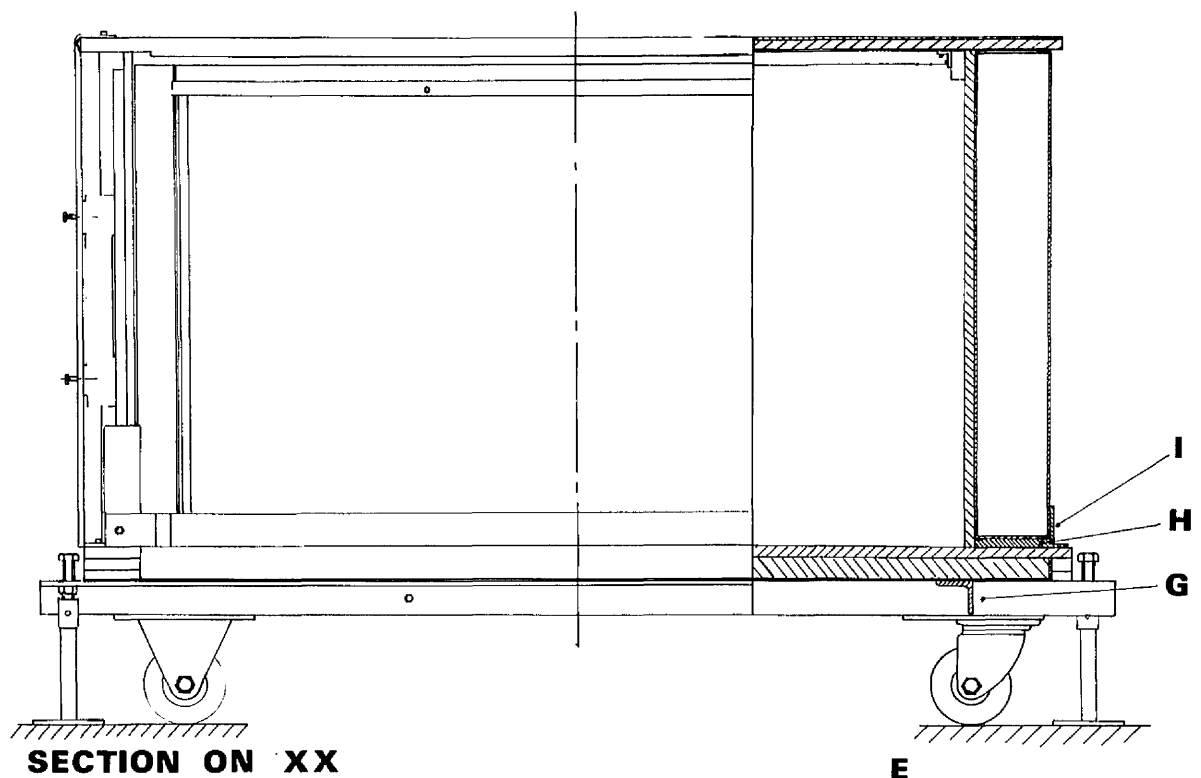
Ph. 1

Passive Solar Systems Test Box. Transwall case.



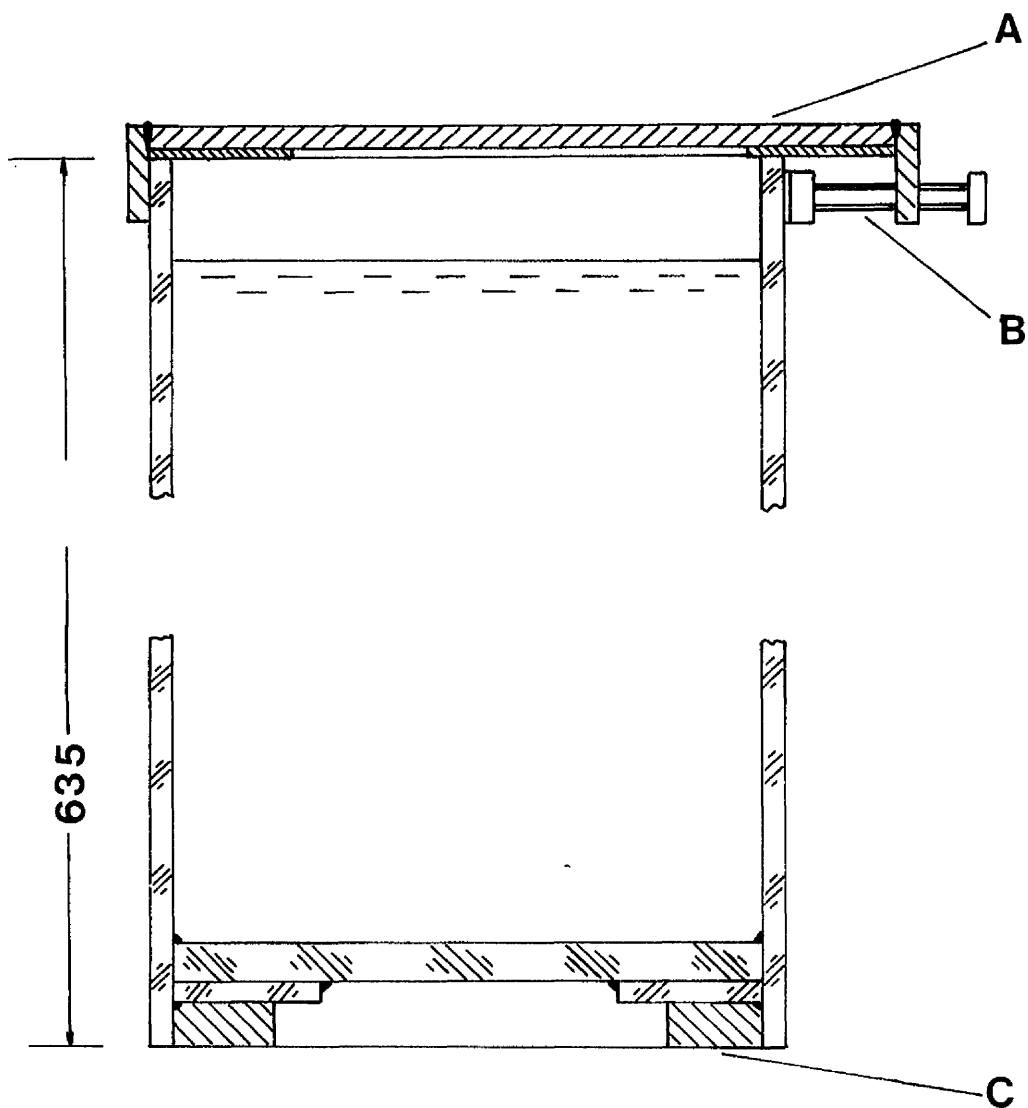
Ph. 2

Passive Solar Systems Test Box - Roof removed. Transwall case.

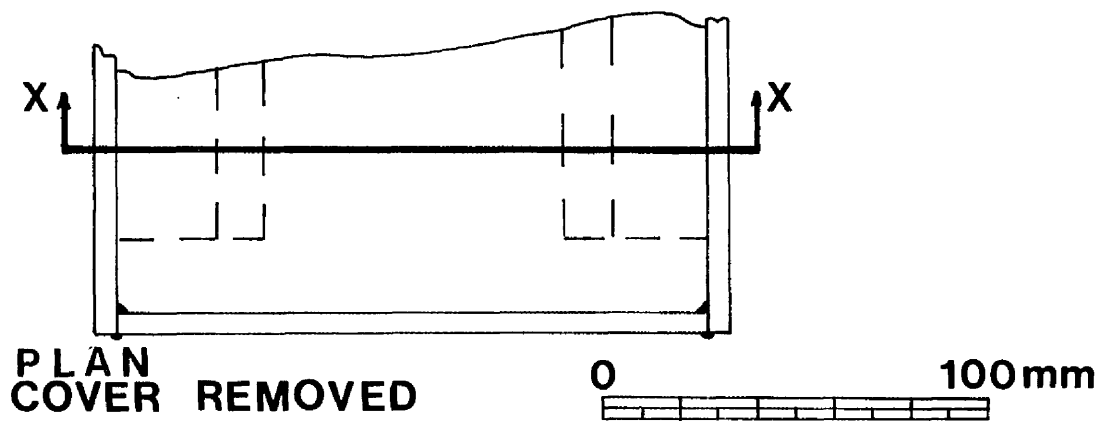


**Passive Solar Systems Test Box, Transwall Case.**

**Fig.2.17**



**SECTION ON XX**



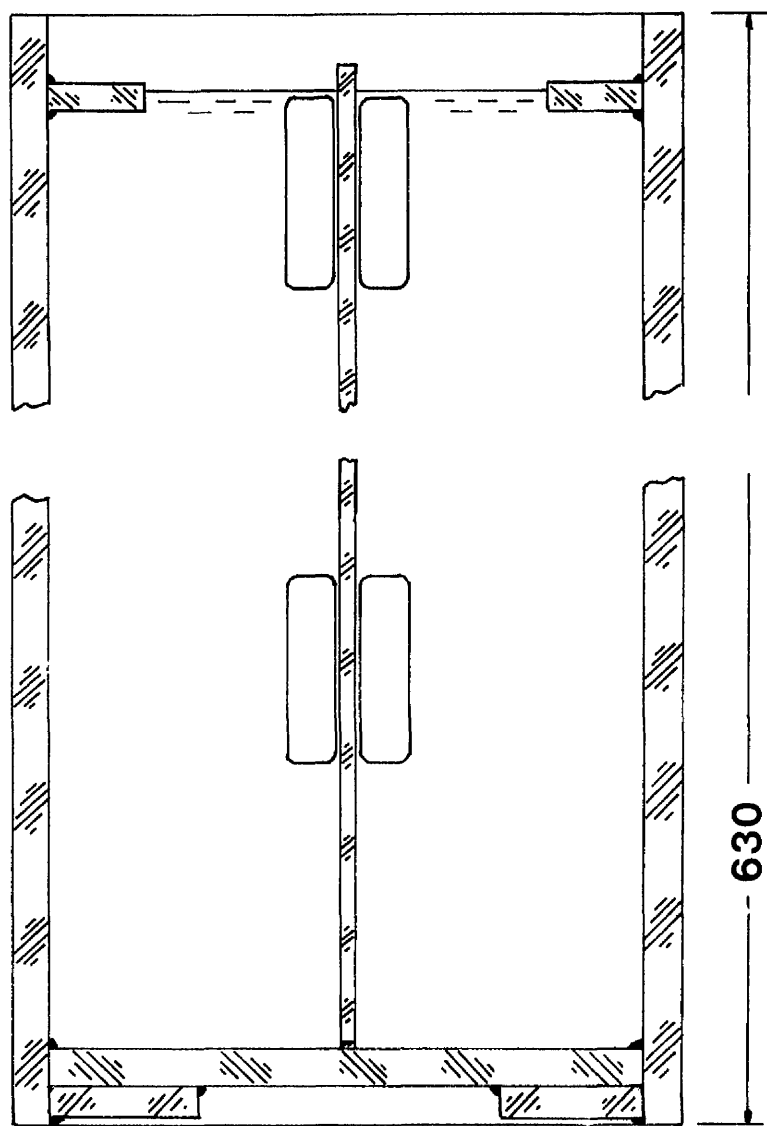
**PLAN  
COVER REMOVED**

0

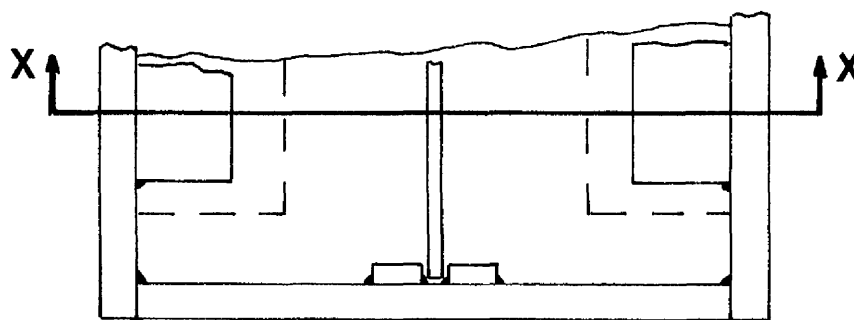
100mm

**Transwall, 6mm Glass.**

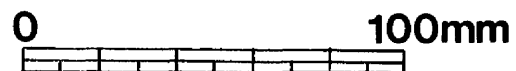
**Fig.2.18**



SECTION ON XX



PART PLAN



Transwall, 10mm Glass, with Central  
Absorbing Plate.

Fig.2.19

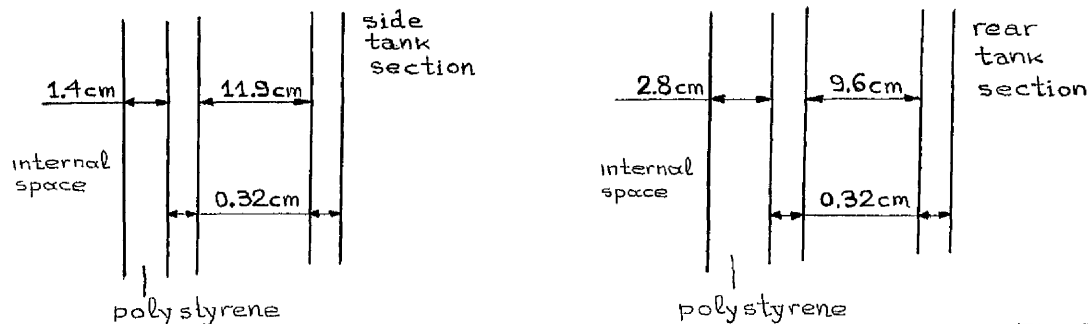


Fig. 2.20

The other internal dimensions of the rear tank are 1.13m (width) x 0.703m (height) and of the side tanks 0.794m (width) x 0.725m (height). The depth of the water inside the tanks is 0.675m and 0.695m, respectively. A layer of oil (1cm) was poured on top of the water to prevent evaporation.

The floor of the test box is based on a strong steel frame (G in Fig. 2.17) with four wheels of 12cm diameter at the four sides of the frame. The dimensions of the floor are 1.50m (width) x 1.20m (depth). Its cross section is shown in Fig. 2.21.

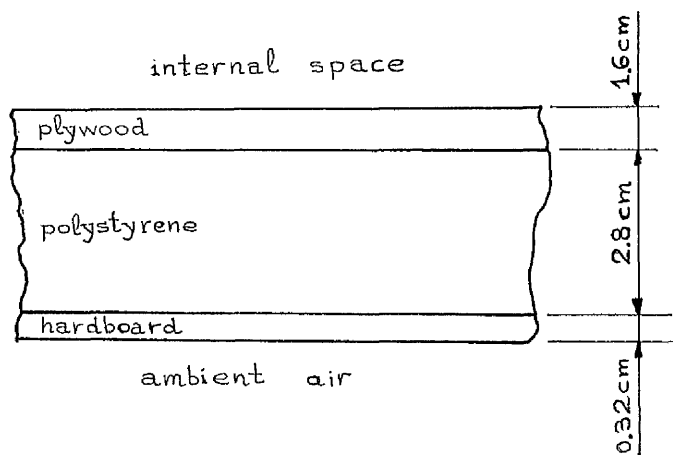


Fig. 2.21

The outside glass plate, transwall and water tanks sit on 20mm foam rubber sheets, thermal insulation grade (H in Fig. 2.17) to cushion the load and to act as an air seal. Any gaps in the box were sealed with tape including adhesive foam. The intention was to monitor air changes by supplying air to the box via the compressed air main, controller and rotameter. However time did not permit this variation and all were undertaken with a test box effectively sealed against ventilation.

The tanks and transwall module were located by angle clamps (I in Fig. 2.17) upper tie bar (Tee-frame, L in Fig. 2.17) and expanded polystyrene blocks (J in Fig. 2.17). Although the height

of the rear tank is less than the height of the two side-tanks, care has been taken so that the Tee-frame is horizontal. This is important because each of the two pieces forming the 'roof' are also supported by the Tee-frame. The height difference between the tanks is overcome by covering the rear tank by an extra polystyrene cover of about 2cm height. A height difference also exists between the transwall module and the outside glass plate. Wooden and insulating material (parts 10,11,15 for the transwall module and 12 for the outside glass plate in Fig. 1.17 of section 1.4) fills the remaining space. The purpose of this construction is to allow the study of various types of passive solar test boxes with different openings and air flow patterns.

The section of each of the two pieces of the 'roof' is shown in Fig.2.22.

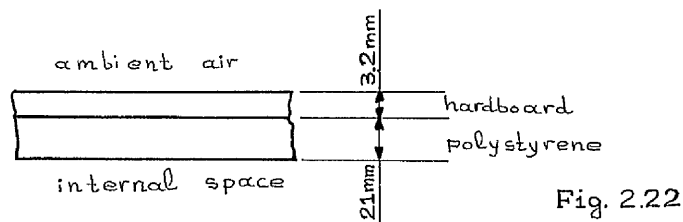


Fig. 2.22

Each edge of the roof is faced with rubber foam to eliminate any possible air passage (Fig.2.23). These interfaces are also sealed from

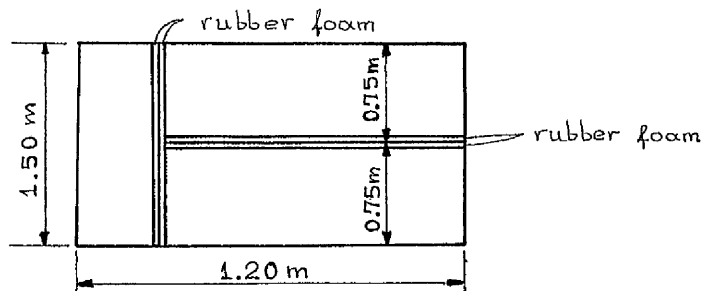


Fig. 2.23

outside using an adhesive tape. A sheet of polythene is stretched over the roof for rain protection.

The wooden parts of the test box have been painted with water-proof paint.

The final position of the various parts of the test-box is such that the heated space filled with air is a parallelepiped with the following dimensions: width, 1.09m; depth, 0.853m; height, 0.725m.

The real solar heated room which is modelled by the small test-box

The dimensions and the thermal properties of the walls of the corresponding solar heated room modelled by the small test-box can be calculated from the solution of the following set of equations (and vice-versa):

Real passive element  $\equiv$  passive element of the test box (2.40)

$$(U_i A_i + \dot{r}_i (\rho c_v)_{\text{air}} V_{\text{air}}) / A_g = (U' i A' i) / A' g \quad i = 1 \text{ to } N_w \quad (2.41)$$

$$i \neq g$$

$$(\rho c_v V)_i / A_g = (\rho' c' v V')_i / A' g \quad i = 1 \text{ to } N_w \quad (2.42)$$

$$i \neq g$$

where,

The superscript ' implies quantities of the small test-box. Its absence implies quantities of the full size room.

$i$  is the subscript that implies a certain wall, the roof or the floor.  $i=g$  for the passive system element.

$U$  is the conductance of the wall, the roof or the floor.

$\rho c_v V$  is the total product of density, specific heat capacity and volume of the wall, the roof or the floor.

$A$  is the area of the solar passive system element (for example of glazing), the wall, the roof or the floor.

$N_w$  is the number of all the walls, the roof and the floor.

$\dot{r}$  is the number of volumes of air per sec. changed because of infiltration in the full size solar heated room.

$(\rho c_v)_{\text{air}} V_{\text{air}}$  is the product of density and specific heat capacity and the volume of air of the full size solar heated room, respectively.

If the test box were not sealed then similar terms implying infiltration should appear at the right side of the equations (2.41).

The relation (2.40) does not imply simply "conservation" of conductance and capacitance of the passive element but the use exactly of the passive solar element of the real room in the small test-box as well.

The above theoretical approach is different from that suggested by Grimmer (52), where instead of solving the system of equations (2.40), (2.41) and (2.42) the system of the following equations has to be solved:

Real passive element  $\equiv$  passive element of the test box

$$\left( \sum_{i=1}^{N_w} (U_i A_i) + \sum_{i=1}^{N_w} (\dot{r}_i (\rho c_v)_{\text{air}} V_{\text{air}}) \right) / A_g = \left( \sum_{i=1}^{N_w} (U' i A' i) \right) / A' g \quad i \neq g$$

$$\left( \sum_{i=1}^{N_w} (\rho c_v V)_i \right) / A_g = \left( \sum_{i=1}^{N_w} (\rho' c' v V')_i \right) / A' g \quad i \neq g$$

These equations demonstrate the flexibility of the dimensions and thermal properties of the test box provided that care is taken



to "conserve", among others, effects of edges, microclimate, the order of positioning of the materials in the test-box walls according to their thermal conductivity and capacity and the distribution of solar radiation inside the test-box. The study of the effect of changing the depth of the parallelepiped on this distribution (section 2.3) shows, at least for those conditions of the examples, a flexibility in choosing the depth of the test-box without changing appreciably the distribution of solar radiation among the internal surfaces and the transwall element of the test-box.

According to this analysis the test-box could model a solar heated room with the following characteristics:

The south-facing transwall assembly consists of 16 modules of the type used in the test-box. The assembly covers an area of about  $11.7\text{m}^2$ .

The internal dimensions of the room are:

4.36 m width  
2.9 m height  
5.4 m depth

The side walls and the wall opposite to the transwall assembly are made of:

25mm wood (facing the heated space)  
15mm polystyrene  
236mm brick, and  
12mm asbestos board

Their U-value is about  $0.87 \text{ W/m}^2\text{K}$ . The U-values of the roof and floor are  $1.05 \text{ W/m}^2\text{K}$  and  $0.65 \text{ W/m}^2\text{K}$ , respectively. It was assumed an infiltration and ventilation rate of 2.0 interior-volume air-changes per hour.

2.6

APPLICATION OF THE ANALYTICAL MODELLING OF A PASSIVE  
SOLAR SYSTEM IN THE CASE OF THE SMALL TEST-BOX.

The existence of insulation at the four small faces of the transwall module and the three tanks can lead to the assumption of one-dimensional heat flow along their small dimension. Edge effects are neglected in relation to other quantities.

By adopting the same assumption for the "floor" and the "roof" the thermal model of the test-box is simplified in such a way that heat flow is considered only along the direction of three separate lines of nodes; normal to the transwall module, normal to the side tanks and normal to the "floor"- "ceiling", respectively. Each line starts and finishes at ambient temperature (see Fig. 2.24). Only the node of the control volume of the heated air space is common in these three lines. In Fig. 2.25 the three lines of nodes are shown with the material filling each control volume. The surfaces for which the temperature is calculated, are also shown with one asterisk (\*). The water in the transwall module and in each tank is separated into three control volumes. The common control volume (air space) is the seventh in the x direction, the seventh in the y direction and the third in the z direction. The volume of each control volume and its dimension along the direction of its line is given in Table 2.13.

Table 2.15 gives the area of interface of each control volume along the direction of its line. The interface  $i$  belongs to the control volume  $i-1$  and  $i$ . The longwave ( $\lambda > 4.1\mu\text{m}$ ) and shortwave ( $\lambda < 4.1\mu\text{m}$ ) estimated values of absorptance of some of these surfaces used in the mathematical model are also given in this table.

Table 2.14 gives the estimated thermal properties of the test-box materials and Table 2.16 the air properties inside the test-box.

The air gap between the outside glass plate and the transwall module had a width of 6.53cm. The height of the gap was 64.9cm.

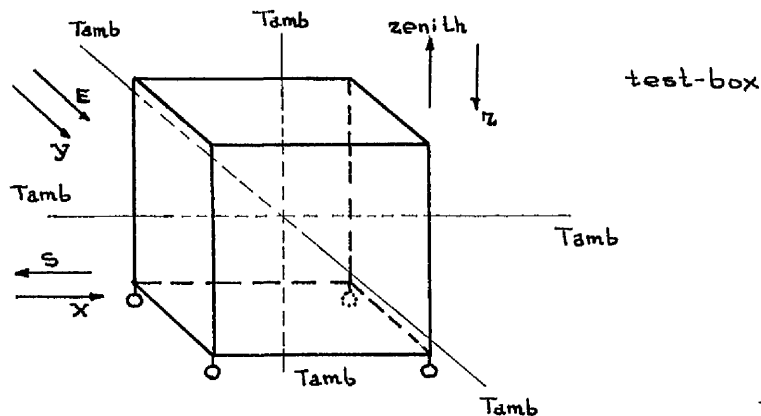
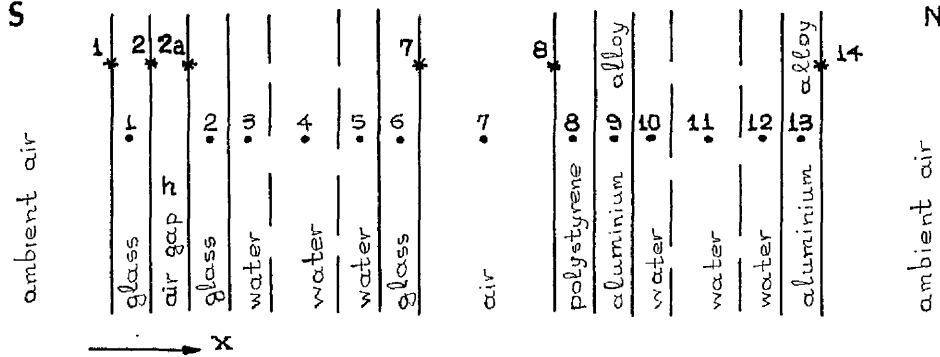


Fig. 2.24

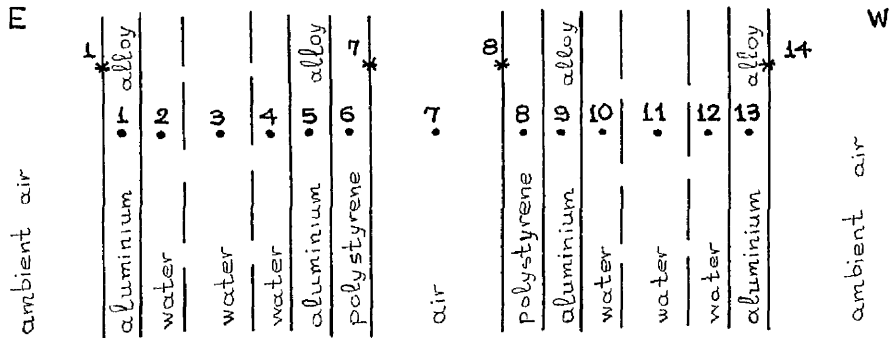


direction normal to the transwall module,  
4° from north-south axis, east of south.

N

ambient air

E

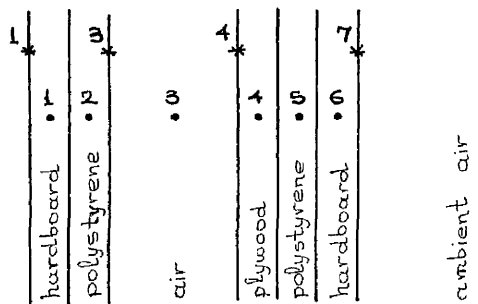


$\rightarrow y$   
direction normal to the side tanks.

W

ambient air

ambient air



$\xrightarrow{\quad} z$   
 direction normal to the 'roof' and 'floor';  
 opposite to the earth-zenith direction.

All the nodes (.) are in the middle of the control volumes in respect to the corresponding direction.

Fig. 2.25

Table 2.13

Dimensions and volumes of the control volumes of the test-box

Control volume	Along x direction		Along y direction		Along z direction	
	dimension m	volume m <sup>-3</sup>	dimension m	volume m <sup>-3</sup>	dimension m	volume m <sup>-3</sup>
1	0.004	0.0032	0.0032	0.0019	0.0032	0.0030
2	0.006	0.0037	0.012	0.0068	0.021	0.0195
3	0.012	0.0078	0.095	0.0539	0.725	0.6741
4	0.126	0.0814	0.012	0.0068	0.016	0.0149
5	0.012	0.0078	0.0032	0.0019	0.028	0.0260
6	0.006	0.0037	0.014	0.0083	0.0032	0.0030
7	0.853	0.6741	1.090	0.6741		
8	0.028	0.0195	0.014	0.0083		
9	0.0032	0.0024	0.0032	0.0019		
10	0.012	0.0084	0.012	0.0068		
11	0.072	0.0502	0.095	0.0539		
12	0.012	0.0084	0.012	0.0068		
13	0.0032	0.0024	0.0032	0.0019		

Table 2.14

Thermal properties of the materials used in the test-box

property →	thermal conductivity W/m *K	specific heat capacity J /Kg*K	density Kg/m <sup>3</sup>
material			
clear float glass	0.800	837.4	2723.1
water (still)	0.604	4179.0	997.4
plywood	0.100	1330.0	720.0
hardboard	0.110	1330.0	900.0
aluminium alloy	160.0	880.0	2707.0
polystyrene (rolled)	0.048	1330.0	20.0

Table 2.15

Area and optical properties of control volumes interfaces (Interface i belongs to the control volumes i - 1 and i)

Surface	Along x direction	Along y direction	Along z direction
	Area m <sup>2</sup>	Area m <sup>2</sup>	Area m <sup>2</sup>
1	0.8119	0.5672	0.9298
2	0.7291	0.5672	0.9298
2a	0.7291		
3	0.6462	0.5672	0.9298
4	0.6462	0.5672	0.9298
5	0.6462	0.5672	0.9298
6	0.6462	0.5672	0.9298
7	0.6976	0.5672	0.9298
8	0.6976	0.5672	
9	0.6976	0.5672	
10	0.6976	0.5672	
11	0.6976	0.5672	
12	0.6976	0.5672	
13	0.6976	0.5672	
14	0.6976	0.5672	

Surface	Absorptance		Absorptance		Absorptance	
	Longwave	Shortwave	Longwave	Shortwave	Longwave	Shortwave
1	0.80		0.24	0.14	0.15	0.65
3					0.95	0.05
4					0.95	0.25
7	0.80		0.95	0.05	0.15	0.82
8	0.95	0.05	0.95	0.05		
14	0.24	0.12	0.24	0.14		

Table 2.16

Properties of Air.

temperature K	Prandtl number	Viscosity, Kinematic m <sup>2</sup> /s	thermal conductivity W/m * K	specific heat capacity J /Kg*K	Density Kg/m <sup>3</sup>
250	0.722	9.49x10 <sup>-6</sup>	22.27x10 <sup>-3</sup>	1017.3	1.45
300	0.708	15.68x10 <sup>-6</sup>	26.24x10 <sup>-3</sup>	1017.7	1.21
350	0.697	20.76x10 <sup>-6</sup>	30.03x10 <sup>-3</sup>	1021.0	1.03

The measuring system provided values of the solar radiation, the wind speed over the test-box and the temperatures of the ambient air and various nodes and surfaces of the test-box. Some climatological values which provide second order effects e.g. dew point temperature of the ambient air, etc., were taken from climatological data (79). The computer program contains measured and estimated values of the climatological data averaged over a quarter of an hour. The time of the day quoted refers to the end of that fifteen minutes averaging period (Fig. 2.26).

The collection of data from the test-box lasted over ten days but time has not permitted more than a partial analysis of this data and so the verification of the analytical model of the test-box is being presented only for two days, from 9<sup>00</sup> solar time of the second of April to the 16<sup>00</sup> solar time of the third of April. The outside glass plate of the transwall system element was covered by a 50mm thick polystyrene sheet from 16<sup>00</sup> solar time of the second of April to 7<sup>55</sup> solar time of the third of April.

#### 2.6.1. The measured input data.

##### Solar radiation

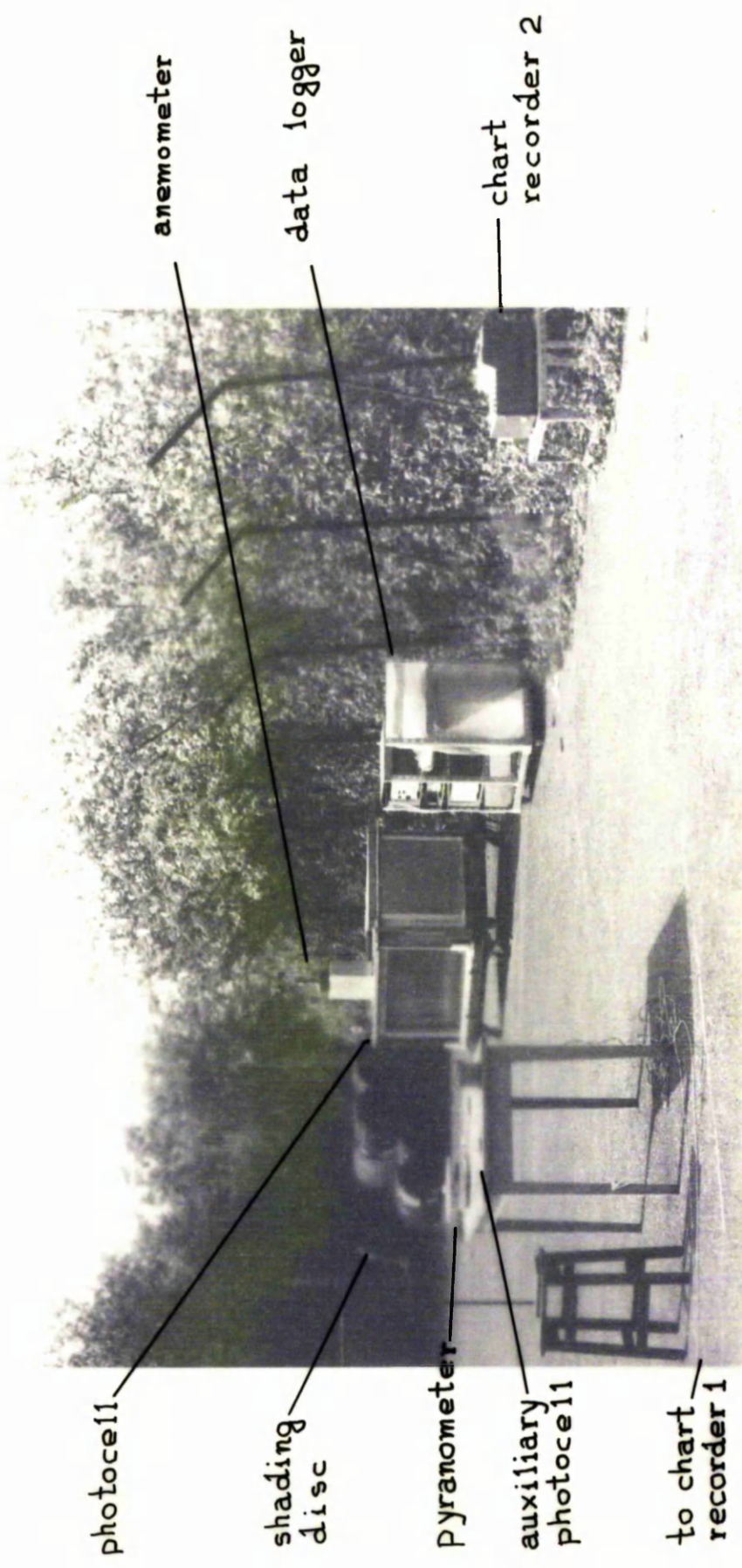
Global solar radiation on a horizontal plane was measured using a Kipp-Zonen type pyranometer, placed on a table near the solar test-box. Global solar radiation on a vertical plane parallel to that of the outside glass plate of the test-box was also measured using a silicon photo-cell. These are shown in photograph 3. Both instruments were connected to potentiometric chart recorders. The diffuse solar radiation falling on the horizontal surface was also recorded on the recorder chart every 10 minutes by shading the pyranometer with a small disc. The pyranometer was calibrated at Met. O. Bracknell. No accuracy is quoted but a figure of  $\pm 5.0\%$  is typical for its use in horizontal position. The photocell was calibrated against the pyranometer to a precision of  $\pm 3\%$  up to an incidence angle of 75<sup>0</sup> beyond which the cosine response becomes too uncertain.

From the measured global  $I_{h,tot}$  and diffuse  $DIF_h$  solar radiation on a horizontal surface, the absolute value of the vector of the direct solar radiation (intensity) is given by the following relation:

$$RAD = (I_{h,tot} - DIF_h) / \sin a$$

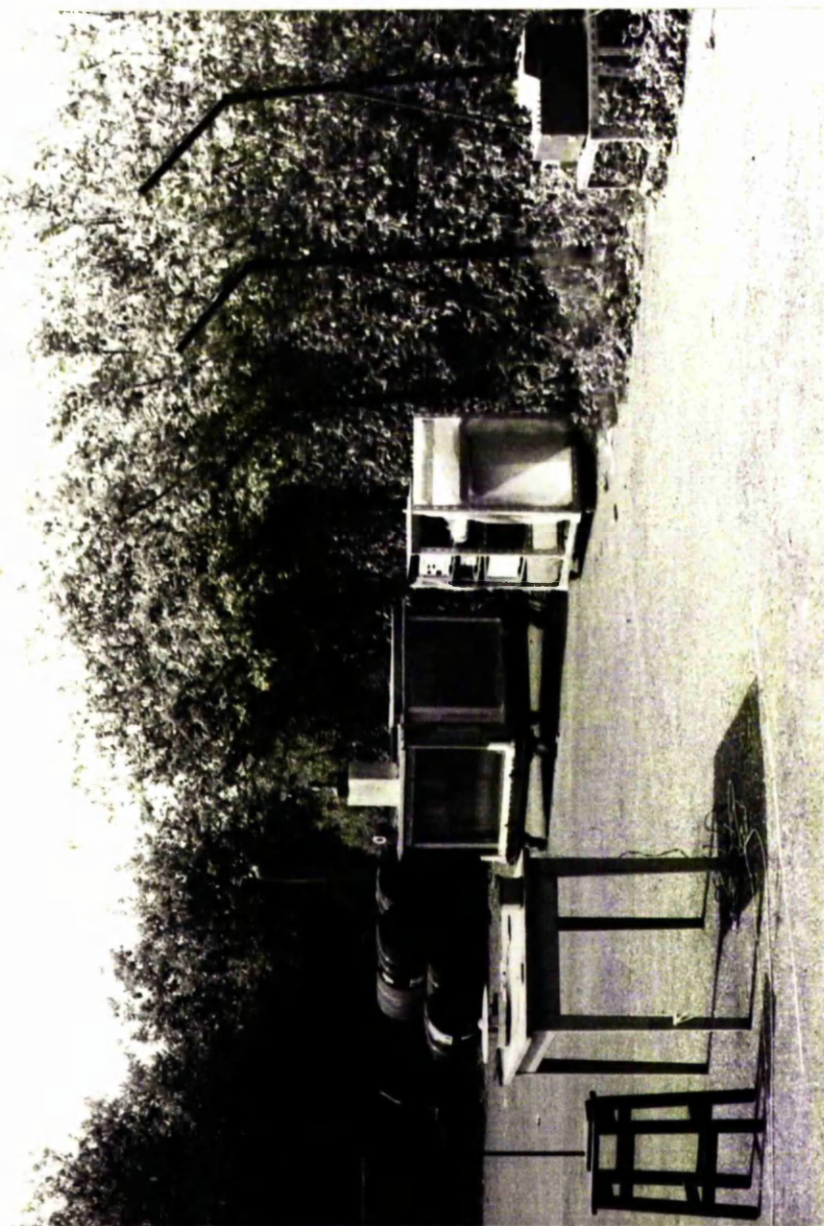
where the solar altitude angle  $a$  is given by the relation F2 of Appendix F.

Fig. 2.27 gives measured values of the intensity of the direct solar radiation



Ph. 3  
Test Box and measuring system.





Ph. 3  
Test Box and measuring system.



and the irradiance of the diffuse solar radiation on a horizontal surface averaged on the previous quarter of an hour for the second and third of April. The small capital letters represent estimated values.

From the values of both the direct solar radiation and the diffuse solar radiation on a horizontal surface, the radiation on every unobscured external plane surface can be calculated. This is presented in section 2.1. The comparison between calculated and measured values from the photo-cell in the vertical position is about 8%, a difference contributed by uncertainties related to the non-uniformity of sky diffuse radiation, adjacent buildings, reflectivity of ground, etc.

#### Wind speed.

Wind speed was measured using a sensitive cup anemometer, Casella, No. 616, calibrated at Glasgow University, Department of Aeronautics. The number of revolutions of the anemometer was recorded every 10 minutes. There was an uncertainty over the direction of the wind. In Fig. 2.28 the measured values of wind speed, averaged on the previous quarter of an hour, are given. Again, the small capital letters represent estimated values.

#### Temperatures of ambient air, various nodes and surfaces.

Chromel-Alumel thermocouples were used to measure the temperatures of ambient air, the temperatures of the nodes of the control volumes 3, 4, 5, 7, 11 in the x direction and 3, 11 in the y direction, and the temperatures of the surfaces 2, 3, 7, 8 in the x direction and 7, 8 in the y direction. The thermocouples were connected to a data logger, with built in cold junction compensation. Care was taken not to expose the ambient air and control volume 7 (in the x direction) thermocouples to direct solar radiation.

Complete scans of the thermocouple inputs were initiated every five minutes during the day and twenty minutes during the night. Each scan was completed within half a minute. The accuracy of the temperature measurements was variable owing to noise in the scanner unit, but generally correct to  $\pm 0.1^{\circ}\text{C}$ .

The values of ambient temperature, averaged over the previous quarter of an hour during the day or interpolated from the available data during the night are given in Fig. 2.28.

#### 2.6.2. The completion of the input data.

##### (a). Wind

The values of wind speed at the surface 1 and 14 along the x-direction for both days and at the surface 1 along the y-direction

for the second of April, 1982, were taken to be those of Tables 2.17 and 2.18. The value of wind speed at the surface 7 along the z-direction was 0.5 m/sec for every time.

The values of wind speed at the remaining external surfaces for the second of April were those at the surface 1 along the y-direction and at the remaining external surfaces for the third of April are those at the surface 1 along the x-direction.

Table 2.17

Wind speed (m/s) on the 2nd of April, 1982

Solar Time	surface 1 x direction	surface 14 x direction	surface 1 y direction
10	2.51	2.31	2.51
11	2.31	2.11	2.31
12	2.62	2.42	2.62
13	2.68	2.48	2.68
14	2.62	2.42	2.62
15	2.83	2.63	2.83
16	2.63	2.43	2.63
17	2.00	1.80	2.00
18	1.50	1.30	1.40
19	1.50	1.30	1.40
20	1.40	1.10	1.30
21	1.40	1.10	1.30
22	1.30	0.90	1.20
23	1.30	0.90	1.20
24	1.20	0.75	1.10

Table 2.18

Wind speed (m/s) on the 3rd April, 1982

Solar Time	surface 1 x direction	surface 14 x direction	Solar Time	surface 1 x direction	surface 14 x direction
1	1.10	0.50	2	1.10	0.50
3	1.10	0.50	4	1.10	0.50
5	1.10	0.50	6	1.10	0.50
7	1.10	0.50	8	1.10	0.50
9	1.55	1.35	10	1.92	1.72
11	1.65	1.45	12	2.16	1.96
13	2.16	1.96	14	2.34	2.14
15	2.23	2.03	16	2.07	1.87

(b) Dew point and ground surface temperature.

The dew point temperature of the ambient air and the ground surface temperature are given in Fig. 2.26 for both days.

(c) Heat transfer coefficients and effective conductivity of water.

For simplicity, the heat transfer coefficient  $h_{x+}$  at each external surface was calculated from the relation:

$$h_{x+} = 5.7 + 3.8 * V \quad (\text{in } W/m^2 * K)$$

where,  $V$  is the wind velocity in m/s.

For the covered transwall system the heat transfer coefficient between the outside glass plate surface (surface 1 along the  $x$  direction) and the ambient air was estimated to be  $1.4 W/m^2 * K$ .

Min's relation for the heat transfer coefficient for vertical surfaces (section 2.4) appears to be low compared to other values in the literature. Its value was increased by one third but is not critical to the analysis.

The effective conductivity at the interface of two water control volumes was taken to be  $5 W/m * K$  for the water tanks and the transwall module when the system was covered. During the rest of the time it was taken to be  $30 W/m * K$  for the transwall module. The enhanced value of the thermal conductivity of the water was chosen from the results of section 3.2, because of circulation effects.

To account for the sheet of polythene stretched over the "roof" the thermal conductivity of the polystyrene layer of the "roof" was reduced to 85% of its value (of Table 2.14).

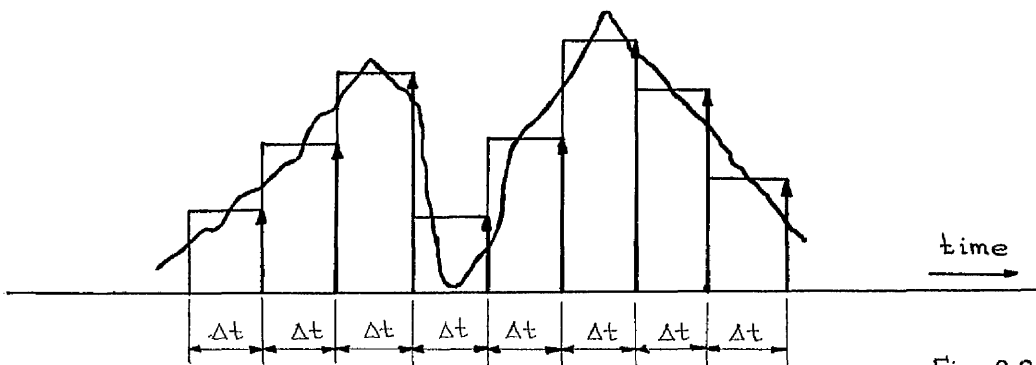


Fig. 2.26

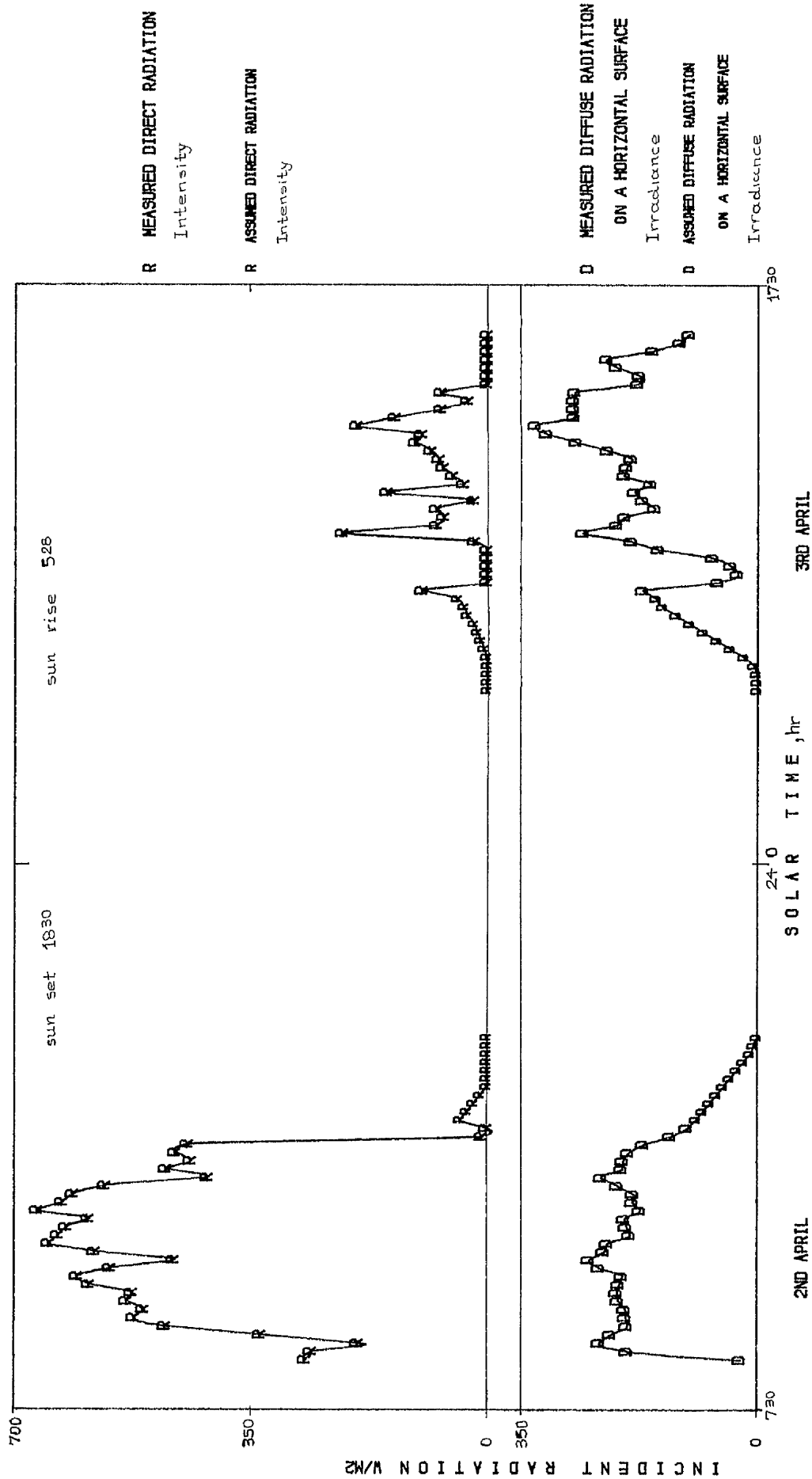


FIG.2.2.7  
SOLAR RADIATION

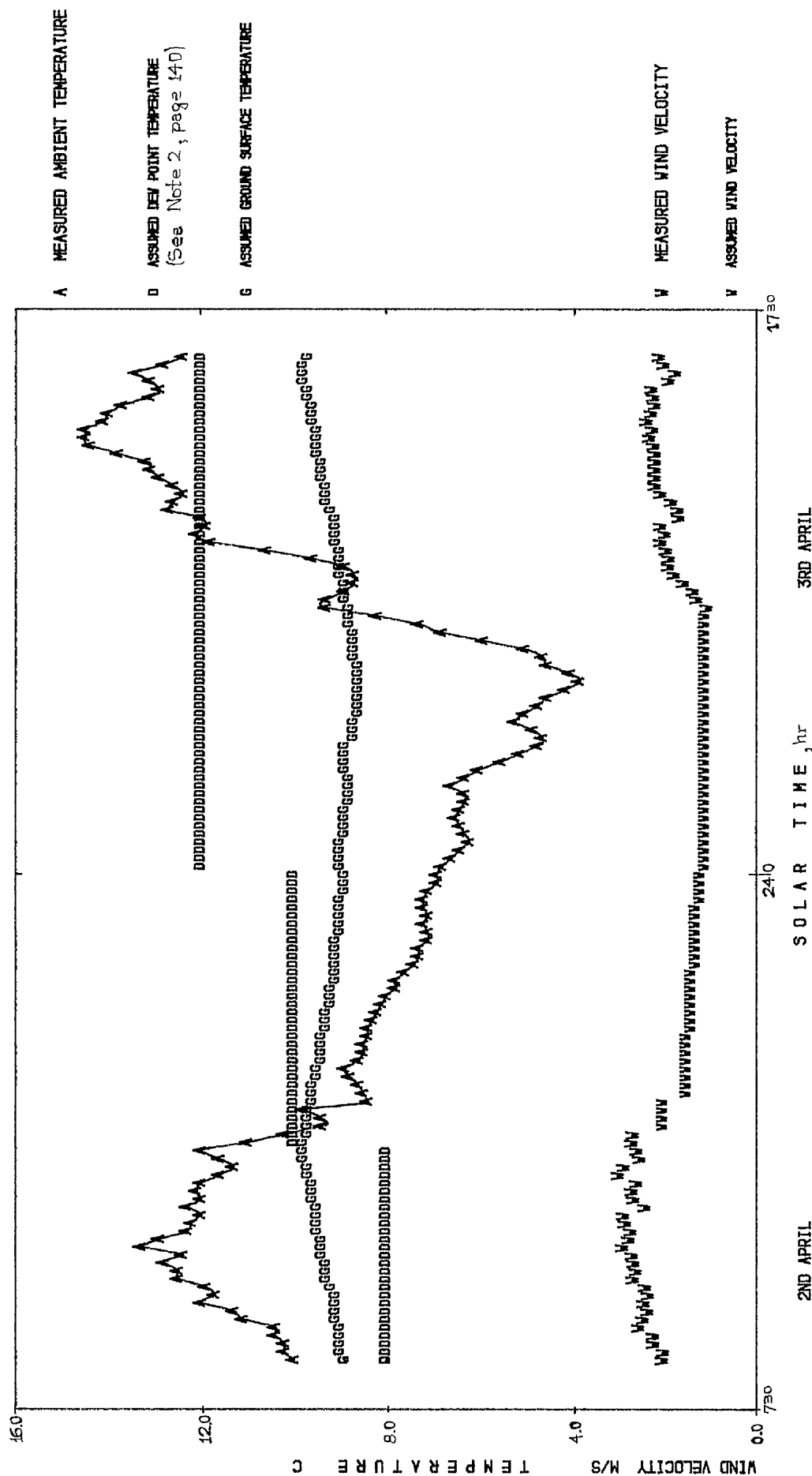


FIG.2.28  
WIND VELOCITY AND TEMPERATURES VALUES

### 2.6.3 Test box measurements and analytical model results.

The uncertainty over the optical properties of the internal surfaces of the test-box led to the comparison of the test-box measurements with three different analytical results. These results are based on three assumed distributions of the solar radiation among the internal surfaces and the transwall system element. The first two distributions correspond to the analysis of section 2.3 (optical properties according to the Tables 2.2a and 2.2b). The distribution resulting from the higher reflectance of the internal surfaces gives a better match between predicted and measured values of temperature. This match is further improved by assuming an enhanced absorption of the solar radiation by the transwall system element. This assumption certainly results in a decrease in the radiation absorbed by the internal surfaces. The values of the absorbed radiation of the third distribution are the product of values of the second distribution and the corresponding factors of Table 2.19. This enhanced absorption of the transwall system element, some 16%, is within the tolerance of the uncertainty in the estimated optical properties of the transwall glass. Note also that the 1-dimensional technique used to calculate the optical properties of the transwall system element will overestimate both the total absorptance and total transmittance of the element relative to the correct 3-dimensional technique. (Table 1.17, section 1.4).

Higher solar radiation absorption of the internal surfaces than that based on the values of reflectance of Table 2.2b could be tolerated if:

- (a) the conductivity of the polystyrene was higher.
- (b) the absorbed solar radiation by the external surfaces of the tanks was lower, and
- (c) the heat loss during the night was lower than assumed.

Fig. 2.29 to 2.37 and Tables 2.20 to 2.27 give values of measured and predicted temperatures of various control volumes and surfaces of the test-box. The reference numbers of the control volumes and surfaces have already been given in Fig. 2.25. The pattern of temperatures over the whole time period generally remains the same for measured and predicted values. The best matching between measured and predicted values occurs usually during the time period with the outside glass plate covered with the polystyrene sheet (from 16<sup>00</sup> solar time of the second of April to 7<sup>55</sup> solar time of the third of April). The matching is less successful during the

Table 2.19

Factors used in calculating the solar radiation absorbed by various control volumes and surfaces of the test-box.

control volume (x direction)	<u>2nd</u> April	<u>3rd</u> April
1	1.11	1.12
2	1.10	1.11
3	1.19	1.19
4	1.21	1.23
5	1.10	1.17
6	1.15	1.18
Surface		
8 (x-direction)	0.80	0.79
7 (y-direction)	0.75	0.78
8 (y-direction)	0.75	0.78
3 (z-direction)	0.83	0.81
4 (z-direction)	0.98	0.98

remaining period of time and this can be attributed, to some extent, to overestimation of solar radiation during the second of April and underestimation of solar radiation during the third of April. The matching of the air temperature in the test-box (control volume 7, along the x-direction), the transwall temperatures (control volumes 3, 4, 5 along the x-direction) and the temperatures of surfaces 7 and 8 along the x-direction is good. But the matching of the temperatures of the water tanks, the temperatures of the surfaces 7 and 8 along the y-direction during the second of April and the temperatures of the surfaces 2 and 2a along the x-direction is less good. This can be attributed not only to the approximation of the real physical phenomena by the assumed mathematical model of the test-box but also to uncertainties over the estimated values of the climatological data, the effective conductivity, the contact resistance between polystyrene and tanks, the optical properties of the external surfaces of the test box and the thermal properties of the various materials.

The following discussion is referred to the best matching (:third type of the internal distribution of the solar radiation).

The maximum difference between measured and predicted values of temperature of the 7<sup>th</sup> control volume along the x-direction is about 2°C for both days and occurs about 11 solar time (Fig. 2.29).

Maximum differences of the same order of magnitude between

measured and predicted values of temperature are also experienced in the case of temperature of the middle nodes of the water tanks. The general pattern of temperature over the whole time period for predicted values is slightly different from that for measured values (Fig. 2.30). The "predicted" pattern has higher and lower peaks. This is likely due to overestimated absorption of radiation during the second of April, overestimated heat losses to the environment during the night and underestimated absorption of radiation during the third of April. Lower values of the effective conductivity of water improves the "predicted" pattern slightly.

The maximum temperature difference between measured and predicted values in the case of surface 7 along the x-direction occurs during the first hours of the second of April and is about  $2^{\circ}\text{C}$ . The same happens for the surface 8 along the x-direction. There is a better matching during the rest of the time period especially during the time the outside glass plate is covered. (there is almost coincidence in the case of the surface 8) (Fig. 2.31 and 2.32).

The matching of measured and predicted values of temperatures of surfaces 7 and 8 along the y-direction is not good during the second of April, with predicted values always higher than the measured ones. The maximum difference is as high as  $3^{\circ}\text{C}$ . Slightly higher values of the conductivity of the polystyrene than those used in the simulation of the test-box improve the matching (Fig. 2.33 and 2.34).

An indifferent matching for both days is evident in the case of the temperature of surface 2 along the x-direction. At least better matching can be achieved during the period of time the outside glass plate is covered with, assuming a higher heat transfer coefficient between surface 1 (along the x-direction) and ambient temperature. (Fig. 2.35). This is in line with the remark of the previous paragraph on the conductivity of the polystyrene.

In the case of surface 2a (x-direction) a very good matching exists for the time period with the outside glass plate covered. This does not happen for the remaining time, where the measured values of temperature are always higher than those predicted with maximum difference slightly less than  $3^{\circ}\text{C}$  in both days, (Fig. 2.36). Some of this difference can be attributed to the radiation absorbed by the thermocouple itself, although it had been covered to decrease the radiation effect.

From Fig. 2.37 and Tables 2.20, 2.21 the difference between measured and predicted values inside the transwall module can be



seen. There is almost coincidence between measured and predicted values of temperature during the second of April. The difference becomes larger after the 3<sup>20</sup> solar time on the third of April with a maximum at about 10<sup>20</sup> solar time, of about 1.1°C.

Studying the relative magnitude of the three measured values of temperature inside the transwall module it is evident, for most of the time points, that the temperature gradient is very small with higher temperatures at the inside side of the module. This is not the case for the three predicted values of temperature inside the transwall module, during the period of time the system is covered. The predicted temperature of the central node is higher than the two others and the temperature of the inside node is generally lower than that of the outside node. This means that a better matching can be achieved during the period of time the system is covered if higher heat losses from the transwall to the environment are assumed than from the transwall to the room.

Finally, Tables 2.22 to 2.27 give some results from the analytical modelling of the small test-box. These are referred to predicted temperatures of the nodes of the various control volumes and surfaces. For these surfaces the associated heat transfer coefficient  $h_{x+}$  and radiation flux  $q_i$  are also given.

It should be mentioned that the chosen time interval was  $\Delta t = 5\text{min}$  with very good convergence. A time interval of  $\Delta t = 15\text{min}$  caused oscillations. The values of the climatological data of the three 5 minute intervals of each quarter are those of the end of the particular quarter. (Fig.2.26). The convergence criterion used was the absolute value of the relative change between two successive iterations in the node values of the temperature to be smaller than 0.08°C. The average number of the iterations before convergence was obtained had been about 3.5 iterations during the period of time the system was uncovered and about 1.5 iterations for the remaining time. This is in agreement with the numerical findings of the section 3.1.5 concerning the importance of the relative magnitude of the source terms of the set of the difference equations on the convergence of their line by line solution. Indeed, during the former period of time the absolute values of the source terms are higher than during the latter because of the presence of the solar radiation absorption. The required computing time for the particular problem was 30 secs for each day on a ICL 2976 computer.

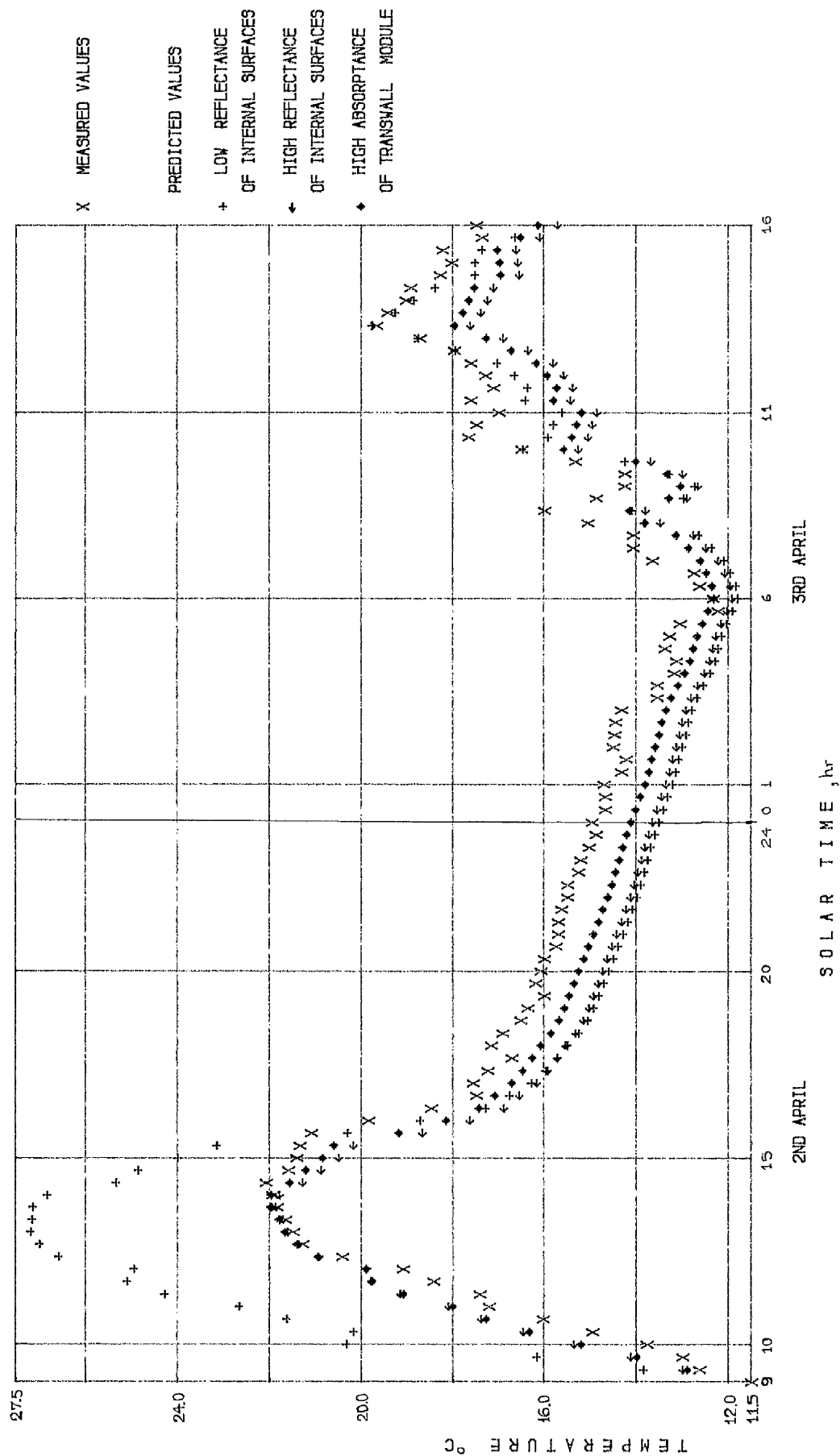


FIG. 2.29 TEST BOX CONTROL VOLUME 7 X-DIRECTION

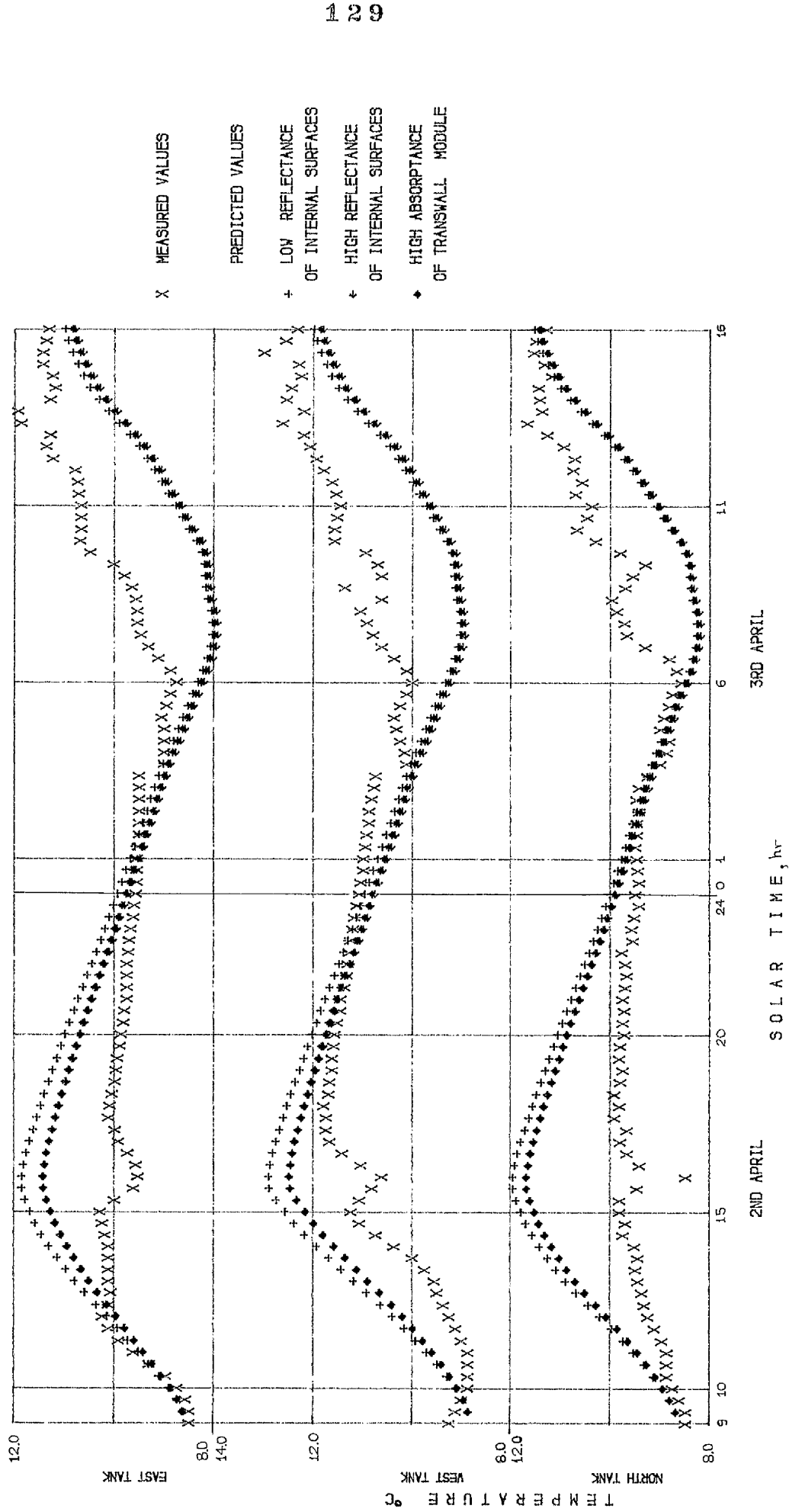


FIG. 2.30  
TEST BOX CONTROL VOLUME 11 X-DIRECTION, 3 Y-DIRECTION AND 11 Y-DIRECTION MIDDLE POINT OF TANKS

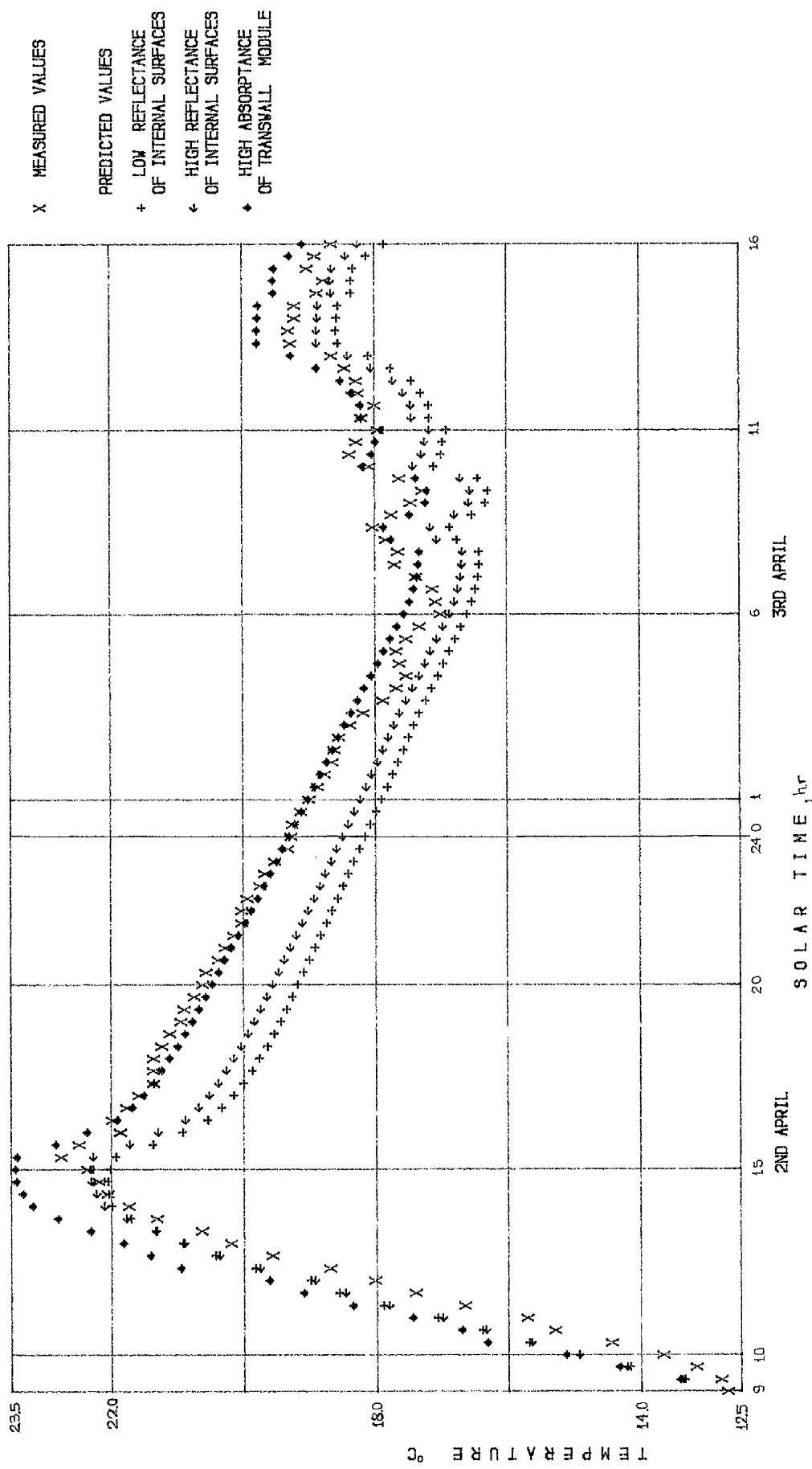


FIG. 2.31

TEST BOX SURFACE 7 X-DIRECTION INNER SURFACE OF TRANSWALL MODULE

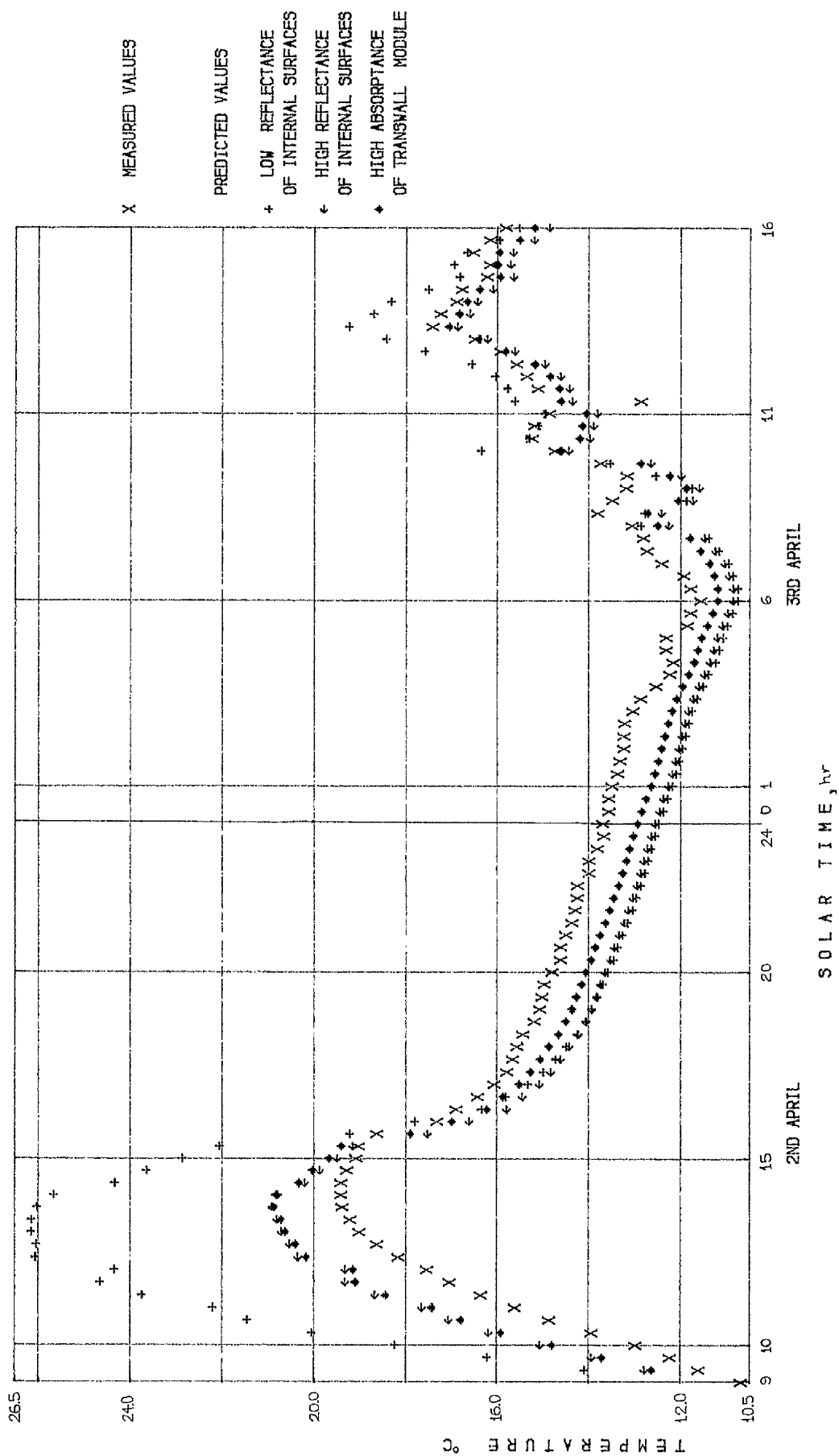


FIG. 2.32  
TEST BOX SURFACE 8 X-DIRECTION

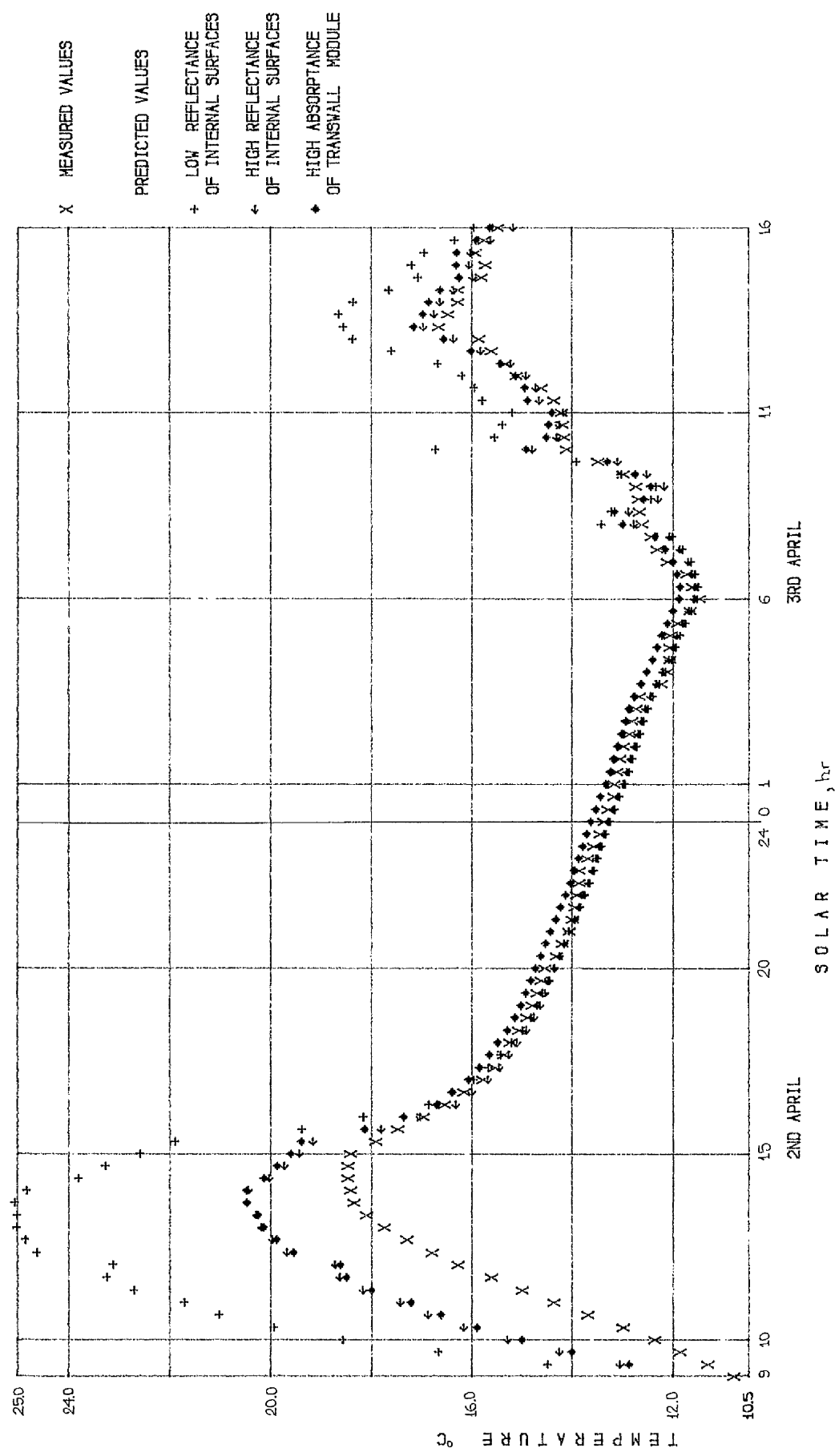


FIG. 2.33  
TEST BOX SURFACE 7 Y-DIRECTION INNER WEST SURFACE

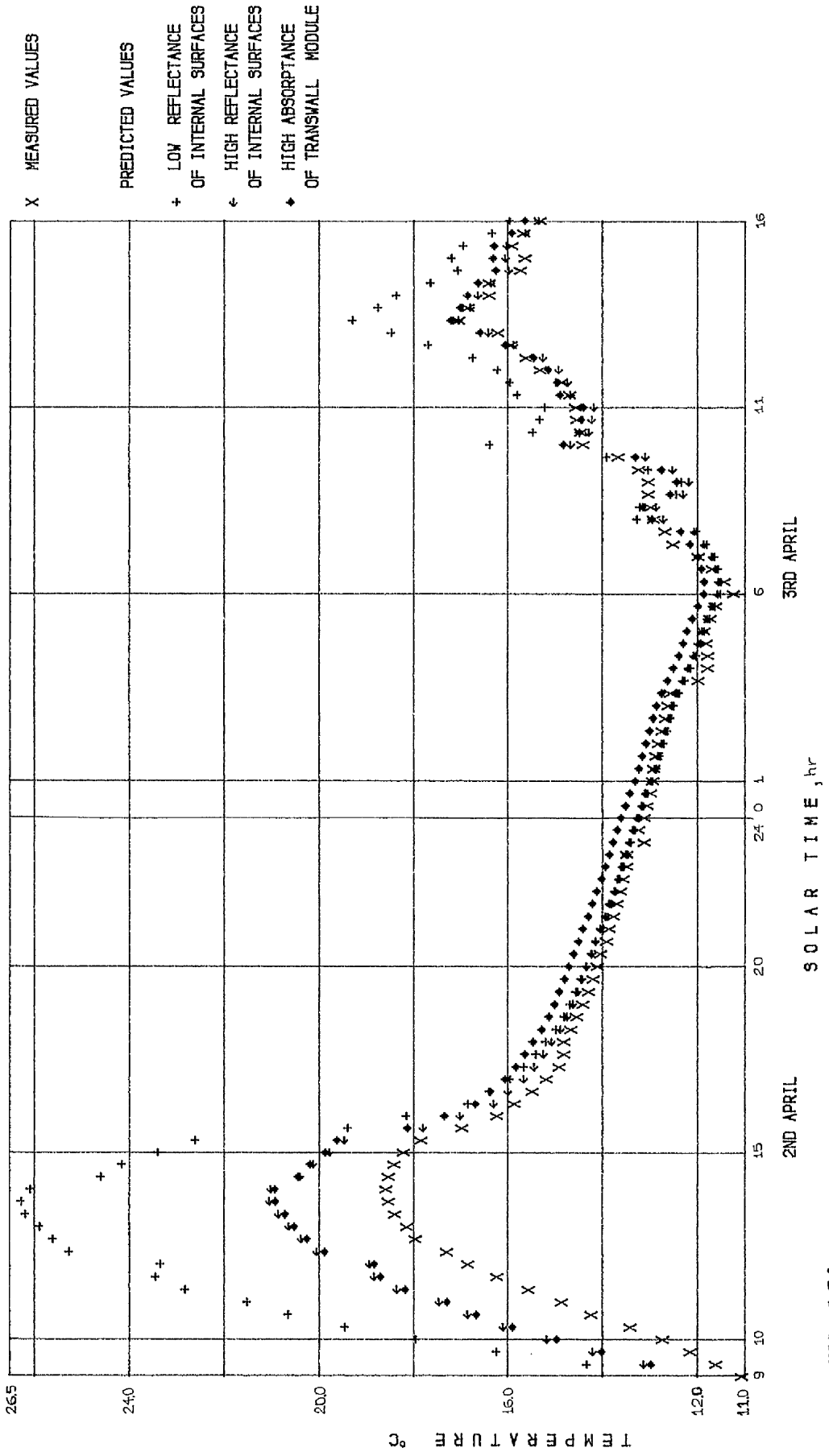


FIG. 2.34  
TEST BOX SURFACE 8 Y-DIRECTION INNER EAST SURFACE

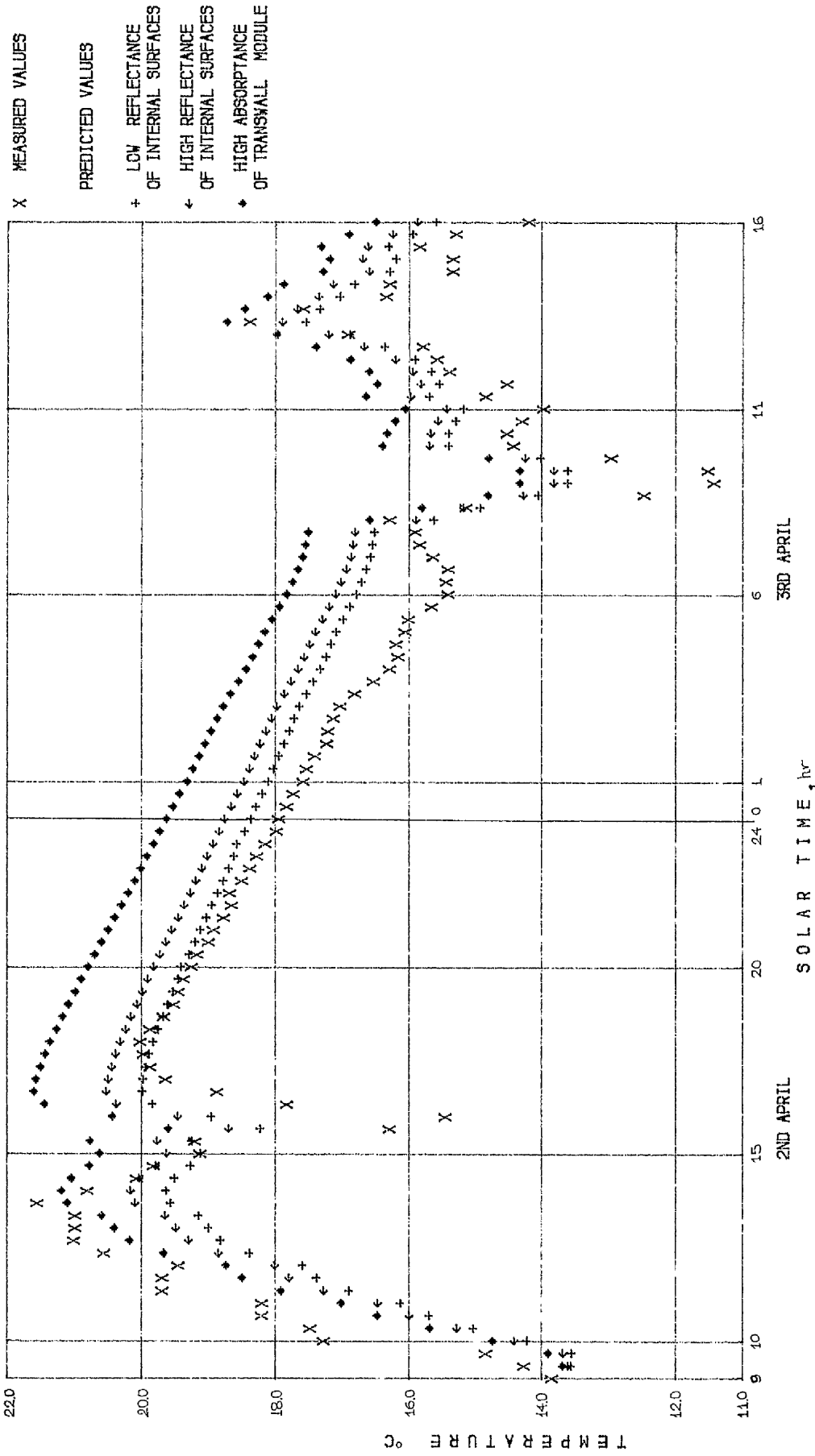


FIG. 2.35  
TEST BOX SURFACE 2 X-DIRECTION INNER SURFACE OF OUTSIDE GLASS PLATE



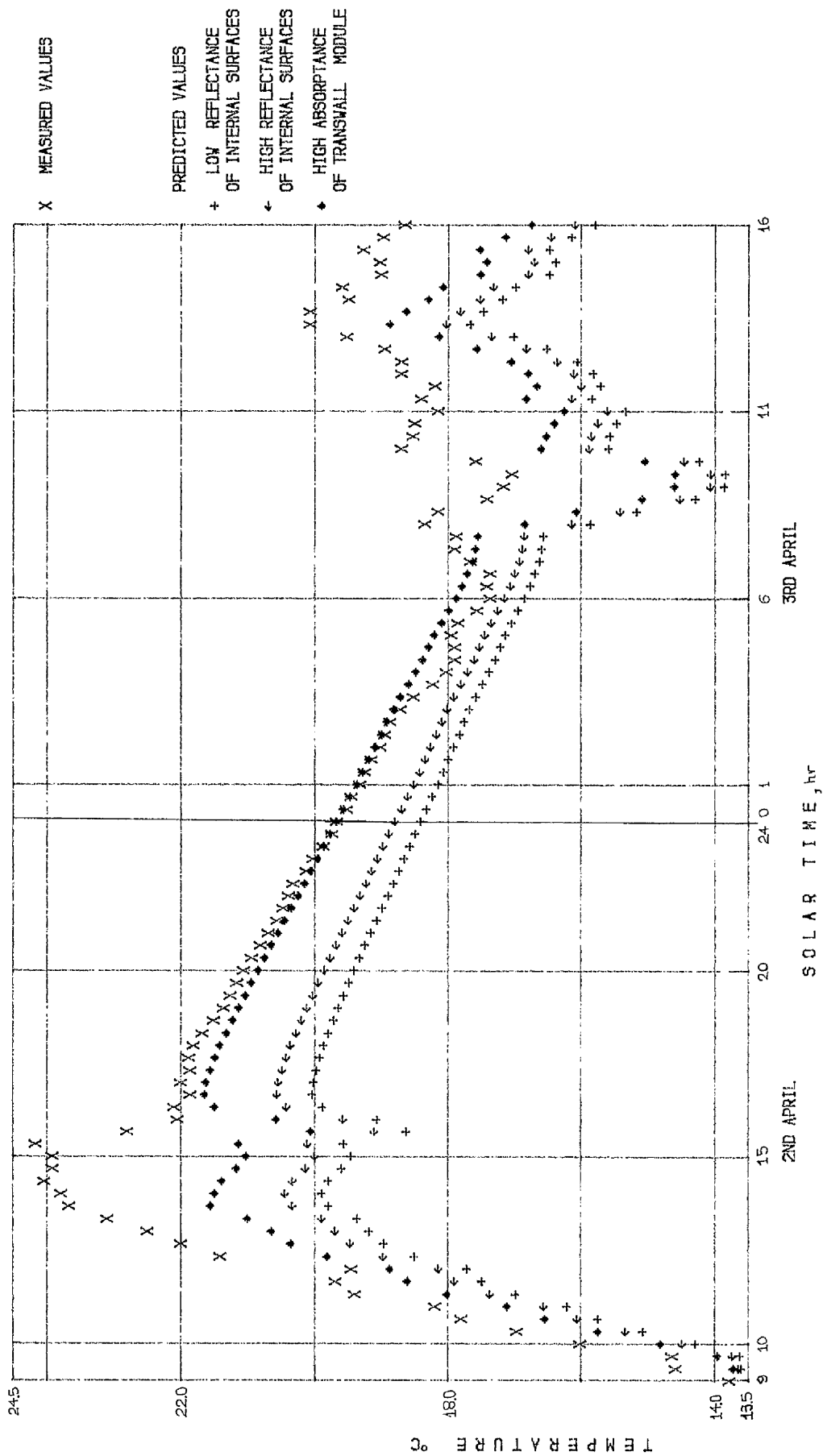


FIG. 2.36

TEST BOX SURFACE 2a X-DIRECTION

OUTER SURFACE OF TRANSWALL MODULE

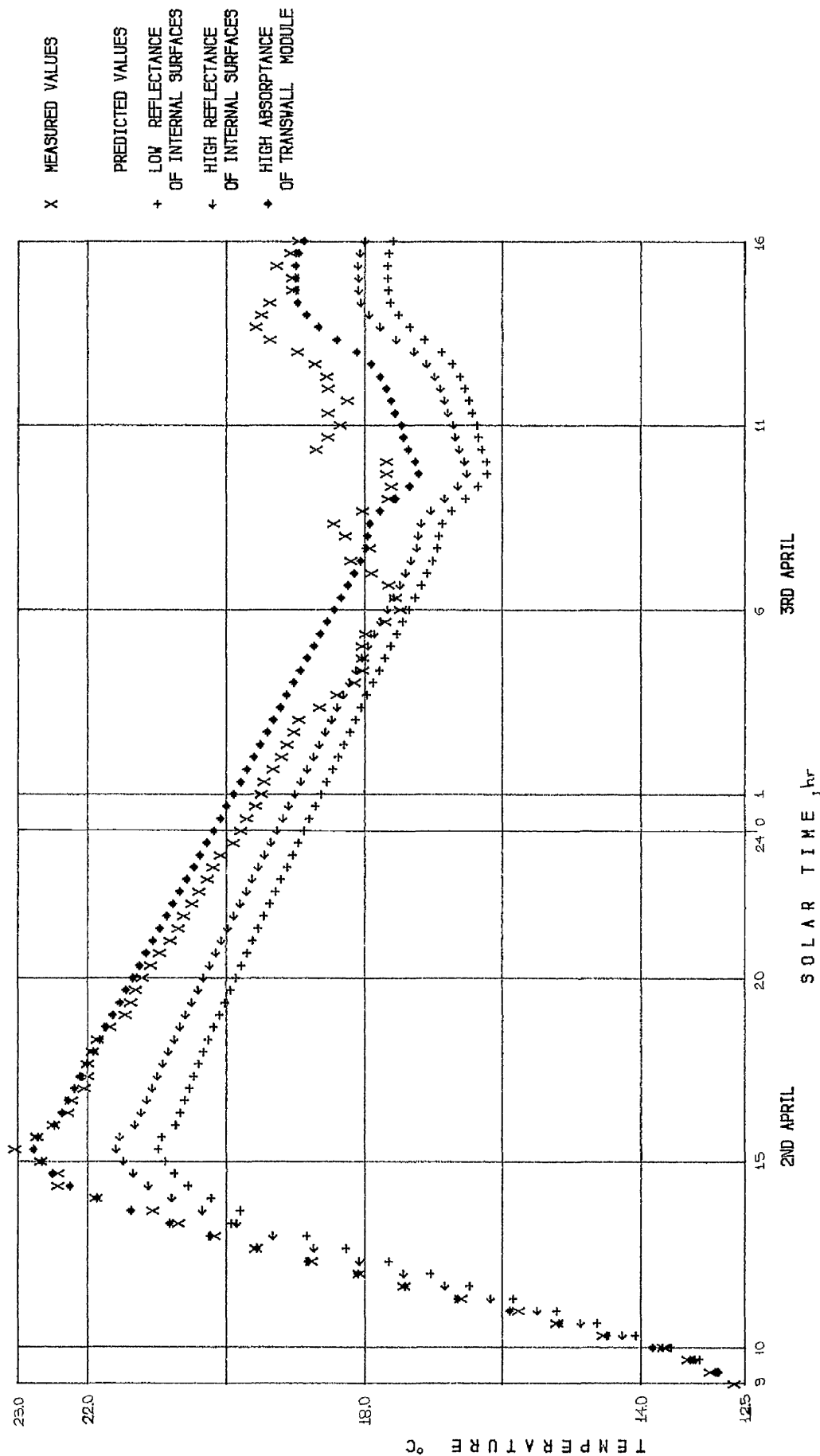


FIG. 2.37

Table 2.20

Measured (m) and predicted (p) values of temperatures of the control volumes 3,4 and 5 in the x direction, on the 2nd of April, 1982 ( °C). Transwa11 module control volumes.

Solar Time	control volume 3		control volume 4		control volume 5	
	m	p	m	p	m	p
9	12.49		12.62		12.89	
10	14.74	14.11	13.64	13.83	13.76	14.02
11	15.51	16.23	15.73	15.89	15.81	16.11
12	17.89	18.38	18.05	18.10	18.12	18.32
13	19.91	20.49	20.14	20.23	20.14	20.47
14	21.70	22.00	21.85	21.87	21.78	22.09
15	22.60	22.56	22.65	22.67	22.72	22.82
16	22.27	21.88	22.40	22.48	22.40	22.52
17	22.12	21.93	22.02	22.19	22.10	21.93
18	21.97	21.69	21.90	21.92	21.90	21.60
19	21.48	21.41	21.43	21.64	21.40	21.29
20	21.13	21.13	21.13	21.35	21.13	20.99
21	20.73	20.83	20.78	21.06	20.83	20.70
22	20.44	20.53	20.46	20.77	20.44	20.40
23	20.11	20.24	20.16	20.47	20.21	20.11
24	19.74	19.96	19.76	20.18	19.84	19.83

Table 2.21

Measured (m) and predicted (p) values of temperatures of the control volumes 3,4 and 5 in the x direction, on the 3rd of April, 1982 ( °C). Transwa11 module control volumes.

Solar Time	control volume 3		control volume 4		control volume 5	
	m	p	m	p	m	p
1	19.44	19.66	19.46	19.89	19.54	19.54
2	19.17	19.38	19.17	19.60	19.24	19.25
3	18.84	19.10	18.92	19.32	18.97	18.97
4	18.10	18.79	18.12	19.03	18.22	18.68
5	18.00	18.50	18.00	18.73	18.05	18.38
6	17.40	18.19	17.45	18.44	17.50	18.08
7	17.75	17.91	17.87	18.15	17.87	17.83
8	18.12	17.77	18.25	17.96	18.34	17.88
9	17.70	16.21	17.63	17.56	17.75	17.51
10	18.12	17.12	17.65	17.27	18.20	17.75
11	18.17	17.06	18.32	17.47	18.40	17.77
12	18.37	17.46	18.50	17.69	18.57	18.08
13	18.84	18.41	18.94	18.12	19.04	18.73
14	19.29	18.87	19.46	18.84	19.44	19.38
15	18.97	18.40	19.01	19.00	19.04	19.34
16	18.79	17.96	18.92	18.88	18.92	19.07

Table 2.22

Temperatures ( $^{\circ}\text{C}$ ) of control volumes along the x-direction - predicted values.

Solar time, hr	1	2	3	4	5	6	7	8	9	10	11	12	13	Tamb
10, 2-4-82	14.74	14.82	14.11	13.83	14.02	15.06	15.20	11.89	9.05	8.96	8.94	9.20	9.56	10.4
15, 2-4-82	20.63	21.03	22.56	22.67	22.82	23.46	20.85	15.65	11.72	11.59	11.51	11.61	11.75	11.3
20, 2-4-82	20.80	20.85	21.13	21.35	20.99	20.58	15.24	12.52	11.00	10.94	10.87	10.63	10.32	8.1
1, 3-4-82	19.32	19.37	19.66	19.89	19.54	19.13	13.80	11.23	9.81	9.76	9.69	9.45	9.14	6.2
6, 3-4-82	17.83	17.88	18.19	18.44	18.08	17.67	12.32	9.91	8.61	8.56	8.48	8.19	7.81	3.8
11, 3-4-82	16.06	16.25	17.06	17.47	17.77	17.93	15.18	11.57	9.13	9.06	9.04	9.32	9.69	12.0
16, 3-4-82	16.50	16.74	17.96	18.88	19.07	19.11	16.12	13.33	11.52	11.46	11.43	11.52	11.64	12.4

Table 2.23

Temperatures ( $^{\circ}\text{C}$ ),  $q_i$  ( $\text{W}/\text{m}^2$ ),  $h_{x+}$  ( $\text{W}/\text{m}^2\text{C}$ ) of some surfaces along the x-direction - predicted values.

Surface $\longrightarrow$	1		2		2a		7		8		14	
Solar time	Tem.	qi	h <sub>x+</sub>	Tem.	h	Tem.	Tem.	qi	h <sub>x+</sub>	Tem.	qi	h <sub>x+</sub>
10,2-4-82	14.47	-46	15.2	14.74	4.1	14.82	15.13	20	1.5	14.80	9	2.1
15,2-4-82	20.09	-69	16.5	20.63	4.5	21.03	23.45	5	3.0	19.68	10	2.6
20,2-4-82		0	1.4	20.80	4.2	20.85	20.47	-13	3.4	14.06	2	2.6
1,3-4-82		0	1.4	19.32	4.2	19.37	19.02	-13	3.4	12.64	2	2.6
6,3-4-82		0	1.4	17.83	4.1	17.88	17.57	-13	3.4	11.20	1	2.6
11,3-4-82	15.83	-47	12.0	16.06	4.2	16.25	17.91	2	3.0	14.06	5	2.6
16,3-4-82	16.25	-46	13.6	16.50	4.3	16.74	19.09	1	3.1	15.18	4	2.5

Note:  $q_i$  is the absorbed radiation flux minus the emitted flux from the surface.

$h_{x+}$  is the heat transfer coefficient at the one side of the surface.

$h$  is the heat transfer coefficient between the internal surface of the outside glass plate (2) and the external surface of the transwall module (2a). The convective-conductive part  $h_c$  takes values from 0.4 to  $0.7 \text{ W}/\text{m}^2\text{C}$

Table 2.24

Temperatures ( $^{\circ}\text{C}$ ) of control volumes along the y-direction - predicted values.

Solar time, hr	1	2	3	4	5	6	7	8	9	10	11	12	13	Tamb
10, 2-4-82	9.82	9.43	9.08	9.20	9.38	12.18	15.20	12.54	10.11	9.96	9.87	10.34	10.85	10.4
15, 2-4-82	12.98	12.56	12.15	12.33	12.56	16.04	20.85	16.27	12.72	12.49	12.27	12.33	12.41	11.3
20, 2-4-82	10.94	11.34	11.74	11.88	11.98	13.34	15.24	13.31	11.93	11.83	11.69	11.30	10.90	8.1
1, 3-4-82	9.69	10.13	10.56	10.69	10.79	12.05	13.80	12.02	10.75	10.66	10.52	10.09	9.66	6.2
6, 3-4-82	8.24	8.76	9.27	9.41	9.50	10.68	12.32	10.67	9.47	9.39	9.25	8.74	8.22	3.8
11, 3-4-82	10.32	9.98	9.65	9.76	9.90	12.13	15.18	12.16	9.95	9.80	9.70	10.03	10.37	12.0
16, 3-4-82	12.03	11.95	11.85	11.96	12.07	13.83	16.12	13.83	12.06	11.94	11.84	11.94	12.02	12.4

Table 2.25

Temperatures ( $^{\circ}\text{C}$ ),  $q_i$  ( $\text{W}/\text{m}^2$ ),  $h_{x+}$  ( $\text{W}/\text{m}^2\text{C}$ ) of some surfaces along the y-direction - predicted values.

Surface $\rightarrow$	1	7	8	14
	Tem.	Tem.	Tem.	Tem.
10, 2-4-82	9.82	14.99	14.96	10.85
15, 2-4-82	12.98	19.60	19.87	12.41
20, 2-4-82	10.94	14.72	14.70	10.90
1, 3-4-82	9.69	13.32	13.31	9.66
6, 3-4-82	8.24	11.88	11.87	8.22
11, 3-4-82	10.32	14.39	14.40	10.37
16, 3-4-82	12.03	15.63	15.63	12.02
	$q_i$	$q_i$	$q_i$	$q_i$
	31	19	16	59
	71	20	22	26
	-11	8	8	-11
	-10	8	8	-10
	-9	7	7	-9
	15	13	13	15
	4	11	11	4
	$h_{x+}$	$h_{x+}$	$h_{x+}$	$h_{x+}$
	15.2	1.9	1.9	15.2
	16.5	2.6	2.5	16.5
	10.6	2.2	2.2	10.6
	9.9	2.2	2.2	9.9
	9.9	2.2	2.2	9.9
	12.0	2.4	2.4	12.0
	13.6	2.2	2.2	13.6

Note:  $q_i$  is the absorbed radiation flux minus the emitted flux from the surface.

$h_{x+}$  is the heat transfer coefficient at the one side of the surface.

Table 2.26

Temperatures ( $^{\circ}\text{C}$ ) of control volumes along the z-direction-predicted values.

Solar time, hr	1	2	3	4	5	6	Tamb
10, 2-4-82	27.44	22.12	15.20	14.31	12.91	11.90	10.4
15, 2-4-82	26.13	23.39	20.85	21.05	17.22	13.98	11.3
20, 2-4-82	9.31	11.00	15.24	12.05	10.91	9.95	8.1
1, 3-4-82	7.60	9.40	13.80	10.48	9.27	8.24	6.2
6, 3-4-82	5.56	7.60	12.32	8.92	7.42	6.15	3.8
11, 3-4-82	20.73	17.68	15.18	13.69	13.36	13.10	12.0
16, 3-4-82	17.30	16.10	16.12	15.20	14.51	13.86	12.4

Table 2.27

Temperatures ( $^{\circ}\text{C}$ ),  $q_i$  ( $\text{W}/\text{m}^2$ ),  $h_{x+}$  ( $\text{W}/\text{m}^2$   $^{\circ}\text{C}$ ) of some surfaces along the z-direction-predicted values.

Surface $\longrightarrow$	1	7	8	14
Solar time	Tem.	Tem.	Tem.	Tem.
10, 2-4-82	22.77	17.08	15.84	11.86
15, 2-4-82	26.25	20.74	21.26	13.81
20, 2-4-82	9.22	12.55	12.17	9.90
1, 3-4-82	7.49	11.06	10.63	8.19
6, 3-4-82	5.45	9.49	9.10	6.09
11, 3-4-82	20.90	14.79	13.82	13.10
16, 3-4-82	17.33	14.93	14.90	13.81
	$q_i$	$q_i$	$q_i$	$q_i$
	287	-19	21	9
	254	-10	3	8
	6	-2	1	10
	6	-1	1	11
	9	-1	2	13
	118	-12	1	8
	69	-8	-4	8
	$h_{x+}$	$h_{x+}$	$h_{x+}$	$h_{x+}$
	15.2	0.2	2.2	7.6
	16.5	1.5	2.0	7.6
	10.6	3.0	0.2	7.6
	9.9	3.0	0.2	7.6
	9.9	3.0	0.2	7.6
	12.0	2.0	0.2	7.6
	13.6	2.5	0.2	7.6

Note 1:  $q_i$  is the absorbed radiation flux minus the emitted flux from the surface.

$h_{x+}$  is the heat transfer coefficient at the one side of the surface.

Note 2: Some of the assumed values of the dew point temperature (Fig. 2.28, page 123) are unrealistic. The importance of this mistake on the present prediction of the test-box thermal performance is almost negligible. Estimates of the dew point temperature based on the average relative humidity values for Glasgow (79) and the measured dry bulb temperature lead to a very small change of the sky emittance according to Table 2.1, page 65.

## Chapter 3

### CHAPTER 3

#### NUMERICAL FLOW PREDICTION AND EFFECTIVE CONDUCTIVITY OF THE TRANSWALL FLUID.

##### Introduction.

The flow of the liquid in the transwall modules induced by the absorption of radiation is predicted numerically by the method presented in section 3.1. The experimental and numerical evidence showed that this phenomenon under the usual solar irradiation and temperature conditions is a 3-dimensional laminar flow. The effect of the volumetric absorption of radiation on the liquid flow has been studied very little by experimental or numerical methods (56). Most of the relevant work concerns solar ponds or solar distillation. In the former case the pure conduction assumption is very common (57). In the latter the effect of the volumetric absorption of radiation is simply neglected (58) (21). The discretization of the governing equations of the 3-dimensional laminar flow follows the basic characteristics of the control volume method. The thermal behaviour of the glass container is also incorporated in this numerical prediction. Although this complicates the whole analysis and increases the required computing time, it is considered important because the modelling of the phenomenon becomes more realistic. The treatment of the heat fluxes at the boundary of two different regions is discussed by Roache (59) and Larson et. al. (65). In section 3.1.4 a new treatment is given in such a way that the coupling of conduction and convection regions is obtained and the line-by-line iterative solution of the system of the energy difference equations is performed from one side of the module to the other. Because of the shape of the module all the control volumes are of parallelepiped shape. The solution of the whole set of difference equations follows the basic features of the SIMPLE procedure suggested by Patankar (68). The set is divided into small sub-sets, e.g. momentum, energy, etc. Each sub-set is solved successively by employing the line-by-line iterative method (section 3.1.6). This iterative method does not guarantee the convergence of the solution of the so-called "pressure correction" sub-set of equations and an explanation based on numerical evidence is given. That is why the Gauss-elimination direct method was finally adopted for the solution of this particular sub-set instead of the line-by-line method.

The numerical method has been applied to various transwall



modules filled with distilled water and the temperature, pressure and velocity fields have been predicted (section 3.3). The number of the temperature control volumes was 302, of the pressure 108, and of the velocity components 126, 144 and 126. It was found that an excessive amount of computer time was required, the ratio of main frame computer time to real time being of the order of 200 to 1. This time problem restricts the numerical method to moderate real time periods of only a few minutes.

The complicated phenomenon of the fluid convection inside the transwall module can be simplified to a conduction one by introducing the effective conductivity concept (section 3.2). The calculation of the effective conductivity is obtained by employing an analytical approach which makes use of the data collected from the application of the numerical method. Values of the ratio of the effective conductivity to the conductivity of the still water are calculated at two interfaces inside the water of four different transwall modules under irradiance conditions of 400 to 500 W/m<sup>2</sup>. These values are higher than those suggested by Fuchs et. al. (3), which have been produced from fitting experimental data. This may be attributable to the fact that the effective conductivity was calculated in this thesis for those periods of time during which the stratification of the transwall liquid was small and could not effect the convective heat transfer.

Measurements of the temperature and the velocity at certain points in a small transwall module irradiated by a solar simulator have been performed to support some of the numerical predictions (section 3.4). The temperature measurements concern the temperature patterns along the small dimension of the transwall module at different heights. These patterns are compared to the numerically predicted ones. The values of the three velocity components were measured by using the "thymol blue technique". This is achieved by photographing the blue lines produced electrolytically inside the solution of the thymol blue into water. An analytical method has been developed to "translate" the position of a point in a pair of photographs taken simultaneously by two cameras into three coordinates referred to the real transwall module.

### 3.1 MODELLING THE PHENOMENON OF THE NATURAL CONVECTION OF A FLUID INDUCED BY THE ABSORPTION OF RADIATION.

#### 3.1.1 Assumptions

The phenomenon of the natural convection of a liquid inside a transwall module induced by the absorption of radiation has been studied numerically under the following assumptions:

- a) The flow is laminar.

The phenomenon has not yet been studied sufficiently to establish criteria of laminar, transition or turbulent flow. The initial intuitive expectation of a laminar flow inside a transwall module under usual solar irradiance ( $400 \pm 500 \text{ W/m}^2$ ) has already been verified experimentally in certain cases (section 3.4). On the other hand, there has not been any evidence from the numerical study of the phenomenon of any laminar instability that would indicate a transition into a new type of flow (59), (60).

- b) The fluid is Newtonian.

The present analysis of the phenomenon concerns very weak solutions of dyes in water. According to Tritton (61) and Massie (62) the water behaves as a Newtonian fluid, typical of fluids with small molecular interaction.

- c) The terms with the second coefficient of viscosity  $\mu'$  in the momentum equations are neglected.

Although there is experimental evidence of the existence and magnitude of the second coefficient of viscosity  $\mu'$  for various fluids (among them, water), doubts expressed on the methods used for its measurements (66) and simplification convenience have led to this omission.

- d) The contribution of the kinematic energy to the total internal energy is negligible.

The total internal energy per unit mass  $e_s$  is defined here by the following expression:

$$e_s = e + k$$

where  $e$  is the internal energy of the liquid

$$e = \int c_v dT$$

$c_v$  is the constant volume specific heat capacity ( $\text{J/Kg}^\circ\text{C}$ )

$T$  is the temperature of the liquid ( $^\circ\text{C}$ )

$k$  is the kinematic energy of the liquid

$$k = 0.5 * V^2$$

$V$  is the absolute value of the velocity vector  $\vec{V}$

For water in ordinary temperatures with velocities of the order of magnitude of 0.04m/s, the second term of the right side of the total internal energy expression is negligible in comparison with the first term ( $c_v \approx 4061 \text{ J/Kg} \cdot ^\circ\text{C}$ ).

e) The constant volume  $c_v$  and constant pressure  $c_p$  specific heat capacities are constant.

This is primarily a numerical convenience adopted to simplify the final expression of the energy equation.

f) The work performed by the viscous stresses and the gravity force are neglected in comparison with conduction, convection and radiation absorption.

This assumption is readily justifiable in natural flows according to References (42), (61), (63) and (65). This is particularly true as the radiation absorption increases.

g) The movement of the upper boundary of the liquid because of its expansion is neglected. (See Fig.3.1).

### 3.1.2 Governing differential equations

#### 1. The continuity equation

$$\frac{\partial(\rho)}{\partial t} + \text{div}(\vec{G}) = 0 \quad (3.1)$$

where  $\rho$  is the density of the fluid.

$\vec{G}$  is the mass-flux vector.

$$\vec{G} = \rho * \vec{V}$$

$\vec{V}$  is the velocity vector.

$$\vec{V} = u * \vec{i} + v * \vec{j} + w * \vec{k}$$

$u, v$  and  $w$  are the three components of the velocity vector  $\vec{V}$  along the three axes of a constant co-ordinate system Oxyz.

The unit vectors of this system are  $\vec{i}$ ,  $\vec{j}$  and  $\vec{k}$ .

In Fig. 3.1 the co-ordinate system Oxyz used in the present analysis is shown in respect to the transwall module and the gravity vector  $\vec{g}$ .

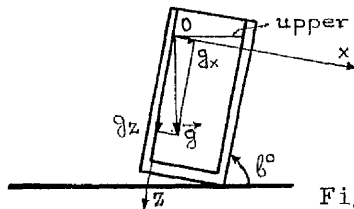


Fig. 3.1

The axis Oy is vertical to the plane of page, towards the reader.

The inclination angle from the horizontal plane is  $\theta^\circ$ .

#### 2. The momentum equations

For the component of velocity  $u$  along the x-direction:

$$\frac{\partial(\rho*u)}{\partial t} + \text{div}(\vec{G}*u) = \text{div}(\mu*\text{gradu}) - \vec{i}*\text{grad}P + \vec{i}*\rho*\vec{g} + \text{div}(\mu*\vec{L}x) \quad (3.2)$$

where  $\mu$  is  $\frac{\partial(\rho*u)}{\partial t}$  first coefficient of viscosity.

P is the hydrostatic pressure of the fluid.

$$\vec{L}_x = (\partial u / \partial x) * \vec{i} + (\partial v / \partial x) * \vec{j} + (\partial w / \partial x) * \vec{k}$$

For the component of velocity v along the y-direction:

$$\frac{\partial(\rho * v)}{\partial t} + \text{div}(\vec{G} * v) = \text{div}(\mu * \text{grad } v) - \vec{j} * \text{grad } P + \text{div}(\mu * \vec{L}_y) \quad (3.3)$$

$$\text{where } \vec{L}_y = (\partial u / \partial y) * \vec{i} + (\partial v / \partial y) * \vec{j} + (\partial w / \partial y) * \vec{k}$$

For the component of velocity w along the z-direction:

$$\frac{\partial(\rho * w)}{\partial t} + \text{div}(\vec{G} * w) = \text{div}(\mu * \text{grad } w) - \vec{k} * \text{grad } P + \vec{k} * \rho * \vec{g} + \text{div}(\mu * \vec{L}_z) \quad (3.4)$$

$$\text{where } \vec{L}_z = (\partial u / \partial z) * \vec{i} + (\partial v / \partial z) * \vec{j} + (\partial w / \partial z) * \vec{k}$$

The terms that have been omitted from the right side of the momentum equations (3.2), (3.3) and (3.4) because of the assumption,  $\epsilon$ , are respectively:

$$\mu' * \text{div}(\vec{L}_x) + (\partial \mu' / \partial x) * \text{div } \vec{V}$$

$$\mu' * \text{div}(\vec{L}_y) + (\partial \mu' / \partial y) * \text{div } \vec{V}$$

$$\mu' * \text{div}(\vec{L}_z) + (\partial \mu' / \partial z) * \text{div } \vec{V}$$

where  $\mu'$  is the second coefficient of viscosity of the fluid.

### 3. The energy equation

According to Eckert et.al. (42) the general form of the energy equation is given by the following expression:

$$\frac{\partial(\rho * e_s)}{\partial t} = - \text{div}(\vec{V} * (\rho * e_s + P)) - \text{div}(\vec{q}) + q_u + \text{div}(\vec{\pi} * \vec{V}) + \rho * \vec{V} * \vec{g}$$

stored energy	convected energy	conducted energy	generated energy	work performed by viscous stresses and gravity forces
------------------	---------------------	---------------------	---------------------	---

where  $\vec{q}$  is the heat flux vector. Fourier's law of heat conduction

for an assumed isotropic medium gives:  $\vec{q} = -\lambda * \text{grad } T$

where  $\lambda$  is the thermal conductivity of the fluid.

$\vec{\pi}$  is the viscous stress tensor. Its elements are:

$$\pi_{11} = \mu' * \text{div}(\vec{V}) + 2 * \mu * (\partial u / \partial x), \quad \pi_{22} = \mu' * \text{div}(\vec{V}) + 2 * \mu * (\partial v / \partial y),$$

$$\pi_{33} = \mu' * \text{div}(\vec{V}) + 2 * \mu * (\partial w / \partial z)$$

$$\pi_{12} = \mu * ((\partial v / \partial x) + (\partial u / \partial y)), \quad \pi_{23} = \mu * ((\partial w / \partial y) - (\partial v / \partial z)), \quad \pi_{31} = \pi_{13}$$

$$\pi_{13} = \mu * ((\partial u / \partial z) + (\partial w / \partial x)), \quad \pi_{21} = \pi_{22}, \quad \pi_{32} = \pi_{23}$$

$q_u$  is the volumetric rate of heat generation. (e.g. absorption of radiation). Because of the assumptions d, e and f the energy equation is written in the following form:

$$\frac{\partial(\rho * c_v * T)}{\partial t} = - \text{div}(\vec{V} * \rho * (c_v * T + P / \rho)) + \text{div}(\lambda * \text{grad } T) + q_u$$

The specific enthalpy h and the constant pressure specific heat capacity  $c_p$  are defined from the following equations:

$$h = \int c_p * dT = \int c_v * dT + P/\rho$$

and the final expression of the energy equation is:

$$\frac{\partial(\rho * c_v * T)}{\partial t} + \text{div}(\vec{G} * c_p * T) = \text{div}(\lambda * \text{grad} T) + q_u \quad (3.5)$$

4. Governing equation of heat conduction in the non-convective parts of a transwall module.

The energy equation for pure conduction with internal sources is given by the following expression, similar to expression (3.5)

$$\frac{\partial(\rho * c_v * T)}{\partial t} = \text{div}(\lambda * \text{grad} T) + q_u \quad (3.6)$$

It is obvious that all the governing equations for both convective and conductive parts of a transwall module have the same general form:

$$\frac{\partial(a * \phi)}{\partial t} + \text{div}(b * \vec{V} * \phi) = \text{div}(c * \text{grad} \phi) + d_\phi \quad (3.7)$$

where  $\phi$  is the general dependent variable

$\vec{V}$  is the velocity vector and

$a, b, c$  and  $d_\phi$  are coefficients generally dependent on  $\phi$ .

### 3.1.3 The discretization of the system of differential equations

The discretization of the distribution of the dependent variable  $\phi$  of the differential equation (3.7) is achieved by employing a control volume method, the basic characteristics of which appear in Patankar's control volume method described in (67) and (68).

The whole domain of interest, no matter if it is a conduction or convection region, is separated into control volumes. Care is taken every boundary between two different conduction or convection regions to coincide with interfaces of adjacent control volumes. A node is located at the geometric centre of each control volume. In Fig. 3.2, an example of a two-dimensional domain is shown, consisting of a conduction and a convection region, with black dots as the nodes of the control volumes.

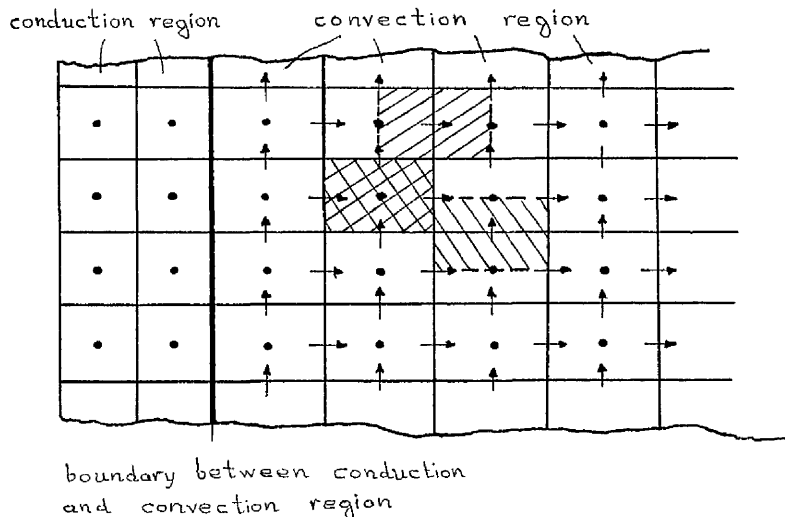


Fig.3.2

A typical control volume is shown cross-hatched. Integrations of the energy and the continuity equation are performed over each of these control volumes. The values of temperature and pressure are calculated at the nodes of these main control volumes. The velocity components are calculated for the points that lie on the faces of the main control volumes. This means that a displaced grid of nodes is used for each velocity component. The horizontal short arrows show the nodes of control volumes that correspond to the velocity component  $u$  along the  $x$ -direction in Fig. 3.2. Equally, the vertical short arrows show the nodes of control volumes that correspond to the velocity component  $v$  along the  $y$ -direction.

Typical control volumes of the  $u$  and  $v$  velocity components are also shown in Fig. 3.2 (single-hatched). Integration of the momentum equation of each velocity component is performed over these control volumes. In this integration the half-control volumes corresponding to the velocity components nodes at the boundary surfaces between two different convection regions, or between a conduction and convection region, are excluded. Not only is space discretization performed but the time is discretized as well. From the known values of dependent variables  $\phi^0$  at time  $t$ , the values  $\phi$  at the next instant  $t + \Delta t$  have to be calculated. The superscript  $0$  is used to denote the values at time  $t$ , while its absence implies values at  $t + \Delta t$ .

The integral of each term differs from term to term, depending on its actual expression. These are generally volume or surface integrals. Their finite-difference representation depends on the assumption of the variation of  $\phi$  between the nodes. The simplest variations are generally adopted, stepwise or piecewise-linear variation. In any case, the compatibility of surface integrals between adjacent control volumes is ensured.

The finite-representation of the various terms of equation (3.7) is:

#### 1. Volume integrals

##### 1a. Unsteady term, $\partial(a*\phi)/\partial t$

Stepwise variation assumption of the values of  $\phi$  and  $a$  over the whole control volume with node  $L$  (Fig. 3.3) gives:

$$(a_L * \phi_L - a_L^0 * \phi_L^0) * \Delta V / \Delta t \quad (3.8)$$

where  $\Delta V$  is the volume of the control volume.

1b. Parts of source term  $d_\phi$ , for example  $\vec{i} * \rho * \vec{g}$  or  $q_u$ .

Stepwise variation assumption of the values of  $\rho$  and  $q_u$  over the control volume, gives:

$$\rho_L * g * \cos \theta * \Delta V, \quad q_{uL} * \Delta V \quad (3.9)$$

1c The pressure terms,

$$\vec{i} * \text{grad } P = dP/dx$$

Integration over the control volume of node L, assuming a linear variation of pressure P between points  $x_+$  and  $x_-$ , gives the following finite-representation:

$$\frac{P_{x_+} - P_{x_-}}{\Delta L_{x_+} + \Delta L_{x_-}} * \Delta V \quad (3.10)$$

Similar expressions are obtained for the other two pressure terms of the corresponding equations.

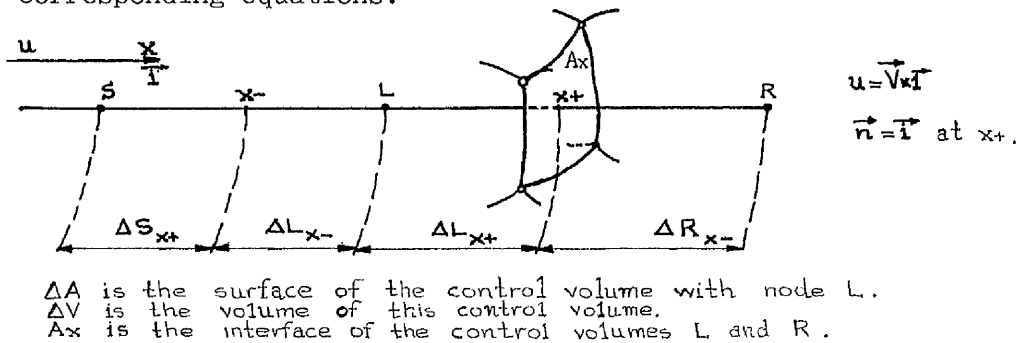


Fig.3.3

## 2. surface integrals

Convection and diffusion terms,  $\text{div} (b * \vec{V} * \phi)$ ,  $\text{div} (c * \text{grad } \phi)$  and the last terms of the momentum equations, for example  $\text{div} (\mu * \vec{L}x)$ .

The integration of these terms over the control volume gives rise to surface integrals according to the Gauss divergence theorem:

$$\iiint_{\Delta V} \text{div} \vec{F} * dV = \iint_{\Delta A} F_n * dA$$

where,  $F_n = \vec{F} * \vec{n}$  is the component of  $\vec{F}$  normal to surface  $\Delta A$  and  $\vec{n}$  is the outer unit vector normal to surface  $\Delta A$ . Assuming  $F_n$  constant all over the area  $A_x$  of surface  $\Delta A$ ,  $\iint_{A_x} F_n * dA = F_n * A_x$ . (3.11)

So the finite representations of the integrals of convection and diffusion terms and of the last terms of the momentum equations at the point  $x_+$  of the interface of the control volumes L and R (according to Fig.3.3) are:

convection term:  $(b * \phi * u)_{x_+} * A_x \quad (3.12)$

$$\text{diffusion term:} \quad (c * (\partial \phi / \partial x))_{x+} * Ax \quad (3.13)$$

$$\text{last term:} \quad (\mu * (\partial u / \partial x))_{x+} * Ax \quad (3.14)$$

The expression of the last term is similar to that of the diffusion term and so the following discussion will be restricted only to the convection and diffusion term finite representations. A linear variation between points L and x+ gives the following finite-representation for the diffusion integral over area Ax:

$$c_{x+} * \left( \frac{\phi_{x+} - \phi_L}{\Delta L_{x+}} \right) * Ax \quad (3.15)$$

The final finite-representation of both integrals, convection and diffusion, that will allow the coupling of the values of the dependent variable  $\phi$  at the two adjacent nodes, L and R, depends on the expression of the variable  $\phi_{x+}$  at the interface. An unsuccessful expression of  $\phi_{x+}$  may produce instability problems because of physical unrealism.

When there is no convection normal to the interface, the final finite representation of the surface integral(s) can be expressed without the explicit appearance of the value of the variable  $\phi_{x+}$  by the appropriate treatment of the relevant fluxes at the interface. This is discussed for heat fluxes at boundaries between conduction and convection regions in the next section.

When there is convection normal to the interface, the expression of the integrals without explicit appearance of the value  $\phi_{x+}$  can be obtained by employing one of the upwind, hybrid or power law schemes, discussed in (59) and (68). In this work the hybrid scheme has been used, taking into account not only the diffusion flux from the typical diffusion term  $\text{div}(c * \text{grad } \phi)$  of equation (3.7) but diffusion fluxes that might arise from the source term  $d_\phi$  - for example, the last term of the momentum equations. This way the hybrid scheme becomes more realistic.

Finally, it should be added that the absence of the superscript o from  $\phi$  from all the above finite representations, apart from (3.8), implies that the present formulation of the system of difference equations is fully implicit.



### 3.1.4 The coupling of conduction and convection regions.

When there is no convection normal to the interface of two control volumes, the finite representation of the diffusion term of the energy equation can be expressed without the explicit appearance of the value of the temperature of the interface. Only the values of the temperature of the nodes of the control volumes appear. This is obtained by the appropriate treatment of the heat balance at the interface. This method of analysis is important because it overcomes the problem of discontinuity between conduction and convection regions. It also allows the line-by-line iterative solution of the algebraic equations derived from the discretization of the energy differential equations to be performed along the total length of the grid lines. The analysis can be extended to mass-fluxes or stresses at the interfaces of their control volumes in corresponding cases of discontinuity.

The computational effort of calculating the temperature of the interface of the control volumes can be by-passed in certain cases where the temperature of the interfaces are not required.

The interface, normal to the direction of axis  $x$ , between the two control volumes A and B is shown in Fig. 3.4

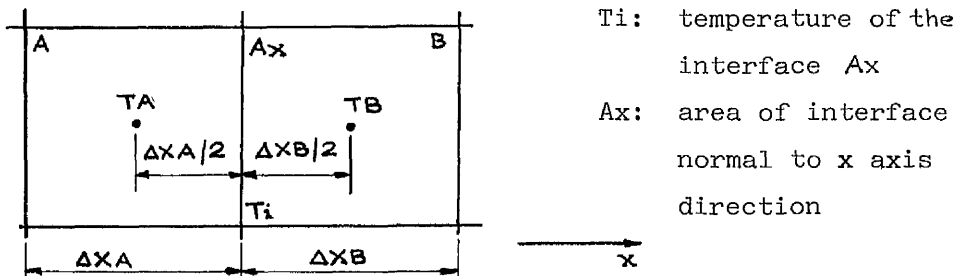


Fig. 3.4

By convention the two nodes of the control volumes, where the temperatures are calculated, are at distance from their common interface half the size of their control volume along the  $x$  axis direction. The nodes are represented in Fig. 3.4 by dots.

The energy balance at the interface is:

$$\vec{Q}_A + \vec{Q}_B + Q_{ra} + Q_{st} = 0 \quad (3.16)$$

where  $\vec{Q}_A$  is the heat flux because of the temperature gradient between the interface and the adjacent region of the control volume A.

$$\vec{Q}_A = -\lambda_{Ai} * A_x * (\partial T / \partial x)_i \quad (3.17)$$

where  $\lambda_{Ai}$  is the thermal conductivity of the material of control volume A at the interface.

$\vec{Q}_B$  is the heat flux because of the temperature gradient between

the interface and the adjacent region of the control volume B.

$$\vec{Q_B} = + \lambda_{Bi} * A_x * (\partial T / \partial x)_i \quad (3.18)$$

where  $\lambda_{Bi}$  is the thermal conductivity of the material of control volume B at the interface. In both cases of heat fluxes  $\vec{Q_A}$  and  $\vec{Q_B}$  the arrow shows the direction of heat flux along the axis x.

$Q_{ra}$  is the net radiation exchange of the interface with the environment. For example:

$$Q_{ra} = A_{Bi} * A_x * q_{in} - E_i * A_x * \epsilon * (T_i)^4 \quad (3.19)$$

where  $A_{Bi}$  is the absorptivity of the interface.

$E_i$  is the longwave emissivity of the interface.

$q_{in}$  is the irradiance ( $W/m^2$ )

$Q_{ra}$  is positive for incoming radiation on the interface and negative for outgoing radiation from the interface.

$Q_{st}$  is the energy 'stored' by the interface. This can be, for example, the heat transferred by evaporation or condensation at a liquid surface

$$Q_{st} = Q_{ev} = -\dot{m}_{we} * A_x * h_{fg}(T_i) \quad (3.20)$$

$$\text{or} \quad Q_{st} = Q_{co} = \dot{m}_{wc} * A_x * h_{fg}(T_i) \quad (3.21)$$

where  $\dot{m}_{we}$ ,  $\dot{m}_{wc}$  is the evaporated or condensed mass flux respectively and  $h_{fg}(T_i)$  is the associated latent heat of the liquid.

If we write:

$$q_i = (Q_{ra} + Q_{st}) / A_x \quad (3.22)$$

the initial energy balance at the interface has the following form,

$$q_i * A_x + \vec{Q_A} + \vec{Q_B} = 0$$

Discretizing the expressions of heat fluxes  $\vec{Q_A}$  and  $\vec{Q_B}$  assuming a linear temperature profile between the nodes and the interface, we obtain:

$$\vec{Q_A} = -\lambda_{Ai} * A_x * (T_i - T_A) / (\Delta X_A / 2) \quad (3.23)$$

$$\vec{Q_B} = +\lambda_{Bi} * A_x * (T_B - T_i) / (\Delta X_B / 2) \quad (3.24)$$

Putting  $h_{Ai} = 2 * \lambda_{Ai} / \Delta X_A$  (3.25),  $h_{Bi} = 2 * \lambda_{Bi} / \Delta X_B$  (3.26)

$$\text{we obtain } q_i * A_x + h_{Ai} * A_x * (T_A - T_i) + h_{Bi} * A_x * (T_B - T_i) = 0 \quad (3.27)$$

The  $h_{Ai}$  or  $h_{Bi}$  could be the conventional heat transfer coefficient of convection between the interface of temperature  $T_i$  and the liquid of temperature  $T_A$  or  $T_B$  respectively.

So from the last relation, we take

$$T_i = (h_{Ai} * T_A + h_{Bi} * T_B + q_i) / (h_{Ai} + h_{Bi}) \quad (3.28)$$

and

$$\vec{Q_A} = (h_{Ai} * h_{Bi} * A_x * (T_A - T_B)) / (h_{Ai} + h_{Bi}) - (q_i * h_{Ai} * A_x) / (h_{Ai} + h_{Bi}) \quad (3.29)$$

$$\vec{Q_B} = (h_{Ai} * h_{Bi} * A_x * (T_B - T_A)) / (h_{Ai} + h_{Bi}) - (q_i * h_{Bi} * A_x) / (h_{Ai} + h_{Bi}) \quad (3.30)$$

Again it is emphasised that using the above expressions for the heat flux at every interface of a control volume during the discretization of the energy differential equations problems of discontinuity are readily overcome and the line-by-line solution procedure can be used without any difficulty.

In the general case the quantities  $h_{Ai}$ ,  $h_{Bi}$ ,  $q_i$  depend on the temperature  $T_i$  of the interface. Therefore giving a first estimate to the temperature of the interfaces the quantities  $h_{Ai}$ ,  $h_{Bi}$ ,  $q_i$ , the temperatures of the grid nodes and finally the temperature of the interfaces are calculated. This procedure is repeated until convergence is achieved for the grid node temperatures.

If the quantities  $h_{Ai}$ ,  $h_{Bi}$ ,  $q_i$ , are independent of the interface temperature  $T_i$ , the above mentioned first estimate and the following calculation of the interface temperature  $T_i$  is not necessary. The calculation of the temperatures of the nodes is performed only once.

The above mentioned calculation of the interface temperature is achieved in the computing program of this thesis by using the Newton-Raphson technique with the appropriate equation derived from relation (3.28).

An example of an air-gap discontinuity is given in Appendix K.

### 3.1.5 The complete difference equations for the transwall module

The present analysis is referred to transwall modules in the vertical position. A typical transwall module is shown in Fig. 3.5. The thick line is the boundary of the system and defines the domain of interest. The particular shape of this typical transwall module allows the domain of interest to be filled with control volumes of parallelepiped shape. (Fig. 3.6). The nodes being at the geometric centre, form a grid with its lines parallel to the three cartesian co-ordinate axes. The number of the control volumes which form the transwall module are NIT, NJT and NKT along the x, y and z axis respectively. In the present work as can be seen from Fig. 3.5

NIT = 8

NJT = 5

NKT = 8

The temperature is calculated at each node of these control volumes. The number of control volumes in the convection region are

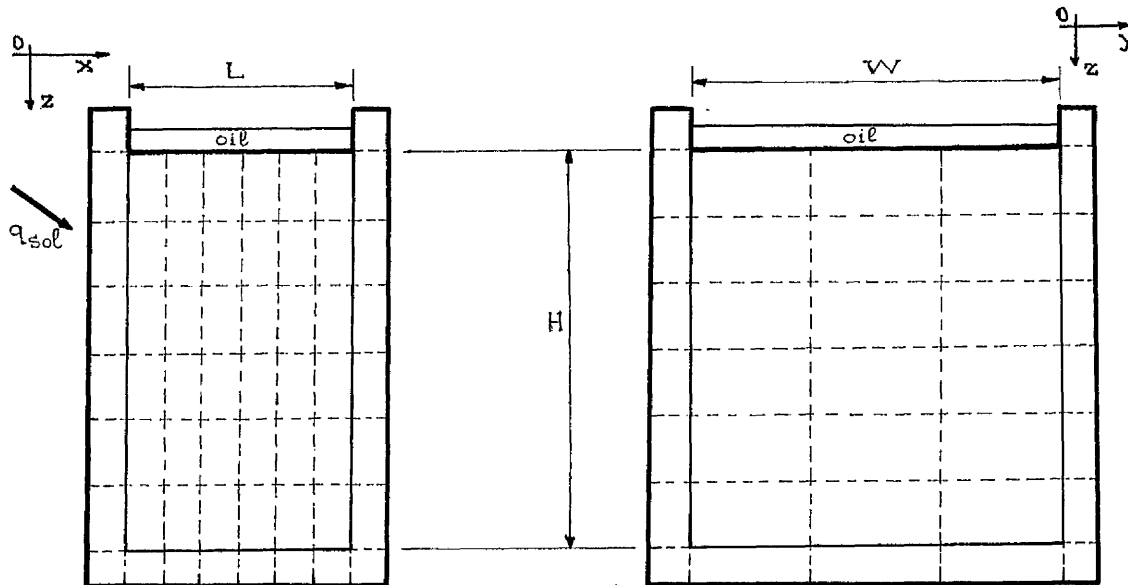


Fig. 3.5

NI, NJ and NK along the x, y and z axis respectively. In the present work:

$$NI = 6$$

$$NJ = 3$$

$$NK = 6$$

The pressure is calculated at the nodes of these control volumes.

The adoption of a displaced grid for each component of velocity is translated into the following number of nodes:

For the velocity component  $u$ , along the x axis, the number of nodes are NI1, NJ and NK along the x, y and z axis respectively. where,  $NI1 = NI + 1$ .

For the velocity component  $v$ , along the y axis, the number of nodes are NI, NJ1 and NK along the x, y and z axis respectively. where,  $NJ1 = NJ + 1$ .

For the velocity component  $w$ , along the z axis, the number of nodes are NI, NJ and NK1 along the x, y and z axis respectively. where,  $NK1 = NK + 1$ .

The velocity component  $u$  is calculated at the nodes (I, J, K), where  $I = 2$  to NI,  $J = 1$  to NJ,  $K = 1$  to NK.

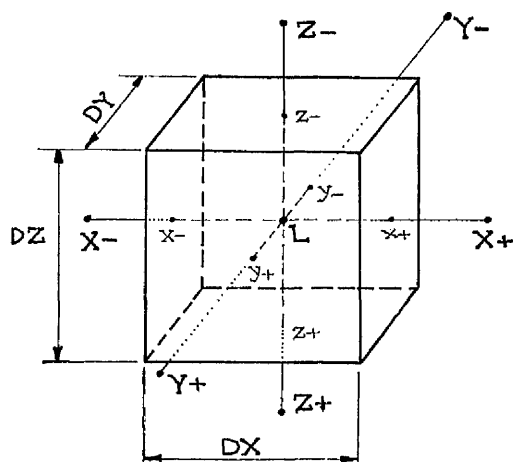
The velocity component  $v$  is calculated at the nodes (I, J, K), where  $I = 1$  to NI,  $J = 2$  to NJ,  $K = 1$  to NK.

The velocity component  $w$  is calculated at the nodes (I, J, K), where  $I = 1$  to NI,  $J = 1$  to NJ,  $K = 2$  to NK.

The nodes  $(I, J, K)$  of the velocity component  $u$  for  $I = 1$  or  $NI$ ,  $J = 1$  to  $NJ$ ,  $K = 1$  to  $NK$ , of the velocity component  $v$  for  $I = 1$  to  $NI$ ,  $J = 1$  or  $NJ$ ,  $K = 1$  to  $NK$  and of the velocity component  $w$  for  $I = 1$  to  $NI$ ,  $J = 1$  to  $NJ$ ,  $K = 1$  or  $NK$  belong to the boundary of the convection region. All the components of velocity at this boundary are of zero value. This is true for all the boundary except for the interface between the liquid and oil. A more accurate approach could require the treatment of the momentum fluxes at this interface.

However to generalize the computing program it has been constructed in such a way that the velocity components at the boundary of the convection region can be of any value. This allows the program to be used easily for many other types of flow, for example forced convection or natural convection with inflows and outflows from the transwall module.

A typical parallelepiped control volume is shown in Fig. 3.6



control volumes (nodes)

L       $(I, J, K)$   
 X+     $(I + 1, J, K)$   
 X-     $(I - 1, J, K)$   
 Y+     $(I, J + 1, K)$   
 Y-     $(I, J - 1, K)$   
 Z+     $(I, J, K + 1)$   
 Z-     $(I, J, K - 1)$

$DX, DY, DZ$  are the dimensions of the control volume  $L$ .

Fig. 3.6

The discretization procedure outlined before, applied to the energy and momentum differential equations gives the following general-difference equation of the dependent variable  $\phi$  for each control volume  $(I, J, K)$ :

$$APC(I, J, K) * \phi(I, J, K) = AP1(I, J, K) * \phi(I+1, J, K) + AP2(I, J, K) * \phi(I-1, J, K) + AP3(I, J, K) * \phi(I, J+1, K) + AP4(I, J, K) * \phi(I, J-1, K) + AP5(I, J, K) * \phi(I, J, K+1) + AP6(I, J, K) * \phi(I, J, K-1) + BPC(I, J, K) \quad (3.31)$$

where  $APC(I, J, K)$ ,  $AP1(I, J, K)$ ,  $AP2(I, J, K)$ ,  $AP3(I, J, K)$ ,  $AP4(I, J, K)$ ,  $AP5(I, J, K)$ ,  $AP6(I, J, K)$  and  $BPC(I, J, K)$  are coefficients. All the values of the dependent variable  $\phi$  correspond to time  $t + \Delta t$ . The value of  $\phi^0(I, J, K)$  at time  $t$  has been absorbed in  $BPC(I, J, K)$ .

Some of the terms of the right side of the equation may not exist at all because, simply, control volumes are not defined for the corresponding sides of the control volume (I,J,K). Then information concerning the corresponding interface of the control volume (I,J,K) is absorbed in  $BPC(I,J,K)$ .

An estimate,  $P^*(I,J,K)$ , of the pressure field, produces a preliminary velocity field  $u^*(I,J,K)$ ,  $v^*(I,J,K)$ ,  $w^*(I,J,K)$  from the solution of the corresponding velocity component difference equations. The superscript \* is used to denote that the values at time  $t+\Delta t$  are simply estimates.

The true pressure  $P(I,J,K)$  is related to the estimated pressure  $P^*(I,J,K)$  by:

$$P(I,J,K) = P^*(I,J,K) + PC(I,J,K) \quad (3.32)$$

where  $PC(I,J,K)$  is the so called pressure correction.

On the other hand the true velocity components are connected to the estimated values via

$$u(I,J,K) = u^*(I,J,K) - \frac{DY(J+NY)*DZ(K+NZ) * (PC(I,J,K)-PC(I-1,J,K))}{APU(I,J,K)} \quad (3.33)$$

$$v(I,J,K) = v^*(I,J,K) - \frac{DX(I+NX)* DZ(K+NZ)*(PC(I,J,K)-PC(I,J-1,K))}{APV(I,J,K)} \quad (3.34)$$

$$w(I,J,K) = w^*(I,J,K) - \frac{DX(I+NX)*DY(J+NY)* (PC(I,J,K)-PC(I,J,K-1))}{APW(I,J,K)} \quad (3.35)$$

where  $DX$ ,  $DY$ ,  $DZ$  are the dimensions of each parallelepiped control volume along the  $x$ ,  $y$  and  $z$  axis respectively. (See Fig. 3.6 )

$NX$ ,  $NY$ ,  $NZ$  are the number of the control volumes in the conduction region before the convection region, along the  $x$ ,  $y$  and  $z$  axis respectively. In this work,  $NX=1$ ,  $NY=1$  and  $NZ=1$ , as seen in Fig. 3.5.

$APU$ ,  $APV$ ,  $APW$  are the coefficients  $APC$  of the general-difference equation (3.31) for the velocity components,  $u$ ,  $v$  and  $w$ , respectively.

Substituting from equations (3.33), (3.34) and (3.35) for the  $u(I,J,K)$ ,  $v(I,J,K)$  and  $w(I,J,K)$  in the finite-difference equation of the continuity equation a finite difference equation of the same type as (3.31) is obtained where the variable  $\phi$  represents now the pressure correction  $PC$ .

The solution of the set of all the equations (3.31) (energy, momentum, pressure correction) and equations (3.32) to (3.35) will provide the values of the dependent variables of temperature  $T$ , pressure  $P$ , and velocity,  $u$ ,  $v$  and  $w$  at the instant  $t + \Delta t$  at each node. The calculation of the coefficients of these equations requires the knowledge of:

- (a) The values of the previously mentioned dependent variables  $T^0$ ,  $u^0$ ,  $v^0$  and  $w^0$  at time instant  $t$ , at each node.
- (b) The properties of density  $\rho$ , constant volume and constant pressure specific heat capacity  $c_v$ ,  $c_p$ , thermal conductivity  $\lambda$  and the first coefficient of viscosity  $\mu$  as functions of temperature.
- (c) The dimensions  $DX$ ,  $DY$ ,  $DZ$  of each control volume.
- (d) The radiation<sup>†</sup> absorbed by each control volume.
- (e) The value of each velocity component at the boundary of the convection region.

The heat balances at the outer boundary of the transwall module (the thick line of Fig. 3.5) and the boundary of the convection region also require:

- (f) The heat transfer coefficient  $h$  between the ambient air and the outer boundary of the transwall system, the longwave radiation ( $\lambda > 4.1\mu\text{m}$ ) falling on this boundary  $q$  and the emissivity  $E$  of the boundary.
- (g) The radiation absorbed by the boundary of the convection region QIN in the case where the absorption of part of the radiation by the water can be considered as a surface phenomenon.

### 3.1.6 The solution of the set of the difference equations

The total set of the finite difference equations consists of six main sub-sets, with each sub-set corresponding to a particular dependent variable: The three momentum equations sub-sets for each velocity component, the pressure correction sub-set for the pressure correction, the sub-set of equations (3.32) to (3.35) for the pressure and each component of velocity, and the sub-set of energy equation for the temperature. Although these equations are in a nominally linear form, they are generally non-linear and interlinked.

The solution of the total set is not a simultaneous one but a sequential one, where successively the sub-sets of equations are solved. The solution of the momentum, pressure correction and energy equations sub-sets is not generally performed by a direct method but by the line-by-line iterative method.

According to the line-by-line method, it is assumed that the values of the dependent variable of equation (3.31) for the nodes along one grid line are unknowns, but that those for the nodes along the four

+ Radiation wavelength  $0.3\mu\text{m}$  to  $4.1\mu\text{m}$ .

neighbouring lines are known. In the case of the 3-dimensional transwall module, there are three grid lines parallel to the three Cartesian co-ordinate axes. Then, the equation (3.31) takes the following form:

$$B(M) * \phi(M) = A(M) * \phi(M+1) + D(M) \quad \text{for } M=1 \quad (3.36)$$

$$B(M) * \phi(M) = A(M) * \phi(M+1) + C(M) * \phi(M-1) + D(M) \quad \text{for } M=2 \text{ to } (MD-1) \quad (3.37)$$

$$B(M) * \phi(M) = C(M) * \phi(M-1) + D(M) \quad \text{for } M=MD \quad (3.38)$$

where, MD is the number of nodes along the line with the unknown value of the dependent variable  $\phi$ .

It is then easy to solve directly this system of MD equations with MD unknowns ( $MD \gg 3$ ) using the well known tri-diagonal-algorithm. The computing listing of this algorithm is given in Appendix 0.

For the values of  $\phi$  along the neighbouring lines (which have been considered to be temporarily known), the best estimates are simply used, which are the values from the previous iteration. In this manner we traverse along all lines in one direction, then, using the resulting solution as the best estimate, the process is repeated along the second direction and finally the same operation is performed along the third direction.

A discussion on the merits of the line-by-line method for the solution of a set of non-linear and interlinked equations and comparison with other direct and alternative methods is given by Patankar (67), (68).

In the case of the present problem of the transwall module, the following procedure has been followed, similar to the SIMPLE Algorithm suggested by Patankar (67), (68):

- (i) Provide initial estimates of all the variables, pressure  $P^*$ , temperature  $T^*$  and velocity components  $u^*$ ,  $v^*$ ,  $w^*$  at time  $t+\Delta t$ .
- (ii) Calculate those quantities like density of the liquid, thermal capacity etc. that depend on the previous variables.
- (iii) Solve the momentum equations, cast in form of equation (3.31), to obtain new estimates of  $u^*$ ,  $v^*$ ,  $w^*$  at time  $t+\Delta t$ , sequentially.
- (iv) Solve the pressure correction equation to obtain the pressure correction PC.
- (v) Calculate the pressure P from equation (3.32) and the corrected velocities u, v and w from the equations (3.33), (3.34), (3.35), respectively.
- (vi) Repeat steps (ii) to (v) another time and then go to step (vii).
- (vii) Solve the energy equation and obtain the temperature T.



(viii) Calculate temperatures at certain boundaries as from equation (3.28).

(ix) Regard the new values of the five dependent variables as improved estimates and return to step (ii).

Repeat until convergence.

In the solution of the total set of equations or of a sub-set of it by the line-by-line iterative method, divergence problems may be overcome by an under-relaxation process. Patankar discusses various under-relaxation schemes in (68) and (71).

Numerical examples have shown that the convergence of the line-by-line iterative method depends on the relative magnitude of all the coefficients APC,  $AP_i$  ( $i=1$  to 6) and BPC of the sub-set of equations (3.31), page 154. These coefficients are always non-negative.

The relative increase of the coefficients APC in relation to the coefficients  $AP_i$  and BPC increases the possibility for convergence of the line-by-line iterative method. If convergence exists, it also increases the rate of convergence. On the other hand the relative increase in the absolute value of BPC in relation to the other coefficients slows this convergence. (A numerical example is given in Appendix M). Indeed studying the various under-relaxation schemes, somebody could recognise the mentioned numerical findings on the importance of the relative magnitude of the coefficients APC,  $AP_i$  and BPC: In both schemes, of under-relaxation factor  $\alpha'$  ( $\alpha' < 1$ ),

$$(APC/\alpha') * \phi_p = \sum_{i=1}^6 (AP_i * \phi_i) + BPC + (1-\alpha') * (APC/\alpha') * \phi'_p$$

and of inertia  $s$

$$(APC+s) * \phi_p = \sum_{i=1}^6 (AP_i * \phi_i) + BPC + s * \phi'_p$$

the objective is the increase of the APC coefficients. But, the possible simultaneous relative increase in the absolute value of BPC coefficients may decrease the benefit of the increase of the APC coefficients.

The same features of the two mentioned under-relaxation schemes are apparent in the case of the negative slope linearization of the source term, BPC. On the other hand, the under-relaxation schemes concerning the various auxiliary variables, e.g. density, viscosity, etc. or the source term, tend actually to favour the relative magnitude of the APC coefficients by trying to "conserve" the old relative magnitude of the various coefficients. Finally, the simplest way of under-relaxation using shorter time steps increases explicitly the magnitude of the APC coefficients.

Comparing the energy and momentum finite-difference equations with the pressure correction equation an inherent disadvantage can be seen in the procedure used in respect of the relative magnitude of the coefficients APC, API, BPC for unsteady flows. This also applies to the SIMPLE and SIMPLER Algorithms, introduced by Patankar. This disadvantage is due to the presence of time step  $\Delta t$  in the denominator only of the APC coefficients of the momentum and energy finite-difference equations and not of the pressure-correction equations (or the pressure equations for the SIMPLER Algorithm). In addition to this, the time step  $\Delta t$  is present in the denominator of one of the terms of the BPC coefficients of the pressure-correction or pressure equations for compressible flows. This means that moderate time steps enhance only the possibility of convergence (or faster convergence) of the momentum and energy equations and have an inverse effect on the convergence of the pressure-correction (or pressure) equations in the line-by-line iterative solution. The divergence of the line-by-line iterative solution of the sub-set of the pressure correction equations was experienced in the first attempts to apply the SIMPLE Algorithm in the case of the transwall module for very moderate time steps of 1 sec. These time steps were sufficient to secure the convergence of the solution of the sub-sets of the momentum and energy equations. Suggested (Patanekar (71)) relaxation factors of  $a' = 0.5$  for the momentum finite-difference equations and  $a_p = 0.8$  for the pressure-correction equation did not work. The absence of an unconditional guarantee that under-relaxation schemes would always allow iterative methods to give convergence led to the adoption of the Gauss elimination method for the direct solution of the sub-set of pressure-correction equations. The disadvantages of storage and time are evident in using the direct method (in comparison with the line-by-line iterative method). The subroutine GAUSS had been constructed according to the flow diagram for the Gauss elimination method given by Stoecker (72). Although the NAG-direct method subroutines may give more accurate solutions they were not used because of larger storage requirements.

### 3.2 EFFECTIVE CONDUCTIVITY

#### 3.2.1 The definition

The concept of effective conductivity arises when the performance of a thermal system is expressed by one diffusion differential equation,

$$\frac{\partial(\rho c_v T_s)}{\partial t} = \text{div} (\lambda_{ef} \text{ grad } T_s) + q_{us} \quad (3.39)$$

instead of a more complex system of differential and algebraic equations, e.g. the one consisting of equations (3.1) to (3.5). This simplified approach implies that the effective conductivity is a function of many parameters. It has two main advantages over the complex approach:

1. For engineering-design calculations there is no need to know the values of all dependent variables on which the thermal performance of the system depends. Interest is mainly concentrated on the determination of the energy stored and absorbed (or produced) by the system and the energy exchanged with the environment of the thermal system.
2. Saving in computing time. The experience of solving complicated systems of differential and algebraic equations with the present computers shows that the required computing time is usually too large to predict numerically the thermal performance of the transwall for real time periods of hours, days or months. The numerical prediction of the thermal performance over long periods of real time is actually achieved only by the simplified equation (3.39) if a successful expression of the effective conductivity,  $\lambda_{ef}$ , can be obtained.

Experimental or numerical ways can be found to establish a general expression of the effective conductivity,  $\lambda_{ef}$ , as a function of some basic parameters and conditions. A number of researchers have used the experimental method to find the effective conductivity of cylindrical, spherical or plane layers of a fluid confined between a hot and a cold surface for steady state free convection. A summary of these results is presented by Eckert et.al. (42) and Kutateladze et.al (63) where the ratio of the effective conductivity to the actual thermal conductivity of the fluid is given as a function of the Rayleigh number, based on the thickness of the layer and on the temperature difference between the hot and cold surfaces. According to Kutateladze et.al (63) the geometry of the fluid layers is also crucial in determining this ratio.

In this thesis numerical ways of predicting the effective conductivity  $\lambda_{ef}$  are discussed and one of them is used to calculate the effective conductivity,  $\lambda_{ef}$ , inside transwall modules. It should be stressed that the computational procedure is related to the control volume method and its associated assumptions used for the discretization of the various terms of the differential equations. In this respect the calculation of the effective conductivity,  $\lambda_{ef}$ , concerns values at the interfaces of control volumes.

### 3.2.2 Effective conductivity at a control volume boundary, at which there is no production or storage of energy.

First of all the domain of interest is separated into control volumes. Over each of these control volumes the energy equation,

$$\frac{\partial(\rho \cdot c_v \cdot T)}{\partial t} + \text{div}(\vec{G} \cdot c_p \cdot T) = \text{div}(\lambda \cdot \text{grad } T) + q_u \quad (3.40)$$

is to be integrated. This is just one differential equation of the system of the differential and algebraic equations, the solution of which will allow the calculation of the effective conductivity  $\lambda_{ef}$  from the equation

$$\frac{\partial(\rho \cdot c_v \cdot T_s)}{\partial t} = \text{div}(\lambda_{ef} \cdot \text{grad } T_s) + q_{us} \quad (3.41)$$

This differential equation is integrated over control volumes,  $S$ , each generally consisting of a number of the control volumes made for the integration of the energy equation (3.40). So in Fig.3.7 the control volume  $S$ , with volume  $\Delta V_s$ , consists of  $n_s$  smaller control volumes. If  $\Delta V_i$  is the volume of the small control volume  $i$  then,  $\Delta V_s = \sum_{i=1}^{n_s} \Delta V_i$  (3.42)

In the same figure the area  $A_s$  of the control volume  $S$  also consists of the  $\kappa_s$  smaller areas that are common interfaces of  $\kappa_s$  pairs of smaller control volumes, with one part of the pair inside and the other part outside the control volume  $S$ . If  $A_j$  is the area of the common interface  $j$  of the pair  $j$  of the smaller control volumes, then  $A_s = \sum_{j=1}^{\kappa_s} A_j$  (3.43)

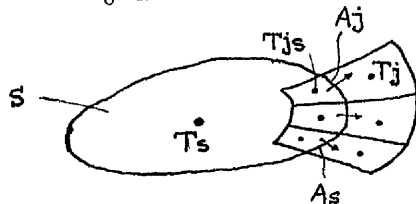


Fig.3.7

Integration of equation (3.41) over the control volume S according to the discretization method of section 3.1.3 gives the source term,  $q_{us} \Delta V_s$ , the unsteady term,

$$((p \cdot c_v)_{Ts} \cdot Ts - (p \cdot c_v)_{Ts}^0 \cdot Ts^0) \Delta V_s / \Delta t$$

and diffusion fluxes. For example for surface  $A_s$ , the diffusion flux will be,  $\sum_{j=1}^{k_s} U A_s A_j (T_j - Ts)$  where  $U A_s$  is the conductance at the surface  $A_s$ .

Conservation of the absorbed (or produced) energy inside the control volume S, requires

$$q_{us} = \left( \sum_{i=1}^{n_s} q_{ui} \Delta V_i \right) / \Delta V_s \quad (3.44)$$

Conservation of the energy stored in the control volume S, requires

$$(p \cdot c_v)_{Ts} \cdot Ts = \left( \sum_{i=1}^{n_s} (p \cdot c_v)_{Ti} \cdot T_i \Delta V_i \right) / \Delta V_s \quad (3.45)$$

where  $T_i$  is the temperature of the individual control volume  $i$ .

From this equation the temperature  $T_s$  of the control volume S is calculated. Finally, conservation of the exchanged energy of control volume S through the surface  $A_s$ , assuming that only convection and possibly diffusion fluxes exist at the small areas  $A_j$ , gives the following relation:

$$U A_s \sum_{j=1}^{k_s} A_j (T_j - Ts) = - \sum_{j=1}^{k_s} G A_j \cdot c_{p A_j} \cdot A_j \cdot T A_j + \sum_{j=1}^{k_s} \lambda_{A_j} \cdot (\partial T / \partial x)_{A_j} \cdot A_j \quad (3.46)$$

$$\text{where } G A_j = \vec{G} \cdot \vec{e}_j \quad (3.47a) \quad \text{and} \quad (\partial T / \partial x)_{A_j} = \overline{\text{grad } T} \cdot \vec{e}_j \quad (3.47b)$$

and  $\vec{e}_j$  is the unit vector normal to surface  $A_j$  towards the surrounding environment. All the values of the quantities of the right side of equation (3.46), are referred to values at the boundary  $A_j$ . The expression of  $T A_j$  and  $(\partial T / \partial x)_{A_j}$  with the temperatures  $T_j$ s and  $T_j$  is discussed in section 3.1.4.

The calculation of the effective conductivity  $(\lambda_{ef})_{A_s}$  requires the definition of an appropriate distance  $\delta$ . Then,

$$(\lambda_{ef})_{A_s} = U A_s \cdot \delta \quad (3.48)$$

A possible distance  $\delta$  for parallelepiped control volumes is shown in Fig.3.8

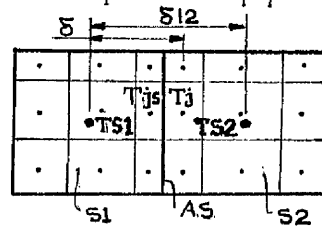


Fig.3.8

If equations (3.44) to (3.48) are applied not only to the control volume S1 but also to the control volume S2, then the effective

conductivity at the interface As is calculated from the following equation

$$(\lambda_{ef})_{As} = \left( \sum_{j=1}^{k_s} GA_j * c_{pAj} * A_j * TA_j + \sum_{j=1}^{k_s} \lambda_{Aj} * (\partial T / \partial x)_{Aj} * A_j \right) / (A_s * (TS_2 - TS_1) / \delta_{12}) \quad (3.49)$$

### 3.2.3 Effective conductivity at the interface of two control volumes, without convection across it.

The heat fluxes  $\overline{QA}$  and  $\overline{QB}$  at the interface of the control volumes A and B of Fig. 3.4 of section 3.1.4 can be written in the following way:

$$\overline{QA} = (\lambda_{ef})_{Ai} * (TA - TB) * A_x / ((\Delta X_A + \Delta X_B) / 2) \quad (3.50)$$

$$(\lambda_{ef})_{Ai} = \left( (\Delta X_A + \Delta X_B) / 2 \right) * h_{Ai} * h_{Bi} / (h_{Ai} + h_{Bi}) - \left( (\Delta X_A + \Delta X_B) * q_i * h_{Ai} / (2 * (TA - TB) * (h_{Ai} + h_{Bi})) \right) \quad (3.51)$$

$$(\lambda_{ef})_{Bi} = \left( (\Delta X_A + \Delta X_B) / 2 \right) * h_{Ai} * h_{Bi} / (h_{Ai} + h_{Bi}) - \left( (\Delta X_A + \Delta X_B) * q_i * h_{Bi} / (2 * (TB - TA) * (h_{Ai} + h_{Bi})) \right)$$

$$Ti = (h_{Ai} * TA + h_{Bi} * TB + q_i) / (h_{Ai} + h_{Bi})$$

$$Ti = (h_{Ai} * TA + h_{Bi} * TB + q_i) / (h_{Ai} + h_{Bi})$$

The definition of the various quantities of the above three equations is given in section 3.1.4. It should be remembered that these equations have been constructed under the assumption of a linear variation in temperature between the interface temperature  $T_i$  and the node temperatures  $TA$  and  $TB$ . The simultaneous solution of these three equations gives the values of  $(\lambda_{ef})_{Ai}$  and  $(\lambda_{ef})_{Bi}$ .

### 3.2.4 Examples of numerical prediction of the effective conductivity in the case of various transwall modules.

The procedure for calculating the effective conductivity at a control volume boundary at which there is no production or storage of energy is applied to four different cases, each one corresponding to four different size transwall modules of the same shape as the module of Fig. 3.9. The effective conductivity is calculated at four surfaces, normal to the x direction, shown in Fig. 3.9.

The dimensions of each transwall module necessary for the construction of the control volumes S (Fig. 3.9) over which the differential equation (3.41) is integrated, are given in Table 3.1. This table also gives the dimensions of the control volumes (Fig. 3.5) over which the differential equation (3.40) is integrated.

Table 3.1

Dimensions of transwall modules (cm). Irradiance ( $\text{mW}/\text{cm}^2$ ) on the module. DX, DY and DZ the control volumes dimensions along the x, y and z axis, respectively.

	case 1	case 2	case 3	case 4	<u>DX(I)</u>	case 1	case 2	case 3	case 4
$q_{\text{sol}}$	38.60	49.74	49.74	49.74	I = 1	0.40	0.40	0.40	0.60
L	7.4	7.4	7.4	15.0	2	1.20	1.20	1.20	1.20
H	23.72	47.44	60.00	56.70	3	1.24	1.24	1.24	3.00
H/L	3.21	6.41	8.11	3.78	4	1.24	1.24	1.24	3.30
W	18.80	18.80	18.80	31.00	5	1.24	1.24	1.24	3.30
L0	0.40	0.40	0.40	0.60	6	1.24	1.24	1.24	3.00
L1	1.20	1.20	1.20	1.20	7	1.24	1.24	1.24	1.20
L2	4.96	4.96	4.96	12.60	8	0.40	0.40	0.40	0.60
L3	1.24	1.24	1.24	1.20	<u>DZ(K)</u>	case 1	case 2	case 3	case 4
H1	0.60	0.60	0.60	0.60	K = 1	0.68	0.68	0.68	2.50
H2	0.68	0.68	0.68	2.50	2	3.95	7.00	9.00	8.00
Lw	0.60	0.60	0.60	0.60	3	3.95	7.00	10.00	9.50
<u>DY(J)</u>	case 1	case 2	case 3	case 4	4	3.96	9.72	11.00	10.85
J = 1	0.60	0.60	0.60	0.60	5	3.96	9.72	11.00	10.85
2	6.26	6.26	6.26	10.00	6	3.95	7.00	10.00	9.50
3	6.28	6.28	6.28	11.00	7	3.95	7.00	9.00	8.00
4	6.26	6.26	6.26	10.00	8	0.60	0.60	0.60	0.60
5	0.60	0.60	0.60	0.60					

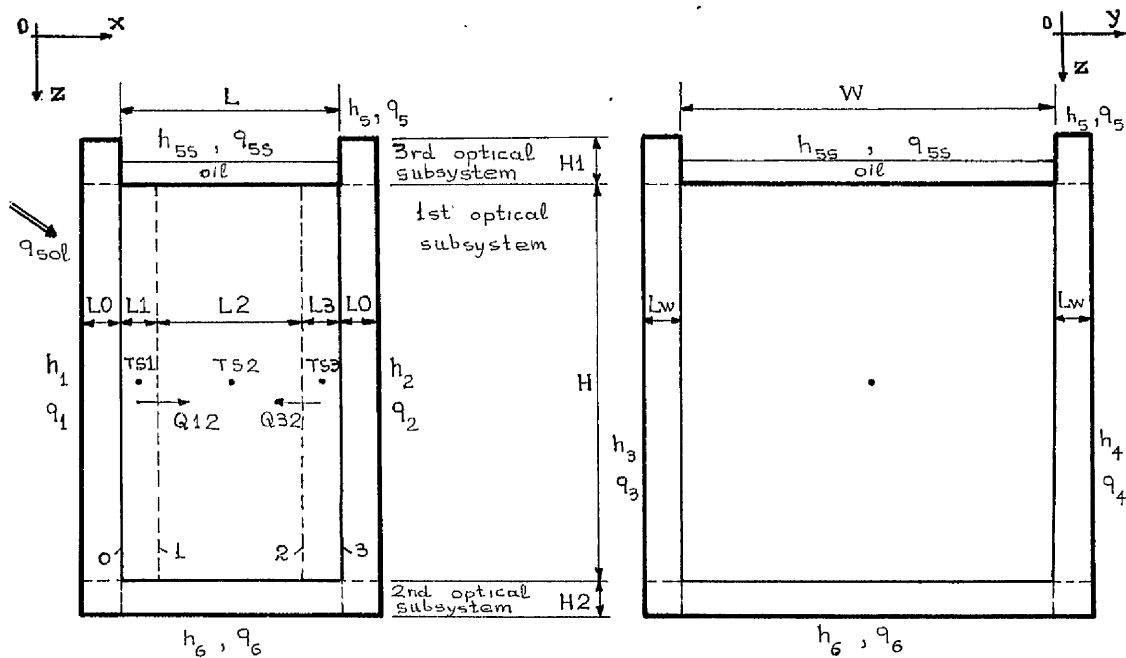


Fig.3.9

Thermal properties, emissivity and viscosity:

The values of density  $\rho$ , specific heat capacity  $c$ , thermal conductivity  $\lambda$  and emissivity  $E$  of the annealed float glass from Pilkington Ltd. at  $20^\circ$  have been used for the conduction region (Table 3.2) and of saturated water at 1atm (14) for the convection region (Table 3.3). In the present numerical analysis it was assumed that the constant volume and constant pressure specific heat capacity of water were equal. Their difference is very small, for example, of the order of 0.7% at  $20^\circ\text{C}$ .

Table 3.2

Properties of annealed float glass at  $20^\circ\text{C}$ .

Density $\text{gr/cm}^3$	Specific heat capacity $\text{mJ/gr}\cdot\text{K}$	Conductivity $\text{mW/cm}\cdot\text{K}$	Emissivity $E$
2.498	770.0	10.0	0.84

Table 3.3

Properties of saturated water at 1 atm.

Temperature $^\circ\text{C}$	Density $\text{gr/cm}^3$	Heat capacity $\text{mJ/gr} \cdot \text{K}$	Conductivity $\text{mW/cm} \cdot \text{K}$	Emissivity
15.56	0.9986	4186.0	5.96	0.96
21.11	0.9974	4179.0	6.04	
26.67	0.9958	4179.0	6.14	
32.22	0.9949	4174.0	6.23	

The temperature  $T$  dependent first coefficient of viscosity is calculated from the following relations, given in the C.R.C. Handbook of Chemistry and Physics (70).

$$\begin{aligned} T \leq 20^\circ\text{C} \quad \mu &= 10^i \quad \text{gr/}(\text{cm}\cdot\text{sec}) \\ T > 20^\circ\text{C} \quad \mu &= 0.01002 * 10^i \quad \text{gr/}(\text{cm}\cdot\text{sec}) \end{aligned}$$

where,

$$i = \frac{1301.0}{998.333 + 8.1855*(T-20.0) + 0.00585*(T-20.0)^2} - 3.3023$$

$$i = \frac{1.3272*(T-20.0) - 0.001053*(T-20.0)^2}{T+105.0}$$

and  $T$  in  $^\circ\text{C}$



Radiation<sup>+</sup>absorption:

Assuming only volumetric radiation absorption, the radiation, QIN, absorbed at the convection region boundary is zero. Certainly, this is not the case for the longwave fraction of the radiation ( $\lambda > 2.1 \mu\text{m}$ ) reaching the glass-water interface, because its absorption by the water is rather more a surface than a volumetric phenomenon.

In the present analysis the fraction of radiation absorbed by each control volume of the transwall module is calculated by using the 1-dimensional technique (section 1.1) which neglects edge effects along the y and z directions. The transwall module optical system is separated into three different sub-systems (see Fig.3.9) and the technique is applied to each of them. Each sub-system consists of a number of layers along the x direction: The first of one layer of glass, six layers of liquid and one layer of glass; the second of eight layers of glass; the third of one layer of glass, six layers of air and one layer of glass (neglecting the thin layer of floating oil). The number of the layers of each sub-system is NIT (=8) equal to the number of the control volumes. The control volume (I,J,K) belongs to the layer I of the corresponding optical sub-system. Table 3.4 gives the thickness of the layers (that is the DX dimension of the control volumes) and the fraction of incident radiation absorbed by them for the transwall module of the first three cases. Similarly, Table 3.5 is referred to the transwall module of the fourth case. It was assumed that the glass was clear float glass from Pilkington Ltd. and that the radiation consisted only of a direct component with an angle of incidence of  $4.1^\circ$ . This is in agreement with the experimental situation in which the transwall module receives radiation from a solar simulator (section 3.4). The values of the fraction of incident radiation of Table 3.4 are referred to the spectrum which corresponds to voltage across the lamps of the simulator of 105 volts and of Table 3.5 to air-mass 2 spectrum.

The irradiance  $q_{\text{sol}}$  ( $\text{mW}/\text{cm}^2$ ) on the module of each case is given in Table 3.1. The radiation absorbed by the control volume (I,J,K) is:

$$\text{ABSO}(I,J,K) = q_{\text{sol}} * \text{DY}(J) * \text{DZ}(K) * P(I) \quad (\text{in mW})$$

where

$\text{DY}(J) * \text{DZ}(K)$ , is the area of the control volume normal to the x direction  
(in  $\text{cm}^2$ )

$P(I)$ , is the corresponding fraction of the absorbed energy.

+ Radiation wavelength  $0.3 \mu\text{m}$  to  $4.1 \mu\text{m}$

Table 3.4

Thickness of each layer - Fraction of radiation absorbed by each layer.  
Total incident radiation = 1. Spectrum corresponding to 105 volts across the simulator lamps.

layer number I →	1	2	3	4	5	6	7	8
thickness (cm) →	0.40	1.20	1.24	1.24	1.24	1.24	1.24	0.40
1 <sup>st</sup> subsystem, P1	0.102	0.164	0.026	0.014	0.009	0.007	0.006	0.033
2 <sup>nd</sup> subsystem, P2	0.100	0.228	0.158	0.109	0.078	0.057	0.043	0.012
3 <sup>rd</sup> subsystem, P3	0.102	0.0	0.0	0.0	0.0	0.0	0.0	0.001

Table 3.5

Thickness of each layer - Fraction of radiation absorbed by each layer.  
Total incident radiation = 1. Air-mass 2 spectrum.

layer number I →	1	2	3	4	5	6	7	8
thickness (cm) →	0.60	1.20	3.00	3.30	3.30	3.00	1.20	0.60
1 <sup>st</sup> subsystem, P1	0.124	0.143	0.035	0.012	0.008	0.007	0.003	0.030
2 <sup>nd</sup> subsystem, P2	0.122	0.165	0.216	0.106	0.055	0.031	0.009	0.004
3 <sup>rd</sup> subsystem, P3	0.0	0.0	0.0	0.0	0.0	0.0	0.0	0.006

Table 3.6

Heat transfer coefficient and incoming longwave radiation at the transwall module outer boundary. Radiation wavelength,  $\lambda > 4.1 \mu\text{m}$ .

According to Fig. 3.9	$h(\text{mW}/\text{cm}^2 \cdot \text{K})$	$q(\text{mW}/\text{cm}^2)$
boundary with the minimum x co-ordinate	$h_1 = 0.58$	$q_1 = 42.5$
boundary with the maximum x co-ordinate	$h_2 = 0.58$	$q_2 = 42.0$
boundary with the minimum y co-ordinate	$h_3 = 0.01$	$q_3 = 0.0$
boundary with the maximum y co-ordinate	$h_4 = 0.01$	$q_4 = 0.0$
boundary with the maximum z co-ordinate	$h_6 = 0.01$	$q_6 = 0.0$
boundary with oil over it	$h_{5S} = 0.10$	$q_{5S} = 0.0$
remaining boundary	$h_5 = 0.10$	$q_5 = 42.0$

Heat transfer coefficients and incoming longwave radiation<sup>†</sup>:

For each part of the outer boundary of the transwall module, as it can be seen in Fig. 3.9, a different heat transfer coefficient and incoming longwave radiation can be assigned. These are given in Table 3.6.

The initial conditions

For each case, the initial conditions for time zero were those of an isothermal module of 20°C, without any convection and radiation absorption. The initial pressure was the hydrostatic pressure of the liquid. The ambient temperature around the module was always constant at 20°C. The almost adiabatic conditions at the sides and bottom of the transwall modules led to much higher corresponding glass temperatures than those of the liquid. To some extent this effect was decreased by decreasing the fraction of radiation absorbed by the second optical subsystem (see Tables 3.4 and 3.5) after a certain number of time steps. The isothermal initial condition was adopted for two main reasons:

- a) It was impossible to know the temperature, velocity components and pressure at each control volume at the same time instant with the measurement system that was available.
- b) It allowed easy detection of numerical instabilities that might lead to divergence after few time steps, because only temperatures above 20°C were physically realistic.

Instabilities that might arise from a false expression of the interface value  $\phi_{x+}$  of the dependent variable  $\phi$  (static instability according to Roache (59)) were overcome by the hybrid scheme. Under-relaxation using moderate time steps (in all cases the time step was chosen as 1 sec) did not always secure convergence. Another source of instability was detected that might lead to divergence after some time steps. This was interpreted as the inaccuracy of the solution of the system of difference equations because of inappropriate computer precision and inappropriate convergence criterion limit. The former was overcome by using double precision. The latter by trial and error procedures. The convergence criterion used in the present iterative solution of the system of difference equations was the absolute value of the relative change between two successive iterations in the node values of the velocity components and the temperature to be smaller than certain convergence limits. The convergence limit for the temperature was not so important in respect to inaccuracies and a

<sup>†</sup>Radiation wavelength,  $\lambda > 4.1 \mu\text{m}$ .

value of  $0.001^{\circ}\text{C}$  was used. The convergence limit for the velocity components was important and a value of  $0.5 \cdot 10^{-6}$  cm/s was necessary - at least at the onset of the flow. As the time passed and the flow was more developed with larger values of velocity components, larger convergence limits could be used without the danger of divergence. The largest value of convergence limit used for the velocity components was  $0.7 \cdot 10^{-5}$  cm/s. It is obvious that larger convergence limits increased the number of results obtained for a certain computing time.

#### Discussion of the results

The results of the present analysis are presented via the so-called ratio of conductivity,  $(\lambda_{\text{ef}}/\lambda)$ . This is the ratio of the effective conductivity  $\lambda_{\text{ef}}$  to the actual thermal conductivity  $\lambda$ .

Interfaces 0 and 3 (Fig.3.9)

As was expected the ratio of conductivity at the glass-water interfaces 0 and 3 is always one because there is no convection normal to these interfaces.

$$(\lambda_{\text{ef}}/\lambda)_0 = 1 \quad (\lambda_{\text{ef}}/\lambda)_3 = 1$$

Interfaces 1 and 2 (Fig.3.9)

Pure conduction

For the first time steps (three or four) the computing program was allowed to run under the assumption of pure conduction inside the liquid of the transwall module. This allowed the establishment of temperature gradients and so density and pressure gradients inside the liquid which in turn were the driving forces for the velocity. The ratio of conductivity at interface 1 and 2 for pure conduction inside the liquid of the four different transwall modules is shown in Fig. 3.10 to 3.33.

This ratio is not one due to the fact that equations (3.40) and (3.41), although absolutely similar in the case of pure conduction, have been integrated over a different number of control volumes. The ratio can also be interpreted as a correction factor which allows for the effect of a less successful approximation of the differential equation by integrating it over a coarser grid-mesh. The ratio always depends on the temperature distribution inside the liquid obtained from the integration of equation (3.40). This is shown in the following values of the ratio of conductivity referred to the transwall module of the fourth case:

Pure conduction without absorption of radiation:

$$(\lambda_{\text{ef}}/\lambda)_{1,\text{cond}} = (\lambda_{\text{ef}}/\lambda)_{2,\text{cond}} = 3.3$$

Pure conduction with absorption of radiation given by Table 3.5:

$$(\lambda_{\text{ef}}/\lambda)_{1,\text{cond}} = 3.1 \quad \text{and} \quad (\lambda_{\text{ef}}/\lambda)_{2,\text{cond}} = 0.7$$

### Convection

In Fig. 3.10 to 3.33 some of the numerical results on the effective conductivity are presented. The ratio of conductivity at interfaces 1 and 2 is given as a function of three different Rayleigh numbers  $Ra$ ,  $Ra_1$  and  $Ra_2$ .

The first Rayleigh number  $Ra$  is based on the distance  $L_2 + (L_1 + L_3)/2$  and the temperature difference  $TS_1 - TS_3$  between the nodes of the first and third liquid layers. The thermal properties which appear in the Rayleigh number  $Ra$  are calculated at the temperature  $TS_2$  of the node of the second liquid layer. Similarly, the second and the third Rayleigh numbers  $Ra_1$  and  $Ra_2$  are based on the distance  $(L_1 + L_2)/2$  and  $(L_2 + L_3)/2$ , respectively and the temperature differences  $TS_1 - TS_2$  and  $TS_3 - TS_2$  between the nodes of the first and the second liquid layers and between the nodes of the third and the second liquid layers, respectively. The thermal properties of the Rayleigh number  $Ra_1$  and  $Ra_2$  are calculated at the temperatures of interfaces 1 and 2 respectively.

The Rayleigh number was adopted as one parameter of the effective conductivity function because it incorporates both the ratio of momentum diffusivity to thermal diffusivity (through the Prandtl number,  $Pr$ ) and the relation of buoyant inertial and viscous forces (through the Grashof number,  $Gr$ ). The Rayleigh number is also being used more and more in natural convection flow problems instead of the Grashof number. The three particular Rayleigh numbers  $Ra$ ,  $Ra_1$ ,  $Ra_2$  were chosen because they could be calculated rather easily during the determination of the effective conductivity  $\lambda_{ef}$ .

From Fig. 3.10 to 3.21 a similarity of the patterns of the ratio of conductivity  $(\lambda_{ef}/\lambda)_1$  at interface 1 for various aspect ratios ( $H/L$ ) is obvious. The same can be said for the patterns of the ratio of conductivity  $(\lambda_{ef}/\lambda)_2$  at interface 2 (from Fig. 3.22 to Fig. 3.33). This similarity can be attributed to the similar pattern of flow inside the liquid of the four transwall modules.

For both surfaces 1 and 2, the absolute value of the Rayleigh numbers  $Ra_1$  and  $Ra_2$  is always smaller than a certain limit. This can be translated into the fact that the temperature difference between the adjacent liquid layers never exceeds a certain value. The temperature gradient actually produces the convection which, in turn, tends to balance the temperature difference. The maximum temperature difference is experienced between the first and second layer. This

maximum temperature difference is higher for higher aspect-ratio (  $H/L$  ) cases with the same total liquid layer thickness (  $L$  ).

The analysis of the results shows that the isothermal assumption can be considered good at least for the four examined cases. The ratio of conductivity at interface 1 exceeds values of about 7.5 in any of the four cases in about one minute from the onset of the flow and reaches values of the order of 50 or more in the next one or two minutes. The almost equal temperatures of the second and third layer is evident from both the small values of the Rayleigh number  $Ra_2$  and the very high values of the ratio of conductivity at interface 2. The energy transfer across this interface is actually determined by convection.

The wide spread of points in the fourth case, especially for interface 2 where it is very difficult to see the pattern of the ratio of conductivity  $(\lambda_{ef}/\lambda)_2$  with the time, is attributed to instabilities due to high convergence criteria limits. However, these instabilities are not sufficient to lead to divergence in the solution of the system of difference equations in the next time steps.

The present numerical analysis has not led to numerical prediction of the ratio of conductivity  $(\lambda_{ef}/\lambda)$  at both interfaces 1 and 2, under the usual conditions encountered in solar energy applications of the transwall system. However, it has supplied evidence on the order of magnitude of this ratio. Obviously, more numerical effort is needed to express this ratio  $(\lambda_{ef}/\lambda)$  at any interface, as function of the appropriate Rayleigh number, aspect ratio ( $H/L$ ), type and intensity of insolation and various liquid properties.

The difference between convection induced by absorption of solar radiation and convection due only to temperature differences between the bulk of the liquid and the glass surfaces should also be established in a quantitative way. Finally, the importance of the 3-dimensional absorption of solar radiation should also be examined against the 1-dimensional absorption which has been adopted in the present analysis.

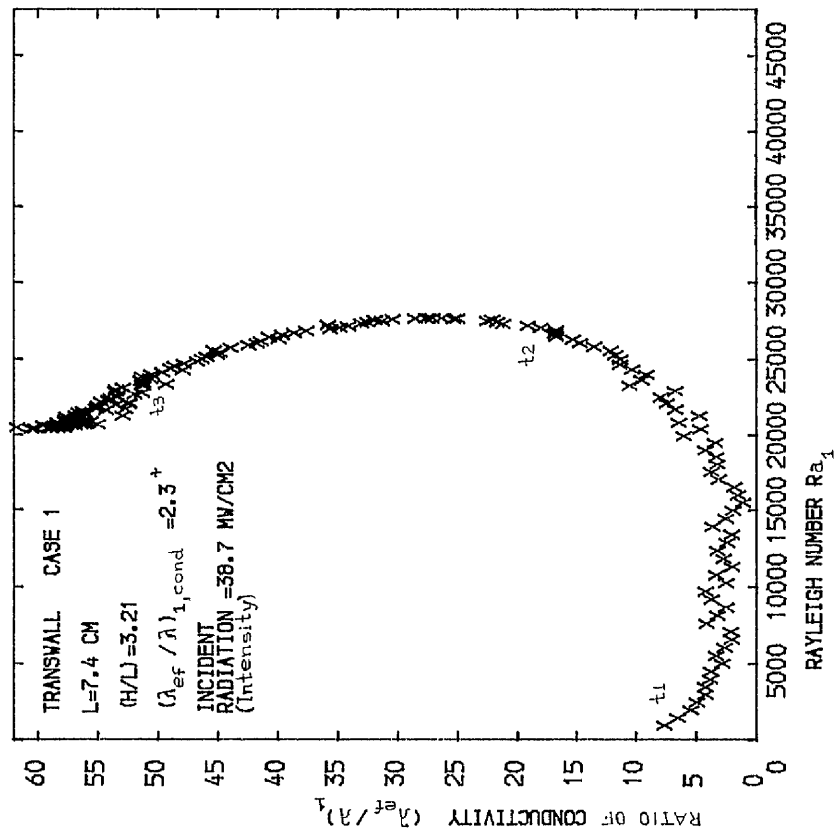


FIG. 3.10  
 EFFECTIVE CONDUCTIVITY AT INTERFACE 1  
 $t_n$  represents time,  $t_n > t_{n-1}$   
 + initial value - pure conduction condition

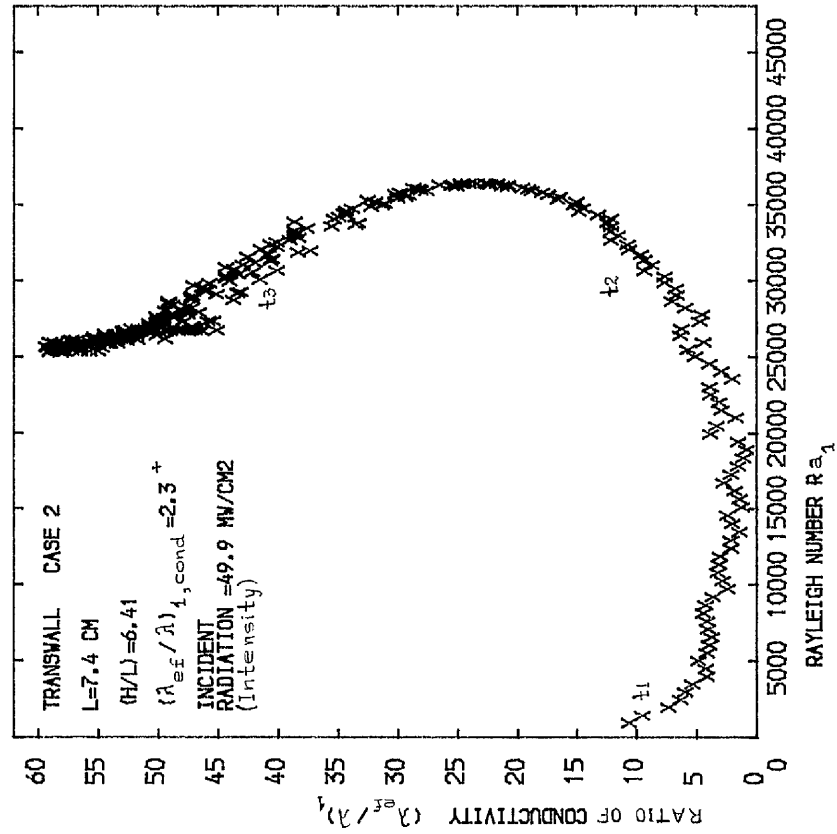


FIG. 3.11  
 EFFECTIVE CONDUCTIVITY AT INTERFACE 1  
 $t_n$  represents time,  $t_n > t_{n-1}$   
 + initial value - pure conduction condition

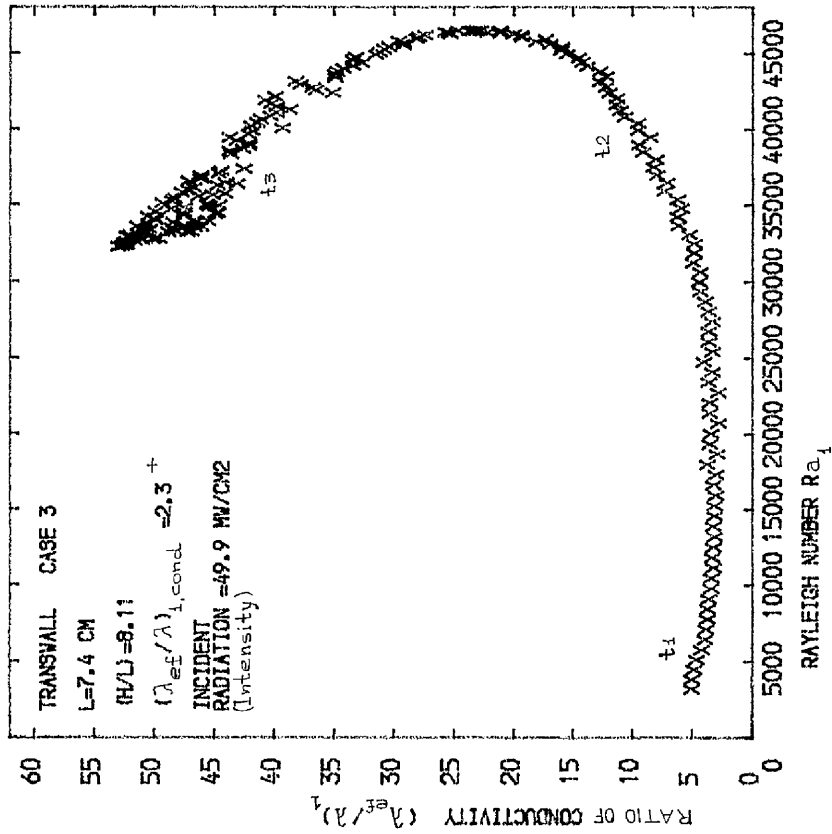


FIG. 3.12  
 EFFECTIVE CONDUCTIVITY AT INTERFACE 1  
 $t_n$  represents time,  $t_n > t_{n-1}$

+ initial value-pure conduction condition

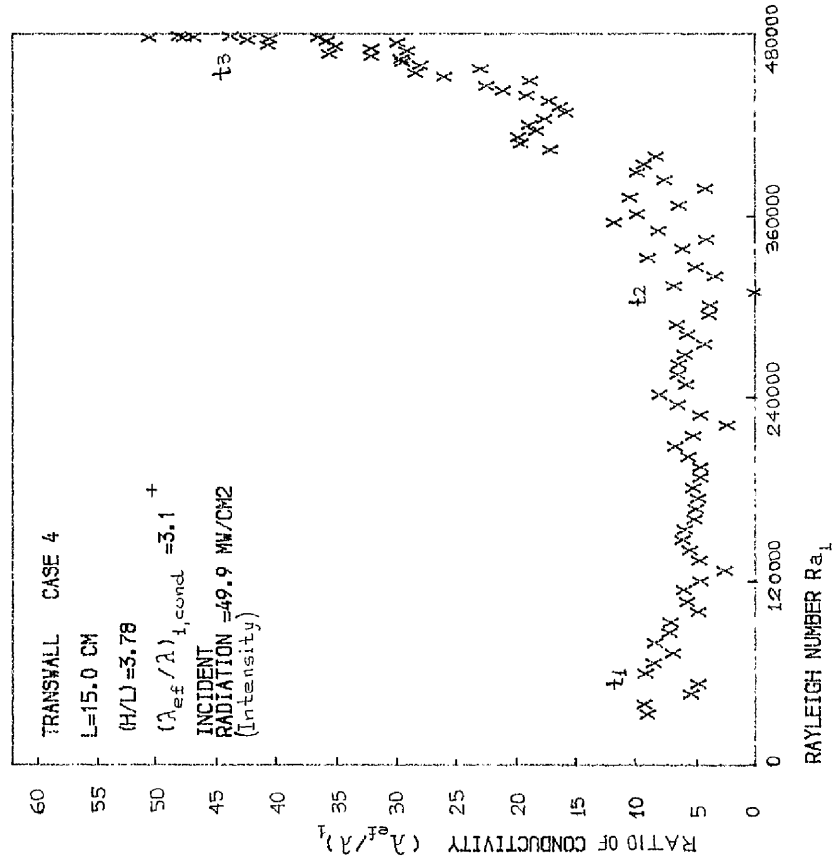


FIG. 3.13  
 EFFECTIVE CONDUCTIVITY AT INTERFACE 1  
 $t_n$  represents time,  $t_n > t_{n-1}$

+ initial value-pure conduction condition



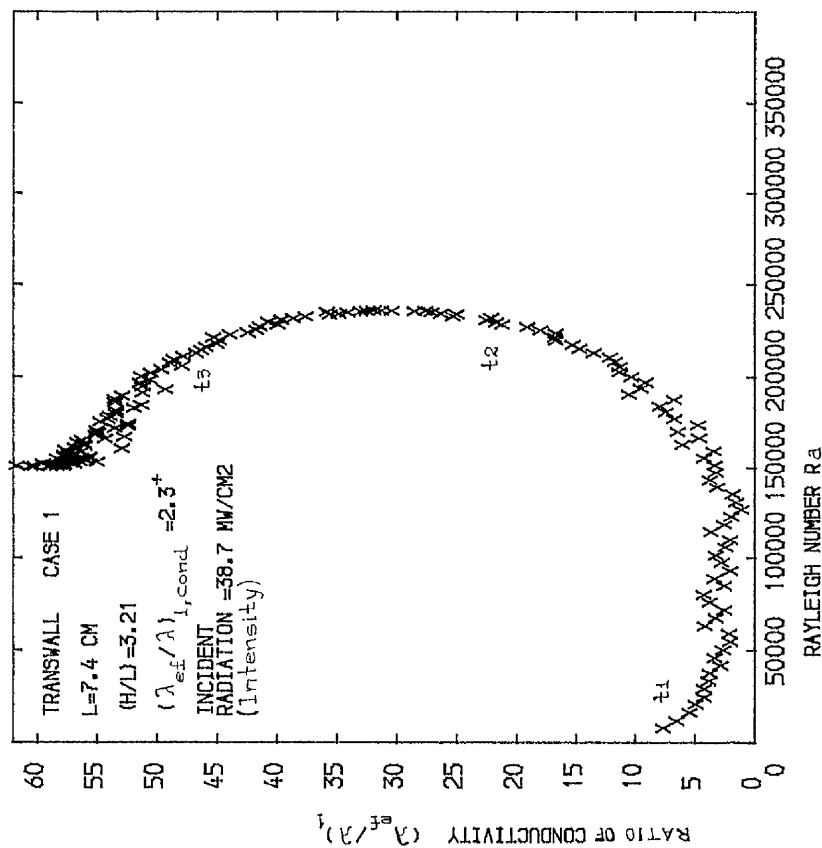


FIG. 3.14  
 EFFECTIVE CONDUCTIVITY AT INTERFACE 1  
 $t_n$  represents time,  $t_n > t_{n-1}$

+ initial value-pure conduction condition.

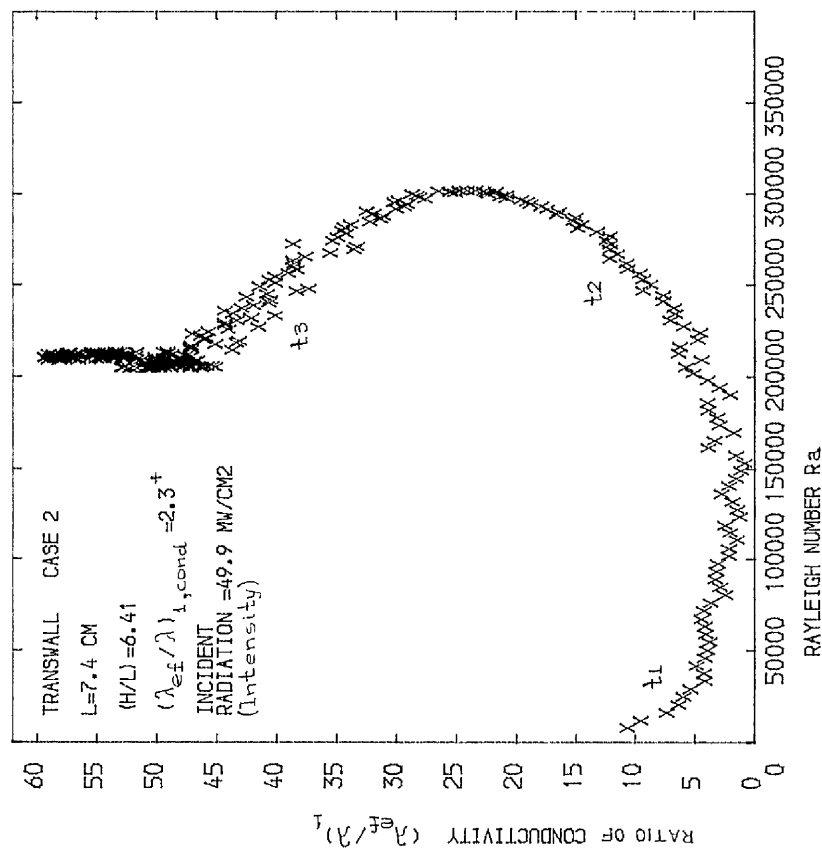


FIG. 3.15  
 EFFECTIVE CONDUCTIVITY AT INTERFACE 1  
 $t_n$  represents time,  $t_n > t_{n-1}$

+ initial value-pure conduction condition.

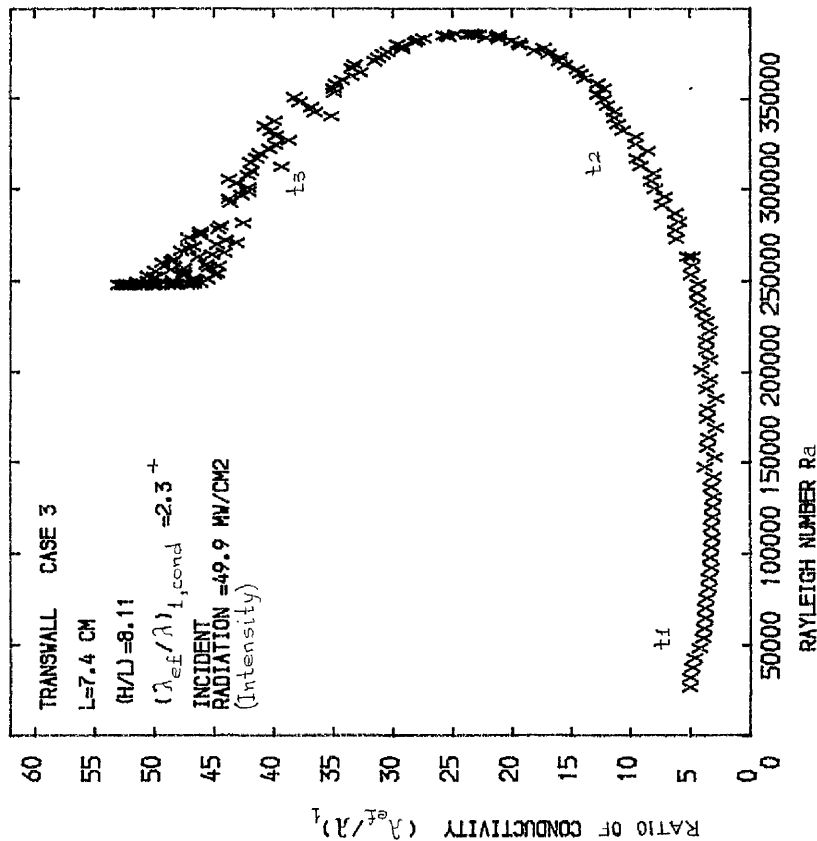


FIG. 3.16  
 EFFECTIVE CONDUCTIVITY AT INTERFACE 1  
 $t_n$  represents time,  $t_n > t_{n-1}$   
 + initial value-pure conduction condition.

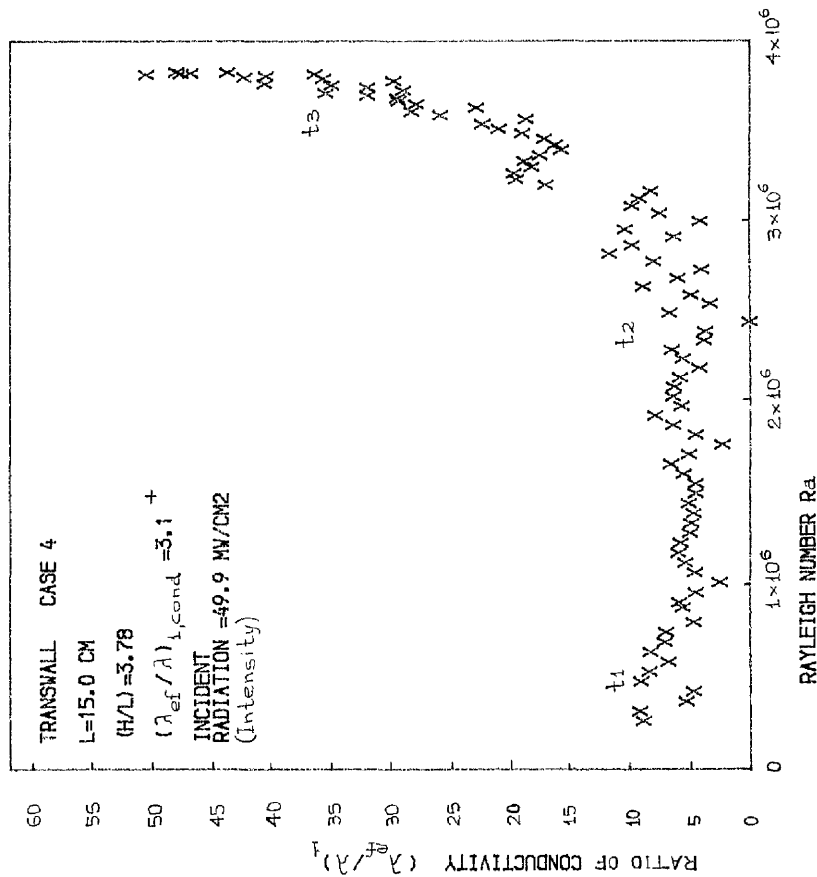


FIG. 3.17  
 EFFECTIVE CONDUCTIVITY AT INTERFACE 1  
 $t_n$  represents time,  $t_n > t_{n-1}$   
 + initial value-pure conduction condition.

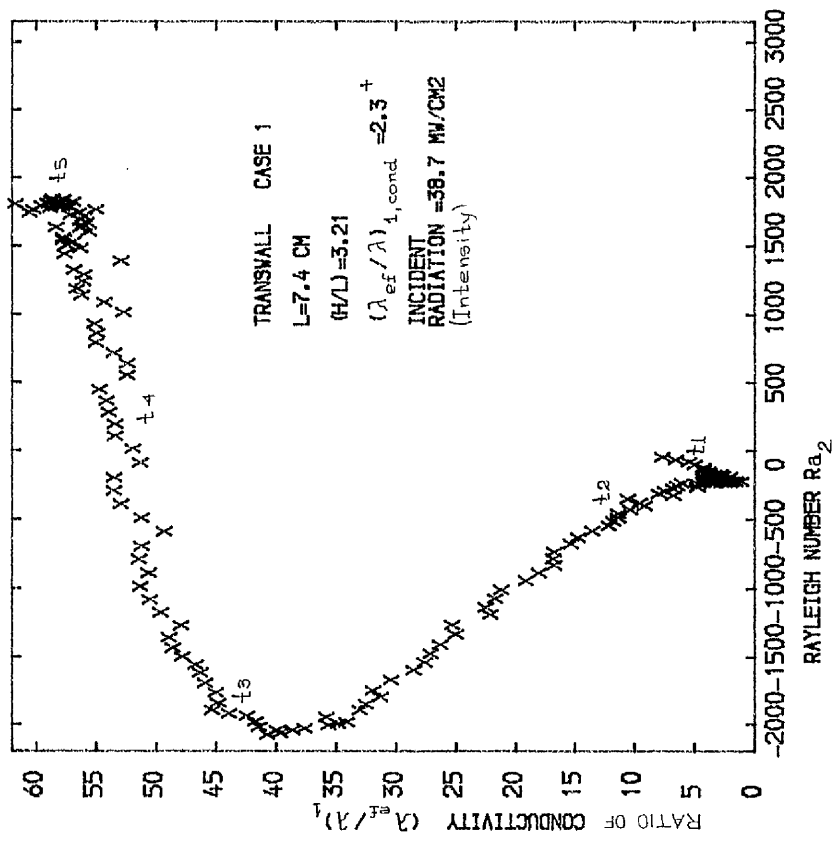


FIG. 3.18  
 EFFECTIVE CONDUCTIVITY AT INTERFACE 1  
 $t_n$  represents time ,  $t_n > t_{n-1}$   
 + initial value-pure conduction condition.

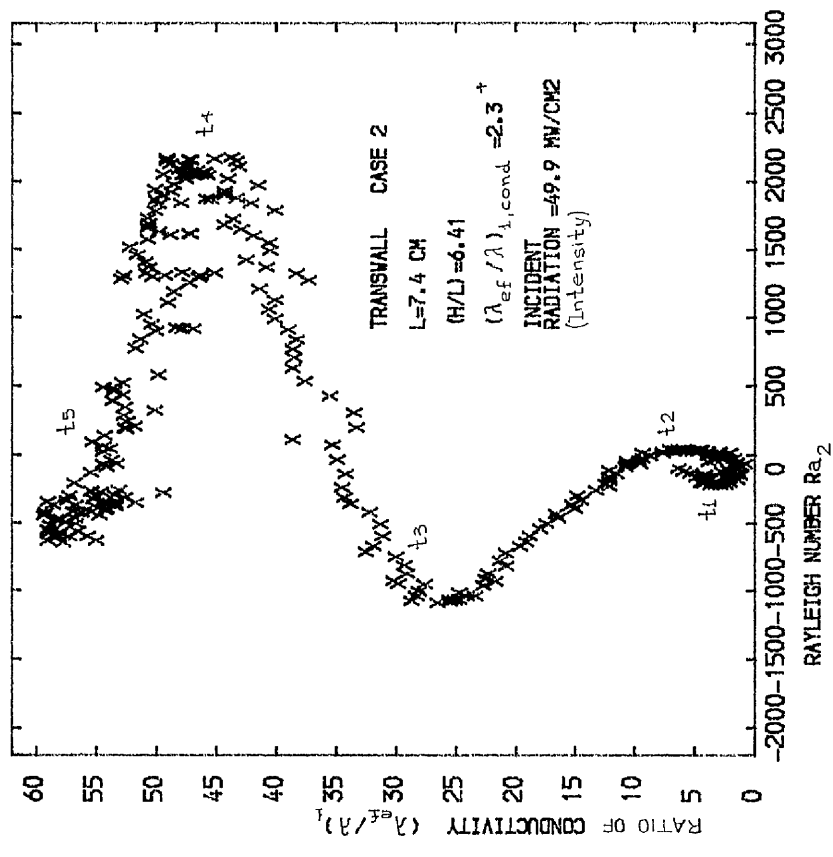


FIG. 3.19  
 EFFECTIVE CONDUCTIVITY AT INTERFACE 1  
 $t_n$  represents time ,  $t_n > t_{n-1}$   
 + initial value-pure conduction condition

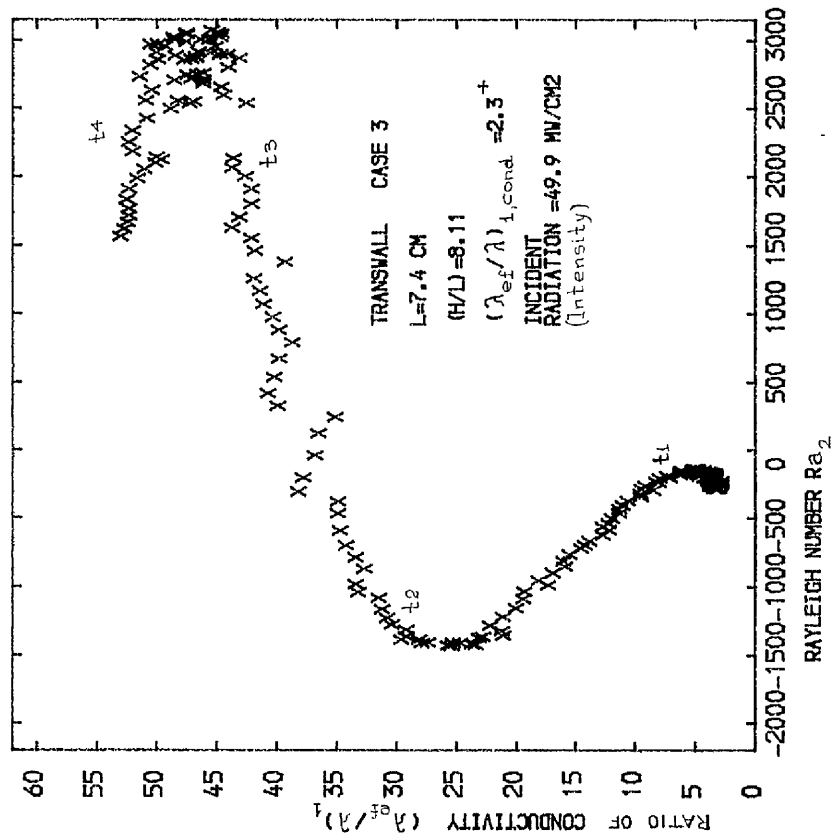


FIG. 3.20  
EFFECTIVE CONDUCTIVITY AT INTERFACE 1

$t_n$  represents time ,  $t_n > t_{n-1}$

+ initial value - pure conduction condition.

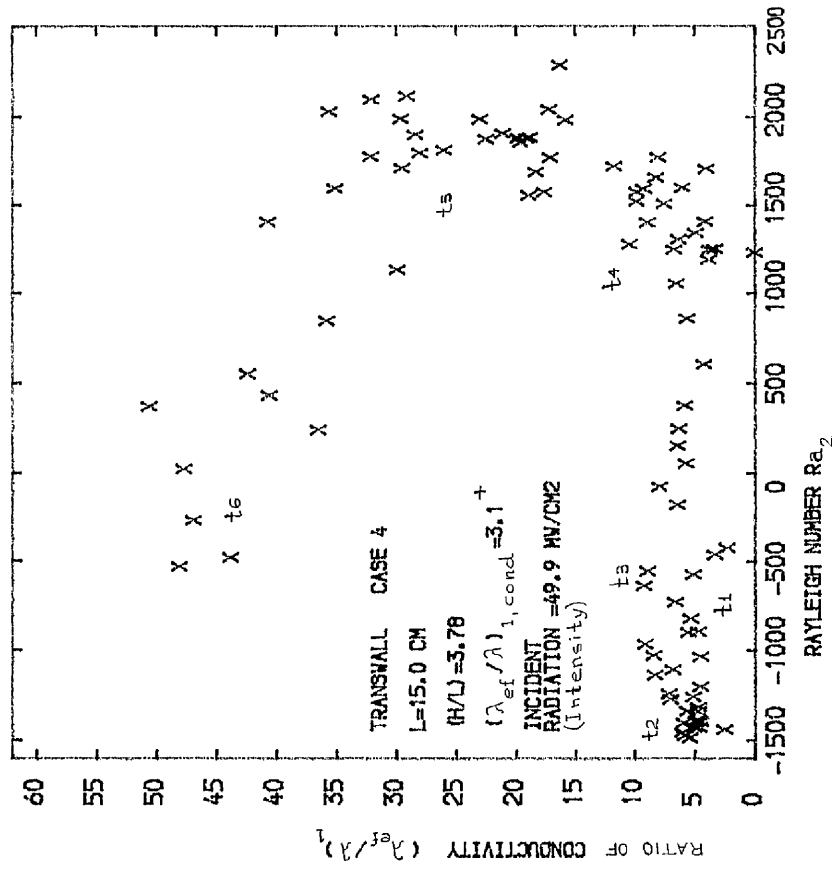


FIG. 3.21  
EFFECTIVE CONDUCTIVITY AT INTERFACE 1

$t_n$  represents time ,  $t_n > t_{n-1}$

+ initial value - pure conduction condition.

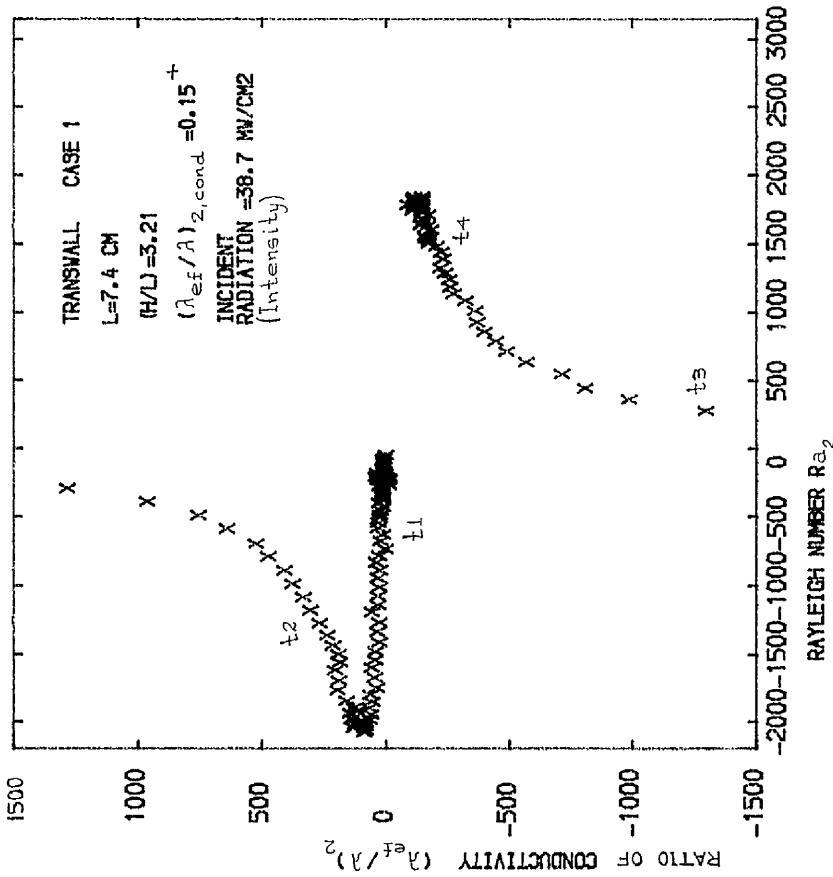


FIG. 3.22  
EFFECTIVE CONDUCTIVITY AT INTERFACE 2

$t_n$  represents time ,  $t_n > t_{n-1}$   
+ initial value-pure conduction condition.

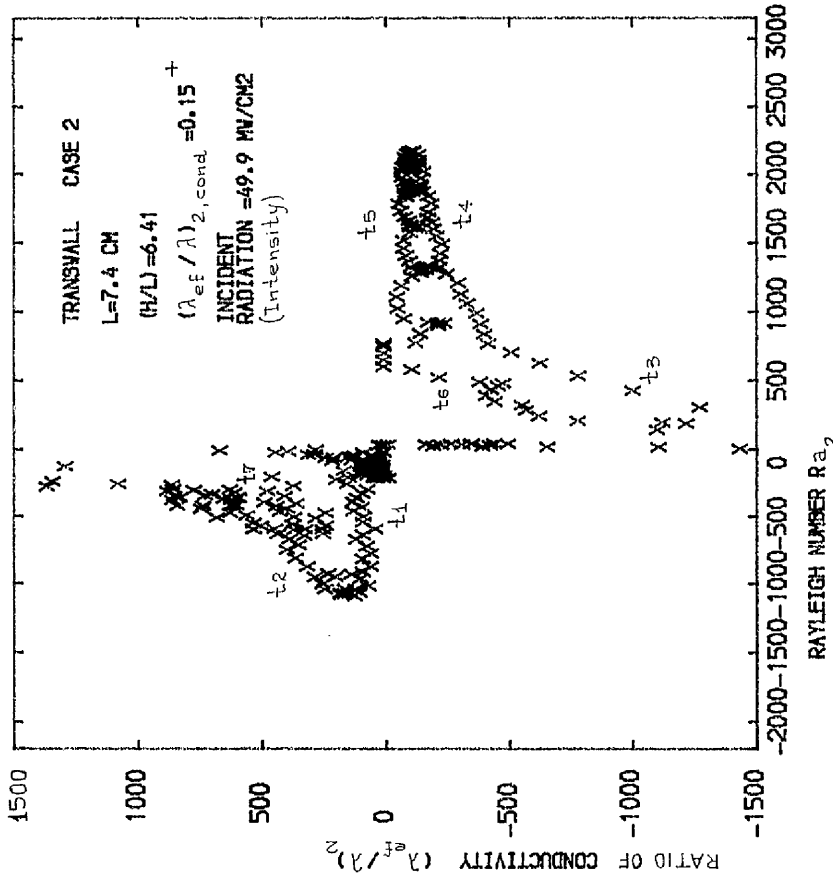


FIG. 3.23  
EFFECTIVE CONDUCTIVITY AT INTERFACE 2

$t_n$  represents time ,  $t_n > t_{n-1}$   
+ initial value-pure conduction condition.

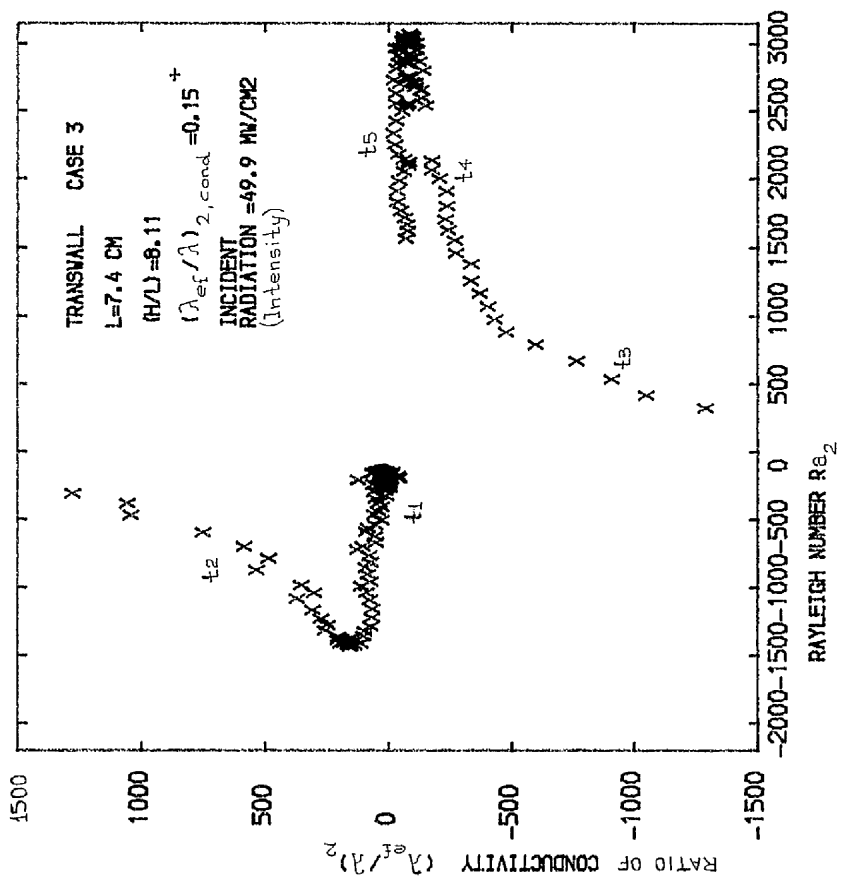


FIG. 3.24  
 EFFECTIVE CONDUCTIVITY AT INTERFACE 2  
 $t_n$  represents time,  $t_n > t_{n-1}$   
 + initial value-pure conduction condition

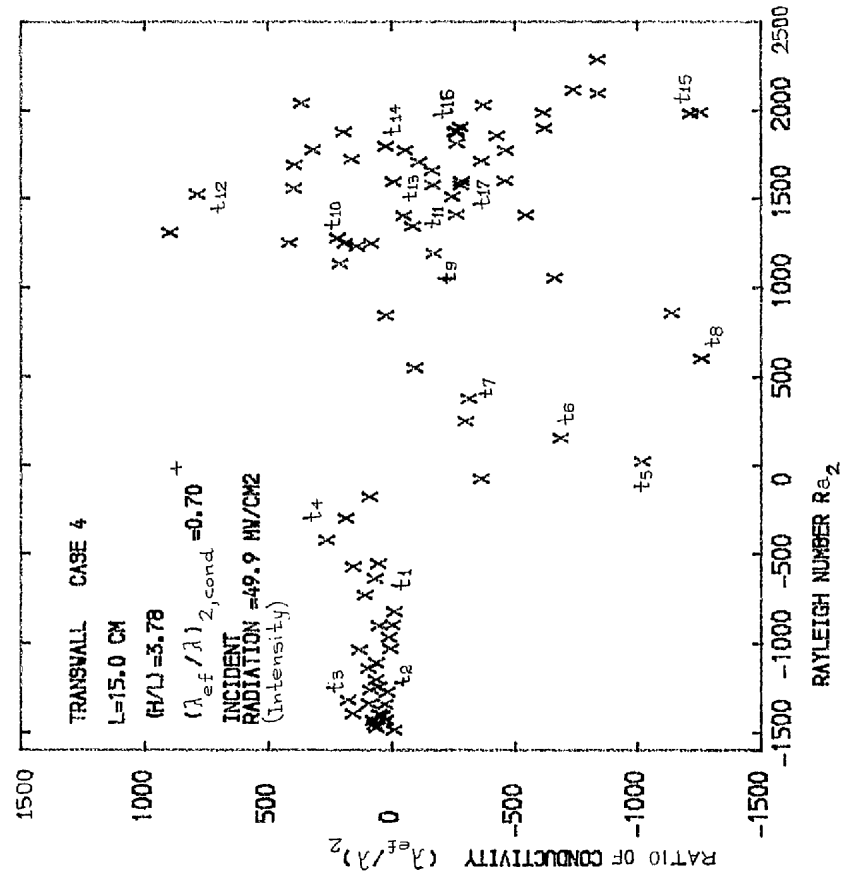


FIG. 3.25  
 EFFECTIVE CONDUCTIVITY AT INTERFACE 2  
 $t_n$  represents time,  $t_n > t_{n-1}$   
 + initial value-pure conduction condition

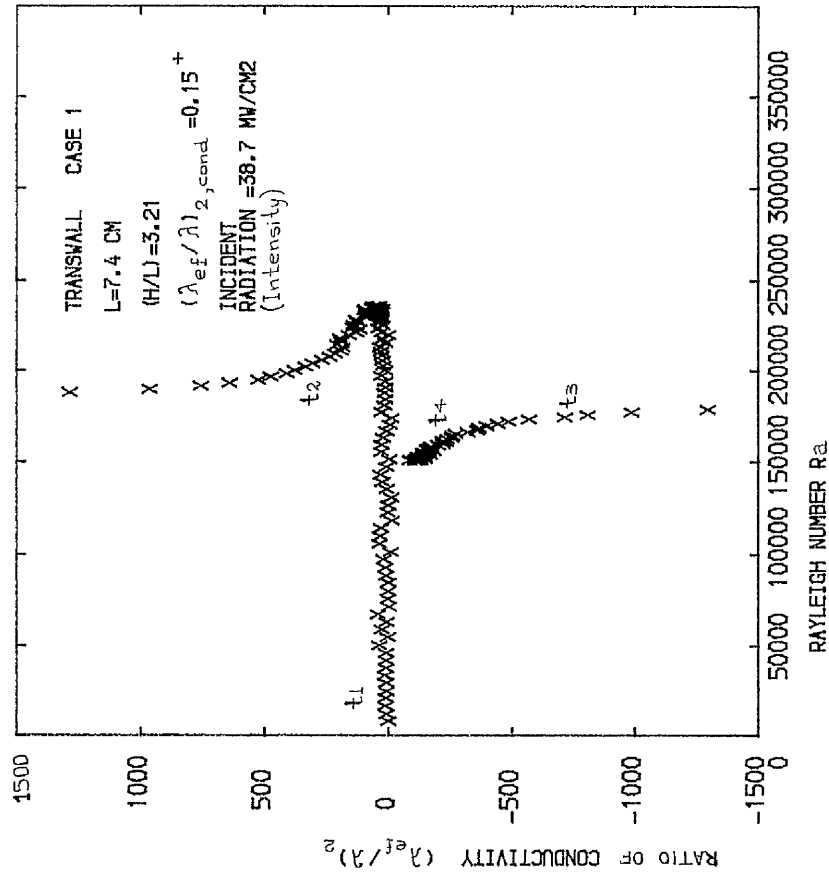


FIG. 3.26

EFFECTIVE CONDUCTIVITY AT INTERFACE 2

$t_n$  represents time,  $t_n > t_{n-1}$

+ initial value-pure conduction condition.

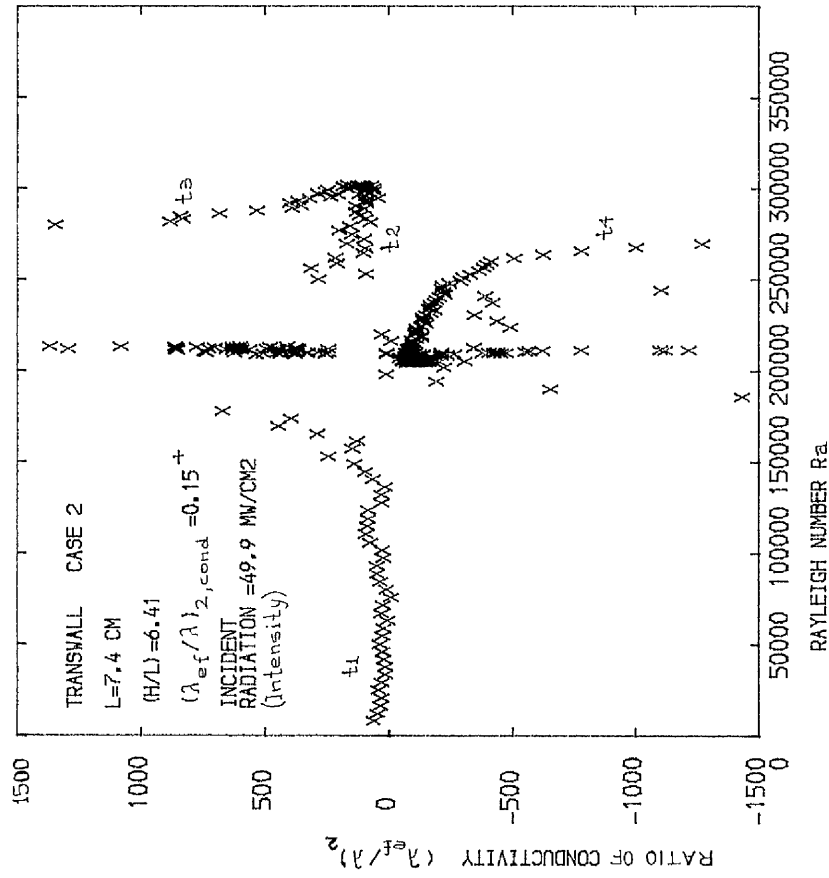


FIG. 3.27

EFFECTIVE CONDUCTIVITY AT INTERFACE 2

$t_n$  represents time,  $t_n > t_{n-1}$

+ initial value-pure conduction condition.

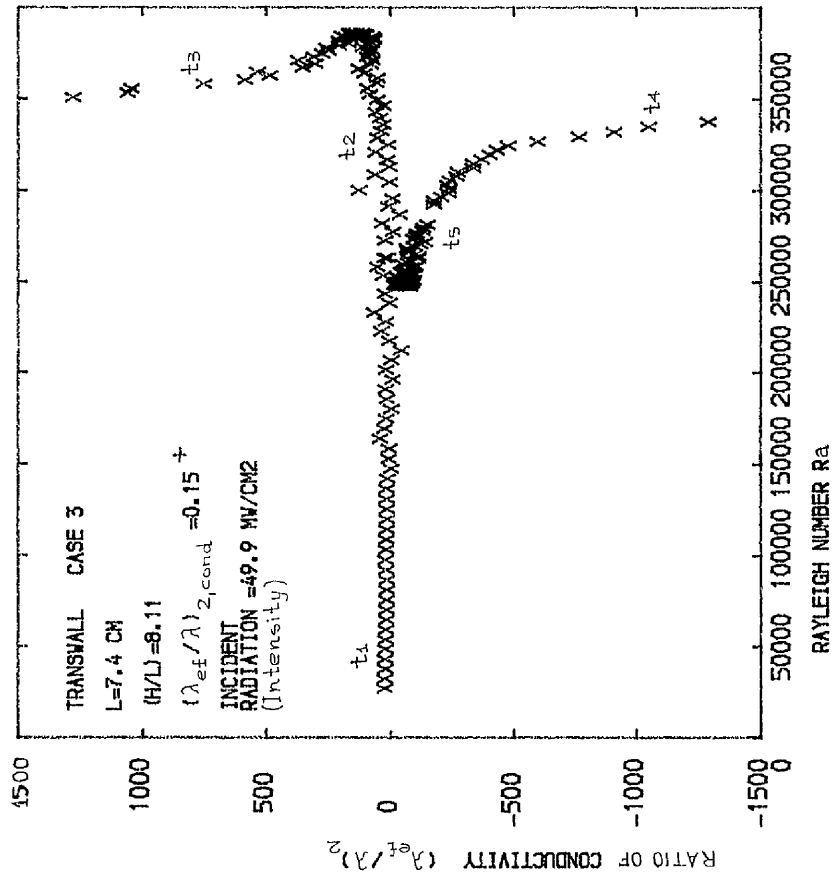


FIG. 3.28  
 EFFECTIVE CONDUCTIVITY AT INTERFACE 2

$t_n$  represents time,  $t_n > t_{n-1}$

+ initial value-pure conduction condition.

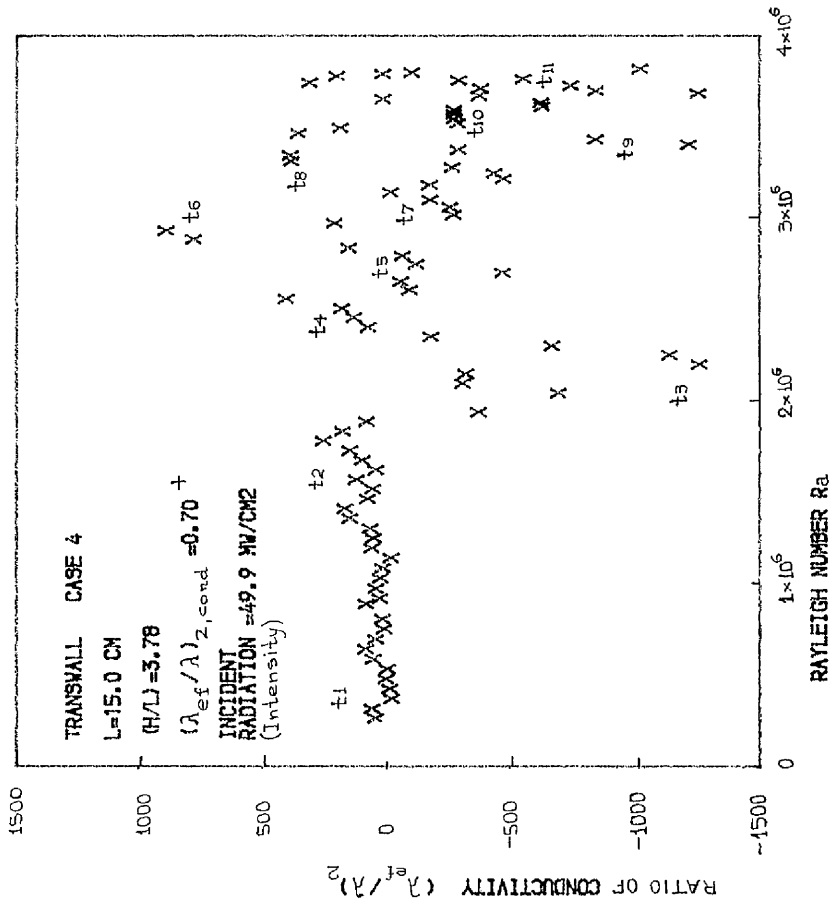


FIG. 3.29  
 EFFECTIVE CONDUCTIVITY AT INTERFACE 2

$t_n$  represents time,  $t_n > t_{n-1}$

+ initial value-pure conduction condition.



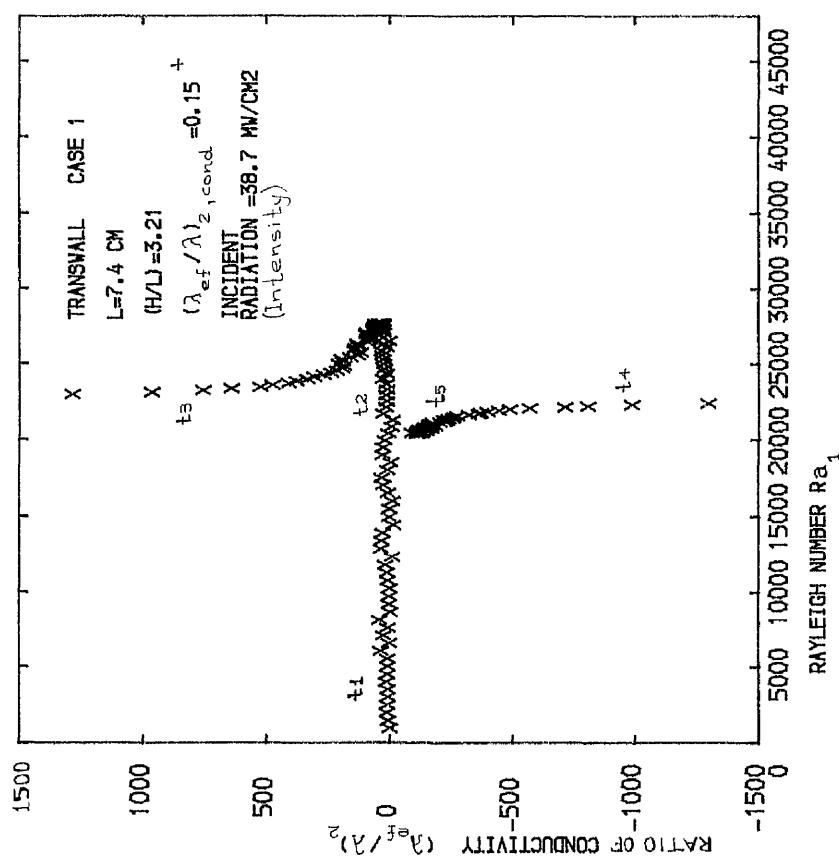


FIG. 3.30  
 EFFECTIVE CONDUCTIVITY AT INTERFACE 2  
 $t_n$  represents time,  $t_n > t_{n-1}$   
 + initial value - pure conduction condition

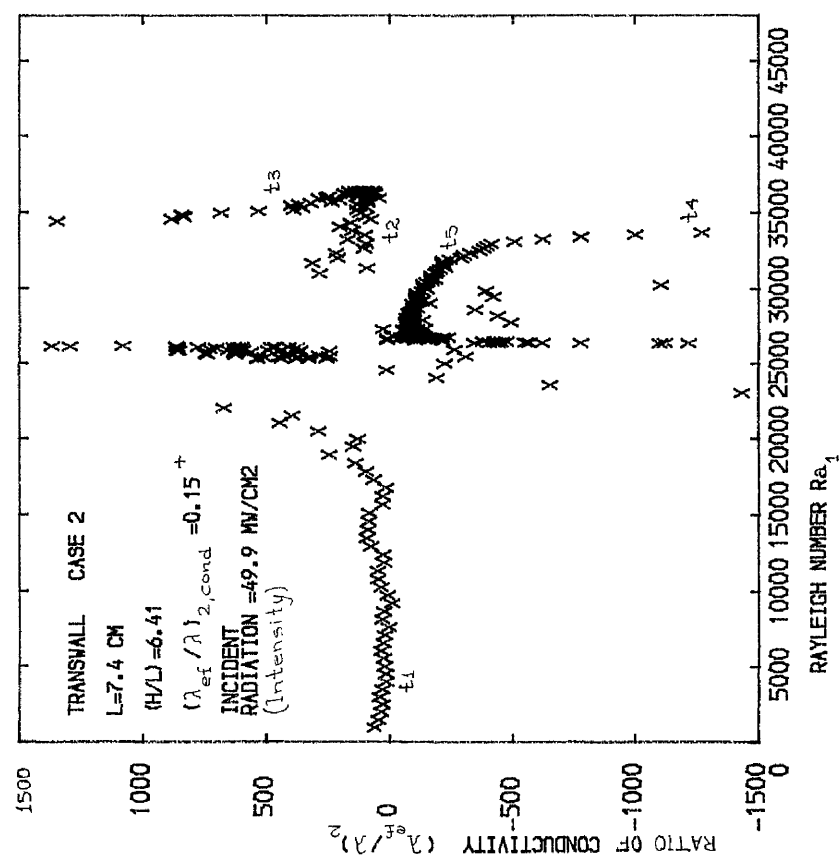


FIG. 3.31  
 EFFECTIVE CONDUCTIVITY AT INTERFACE 2  
 $t_n$  represents time,  $t_n > t_{n-1}$   
 + initial value - pure conduction condition

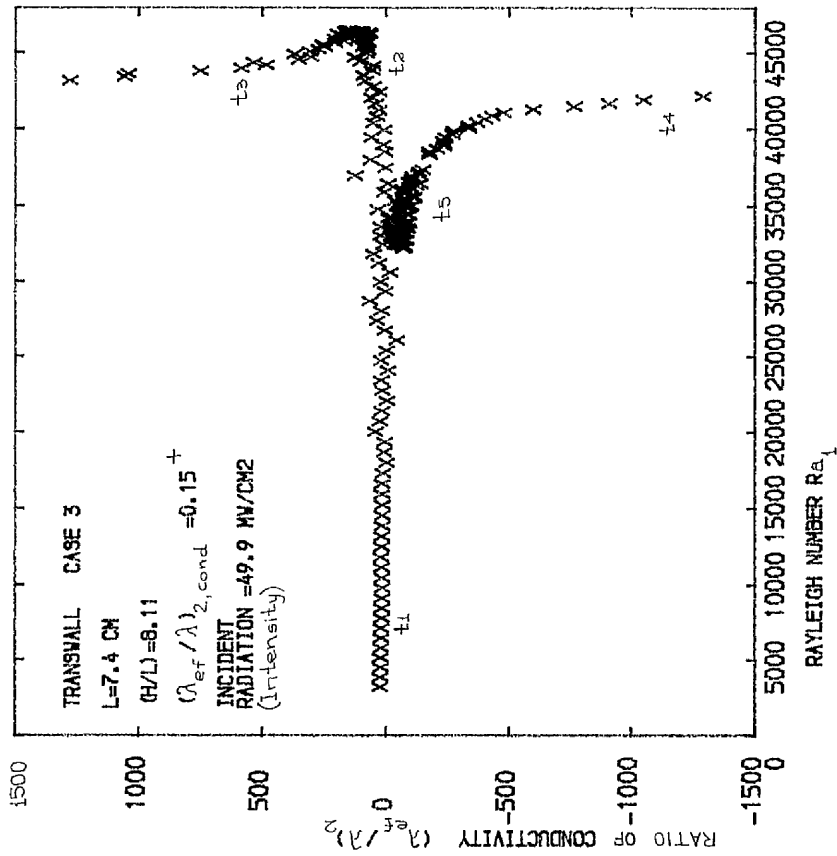


FIG. 3.32  
 EFFECTIVE CONDUCTIVITY AT INTERFACE 2  
 $t_n$  represents time,  $t_n > t_{n-1}$   
 + initial value - pure conduction condition.

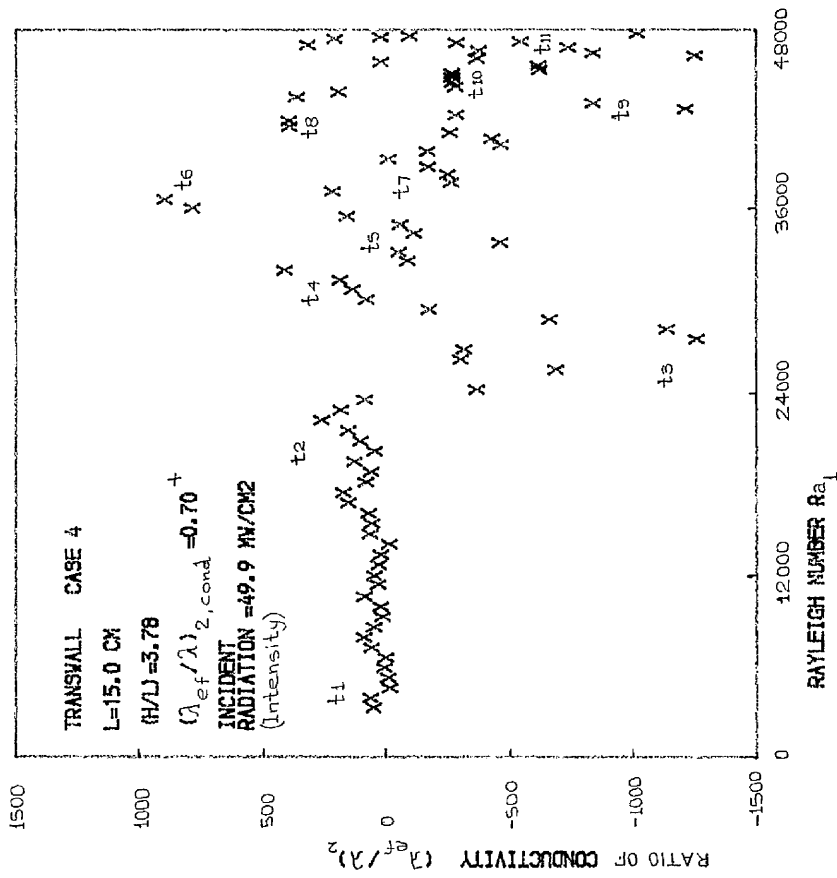


FIG. 3.33  
 EFFECTIVE CONDUCTIVITY AT INTERFACE 2  
 $t_n$  represents time,  $t_n > t_{n-1}$   
 + initial value - pure conduction condition.

### 3.3 EXAMPLES OF THE NUMERICAL PREDICTION OF THE VELOCITY, PRESSURE AND TEMPERATURE FIELD.

These examples are referred to the flow inside the transwall modules of cases 1, 2 and 3<sup>+</sup>, defined in the previous section, pages 163 to 167. At present only the velocity, pressure and temperature fields in the central plane xz are given (Fig. 3.34 to Fig.3.38).

In Fig. 3.34 and 3.35 the real dimensions of the control volumes in the central xz plane are given for case 1. Only the components of velocity normal to the interfaces of the control volumes are shown, which are the components of velocity along the x and z directions. The length of each vector represents the relative value of the velocity component. It is quite easy to understand the flow pattern from Fig. 3.34 and 3.35 at the three different time instants, 20th, 90th and 160th seconds after the onset of the flow. The following points for the flow pattern at the three different time instants of case 1 are worthy of stressing: The boundary layer thickness for the 20th instant is almost constant along the z direction (of the order of magnitude of about 1.5cm). The boundary layer is defined here as the liquid region near the front-glass plate of the module in which the liquid velocity changes from zero value at the glass-liquid interface to zero inside the liquid. The boundary layer seems to be slightly wider in the middle of the transwall height. The predicted maximum velocity component along the z direction is about 0.04 cm/s, and occurs at about 7.9 cm distance from the oil bottom. For the 90th time instant, the boundary layer thickness becomes slightly thinner at the bottom of the transwall module but much thicker at the top of the transwall module (about 2.7 cm at a distance of about 3.95 cm from the oil layer bottom). At the right bottom of the transwall module a weak second circulation of the liquid is evident. For the 90th second the predicted maximum velocity component along the z direction occurs at slightly higher position than that of the 20th second with a value of about 0.39 cm/s. The acceleration of the circulation of the fluid will stop after about three seconds. The rate of deceleration will be lower than the experienced rate of acceleration and leads to a predicted maximum velocity component along the z direction of about 0.27 cm/s at the 160th second, at about the same position as previously. The boundary layer pattern remains the same as for the 90th second but the thickness is smaller. This has been predicted to be about 1.2 cm at a distance of about 20 cm and

+ same dimensions apart from the varying water height.

about 2.4 cm at a distance of about 3.95 cm from the oil layer bottom. The second circulation of the liquid is much more enhanced at the 160th second.

In Fig.3.37, the components of velocity along the x and z directions in the central xz plane are also given for the second and third case. The dimension of the control volumes along the z direction in Fig.3.37 do not represent the real dimension. It is obvious that the flow pattern, referred to the 200th second after the onset of the flow for both cases, is almost identical to that of the 160th second of the first case. The predicted maximum velocity component along the z direction is about 0.38 cm/s in the second case and about 0.49 cm/s in the third case for the 200th second. The position of the maximum velocity component along the z direction is predicted to occur at about 14 cm in the second case and at about 19 cm in the third case from the bottom of the oil layer.

The numbers written in each control volume of Fig.3.34, 3.35 and 3.37 represent predicted relative values of pressure in  $\text{gr} \cdot \text{cm} / \text{cm}^2 \cdot \text{s}^2$ .

The temperature variation along the x direction for six different heights on the central xz plane is given in Fig.3.36 for the first case and in Fig.3.38 for the second and third case. These heights are actually the heights of the rows of nodes along the x direction on the central xz plane. As can be seen from Fig.3.36 the nodes of the same x co-ordinate at the 20<sup>th</sup> sec. have almost the same temperature. As the time passes the top liquid layers have higher and higher temperatures compared with the lower liquid layers. This finally results in the situation where the temperature difference along the z axis is larger than the temperature difference along the x axis (Fig.3.36 and Fig.3.38). From Fig.3.38, it is easily seen that this temperature difference along the z direction increases as the aspect ratio of the transwall module increases. The temperature pattern along the x-axis is established after a certain time from the onset of the liquid circulation and is shown for the 160th sec. of the first case and for the 200th sec. of the second and third case. The pattern is almost identical in every case.

Case 1. Relative pressure values and velocity components  $u$  and  $w$

Pressure in  $\text{g/cm}^2 \cdot \text{sec}^2$   
 $\rightarrow \approx 5.0 \cdot 10^{-3} \text{ cm/sec}$   
 20<sup>th</sup> sec.

0  
 $x$   
 $u$   
 $w$   
 $z$

Pressure in  $\text{g/cm}^2 \cdot \text{sec}^2$   
 $\rightarrow \approx 7.5 \cdot 10^{-2} \text{ cm/sec}$   
 90<sup>th</sup> sec.

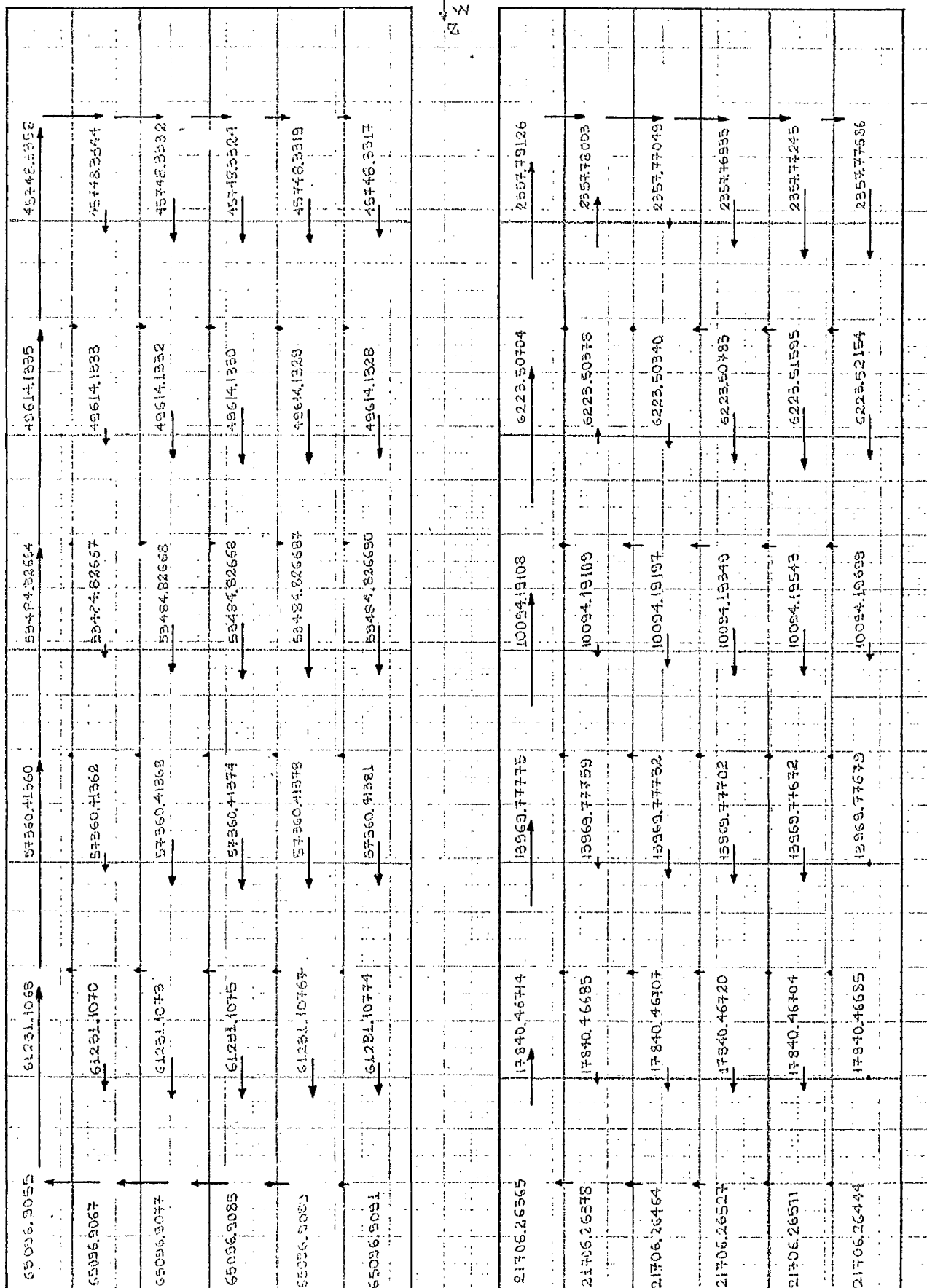


Fig. 3.34

case 1. Relative pressure values and velocity components  $u$  and  $w$

Pressure in  $\text{g/cm}^2$

$\rightarrow 5.0 \times 10^{-2} \text{ cm/s}$

160 th sec.

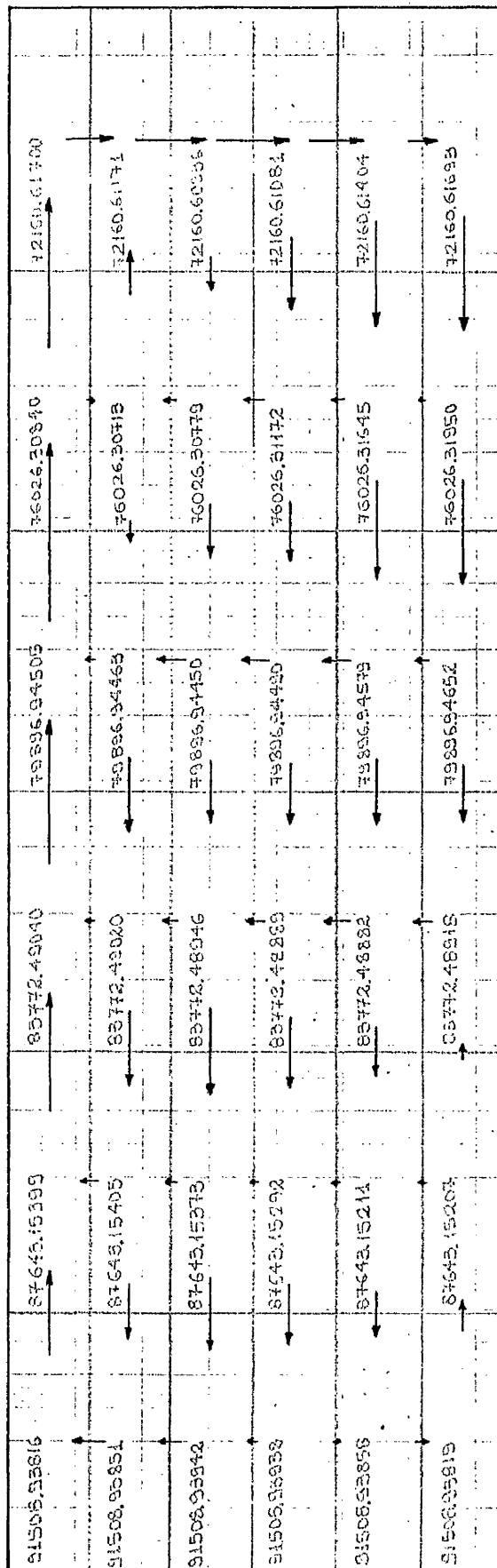
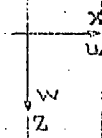


Fig. 3.35

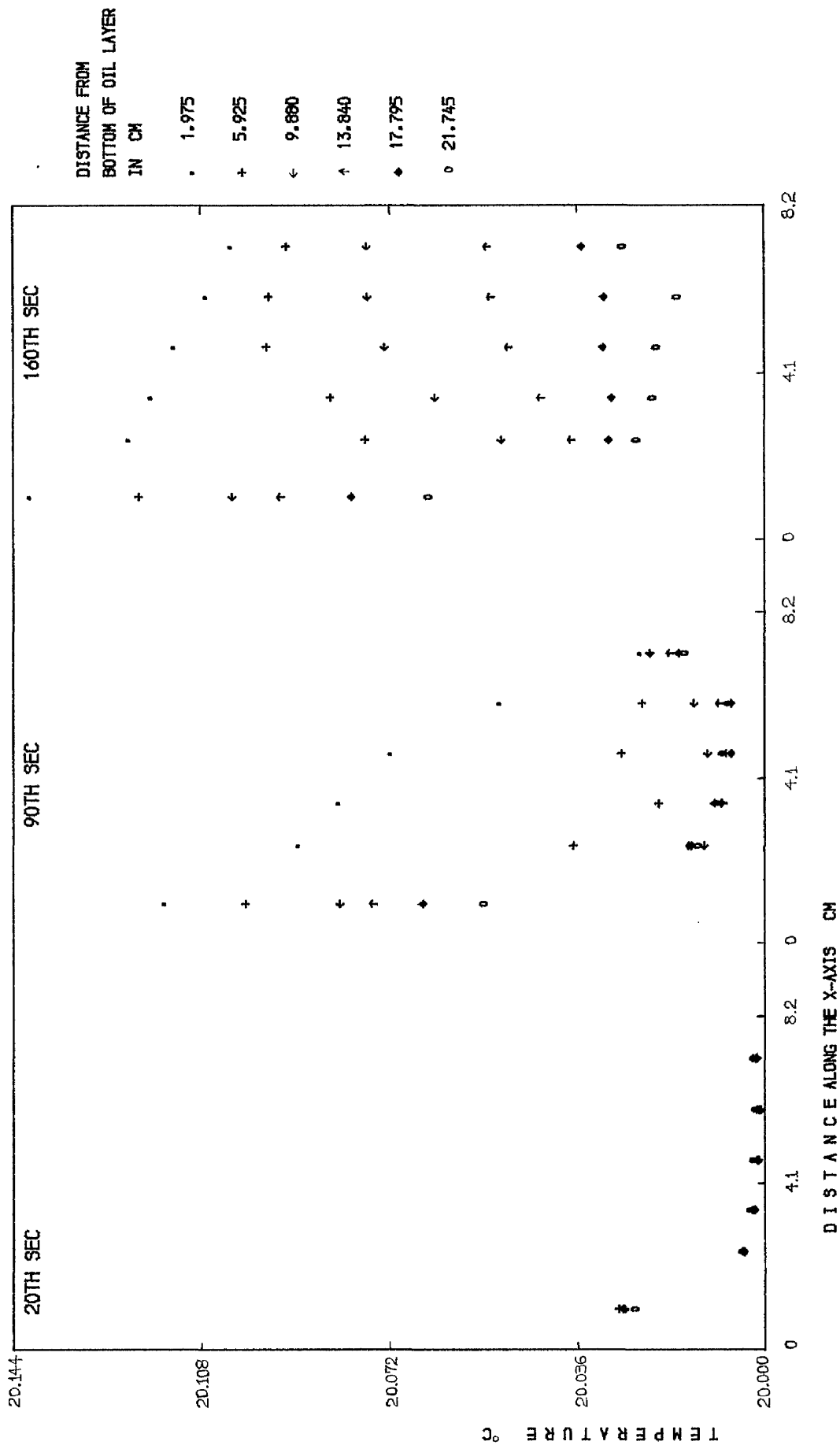


FIG. 3.36  
TEMPERATURE VARIATION ALONG THE X-AXIS. CASE 1  
The distance is measured from the outside  
surface of the front glass of the module.

case 2

$\rightarrow \equiv 5.0 \times 10^{-2} \text{ cm/s}$  200th sec

-37517.76065	-44368.50928	-52550.22238	-62062.88216	-70244.49391	-77095.02725
-37517.76045	-44368.50909	-52550.22235	-62062.88293	-70244.50073	-77095.03036
-37517.75957	-44368.50906	-52550.22261	-62062.88263	-70244.50053	-77095.03140
-37517.75926	-44368.50940	-52550.22253	-62062.88274	-70244.49734	-77095.03068
-37517.75914	-44368.50987	-52550.22305	-62062.88252	-70244.49301	-77095.02745
-37517.76018	-44368.50989	-52550.22293	-62062.88228	-70244.49313	-77095.02527

W  
Z

case 3

$\rightarrow \equiv 6.1 \times 10^{-2} \text{ cm/s}$  200th sec

-352.71079	-9650.13476	-19926.17440	-30691.47754	-40967.37125	-50264.43350
-352.71056	-9650.13459	-19926.17442	-30691.47777	-40967.37199	-50264.43695
-352.70973	-9650.13459	-19926.17472	-30691.47304	-40967.37189	-50264.43822
-352.70949	-9650.13432	-19926.17504	-30691.47824	-40967.36895	-50264.43705
-352.70934	-9650.13552	-19926.17512	-30691.47211	-40967.36500	-50264.43463
-352.71029	-9650.13534	-19926.17497	-30691.47791	-40967.36229	-50264.43362

Relative pressure values ( $\text{g/cm}^2 \cdot \text{s}^2$ ) and velocity components u and w

Fig. 3.37



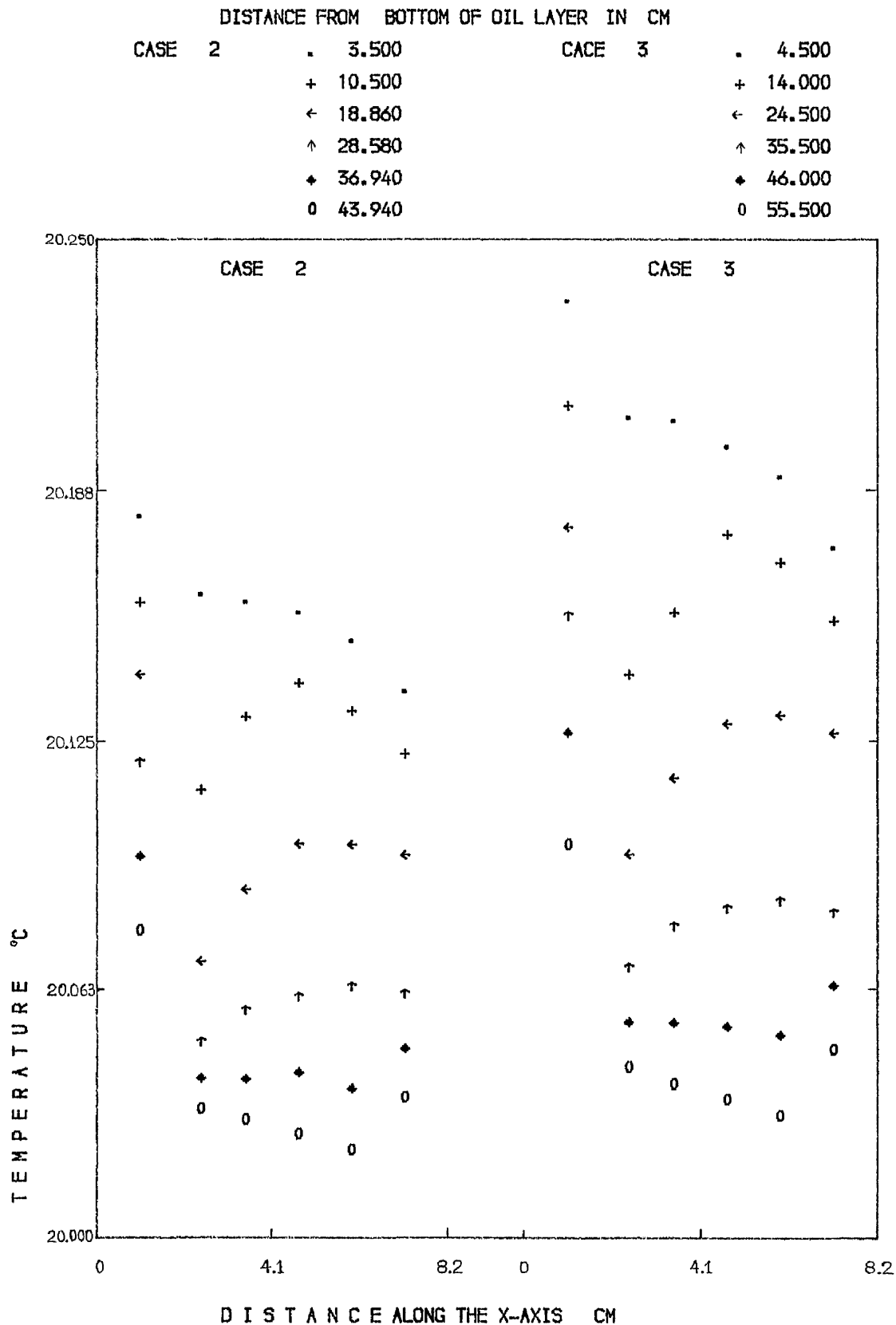


FIG. 3.38

TEMPERATURE VARIATION ALONG THE X-AXIS 200TH SEC

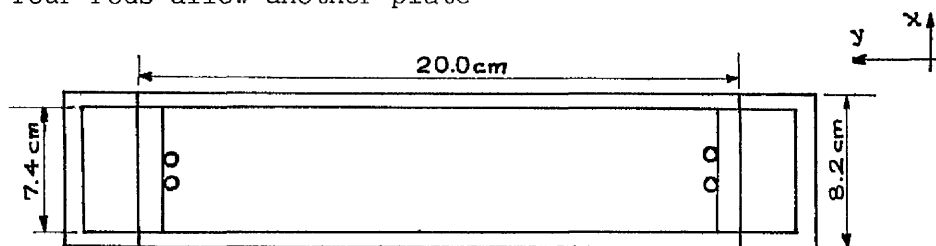
The distance is measured from the outside surface of the front glass of the module.

### 3.4 MEASUREMENTS OF TEMPERATURE AND VELOCITY

An experimental rig has been constructed in M.E.R.A., University of Glasgow, for indoor testing of small transwall modules. The modules are irradiated by a solar simulator. Experimental evidence was sought to support some of our numerical predictions and results of the elaborate computing program used to predict convective effect in a radiation absorbing liquid. The basic parts of the experimental rig are shown in Ph. 4, 5 and 6.

#### 3.4.1 The transwall module

The transwall module (No.1, in Ph. 4, 5 and 6) made from clear float glass from Pilkington, has the shape given in Fig. 3.9, page 164. The dimensions of the liquid and the various glass parts are also given in page 164 - Table 3.1, case 1. This means that the external dimensions of the module are 8.2 cm, 20.0 cm and 25.0 cm along the x, y and z direction, respectively. Two plastic rods of about 0.4 cm diameter and about 16 cm length have been attached on each internal surface of its two sides along the z direction, as Fig. 3.39 shows. The four rods allow another plate



Plan view of the transwall module

Fig. 3.39

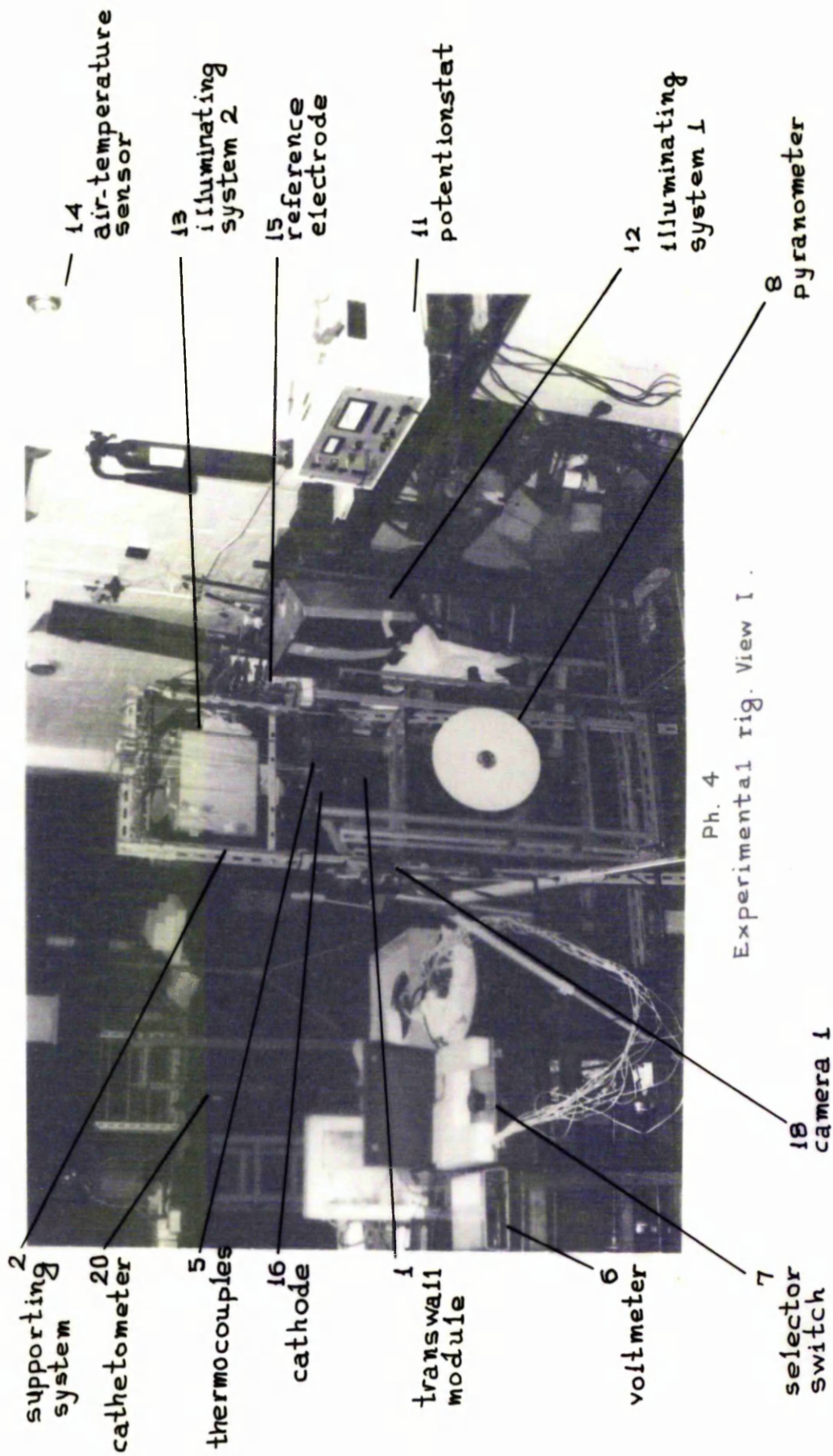
of about 0.4 cm thickness (along the x direction) and about 20.0 cm width (along the y direction) to be inserted inside the transwall module normal to the x direction - middle absorbing glass. Closed perspex channels were attached to the sides normal to the y direction to decrease heat losses, as shown in Fig. 3.39.

#### 3.4.2 The supporting system

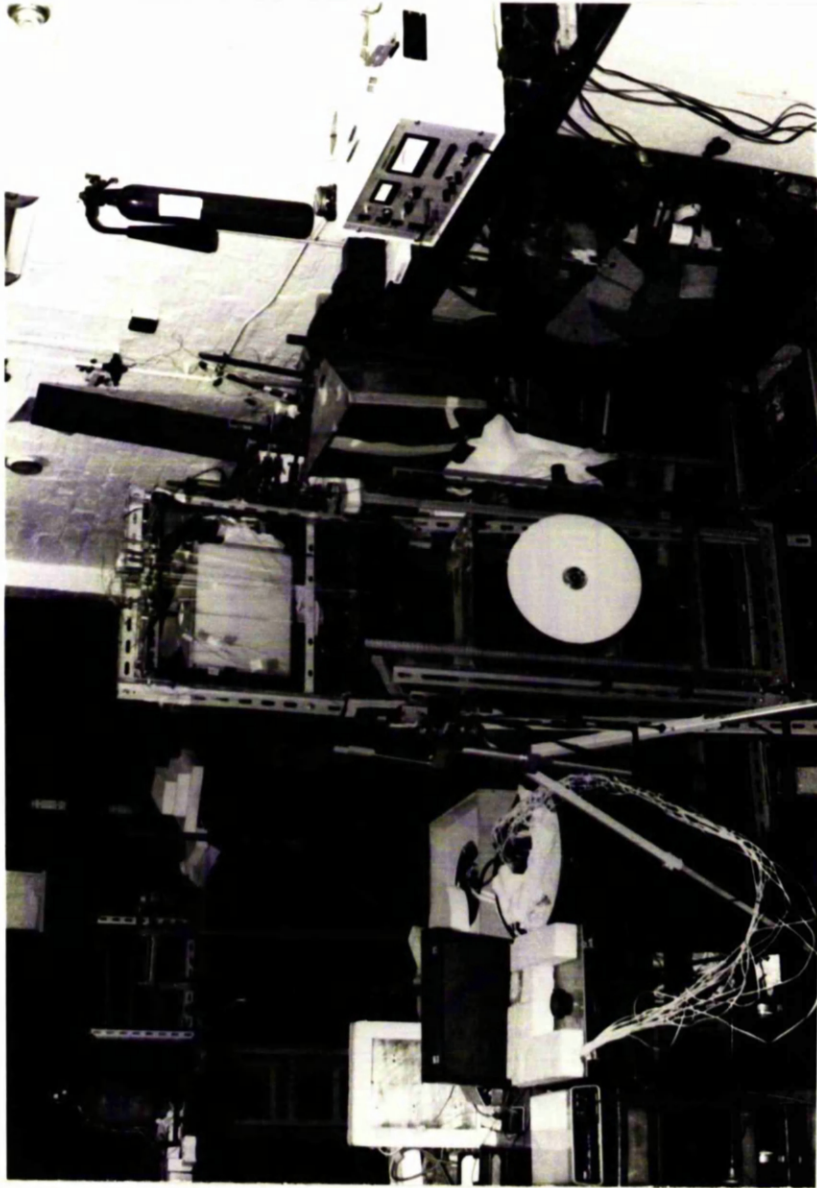
The transwall module was secured to a thick sheet of perspex screwed to a handy angle frame capable of tilting the transwall if so required.

Thermocouples and cathode rods<sup>+</sup> enter the open transwall and are secured in position by the following method. Each passes through an external screwed brass tube carrying collars. The tubes are clamped onto a slotted plate and a wedge washer rotated to provide a varying inclination (See Fig. 3.40 and Ph. 6).

<sup>+</sup> required for thymol blue technique, section 3.4.5.

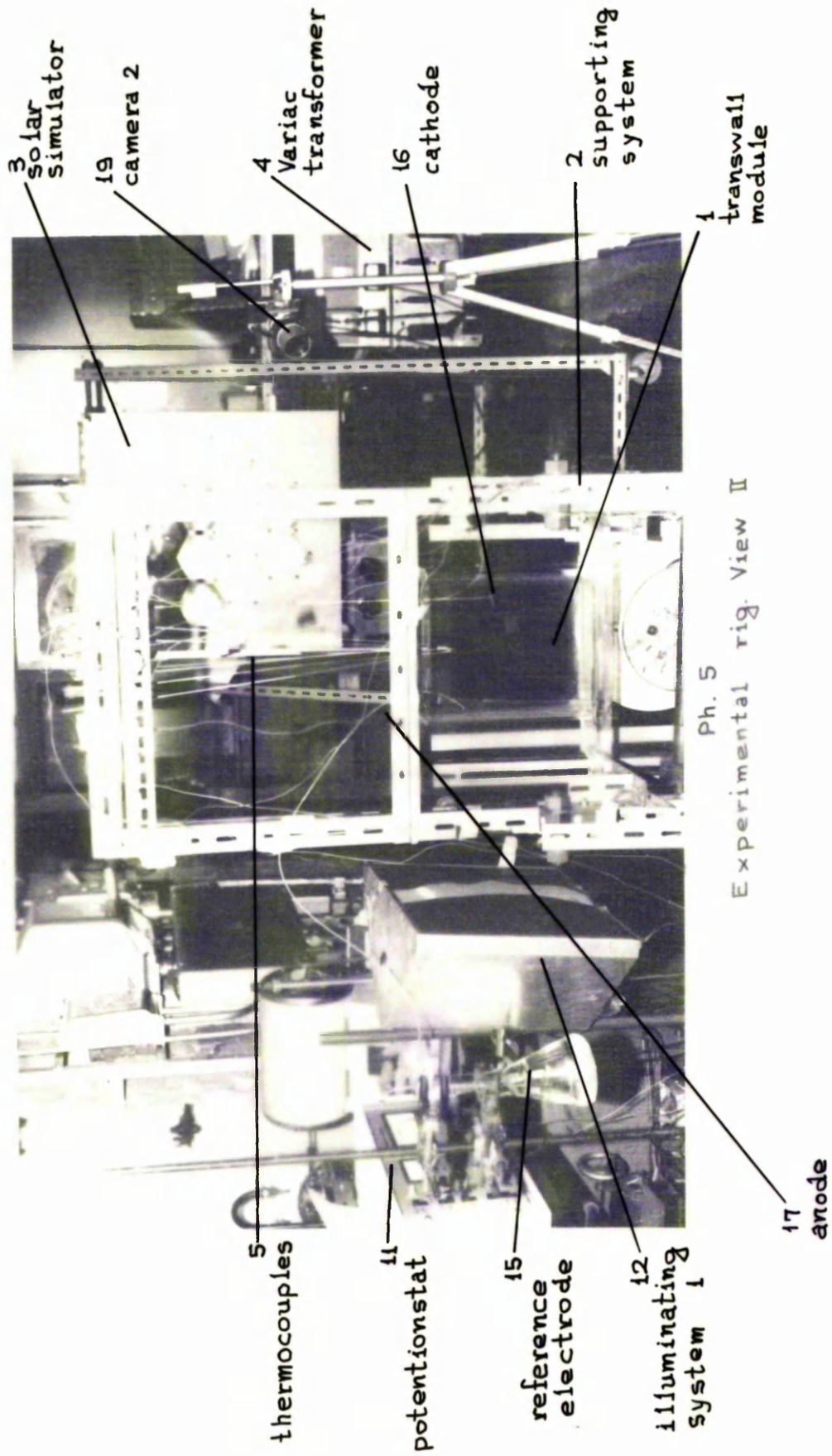


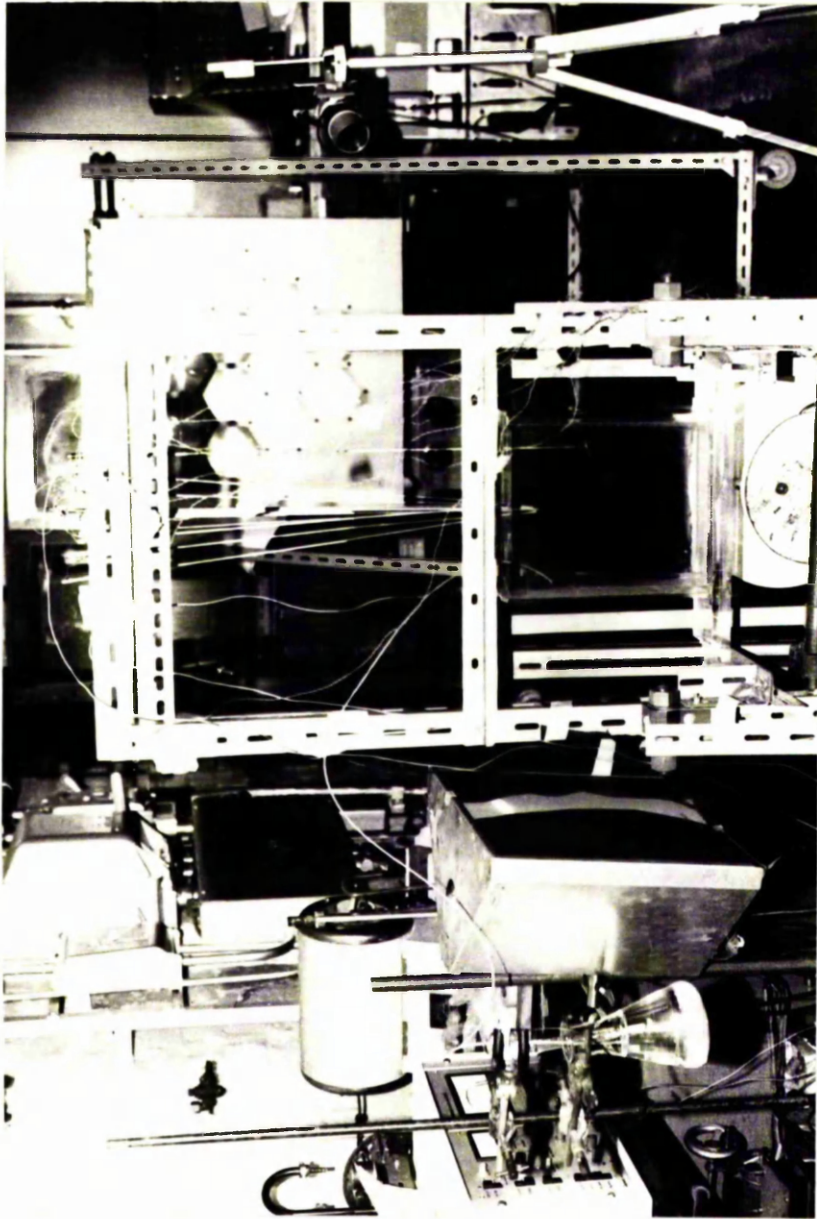
Ph. 4  
Experimental rig. View I.



Ph. 4  
Experimental rig. View I .

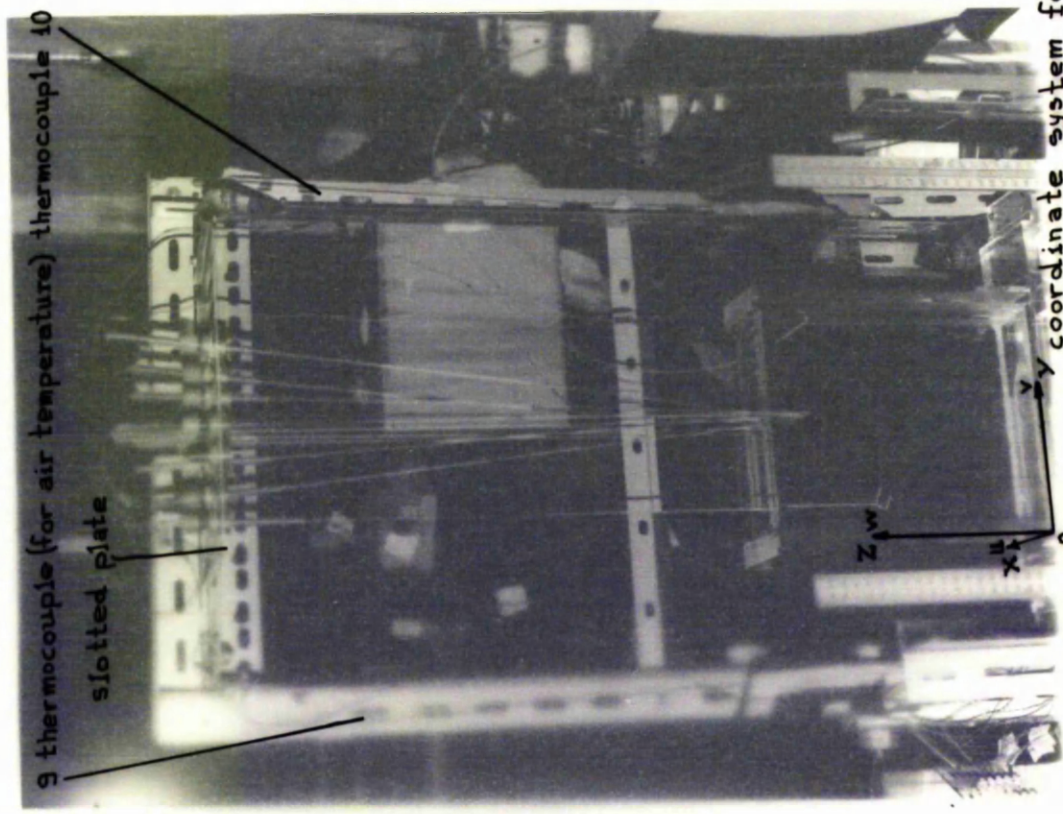




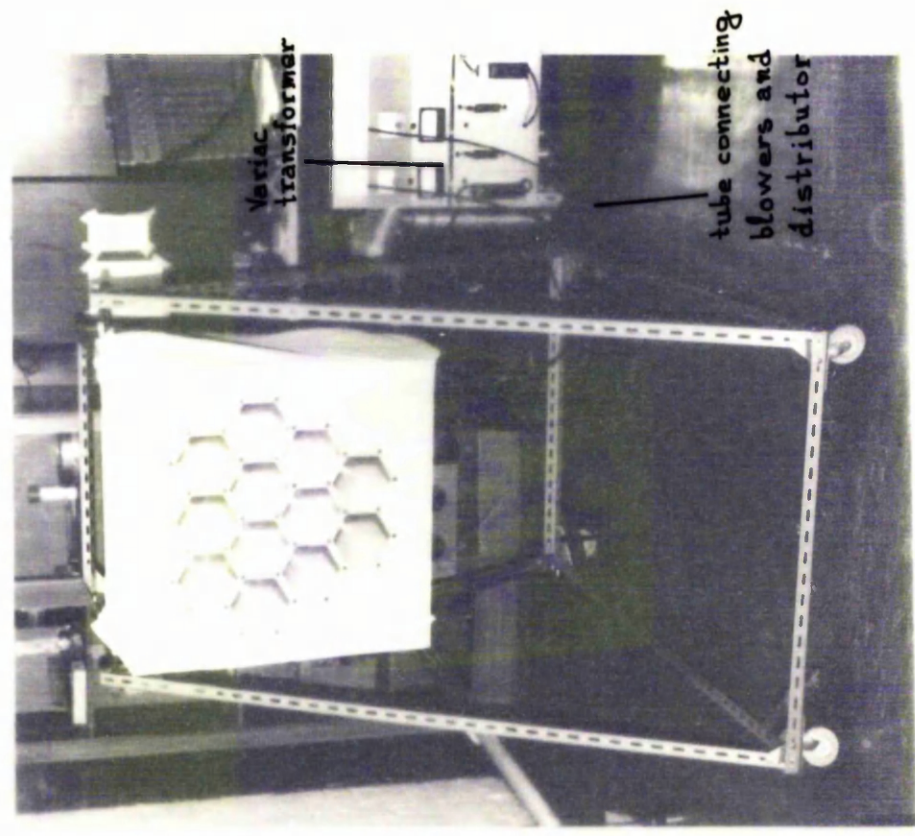


Ph. 5  
Experimental rig. View II

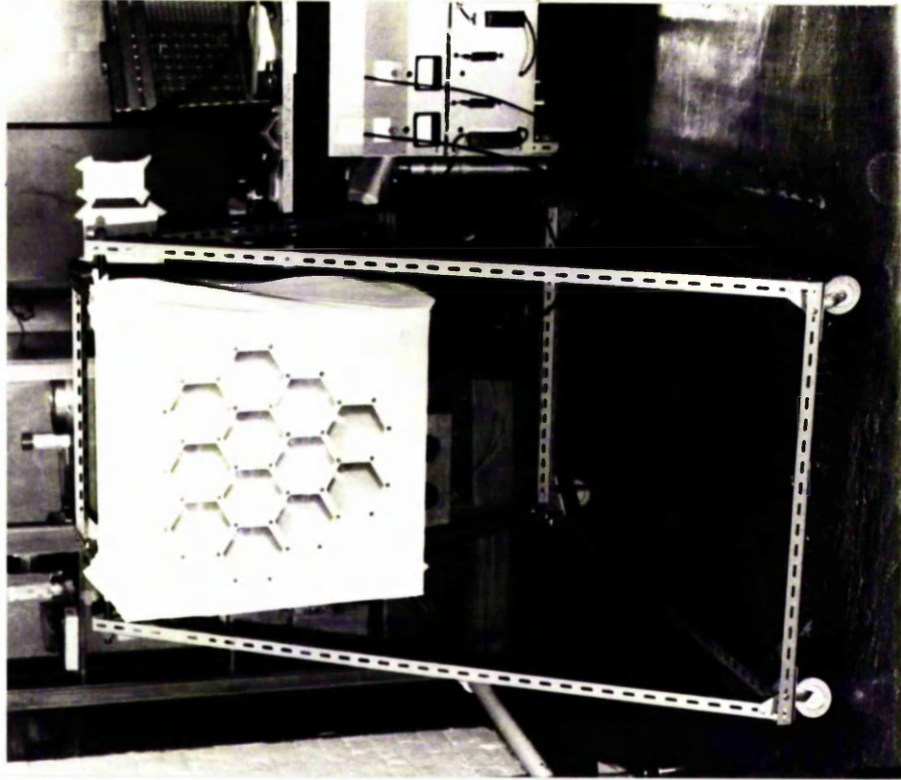




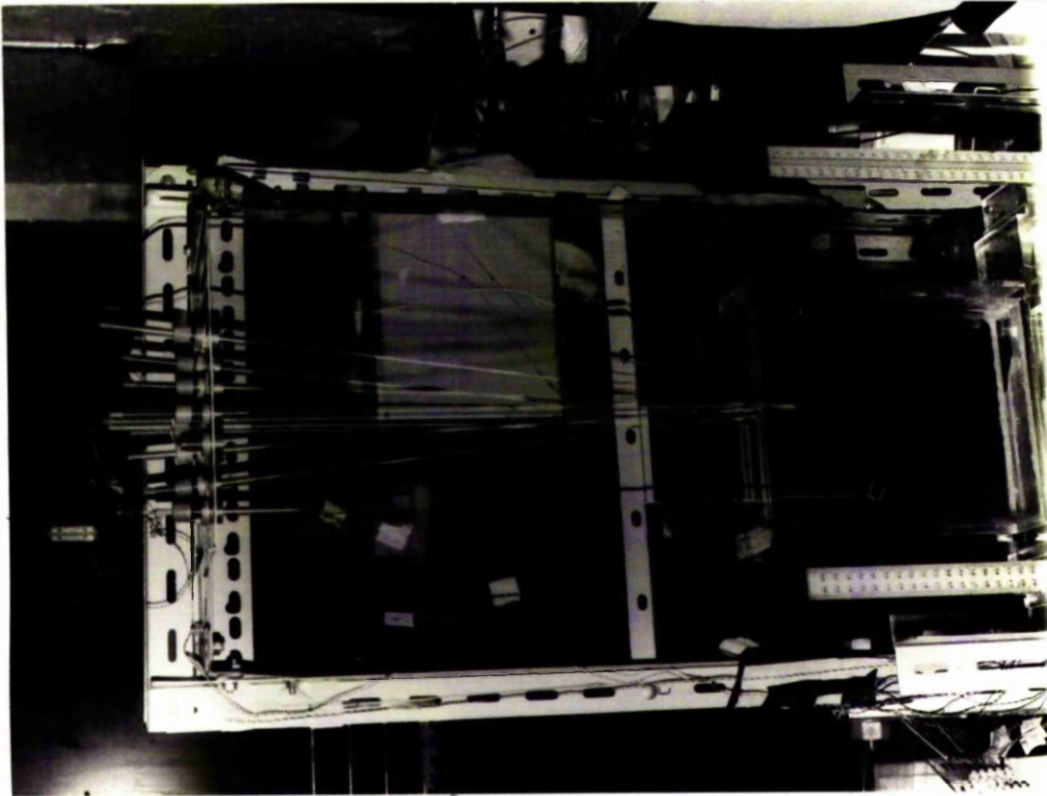
Ph. 6  
Experimental rig. View III



Ph. 7  
Solar Simulator



Ph. 7  
Solar Simulator



Ph. 6  
Experimental rig. View III



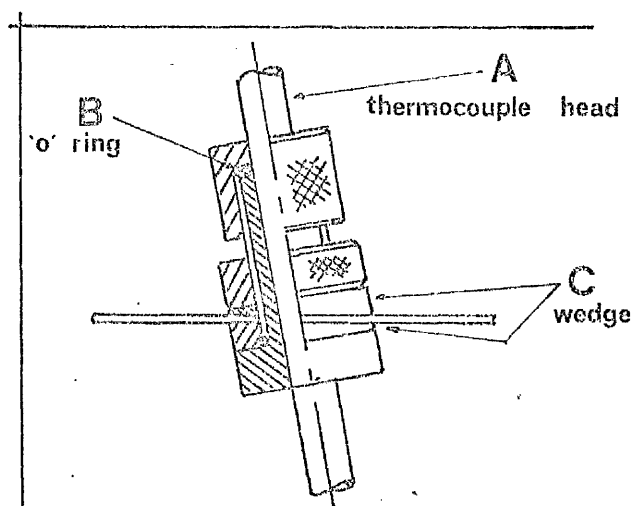
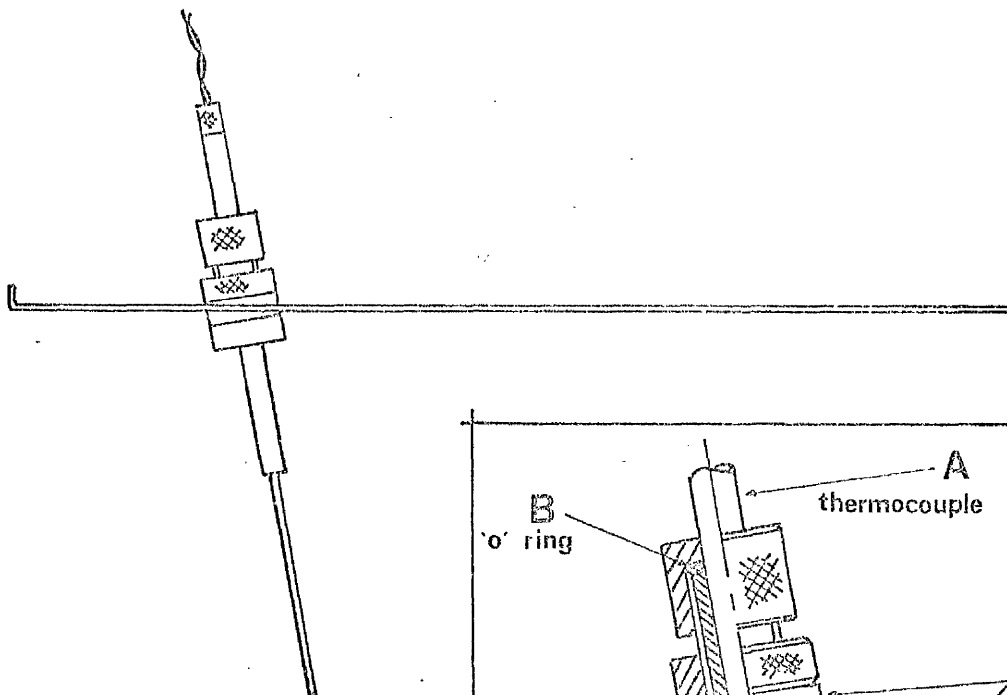
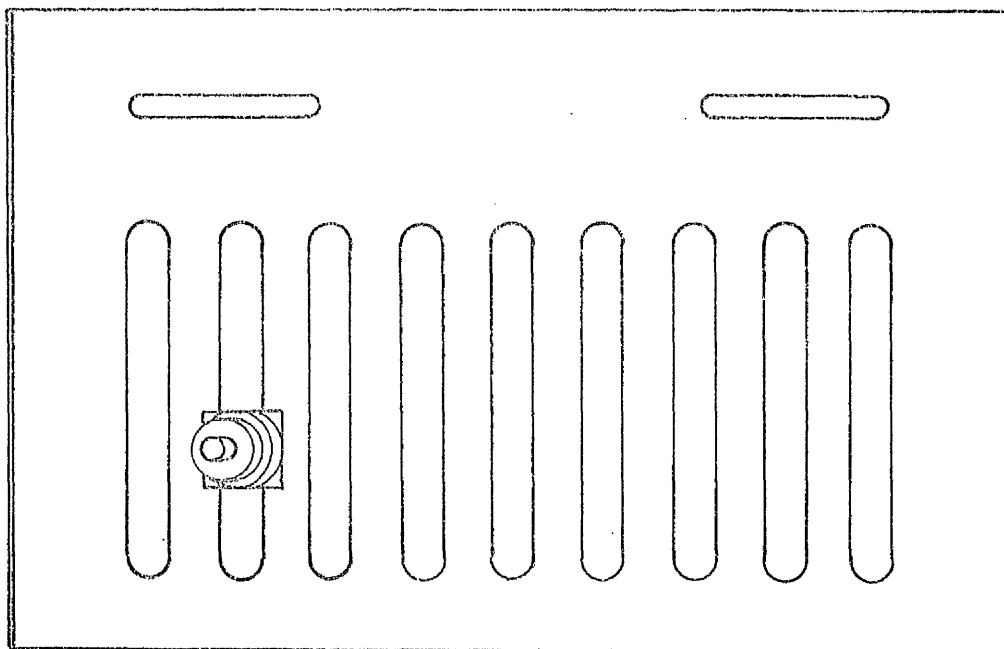


Fig.3.40  
Thermocouple  
Mounting  
Scale 1/2

Clamp  
Scale f.s.

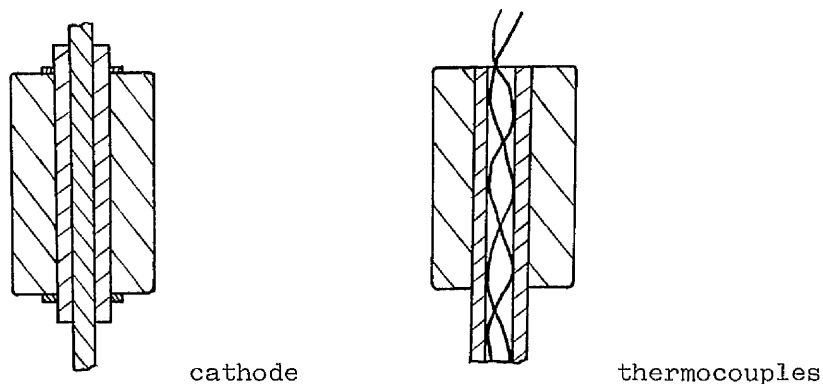


Fig.3.41

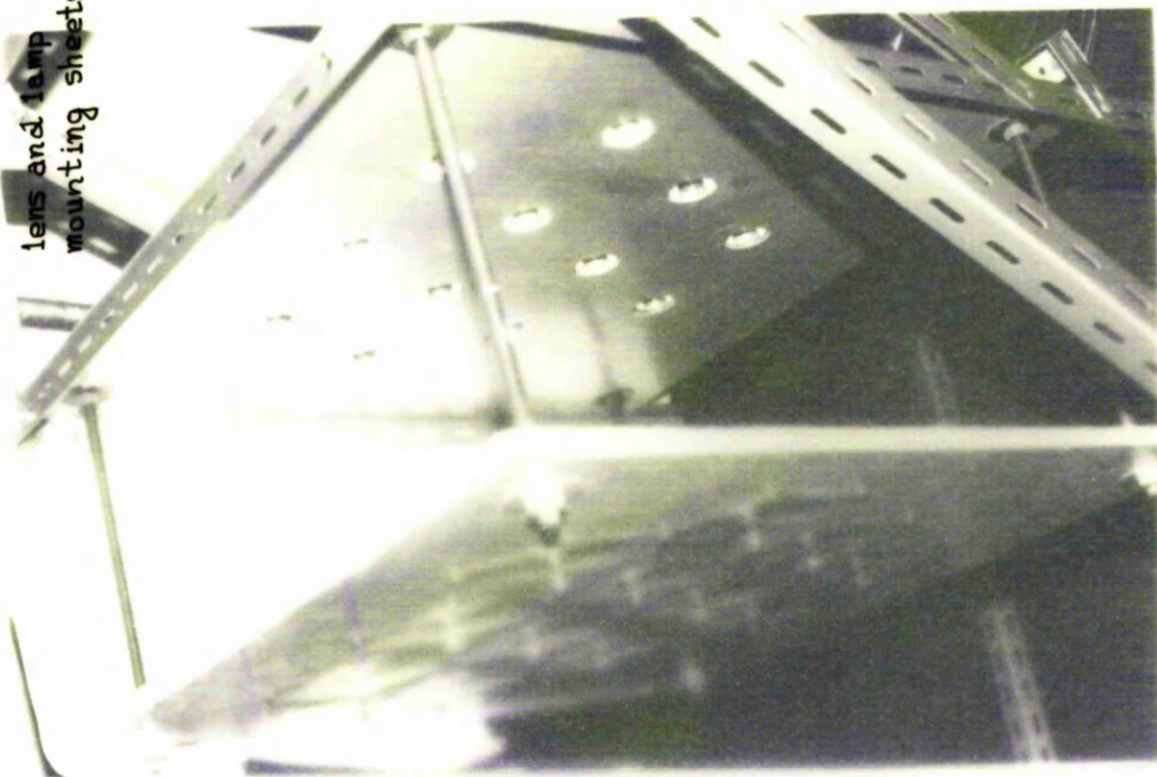
### 3.4.3 The Solar Simulator

The transwall module is irradiated by a solar simulator, constructed to produce direct radiation with spectrum of air-mass 2 (see Ph.7 , Ph.8 and Ph.9 ). It is a simulator of lamp-lens combination, with twelve ELH Quartzline projector lamps with dichroic reflectors mounted on an 0.32 cm thick aluminium sheet, 76.2 cm by 76.2 cm with round holes for the lamps. The twelve Fresnel lenses are mounted on a 1.91 cm thick plywood sheet, 76.2 cm by 76.2 cm with hexagonal holes for the lenses. The distance  $\ell$  between the lamp and lens mounting sheets, being parallel to each other, can be varied by the four threaded rods and their accompanying washers and nuts, as can be seen in Ph.7 and Ph.8. Fig.3 and Fig.4 of Appendix P give details of the aluminium lamp-mounting sheet and the lens-mounting sheet, respectively.

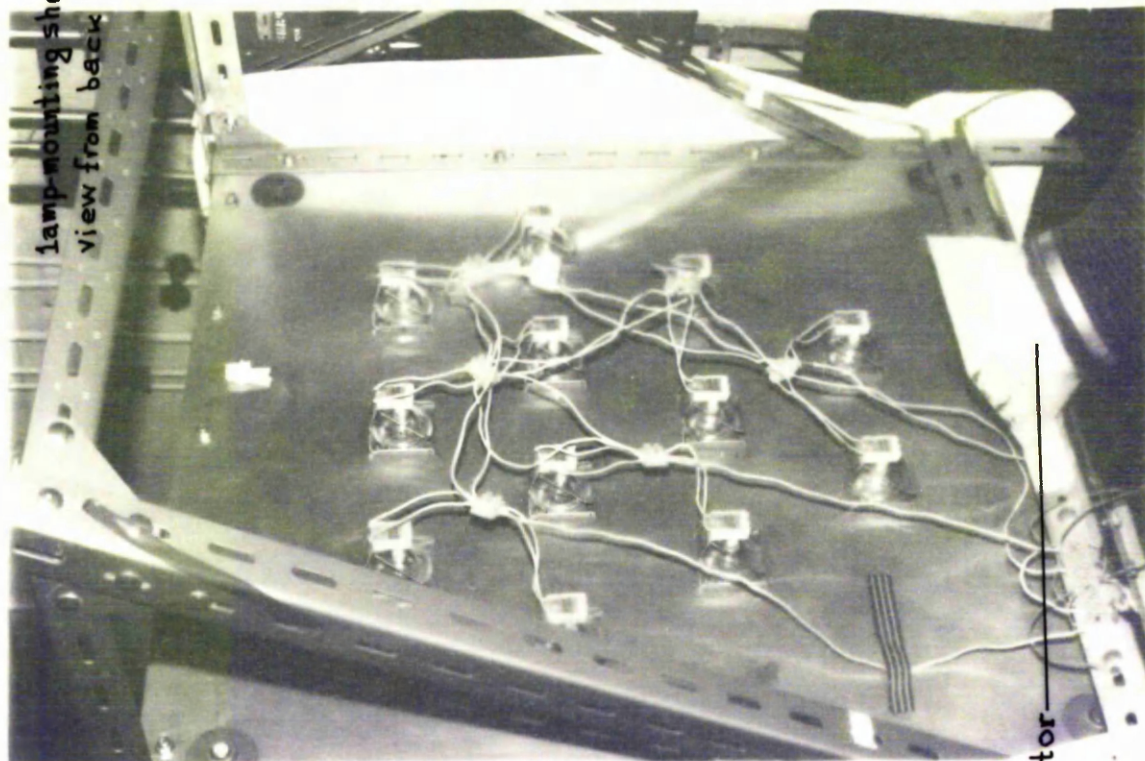
Power to the lamps, each of which is rated at 120 volts, 300 watts is supplied by a triple-ganged Variac transformer (Ph.5 and Ph.7 ). Only two windings are used, each supplying six of the lamps connected in parallel. The use of the transformer is necessary to lengthen the life of these lamps by controlling the voltage. The total power of the simulator is 3.5 KWatts and provision has been made for cooling the lamps with air supplied by two C.F. blowers each of 0.5 hp through a distributor which gives an almost uniform air distribution over the rear of the lamps (Ph.7 and Ph.9 ). The life of a lamp is directly related to its applied voltage, the type of cooling and its position (horizontal, vertical and so on), according to Yass et.al (33) (73) .

As can be seen from Ph.7 , the simulator can easily be moved to another position by means of its four wheels and secured by the four jacks . The need to produce radiation at various angles

lens and lamp  
mounting sheets



Ph. 8

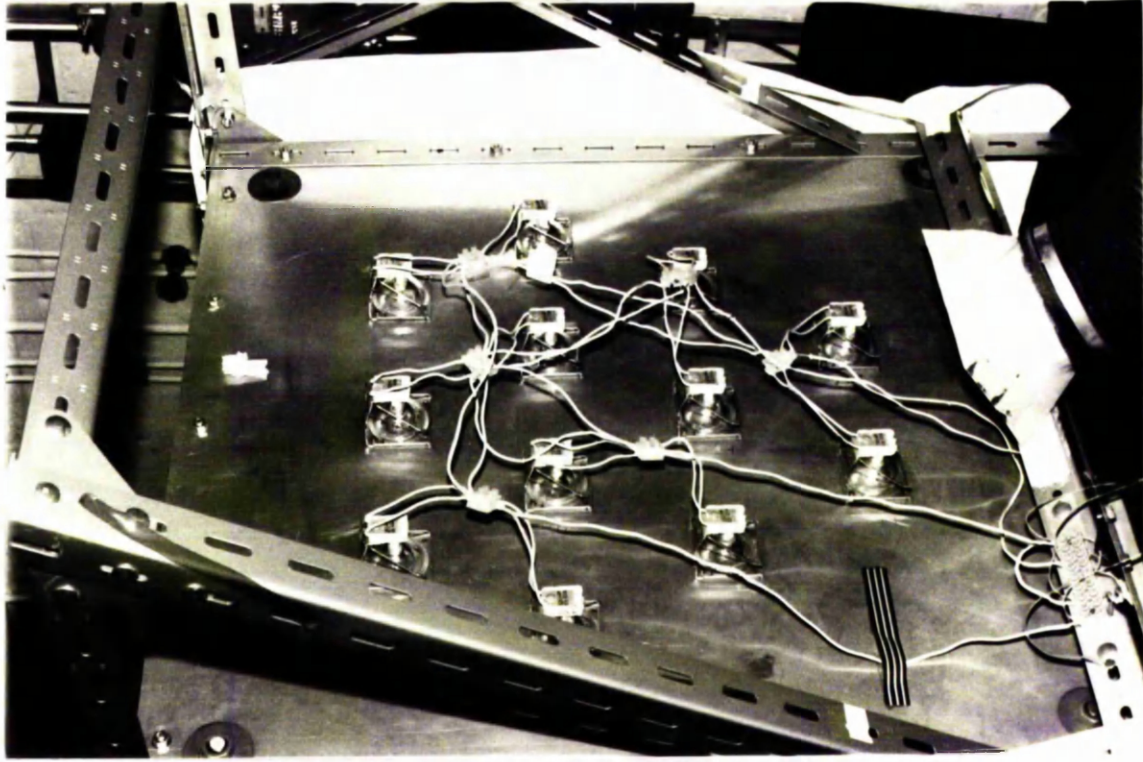


lamp-mounting sheet  
view from back

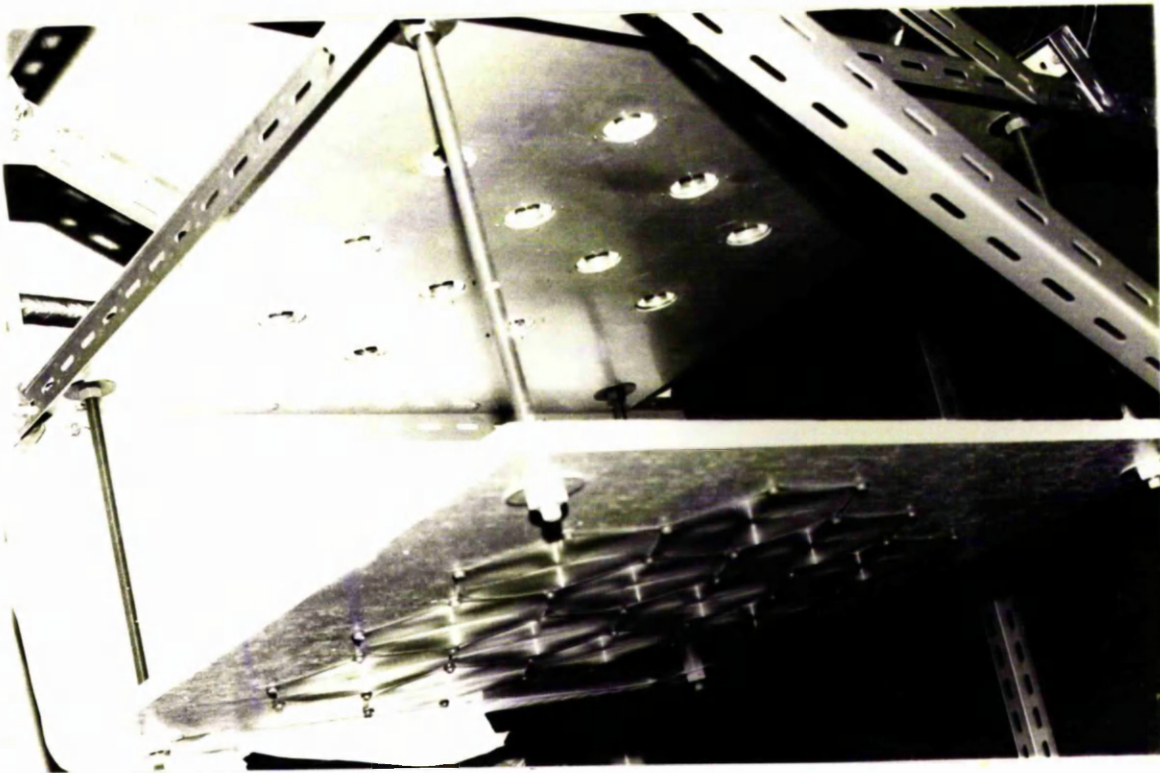
air  
distributor

Ph. 9





Ph. 9



Ph. 8

of incidence has led to the particular construction of the simulator shown in Ph.5 and Ph.7, in which the aluminium lamp-mounting plate is hung from the two threaded rods of 1.9 cm diameter. These threaded rods are 1.65 m high, sufficient to allow for operation with the lamp-mounting plate horizontal.

The construction of the solar simulator at M.E.R.A. followed the lines put by Yass et al. (33), (73) and Grimmer et al. (74) to ensure a long term radiation similar to air-mass 2 radiation. Table 3.7 gives the fractioned average radiation produced by the solar voltage across the lamps. This table was derived from digitisation of the curves given by Yass et al. (73) after measurements of the radiation spectrum of two similar combinations of lens-lamp. The first combination is referred to voltages of 90, 105 and 120 volts and the second one to voltages of 101 and 117 volts. The combination lens-lamp used in the construction of the solar simulator at M.E.R.A. is the one suggested by Grimmer et al. (74) similar to those used by Yass et al. (73) in respect to the radiation spectrum. A comparison of Table 3.7 with Table 1.2, page 22, reveals that the simulator radiation has generally a very small ultraviolet portion and an enhanced visible portion. It can be said that the simulator radiation spectrum at 90 volts voltage is closer to the air-mass 2 spectrum, but for voltages higher than 101 volts the simulator radiation spectrum is closer to the air-mass 1 spectrum. As the voltage increases an enhancement of the visible portion of the simulator radiation occurs at the expense of the infrared portion. This variation in the simulator radiation spectrum by lowering voltages has an additional benefit of prolonging lamp life beyond the 35hrs at 120 volts (73). The change in the output and radiation spectrum of the lens-lamp combination over a long period of time because of degredation of both lens and lamp is negligible, according to measurements by Yass et al. (33), (73). The almost constant output over the whole life of a lamp has been experienced in the case of the solar simulator at M.E.R.A..

Apart from the spectral distribution of the produced radiation, other essential considerations for the construction of a solar simulator should be the average total irradiance on the test plane,

the uniformity of the total irradiance, the volume uniformity and the subtense angle of the produced radiation. These considerations have been dealt with by Paparsenos (75) in "Optimization of solar simulators", (Appendix P), in which a theoretical analysis has been presented for the optimization of solar simulators consisting of  $N$  light sources positioned at  $N$  different positions on a mounting plane at distance  $d$  from the test plane. The theoretical analysis employs the integer programming method of operation research to give the optimum answers to the considerations mentioned above. The improvement in the uniformity of total irradiance over a specified area of the test plane produced by a specified solar simulator can be achieved by an appropriate positioning of the available lamps on the mounting plane. Thus the difficulty and cost of improving the uniformity by varying the lamp output can be bypassed. On the other hand, the tedium of trial and error lamp arrangement or the expensive of replacing lamps, that are exceptionally bright or dim, is eliminated. The application of the method requires the knowledge of two quantities (1). The relative radiant output of each lamp,  $R_v$ ,  $v = 1$  to  $N$ . (2) The distribution of irradiance in the test plane from each light source  $v$ ,  $f_v(x)$ ,  $v = 1$  to  $N$  and  $x$  the distance from the point  $x = 0$ , that is the projection of the centre of light source  $v$  on the test plane. Fig.4 of Appendix P gives the measured relative irradiance of twelve lamps as functions of the lamp voltages. Fig.5 of Appendix P, gives two typical irradiance distributions  $F(x)$ , as functions of the distance  $x$ , normalized at  $x = 0$ . These two distributions correspond to two cases of the lamp-lens combination used in the solar simulator at M.E.R.A. with different distances between the two mounting planes  $\ell$  and between the lens-mounting plane and the test plane  $d$ .

The computing programs based on the theoretical analysis, use the H02BAF NAG subroutine to solve the integer programming problem. Because the present integer programming problem is actually a Knapsak problem (with solution only 1 or 0) another computing subroutine was developed based on the algorithm by Kucharczyk (76), that solves the Knapsak problem. Unfortunately the new subroutine required so much more computing time than the H02BAF NAG subroutine so that it was abandoned. However, a disadvantage in using the H02BAF NAG subroutine was experienced for the particular magnitude of the relative radiant output of the light sources (lamp + lens)

used in the M.E.R.A. solar simulator for number of twelve ( $N = 12$ ) light sources and positions and number of twenty five ( $K = 25$ ) points on the test-plane: the maximum integer number of the machine was exceeded as the process of the theoretical analysis approached the optimum solution. As a result it was necessary to resort to a higher maximum integer number of the machine with the consequence of a much longer computing time. Again the new sub-routine of the Knapsak problem seemed to require much more computing time.

The experimental verification of the theoretical analysis which was achieved using the M.E.R. A. solar simulator was very satisfactory. Some of these results are presented in Appendix P. Fig. 3.42 and Fig. 3.43 give an optical representation of the predicted and measured results on total irradiance of Table 1 of Appendix P. The second case with distances  $\ell = 35$  cm and  $d = 270$  cm gives better optimum uniformity of the total irradiance over the hexagon area of about  $0.5\text{m}^2$  of the test plane in comparison with the first case with distances  $\ell = 29$  cm and  $d = 340$  cm, for both predicted and measured values. The optimum uniformity, in both cases, is achieved by the same positioning of the available twelve lamps. For the second case smaller subtense angles are also predicted but the average total irradiance is smaller than for the first case (average measured values,  $468\text{ W/m}^2$  for the first case and  $413\text{ W/m}^2$  for the second case).

Table 3.7

Fractioned average radiation produced by the solar simulator.

(Total radiation = 1.0)

wavelength band	Voltage, volts					
$\mu\text{m}$	90	101	105	117	120	
$0.3 \div 0.35$	0.0	0.0	0.0	0.0	0.0	) ultraviolet
$0.35 \div 0.4$	0.004	0.002	0.008	0.005	0.008	
$0.4 \div 0.6$	0.204	0.237	0.232	0.251	0.258	) visible
$0.6 \div 0.75$	0.336	0.298	0.350	0.335	0.352	
$0.75 \div 0.9$	0.174	0.139	0.170	0.151	0.170	) near
$0.9 \div 1.2$	0.119	0.124	0.106	0.106	0.097	
$1.2 \div 2.1$	0.163	0.188	0.134	0.149	0.115	) infrared
$2.1 \div 4.1$		0.012		0.004		

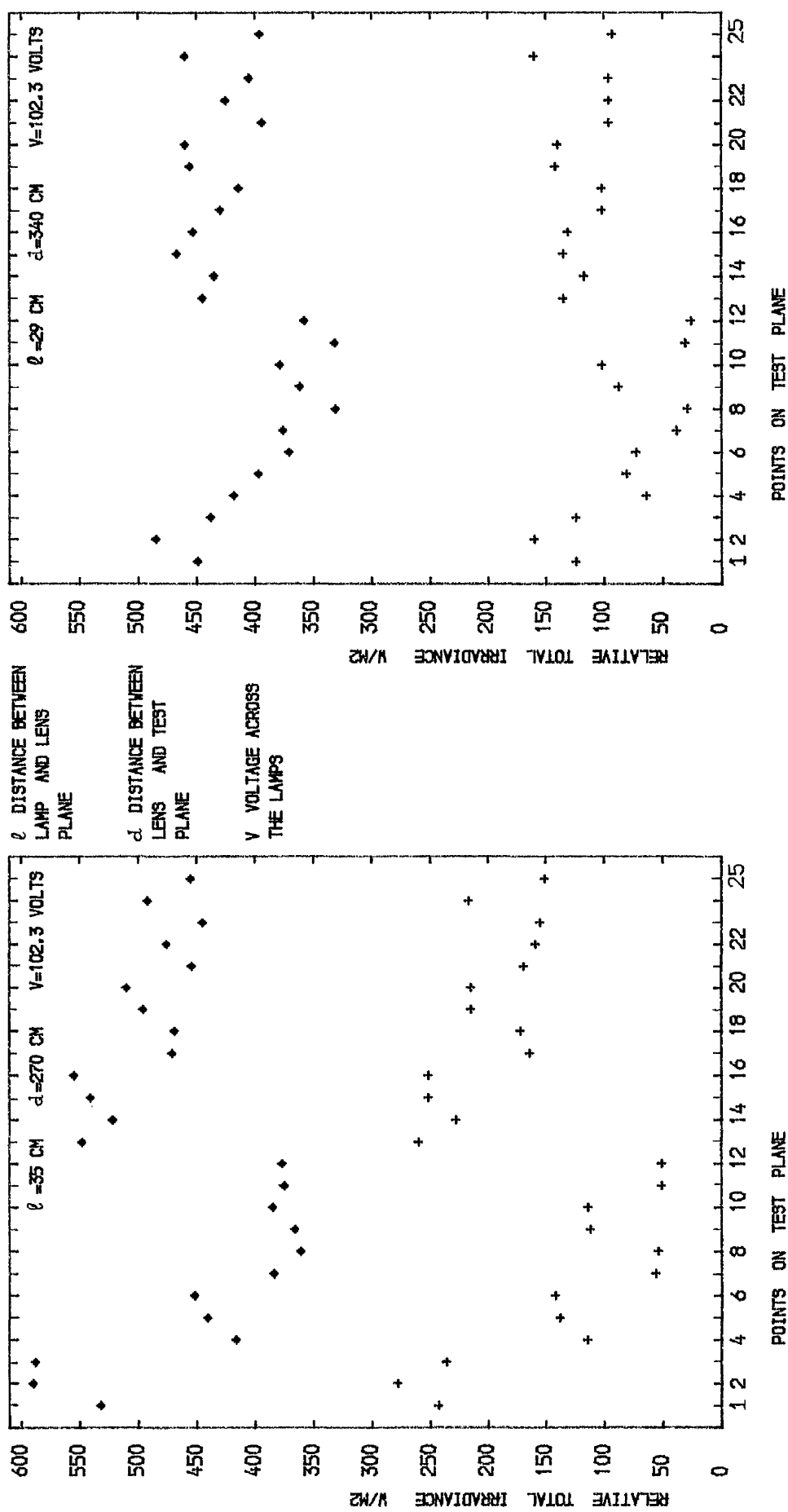


FIG. 3.4.2

MEASURED ♦ AND PREDICTED + TOTAL IRRADIANCE

The values with \* are real values.

The values with + are real values minus  $300 \text{ W/m}^2$ 

FIG. 3.4.3

MEASURED ♦ AND PREDICTED + TOTAL IRRADIANCE

The values with \* are real values.

The values with + are real values minus  $300 \text{ W/m}^2$



#### 3.4.4 Temperature measurements

The thermocouples, used for the temperature measurements inside the transwall module, were constructed from P.T.F.E. insulated chromel-alumel wires of 0.2 mm diameter. The wires were passed through a twin-bore ceramic tube 1 mm o.d. inserted in and attached to a single-bore ceramic tube 2 mm o.d., which in turn was attached to a brass tube 6.3 mm o.d. again by Araldite (see also Fig.3.41 , page 196).

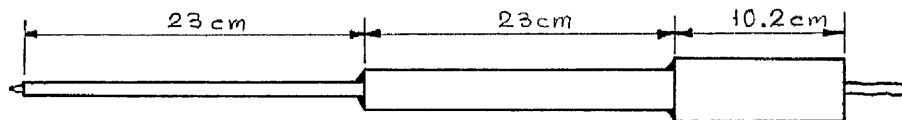


Fig.3.44

#### Calibration

The thermocouples were calibrated against a Tinsley platinum resistance thermometer (number 207258) the resistance of which was measured by an 8 decade Tinsley A/C Bridge, model 5650. The voltage output of each thermocouple was measured by a digital voltmeter, Solatron model 7045 which was calibrated against a D.C. voltage standard, Time Electronics model 2003 whose accuracy in turn was checked against N.P.L. calibrated standard cells via a Tinsley "special order" potentiometer type 5205A.

The calibration of the thermocouples was performed using a calibrated triple point cell and a controlled temperature paraffin bath for temperatures from 15°C to 35°C. The temperature variation at every temperature in this range was of 0.01°C order of magnitude. To overcome possible temperature difference between the resistance thermometer and the thermocouples these were inserted into drilled holes in an aluminium cylinder block of 7.5 cm diameter and 12.6 cm length, placed inside the paraffin bath. Five readings were taken at each temperature for the resistance thermometer and each thermocouple. Applying the least square technique, calibration polynomials of the type  $t = A \cdot E^2 + B \cdot E$  were formed for each thermocouple ( $t$ : temperature in °C and  $E$ : voltage output in mvolts).

#### Measurements

Each thermocouple was connected to the digital volt meter (No.6 in Ph.4) via a Cropico SP2 selector switch (No.7 , in Ph.4). Successively, every five seconds, the voltage output of each thermocouple was recorded. Five seconds after the last thermocouple voltage recording, the voltage output of a Kipp pyranometer (No.8 in

Ph.4 ) was recorded by the same digital voltmeter at a point close to the transwall module. The relationship between the radiation intensity at the pyranometer position and at various positions of the front plane of the transwall module was established by a number of measurements of the radiation intensity before the beginning of the experiments. Each cycle of the thermocouples voltage output recording lasted ninety seconds. Two of the thermocouples measured the temperature of the air of the laboratory room (No. 9 and No.10 in Ph.6 ), activated by a temperature sensor, placed about two meters distance from the transwall module. The type of temperature variation of the room air during the experiments is shown in Fig.3.46,3.48,3.50,3.52,3.54 and 3.56. It is clear from the figures that it was difficult to establish a predetermined, almost constant, air temperature.

The numerical prediction of the flow inside the various transwall modules has shown that a certain time after the onset of the flow, the temperature pattern along the x axis (along the small dimension of the transwall module) remains almost unchanged. Fig.3.45 shows the predicted pattern of temperature along the x axis at different height ratios,  $(Z/H)$ , for a vertical transwall module of  $L = 7.4$  cm dimension along the x axis ( $Z$  is the height of the plane of measurements from the bottom of the module and  $H$  is the total height of the liquid in the module). Fig.3.45 is valid for the three cases with different aspect ratio,  $(H/L)$ , 3.21, 6.41 and 8.11, examined numerically in section 3.2.4. This means that the aspect ratio, at least for the examined cases, is not a critical factor in determining the temperature pattern along the x-axis. This also holds for small variations ( $\sim \pm 12\%$ ) of the average value of the intensity of the incident radiation ( $440 \text{ W/m}^2$ ).

The almost unchanged character of the temperature pattern along the x-axis is evident from measurements as well, as Fig.3.47,3.49,3.51, 3.53,3.55 and 3.57 show. This fact suggested comparisons between the predicted and measured temperature patterns along the x-axis on the basis of similar height ratios,  $(Z/H)$ . These comparisons could be considered as an indirect verification of the numerical prediction of the flow inside the transwall modules. The heat fluxes between the air and the outside glass surfaces of the transwall module encountered in some of the experiments are much higher than those used in the numerical analysis. The importance of this on the

temperature pattern has not yet been examined. There is evidence, (Fig.3.47, 850 secs curve) that indicates a difference in temperature pattern occurring for a substantial change in outside temperature conditions. Thus, the following discussion on the comparison of predicted and measured temperature patterns along the x axis should be seen under these limits of knowledge.

The four pairs of figures (3.46, 3.47), (3.48, 3.49), (3.50, 3.51) and (3.52, 3.53) are referred to the case of the transwall module filled with distilled water. The average received radiation, the aspect ratio and the height ratio are shown in each of these figures.

Fig.3.54 and Fig.3.55 are referred to the transwall module filled with a strong solution of thymol blue in distilled water and an average received radiation of  $364 \text{ W/m}^2$ . The measurements were taken at a height ratio of 0.80. The aspect ratio was 2.97.

Fig.3.56 and Fig.3.57 are referred to the transwall module with Antisun glass plate as middle absorbing glass, filled with distilled water and an average received radiation of  $363 \text{ W/m}^2$ . The measurements were taken at a height ratio of 0.42. The temperature pattern concerns only the front part of the liquid of the module in respect to the incoming radiation from the solar simulator. The aspect ratio of this part was 6.63.

The radiation absorption effect on the thermocouples response has been taken into account in the abovementioned figures (from Fig.3.46 to Fig.3.57). This is achieved by subtracting the the voltage of  $0.004 * e^{-3.3 * X}$  mvolts in the cases of the distilled water and the voltage of  $0.004 * e^{-4.5 * X}$  mvolts in the case of the thymol blue solution from the voltage output of each thermocouple. (X is the distance of the thermocouple, in cm, from the inside surface of the front glass of the transwall module). The radiation effect corrections are simplified expressions of preliminary experimental evidence. The actual expression may be critical on the temperature pattern near the front glass. For example a correction of  $A * e^{-0.8 * X}$  mvolts for distilled water (where,  $A = 0.0035$ , if  $X = 0$  and  $A = 0.0025$  if  $X > 0$ ) gives temperature patterns closer to those of Fig. 3.45 than the voltage correction of  $0.004 * e^{-3.3 * X}$ .

For the first case of the transwall module with distilled water, it is easy to see that the temperature pattern of Fig.3.47 3.49 and 3.53 is similar to the predicted temperature pattern which would result from an interpolation between the appropriate curves of Fig.3.45, at  $(Z/H) = 0.11$ ,  $(Z/H) = 0.28$  and  $(Z/H) = 0.88$  respectively.

A difference in the pattern about the distance of  $X = 1$  cm could be attributed to a false radiation effect correction. The temperature pattern of Fig. 3.51 for height ratio,  $(Z/H) = 0.57$ , is different from the predicted of Fig. 3.45, at  $(Z/H) = 0.58$ . A different radiation effect correction,  $A * e^{-0.8 * X}$ , mentioned before, improves the pattern, as Fig. 3.58 shows.

Although in the second case the transwall module is filled with thymol blue instead of distilled water (Fig. 3.55), a comparison can be made on the assumption that the higher absorptance of the thymol blue is not so important as to change the flow pattern inside the transwall module. It is easy to see that the temperature pattern of Fig. 3.55 is close to the predicted temperature pattern which would result from a kind of interpolation of the curves  $(Z/H) = 0.75$  and  $(Z/H) = 0.92$  of Fig. 3.45, at  $(Z/H) = 0.80$ .

The comparison of the curves of Fig. 3.57, third case, for which the height ratio is  $(Z/H) = 0.42$  with the predicted temperature patterns of Fig. 3.45, shows that the most similar temperature pattern is that with  $(Z/H) = 0.75$ . This slight change of pattern may be attributed to two reasons. a) the dimension along the x direction is  $L = 3.5$  cm in the third case, b) the middle absorbing glass plate absorbs a higher fraction of radiation than the back glass of the transwall module without the absorbing middle glass plate.

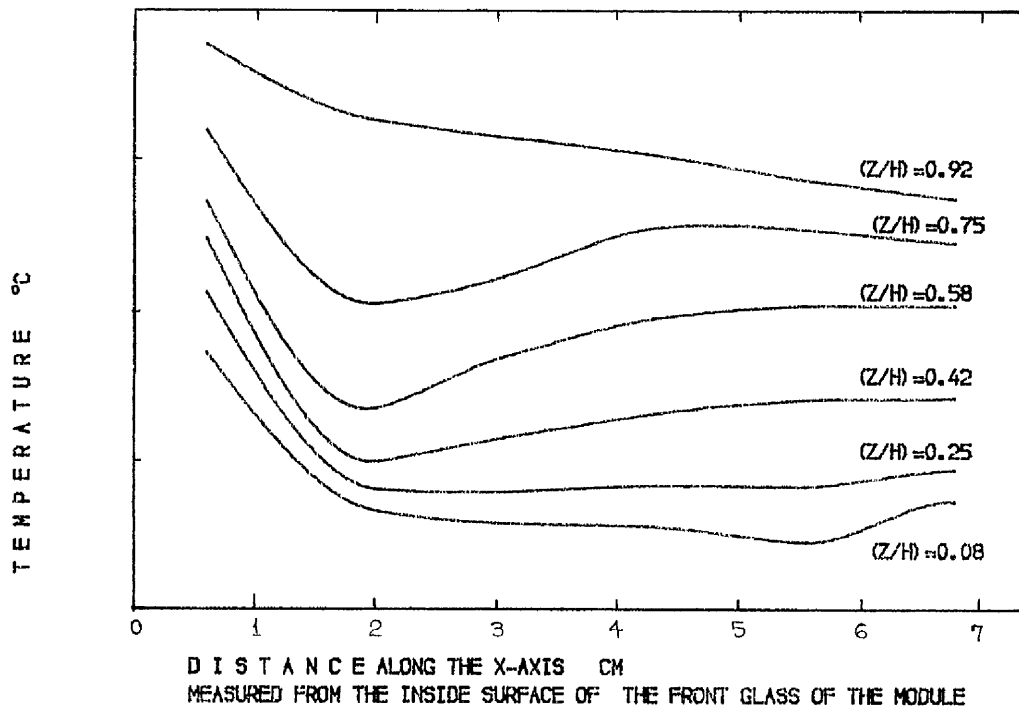


FIG. 3.45  
TEMPERATURE VARIATION ALONG THE X-AXIS (Predicted)  
Z IS THE HEIGHT OF A PLANE FROM THE BOTTOM OF THE MODULE.  
H IS THE HEIGHT OF THE LIQUID LAYER (Total).

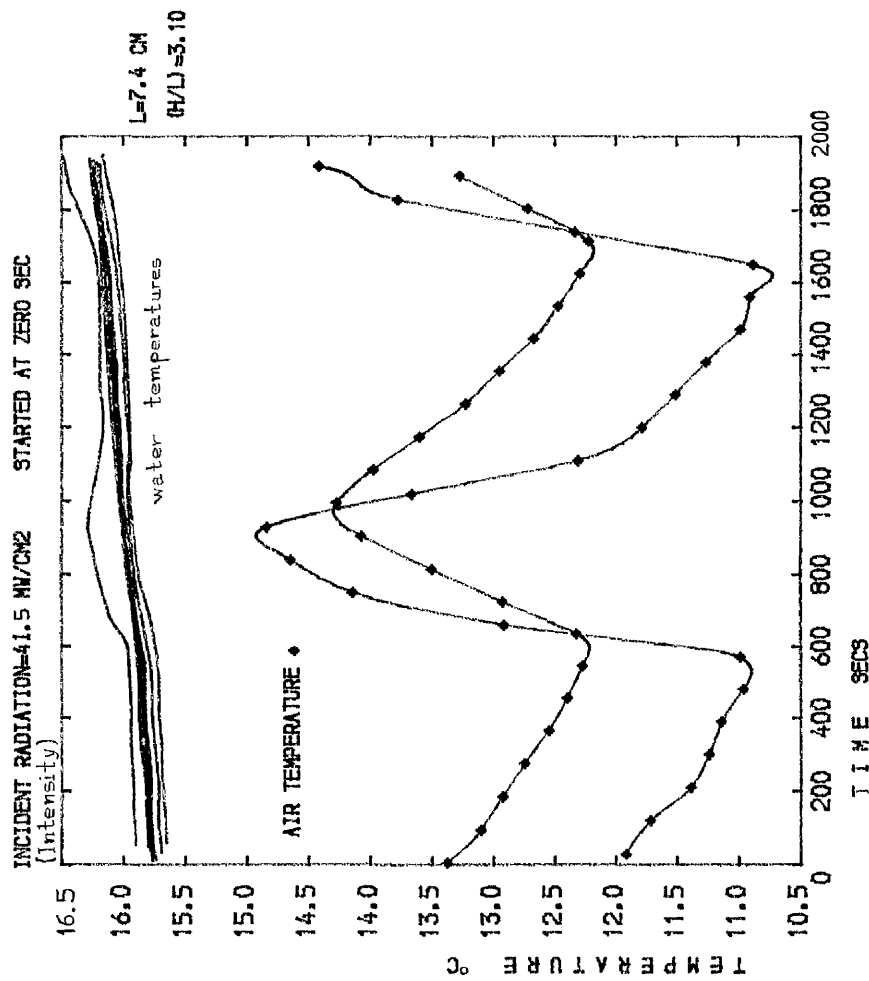


FIG. 3.46  
 TEMPERATURE MEASUREMENTS AT  $(Z/H)=0.11$

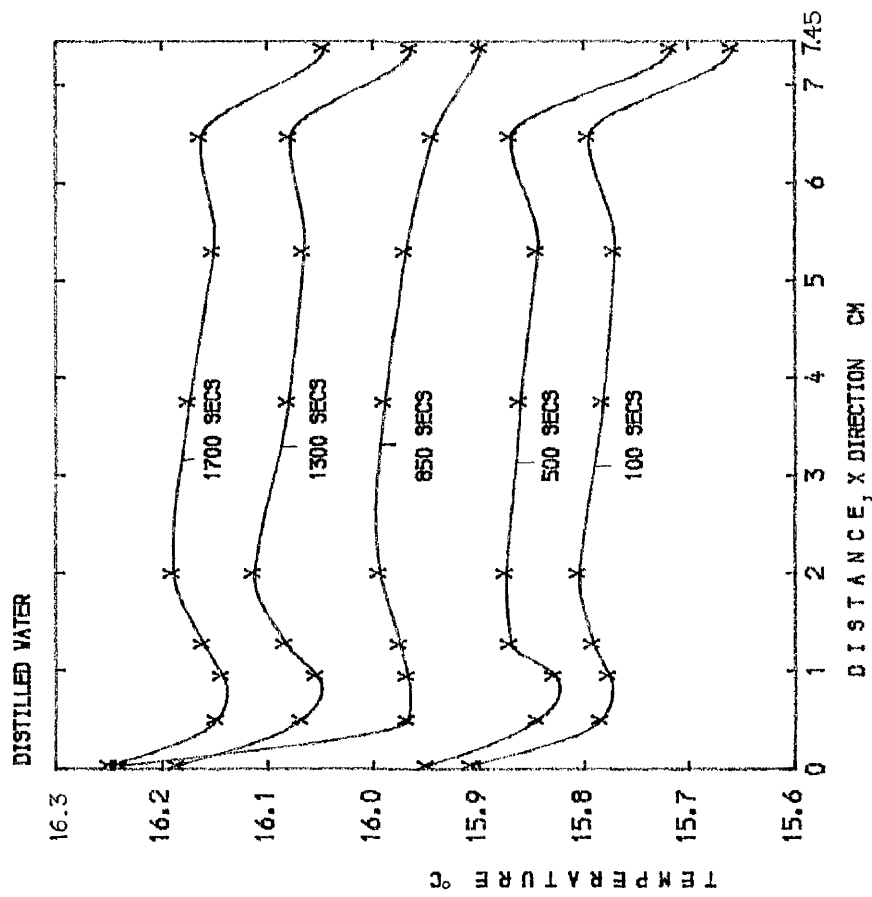


FIG. 3.47  
 TEMPERATURE MEASUREMENTS AT  $(Z/H)=0.11$   
 The distance is measured from the inside surface of the front glass of the module.

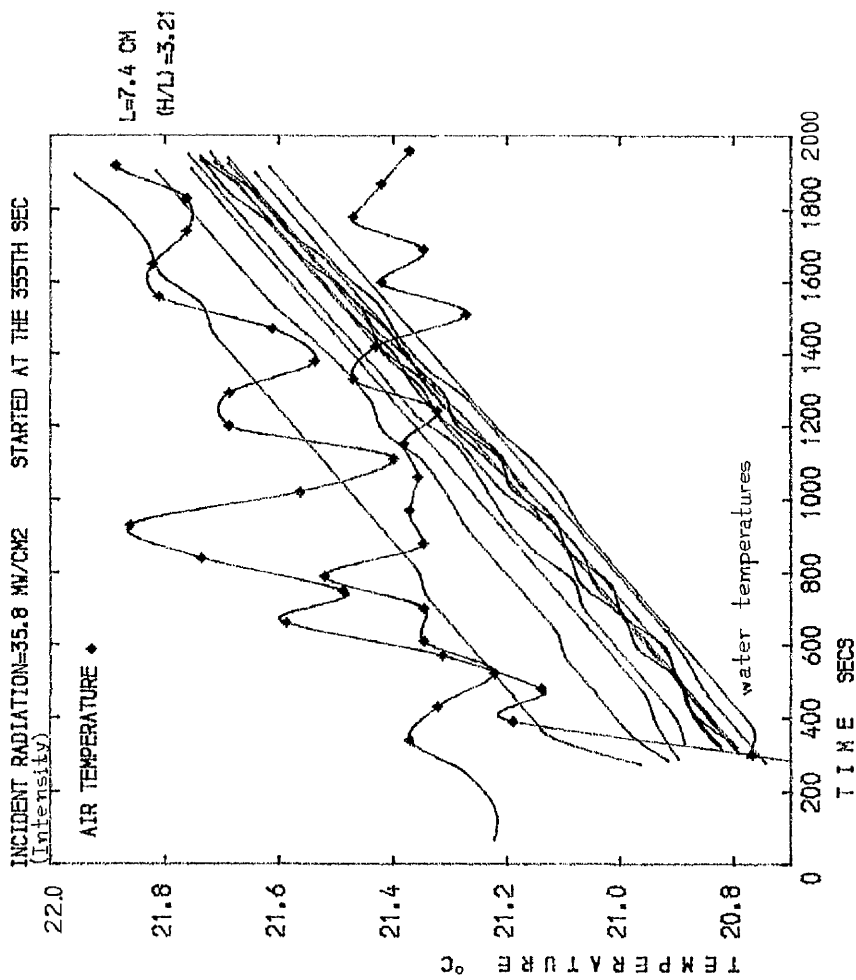


FIG. 3.48

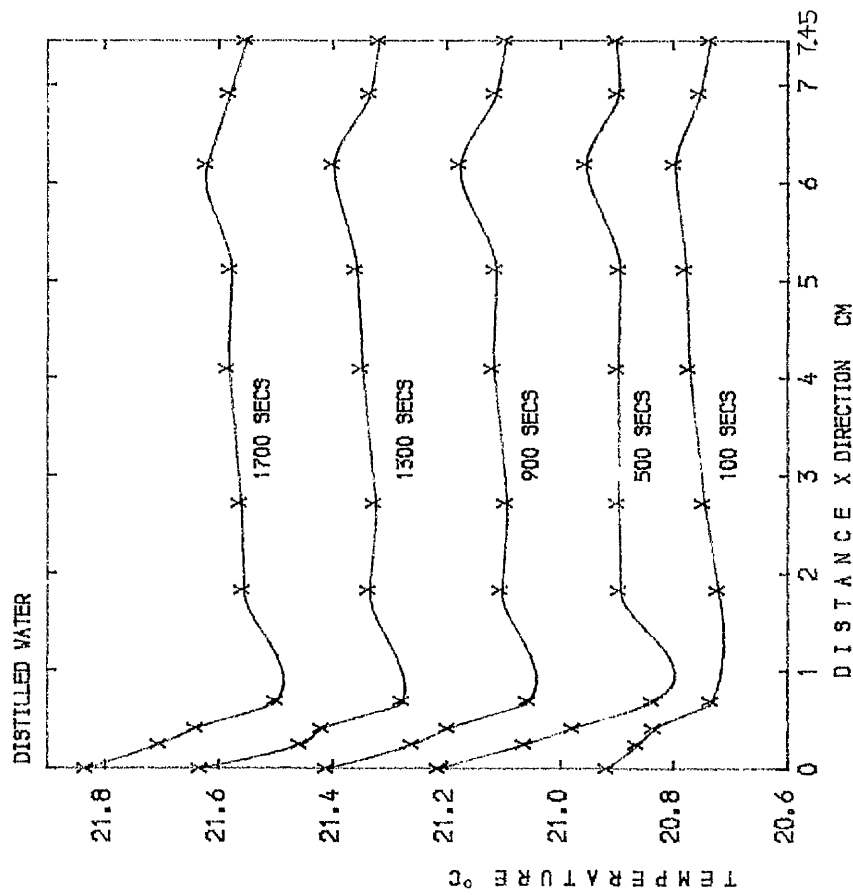
TEMPERATURE MEASUREMENTS AT  $(Z/H)=0.28$ 

FIG. 3.49

TEMPERATURE MEASUREMENTS AT  $(Z/H)=0.28$ 

The distance is measured from the inside surface of the front glass of the module.

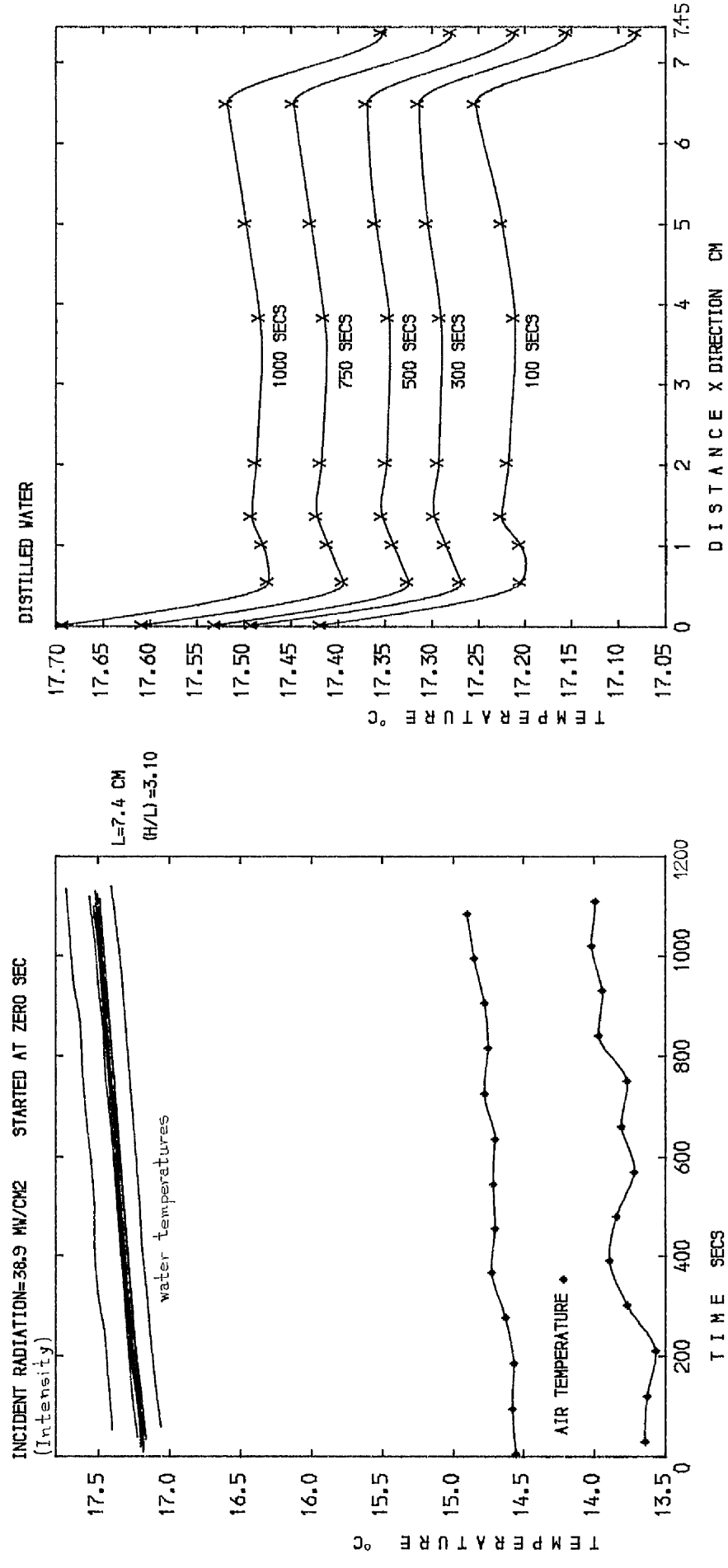


FIG. 3.50

TEMPERATURE MEASUREMENTS AT (Z/H)=0.57

FIG. 3.51

TEMPERATURE MEASUREMENTS AT (Z/H)=0.57

The distance is measured from the inside surface of the front glass of the module.

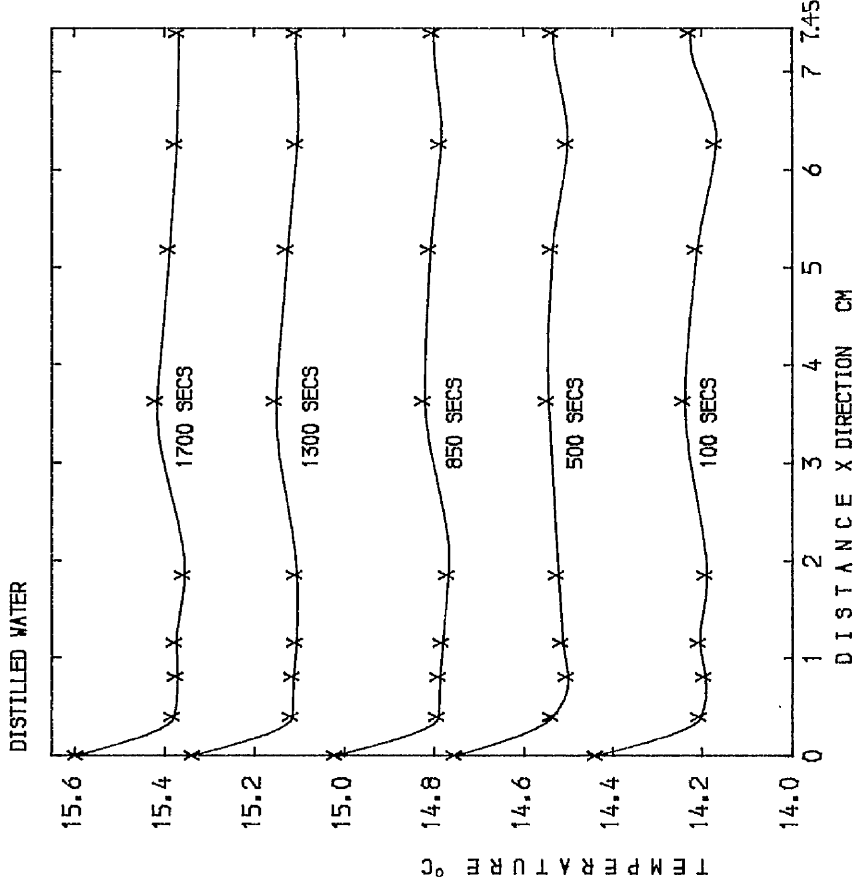


FIG. 3.53  
TEMPERATURE MEASUREMENTS AT  $(Z/H)=0.88$   
The distance is measured from the inside  
surface of the front glass of the module.

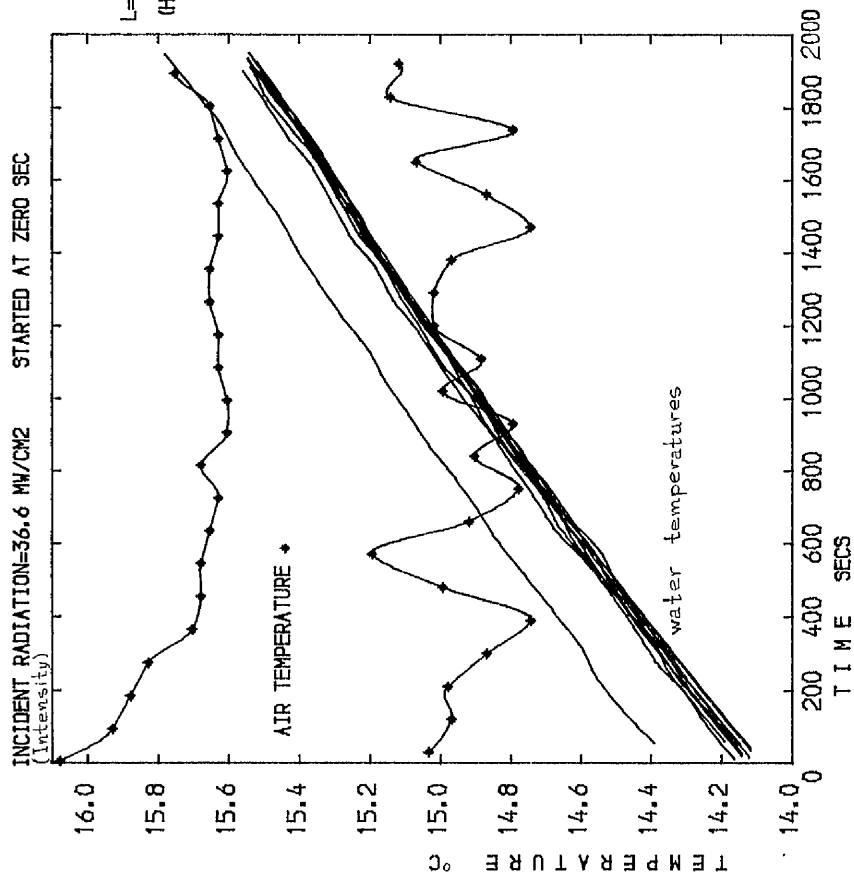


FIG. 3.52  
TEMPERATURE MEASUREMENTS AT  $(Z/H)=0.88$



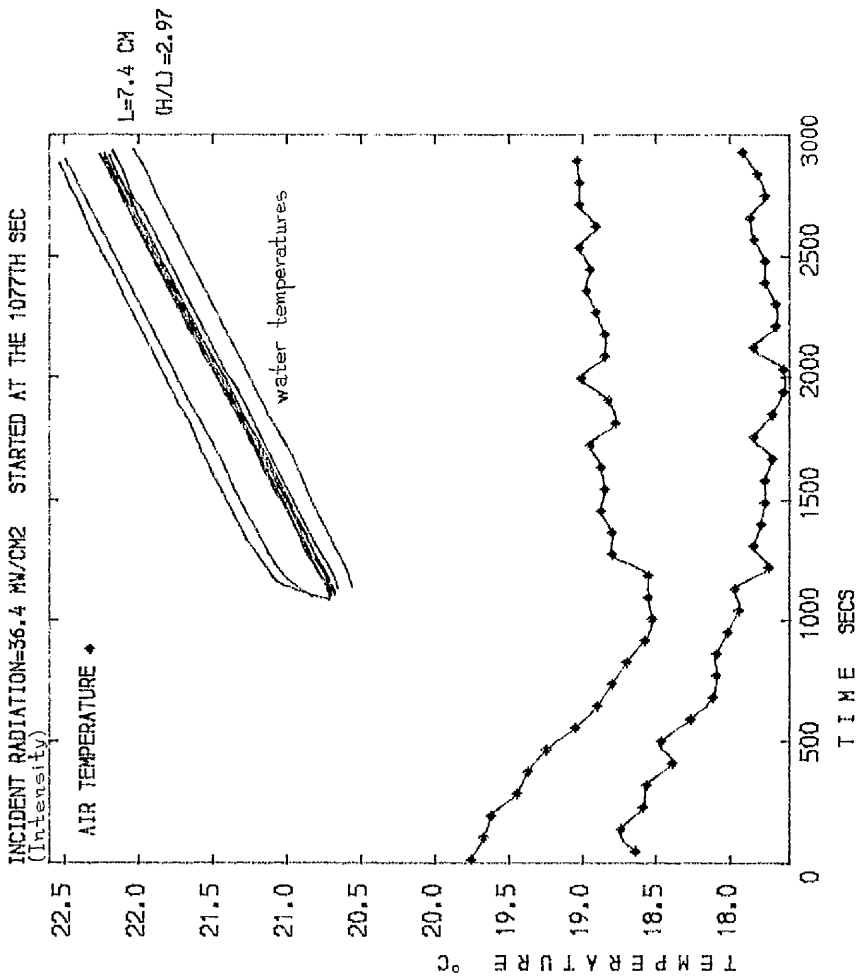


FIG. 3.54  
TEMPERATURE MEASUREMENTS AT  $(Z/H)=0.80$

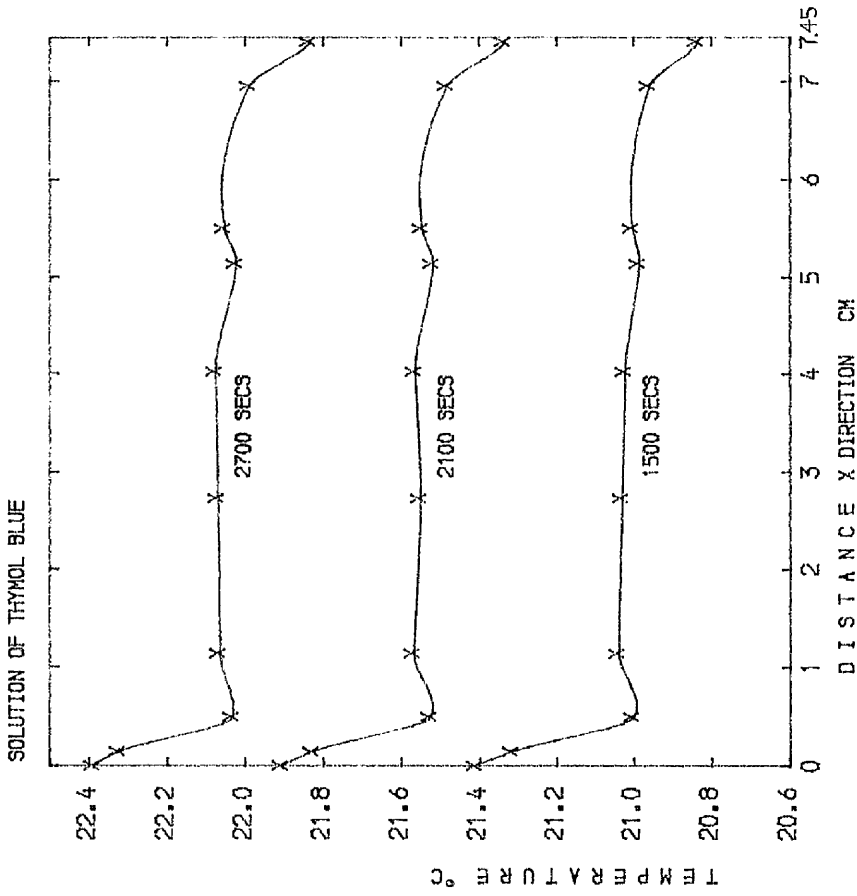


FIG. 3.55  
TEMPERATURE MEASUREMENTS AT  $(Z/H)=0.80$   
The distance is measured from the inside surface of the front glass of the module.

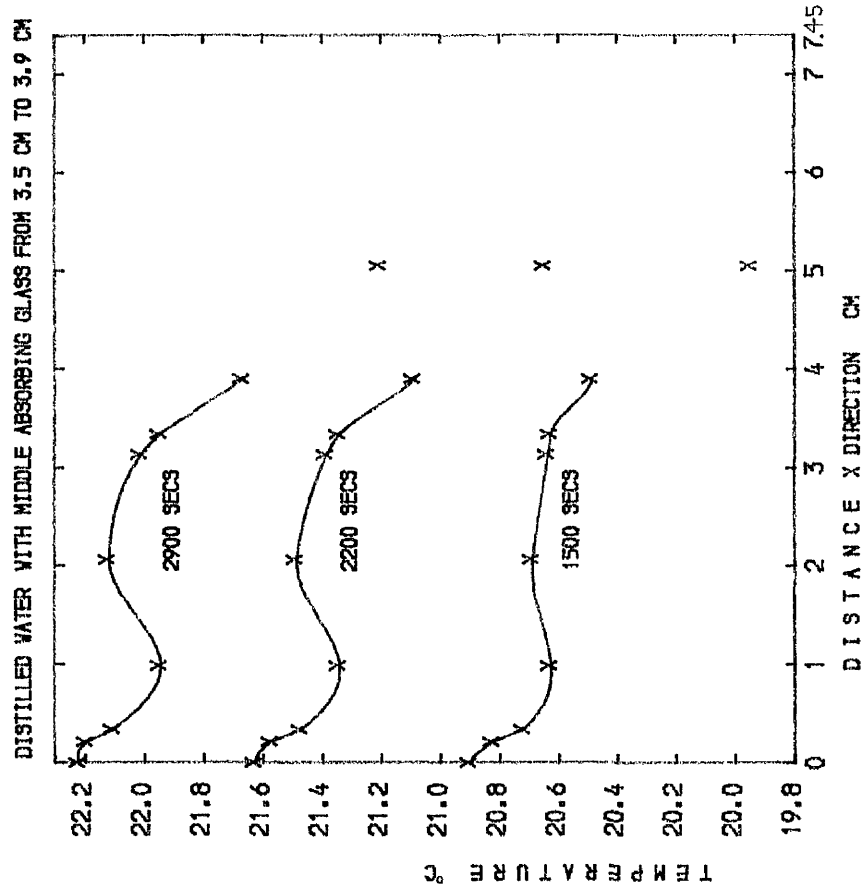


FIG. 3.56  
TEMPERATURE MEASUREMENTS AT  $(Z/H)=0.42$

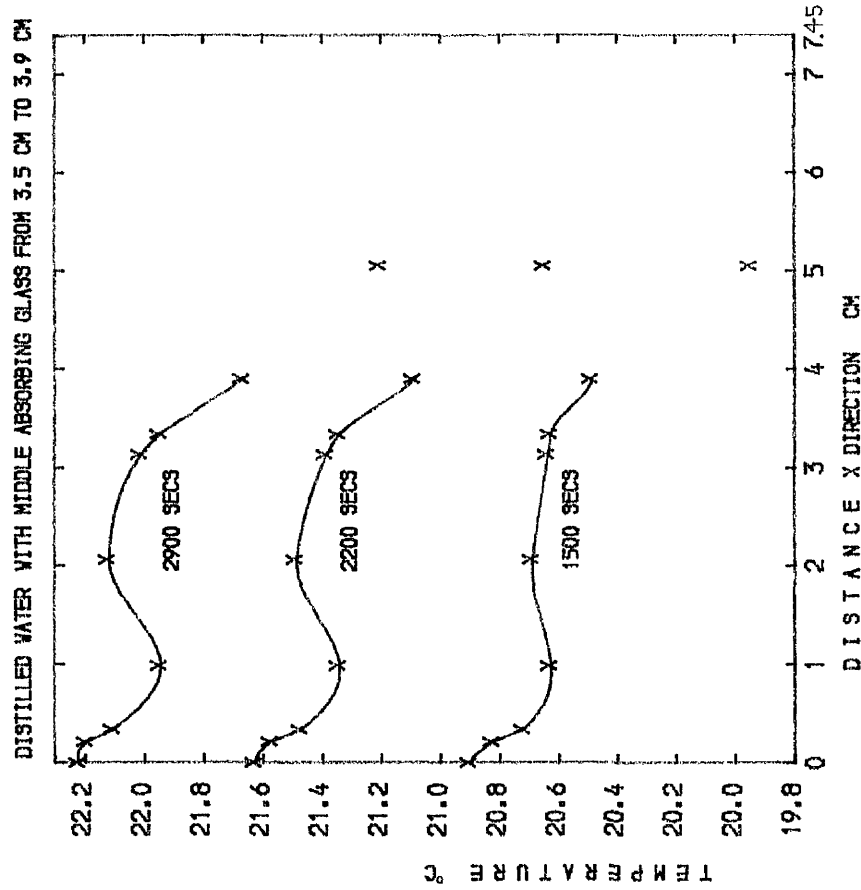


FIG. 3.57  
TEMPERATURE MEASUREMENTS AT  $(Z/H)=0.42$   
The distance is measured from the inside surface of the front glass of the module.

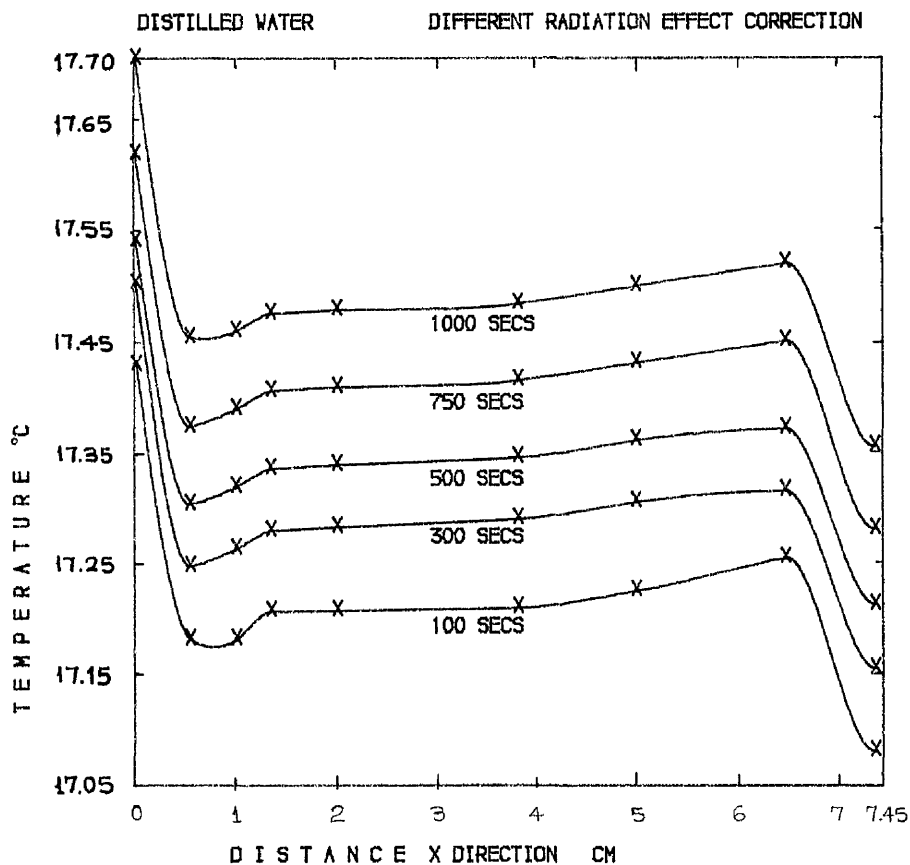


FIG. 3.58

TEMPERATURE MEASUREMENTS AT  $(Z/H)=0.57$   $(H/L)=3.10$ ,  $L=7.4$  CMDetermination of the position of the thermocouple junction.

The position of the thermocouple junction is determined as the intersection point of three planes. Each plane is calculated from cathetometer sighting and contains the thermocouple junction and the telescope vector after being twice refracted at the air-glass and the glass-liquid interfaces. The telescope vector before its first refraction at the air-glass interface is normal to the telescope scale as it is shown in Fig. 3.59. The horizontal plane passing through the junction is determined from a sighting by the telescope in which the scale of the telescope should be in a vertical position. Because it is quite difficult to position the cathetometer scale parallel to the outside surfaces of the transwall module and, at the same time, maintain the horizontal position, another approach is adopted to determine the intersection line of the remaining two planes. This approach is shown in Fig. 3.59.

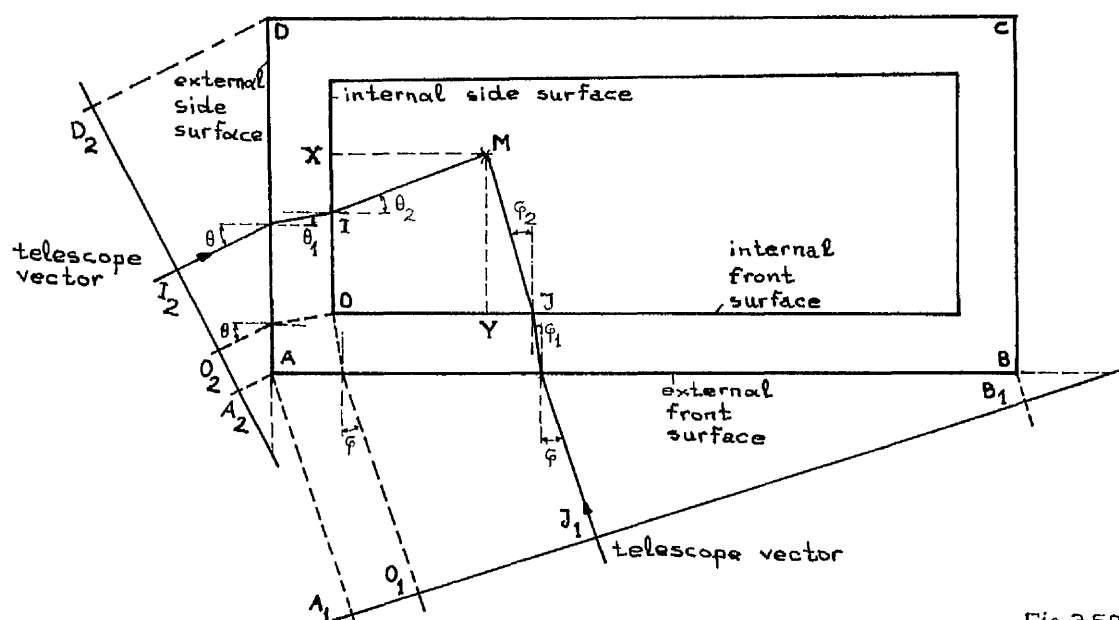


Fig.3.59

The cathetometer scale, being in a horizontal position, forms an angle  $\varphi$  with the front surfaces and, successively, an angle  $\theta$  with the side surfaces of the transwall module. The distance  $OX$  and  $OY$  of the intersection line (shown with the asterisk  $M$  in Fig. 3.59) from the inside front surface and the inside side surface, respectively, are given by the following relations (corresponding to the relative positions of Fig. 3.59).

$$OX = (OI + OJ * \tan \theta_2) / (1 - (\tan \theta_2) * \tan \varphi_2) \quad (3.52)$$

$$OY = (OJ - OI * \tan \varphi_2) / (1 + (\tan \theta_2) * \tan \varphi_2) \quad (3.53)$$

where the angles  $\varphi_2$  and  $\theta_2$  are calculated from the following relations:

$$\sin \varphi_2 = (\sin \varphi) * n_a / n_w$$

$$\sin \theta_2 = (\sin \theta) * n_a / n_w$$

where  $n_a$  and  $n_w$  are the refractive indices of air and water respectively.

The distances  $OI$  and  $OJ$  are calculated from the following relations:

$$OI = O_2 I_2 / \cos \theta$$

$$OJ = O_1 J_1 / \cos \varphi$$

where  $O_2 I_2$  and  $O_1 J_1$  are reading differences in the telescope scale.

Because the distances  $AB$  and  $AD$  are known, the angles  $\varphi$  and  $\theta$  are calculated from the following relations:

$$\cos \varphi = A_1 B_1 / AB$$

$$\cos \theta = A_2 D_2 / AD$$

where  $A_1B_1$  and  $A_2D_2$  are reading differences in the telescope scale.

The signs of relations (3.52) and (3.53) depend on the relative position of the telescope vectors in respect to side and front surfaces. Inaccuracies in calculating the co-ordinates  $OX$  and  $OY$  are larger for the position of the cathetometer which produces negative signs in the two denominators.

### 3.4.5 Velocity measurements

The velocity at certain points of the liquid of the transwall module is measured by using the thymol blue technique. Extensive description of the technique is given by Merzkirch (77), where some difficulties experienced during the application of the technique are also discussed. The liquid should be solution of thymol blue dye in distilled water, which is a pH indicator that turns its mainly yellow colour to blue when its pH becomes higher than 8, the titration point of thymol blue. Two electrodes are introduced inside the liquid. The cathode is a thin straight wire placed in the regime of flow to be measured. Applying a d-c voltage between the electrodes, the liquid turns its yellow colour to blue around the naked spots of the cathode because it becomes more alkaline with pH higher than 8 at these areas. The blue spots formed this way are swept downstream by the flow, the velocity of which is measured by photographing them. The technique is appropriate for low-speed liquid flows and especially for flows exhibiting density differences, since there is no density difference between the blue and yellow thymol blue.

Owing to the electrolytic reaction  $H_2$  is produced at the cathode. The rate of hydrogen production should be kept low enough in order to avoid the formation of hydrogen bubbles. This means that the voltage applied between the electrodes should be low. In the case of the velocity measurements at the small transwall module a third reference electrode, Pye Unicam cat. 303, was used and the alkalinity of the cathode was controlled by a potentiationstat, Hermes Controls model 1, (No. 11 in Ph. 4, 5 and 6). As can be seen from these photographs the reference electrode was located in a separate beaker in order not to disturb the flow pattern of the transwall module. Continuity between the thymol blue of the transwall module and of the beaker was maintained via a plastic pipe.

It was noticed that the bubble production almost always started and remained stronger at the edges of the naked spots of the varnished cathode<sup>†</sup>. The blue lines themselves were stronger at the edges. This is evident from the photographs of pages 225 to 230. The length of the naked spots seemed also to be important; with the bubble production being stronger at the shorter naked spots of the cathode. The position of the anode inside the liquid was important not only in the formation of the bubbles themselves but of irregular blue lines around the cathode. This was experienced by Buzyna et al (78) as well. The arrangement of introducing the anode about one centimeter in length inside the liquid substantially improved the situation.

Keeping a low voltage to avoid the formation of hydrogen bubbles is in conflict with the desire to produce strong blue lines in contrast to the surrounding yellow liquid which would help to improve the photographic results. The strength of the blue lines increases with the strength of the solution of thymol blue and the area of the naked spots of the cathode normal to it and decreases with the diffusion of the blue solution to the surrounding yellow solution. The rate of diffusion increases with the mean velocity of the flow and the difference of the pH between the blue and yellow thymol blue. The yellow colour of the low pH ( $\sim 5.5$ ) thymol blue does not turn spontaneously to blue colour at the titration point of 8 pH. Instead, there is a gradual change of the yellow colour to reddish colour as the pH approaches the titration point with a simultaneous weaker contrast between the blue lines and the rest of the liquid. This is easily shown in Fig.3.61 which is referred to four different pHs of a thymol blue solution of  $W^* = 0.0003556$  Kg of thymol blue/Kg of water strength. In this respect there is a conflict in decreasing the diffusion of the blue lines and in maintaining their contrast with the surrounding liquid. The initial attempts to produce streak lines that would fill the whole cell was abandoned because slow diffuse of the blue spots was obtained only at pH values very close to the titration point where the contrast was too weak to produce satisfactory photographic results. Furthermore, it has been found that the gradual colour change and therefore the weakening of the contrast starts from lower pH values as the strength of the solution of the thymol blue increases. As far as the diameter

<sup>†</sup> See Table 3.8 for cathode details.

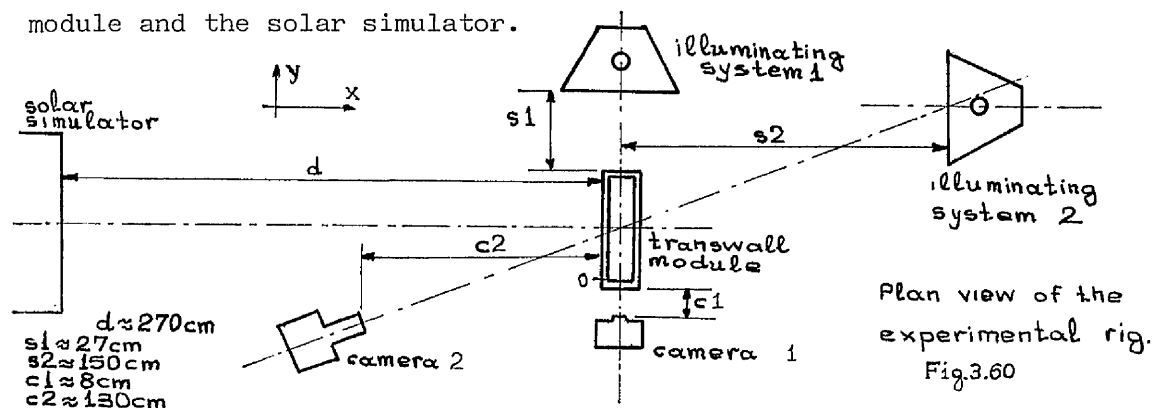
of the cathode and therefore the area of the naked spots normal to the cathode is concerned, this should be kept small to limit the change of the flow pattern because of the presence of the cathode. A trial and error approach led to the adoption of two types of cathodes which gave satisfactory results for thymol blue solutions of 0.005 to 0.04 Kg thymol blue/Kg distilled water. The dimensions of the two cathodes and other relevant information is given in Table 3.8 . The anode was made from copper plate of 1cm width and 0.5mm thickness and was introduced about 1cm inside the liquid of the transwall module. Nail varnish was used for the cathode insulation.

Table 3.8

Material and dimensions of the electrodes

	material	length	naked spots diameter	naked spots length	distance between naked spots	voltage between electrodes	order of magnitude of current
long electrode	copper	176mm	0.152mm	4mm	18mm	3 volts	250 $\mu$ A
short electrode	copper	24mm	0.152mm	0.5mm	6.5mm	3 volts	30 $\mu$ A

In addition to the abovementioned difficulties, the reflection of the radiation by the transwall module back to the cameras decreased further the effective contrast. This was partially overcome by the introduction of two illuminating systems, placed opposite to the cameras on the far side of the transwall module. These two illuminating systems are shown in photograph 4 (No.12 and No.13 ). Their design is such that the radiation of the illuminating source is directed onto a diffusing glass plate opposite and parallel to the transwall module. Fig.3.60 shows a plan view of the illuminating systems, the cameras, the transwall module and the solar simulator.



Two openings at the bottom and top of the illuminating systems allow for the cooling of the illumination sources by natural convection. The source of system 2 consisted of two filament lamps of 200 watts each. The source of system 1 is a 250 W MBI/BU Metal-Halide Thallium lamp.

As Fig. 3.61 shows, the highest contrast is expected in the spectral regions from 0.4 to 0.47  $\mu\text{m}$  (Blue region) and from 0.51 to 0.63  $\mu\text{m}$  (green and yellow region). The two different illuminating sources were chosen to accommodate this, although there was an uncertainty over the real spectrum of the illuminating systems due to lack of knowledge over the spectral properties of their diffusing glass plate.

The change of the flow pattern inside the transwall module because of the two illuminating systems is expected to be small - almost negligible with the solar simulator in operation. The measured average irradiance from illumination system 1 was 17  $\text{watts/m}^2$  at the transwall module side at distance  $s_1 = 27\text{cm}$  from illuminating system 1. The measured average irradiance from illumination system 2 was 25  $\text{watts/m}^2$  at the transwall module back side at distance  $s_2 = 1.5\text{ m}$  from illuminating system 2.

Photographs were taken by both cameras (see Fig. 3.60) at the same instant. The activation of the cameras was performed manually. Camera 2 was a Canon AT-1 model with a 200mm, 1:3.5 Auto Tamron telescope lens. Camera 1 was a Canon FT-b model with a 50mm FD Canon and a 52mm Hoya Close-up lens. Six pairs of photographs are shown in pp.221 to 226, each pair corresponding to a certain instant. The first three pairs refer to the cooling of the transwall module by the cooler air of the laboratory without any radiation coming from the solar simulator. The average temperatures of the liquid and the surrounding air were 15.4°C and 12.3°C, respectively. The operation of the solar simulator started 290 secs (1800<sup>th</sup> sec) after the third shooting with an almost constant radiation output of about 370  $\text{W/m}^2$ . The last three pairs of photographs were taken at the 2350<sup>th</sup> sec, 2362<sup>nd</sup> sec and 2375<sup>th</sup> sec, respectively. The average temperatures of the liquid and the surrounding air were 17.5°C and 13.2°C, respectively, 45 seconds before the fourth shooting. The solution of thymol blue in water had a strength of 0.0001 Kg thymol blue/Kg of water and a pH value of 6.7.



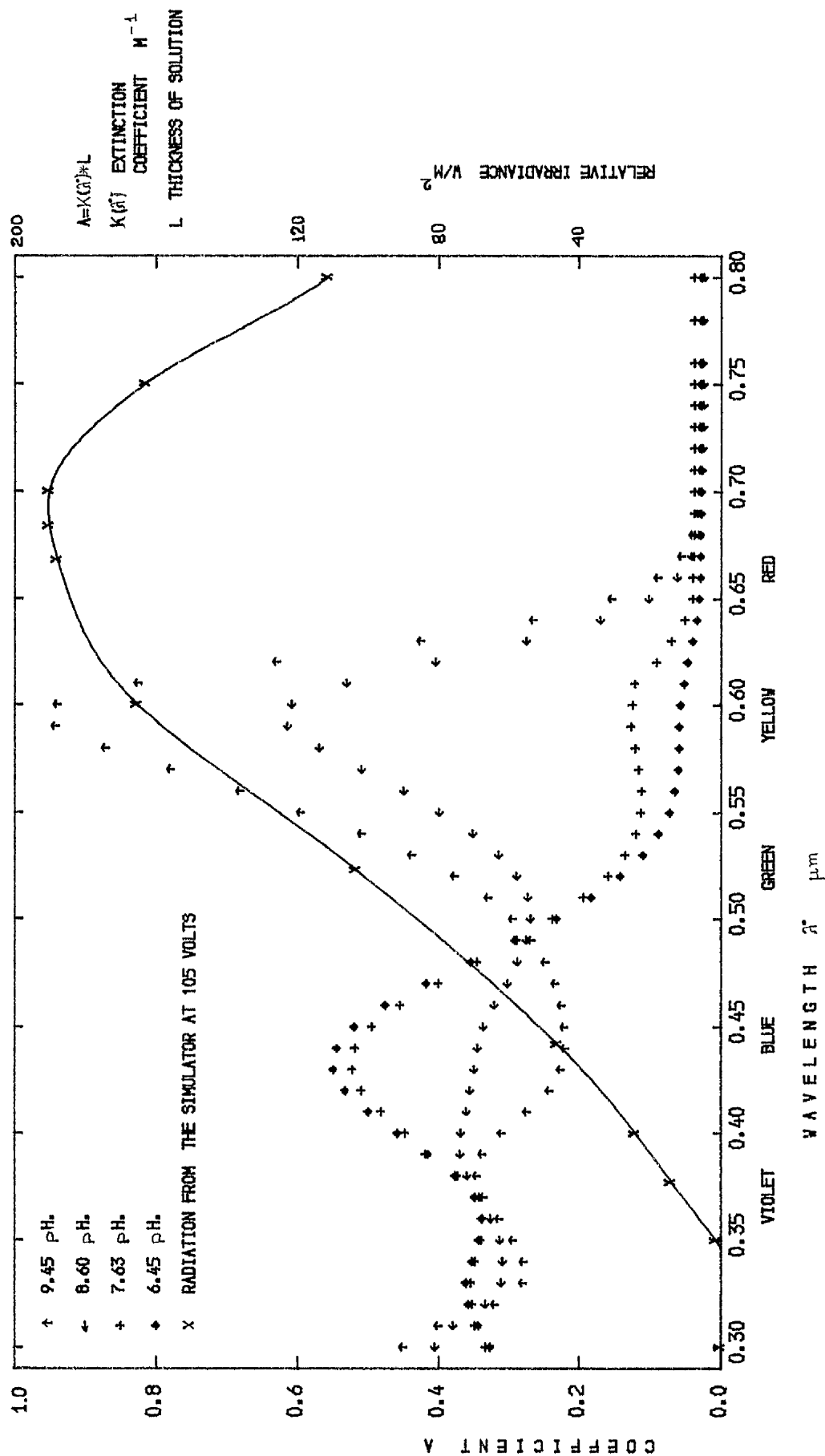
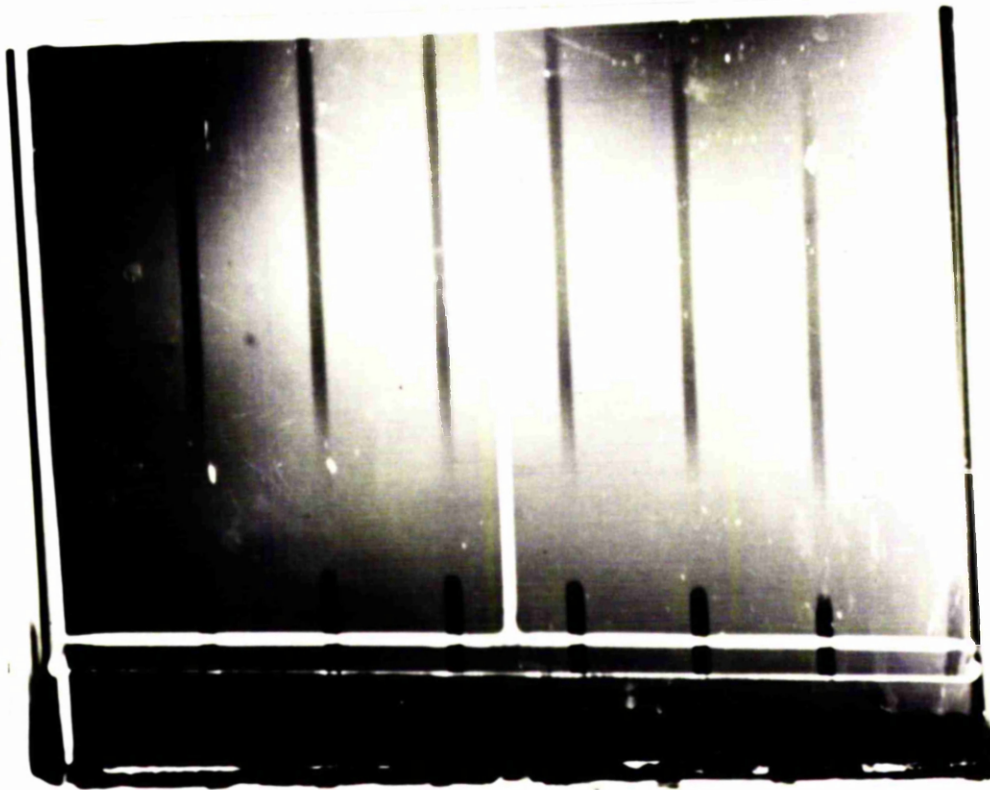


FIG. 3.61

COEFFICIENT A OF 1 MM THICK SOLUTION OF THYMOL BLUE AT VARIOUS pH. (solution strength:  $W = 3.556 \times 10^{-4} \frac{\text{kg of thymol blue}}{\text{kg of water}}$ )



Ph. 10  
Blue lines produced by the long electrode

Calculation of the three co-ordinates X, Y and Z  
(in respect to a constant rectangular system O.XYZ of axes)  
of a point inside the liquid of the transwall module from the  
pair of photographs taken by the two cameras at the same instant.

Each point on a photograph is determined by the two co-ordinates  $a_1$  and  $b_1$ , in respect to a constant cartesian system O1.ab of axes on the plane of the photograph. Each co-ordinate  $a_1$  and  $b_1$  can be expressed by the following relations:

$$a_1 = Ca_1 * X^{na_1x} * Y^{na_1y} * Z^{na_1z}$$

$$b_1 = Cb_1 * X^{nb_1x} * Y^{nb_1y} * Z^{nb_1z}$$

that imply that each co-ordinate is a function of the three co-ordinates X, Y and Z. Additionally other factors, for example, the magnification of the camera and printing apparatus, the refraction indices of the air, the glass and the liquid, etc., are expressed via the constants and the exponents of the above relations.

The knowledge of the co-ordinates ( $X_i, Y_i, Z_i$ ) of four points of the photograph allows for the calculation of the constant and the three exponents of each relation, from the systems of four linear equations:

$$na_1x * \ln(X_i) + na_1y * \ln(Y_i) + na_1z * \ln(Z_i) + Ka_1 = \ln(a_{1i}), \quad i=1 \text{ to } 4$$

and  $nb_1x * \ln(X_i) + nb_1y * \ln(Y_i) + nb_1z * \ln(Z_i) + Kb_1 = \ln(b_{1i}), \quad i=1 \text{ to } 4$

$$\text{where, } Ka_1 = \ln(Ca_1) \quad Kb_1 = \ln(Cb_1)$$

and  $(na_1x, na_1y, na_1z, Ka_1)$  or  $(nb_1x, nb_1y, nb_1z, Kb_1)$  are the four

unknown of each system of equations, respectively. The four known points  $(X_i, Y_i, Z_i)$ ,  $i = 1$  to 4 are chosen in the region of the

focus of the photograph. In the present analysis the method used

for the calculation of the position of the junctions of the thermocouples, has been adopted for the calculation of the co-ordinates

$(X_i, Y_i, Z_i)$  of these four points. Choosing as the origin O of the

axes of the 3-dimensional rectangular system of co-ordinates O.XYZ

the common point of the three internal glass surfaces that is closer

to both cameras (see Fig.3.60<sup>+</sup>) and at the bottom of the liquid of

the transwall module, Table 3.9 gives the co-ordinates of eight

points (shown in photograph 11 )

+ see also Ph.6 , page 194.

Table 3.9

The co-ordinates of the known points

Point (See Ph.11)	1	2	3	4	5	6	7	8
X in cm	0.62	0.19	2.47	2.01	0.79	0.16	2.28	1.50
Y in cm	15.19	14.22	12.84	13.12	10.47	9.10	7.51	8.25
Z in cm	11.49	6.25	6.24	6.20	14.31	8.95	9.14	9.05

Table 3.10 has been constructed according to the above analysis. The results of this table and those of the consequent tables are based on the first printed group of negatives. The photographs presented in this thesis have been printed with a different magnification of the printing apparatus.

Table 3.10

Pair of photographs	1	2	3	4	5	6
Time instant in secs	1470	1490	1510	2350	2362	2375
Points from Table 3.9 used	1, 2, 3 and 4			5, 6, 7 and 8		
photographs $na_1x$	-0.123	-0.126	-0.120	-0.056	-0.051	-0.051
taken $na_1y$	0.257	0.280	0.262	1.454	1.488	1.487
with $na_1z$	0.062	0.061	0.063	-0.509	-0.558	-0.570
camera 1 $Ca_1$	3.438	3.161	3.391	1.074	1.131	1.164
$nb_1x$	0.026	0.030	0.020	-0.010	-0.006	-0.019
$nb_1y$	0.988	1.226	0.727	-0.537	-0.269	-0.510
$nb_1z$	1.281	1.571	0.919	2.436	1.717	2.198
$Cb_1$	0.033	0.007	0.198	0.068	0.301	0.128
Points from Table 3.9 used	1, 2, 3 and 6			3, 5, 6 and 7		
photographs $na_2x$	-0.012	-0.012	-0.012	-0.044	-0.043	-0.038
taken $na_2y$	1.528	1.565	1.513	1.829	1.853	1.813
with $na_2z$	0.027	0.047	0.034	0.072	0.107	0.099
camera 2 $Ca_2$	0.171	0.146	0.177	0.074	0.065	0.074
$nb_2x$	0.004	0.006	0.003	0.011	0.005	0.002
$nb_2y$	-0.142	-0.133	-0.135	0.011	-0.053	-0.107
$nb_2z$	1.165	0.968	1.068	1.163	1.288	1.430
$Cb_2$	0.747	1.342	0.985	0.583	0.458	0.335

Note: The letter a is referred to the short dimension of the photographs and letter b to the long (cartesian system 01.ab)

In each pair of photographs, four co-ordinates ( $a_{1j}$ ,  $b_{1j}$ ) and ( $a_{2j}$ ,  $b_{2j}$ ) correspond to each point.<sup>+</sup> The three co-ordinates are enough to give the co-ordinates (X, Y, Z) of the point in the coordinate system O.XYZ by solving a system of three linear equations, for example,

$$na_1x * Sx + na_1y * Sy + na_1z * Sz = \ln(a_{1j}) - \ln(Ca_1)$$

$$nb_1x * Sx + nb_1y * Sy + nb_1z * Sz = \ln(b_{1j}) - \ln(Cb_1)$$

$$na_2x * Sx + na_2y * Sy + na_2z * Sz = \ln(a_{2j}) - \ln(ca_2)$$

where,  $Sx$ ,  $Sy$ ,  $Sz$  the three unknowns of the system of equations.

It is obvious that,

$$X = e^{Sx}$$

$$Y = e^{Sy}$$

$$Z = e^{Sz}$$

#### Calculation of the velocity components

By applying the method to the end point of the blue line, number 2 (see first pair of photographs) of the first three pairs of photographs, Table 3.11 is constructed. Similarly, by applying the method to the end point of the blue lines, number 2 and number 3 (see fourth pair of photographs) of the last three pairs of photographs, Tables 3.12 and 3.13 are constructed, respectively. Each Table contains values of the co-ordinates (X, Y, Z) of the end point of the blue lines, calculated from two different sets of co-ordinates on the photographic plane, ( $a_{2j}, b_{2j}, a_{1j}$ ) and ( $a_{2j}, a_{1j}, b_{1j}$ ). A comparison between the results of the two different sets of co-ordinates is a measure of the validity of the method. Average values of the velocity components  $u$ ,  $v$  and  $w$  along the axes OX, OY and OZ, respectively, are also given in these tables, 3.11, 3.12, 3.13. These average values are referred to the time and space points written between brackets in these tables. These are actually mid point values.

The values of the velocity components obtained by the present method are believed to be reasonably consistent within themselves having due regard to the uncertainties of measurement. When compared to the theoretical values predicted in Fig. 3.35 it is seen that vertical measured velocities tend to be very roughly one quarter of those of Fig. 3.35. This may seem a wide divergence but it should be noted that the time lapse from the start of circulation is different, some 15 minutes, sufficient to allow for stratification to have some effect. The electrodes will have shielded the flow to some extent.

<sup>+</sup> subscript 1 (2) for photographs taken with camera 1 (2).

The differences in values of position and velocity components by using different sets of co-ordinates of the photographs can mostly be attributed to inaccuracies in measuring and calculating the co-ordinates (X, Y, Z) of the known points. Although this is an inherent disadvantage of the method for the accurate prediction of the velocity components of a 3-dimensional flow, the simplicity in taking the photographs and "translating" them compensates to some extent for this disadvantage.

In the present analysis the following possible errors in the calculation of the velocity have been ignored; the diffusion of the blue dye into the surrounding fluid, the presence of the cathode in the flow or the higher radiation absorption of the blue dye in comparison with the surrounding fluid. The radiation absorbed by the thymol blue of 0.1mm thickness, 0.0003556 (Kg of thymol blue/Kg of water) strength and 9.45 pH just behind a 4mm clear float glass plate receiving radiation of air-mass 2, is about 16.4% of the total incident radiation. Respectively, the radiation absorbed by the same type and thickness thymol blue of 6.98 pH under the same conditions is about 15.5% of the total incident radiation. This difference between the blue dye and the surrounding liquid absorption, roughly 1% of the total incident radiation, represents an extreme case. More moderate differences are expected and according to Fig. 3.61 they will give smaller difference of radiation absorption between the blue dye and the surrounding liquid.

Table 3.11

By using the set of co-ordinates ( $a_2j, b_2j, a_1j$ )												By using the set of co-ordinates ( $a_2j, a_1j, b_1j$ )			
TIME(s)	X(cm)	u(cm/s)	Y(cm)	v(cm/s)	Z(cm)	w(cm/s)	X(cm)	u(cm/s)	Y(cm)	v(cm/s)	Z(cm)	w(cm/s)			
1470	0.29		14.06		5.93		0.29		14.06		5.87				
(1480)	(0.28)	-0.002	(14.11)	-0.006	(5.73)	-0.020	(0.27)	-0.003	(14.13)	-0.008	(5.40)	-0.047			
1490	0.26		19.17		5.53		0.27		14.21		4.93				
(1500)	(0.24)	-0.001	(14.15)	-0.001	(5.22)	-0.031	(0.24)	-0.001	(14.18)	-0.003	(4.83)	-0.010			
1510	0.23		14.14		4.91		0.23		19.15		4.74				

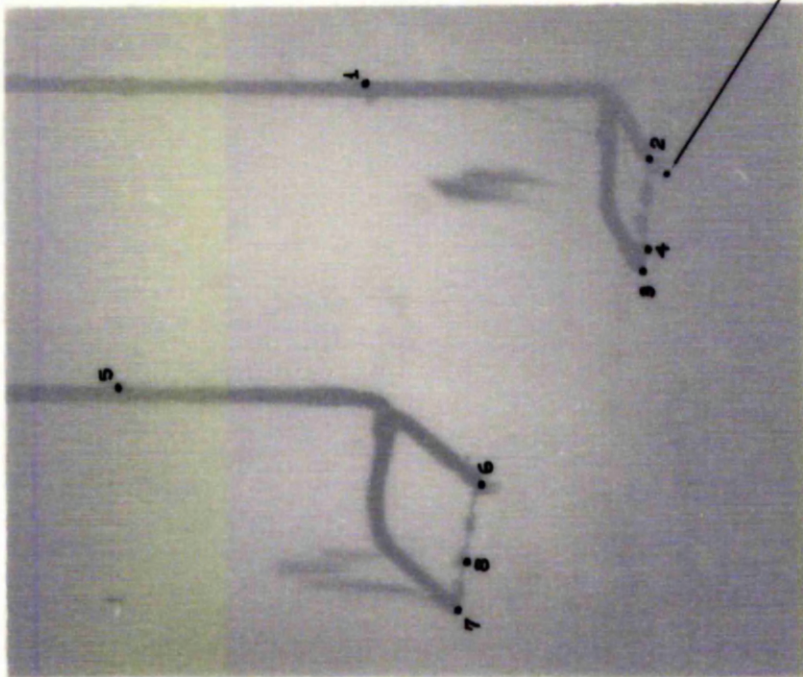
Table 3.12

By using the set of co-ordinates ( $a_2j, b_2j, a_1j$ ) By using the set of co-ordinates ( $a_2j, a_1j, b_1j$ )												
TIME(s)	X(cm)	u(cm/s)	Y(cm)	v(cm/s)	Z(cm)	w(cm/s)	X(cm)	u(cm/s)	Y(cm)	v(cm/s)	Z(cm)	w(cm/s)
2350	0.04		8.70		10.12		0.06		8.80		9.95	
(2356)	(0.02)	-0.003	(8.47)	-0.038	(10.87)	0.125	(0.03)	-0.004	(8.66)	-0.024	(10.59)	0.107
2362	0.001		8.42		11.62		0.005		8.52		11.22	
(2368.5)	(0.000)	-0.000	(3.10)	-0.021	(12.54)	0.142	(0.004)	-0.000	(8.46)	-0.008	(11.87)	0.100
2375	0.000		7.96		13.46		0.002		8.41		12.52	

Table 3.13

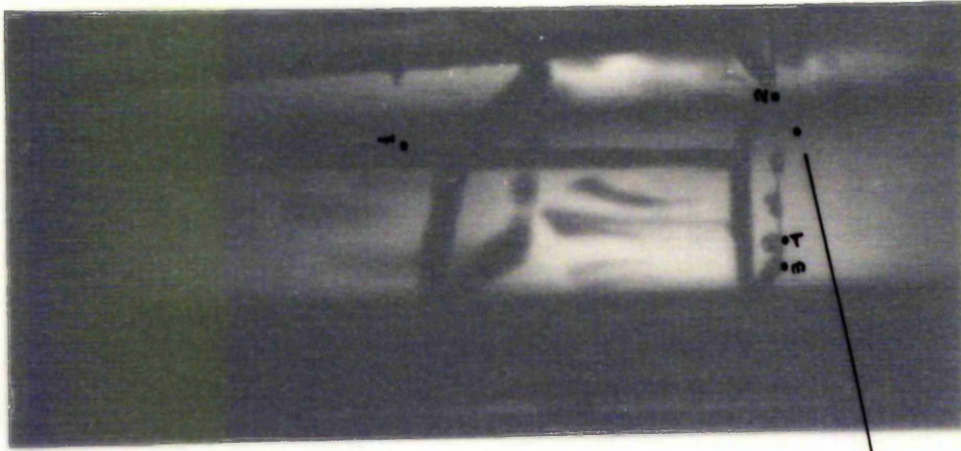
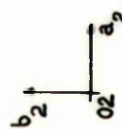
By using the set of co-ordinates ( $a_2j, b_2j, a_1j$ ) By using the set of co-ordinates ( $a_2j, a_1j, b_1j$ )												
TIME(s)	X(cm)	u(cm/s)	Y(cm)	v(cm/s)	Z(cm)	w(cm/s)	X(cm)	u(cm/s)	Y(cm)	v(cm/s)	Z(cm)	w(cm/s)
2350	0.29		8.62		9.37		0.33		8.65		9.32	
(2356)	(0.16)	-0.021	(8.50)	-0.021	(9.86)	0.051	(0.20)	-0.023	(8.57)	-0.013	(9.58)	0.044
2362	0.03		8.37		9.99		0.06		8.47		9.84	
(2368.5)	(0.03)	-0.001	(8.46)	0.014	(10.46)	0.073	(0.04)	-0.003	(8.56)	0.011	(10.32)	0.073
2375	0.02		8.55		10.93		0.03		8.64		10.79	

Pair 1



Ph. 11

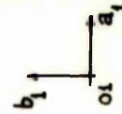
From camera 2-1470s - without radiation from simulator



Ph. 12

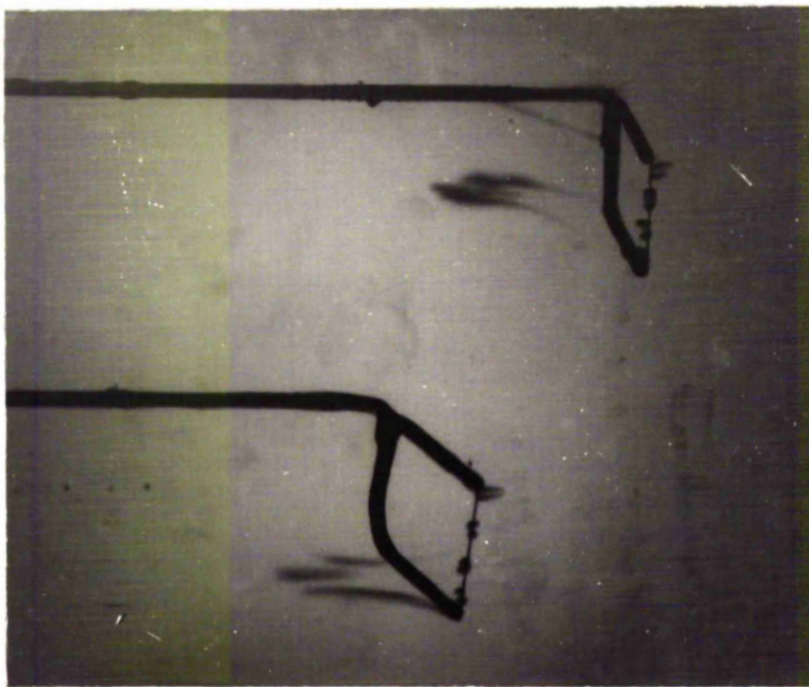
From camera 1-1470s - without radiation from simulator

end point  
line No.2





Pair 1



Ph. 11

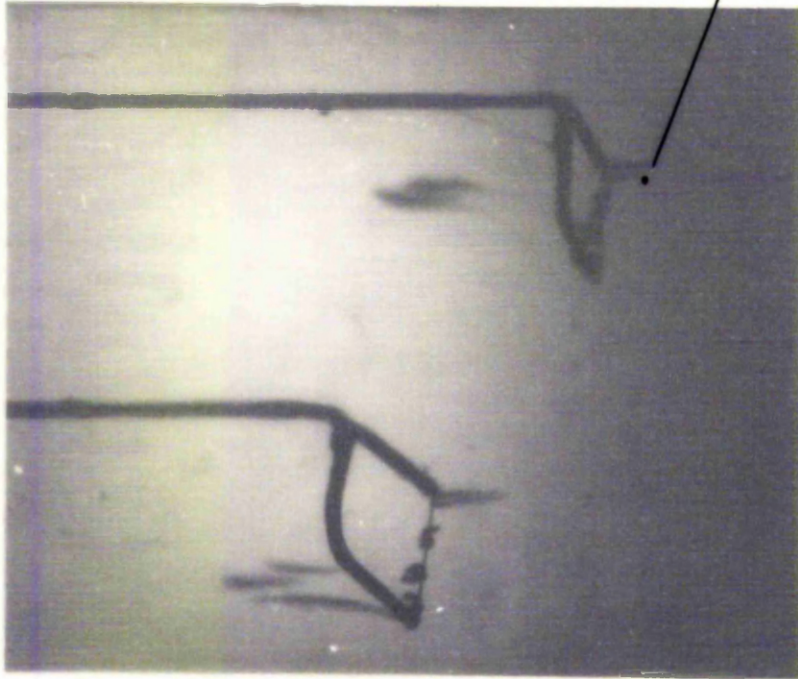
From camera 2 - 1470s - without  
radiation from simulator



Ph. 12

From camera 1 - 1470s - without  
radiation from simulator

Pair 2



Ph. 13

From camera 2-1490 s - without  
radiation from simulator

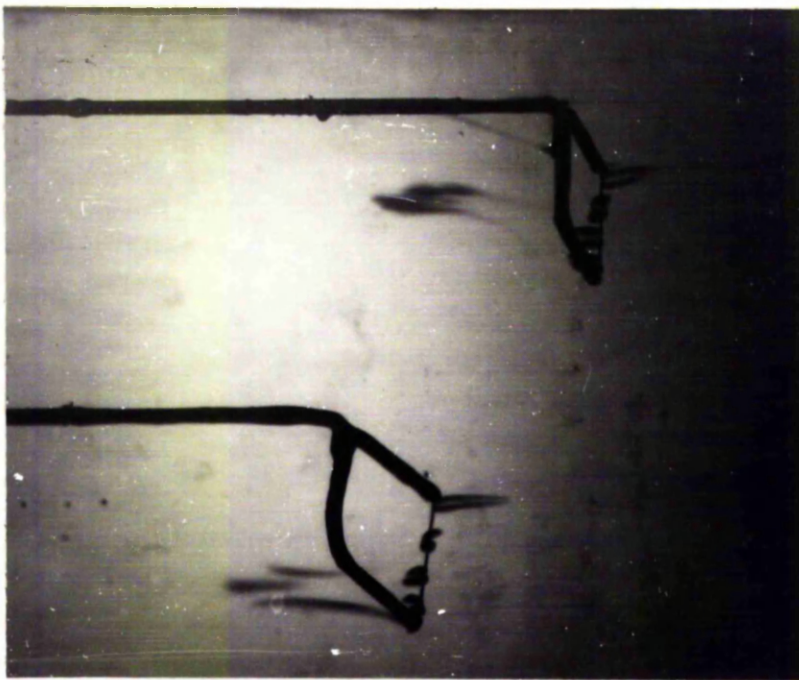
end point  
line No. 2



Ph. 14

From camera 1-1490 s -  
without radiation from  
simulator

Pair 2



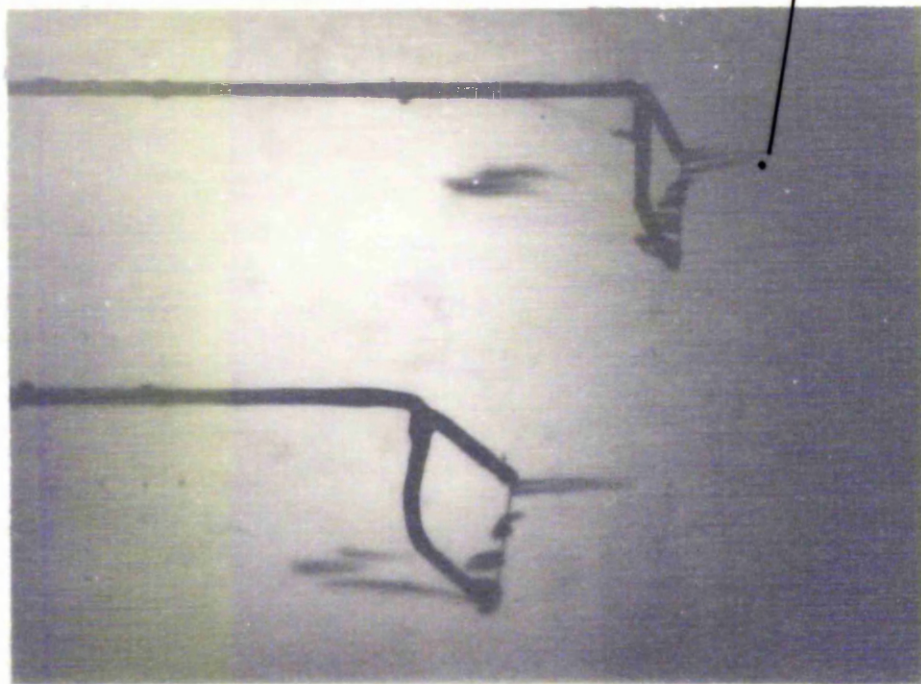
Ph. 13  
From camera 2 - 1490 s - without  
radiation from simulator



Ph. 14  
From camera 1 - 1490 s -  
without radiation from  
simulator



Page 3



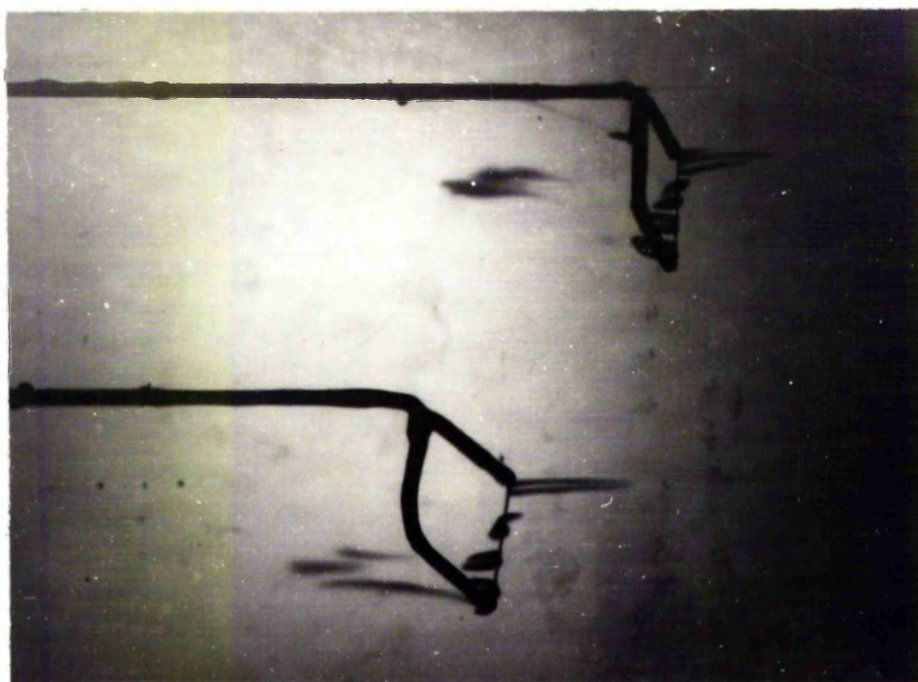
Ph. 15  
From camera 2-1510s - without  
radiation from simulator



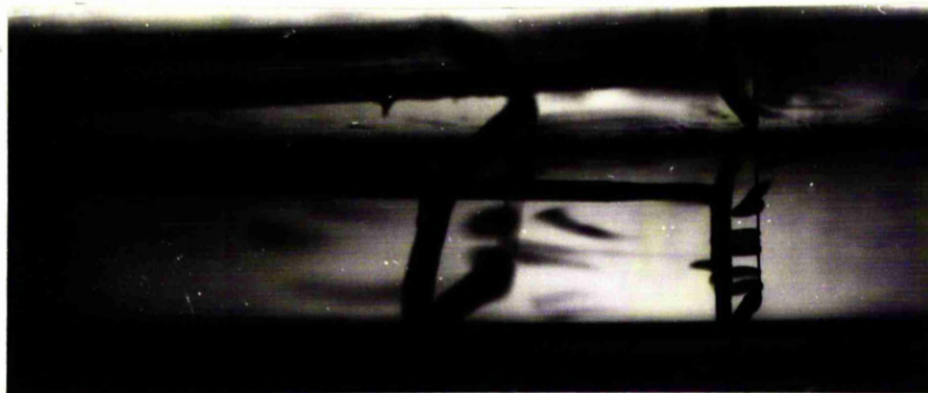
Ph. 16  
From camera 1-1510s  
without radiation from  
simulator

end point  
Line No. 2

Pair 3

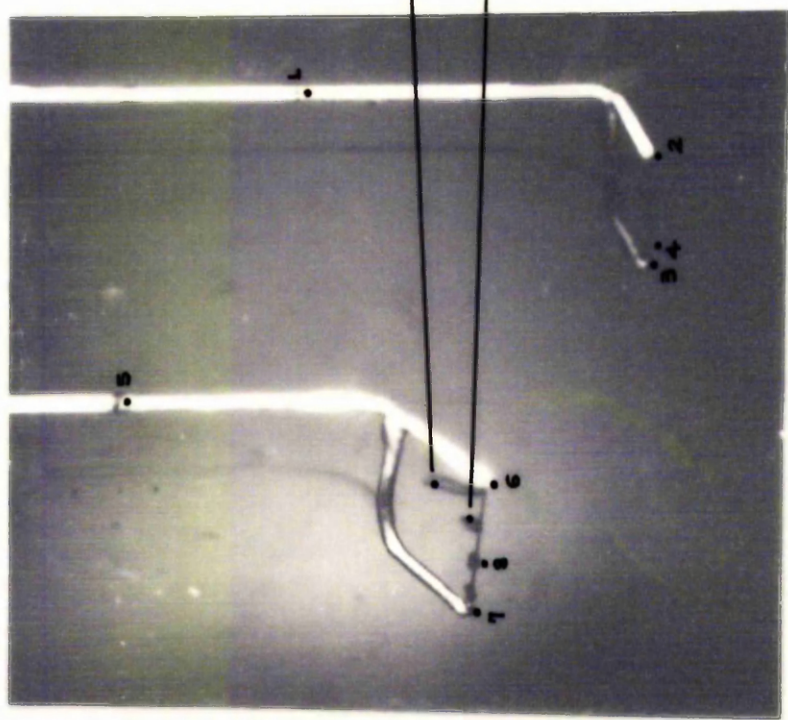


Ph. 15  
From camera 2-1510 s - without  
radiation from simulator

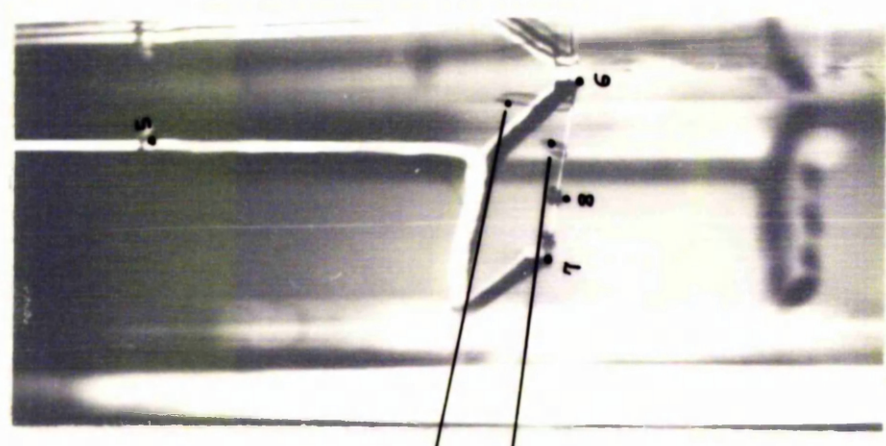
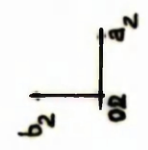


Ph. 16  
From camera 1-1510 s  
without radiation from  
simulator

Page 4



Ph. 17  
From camera 2 - 2350 s  
Simulator in operation



Ph. 18  
From camera 1 - 2350 s  
Simulator in operation



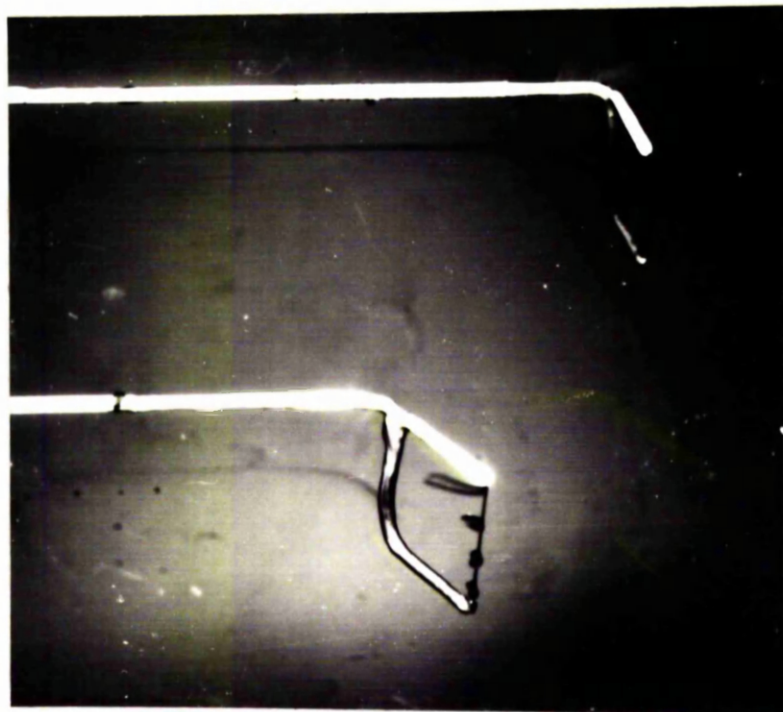
end points

line No.2

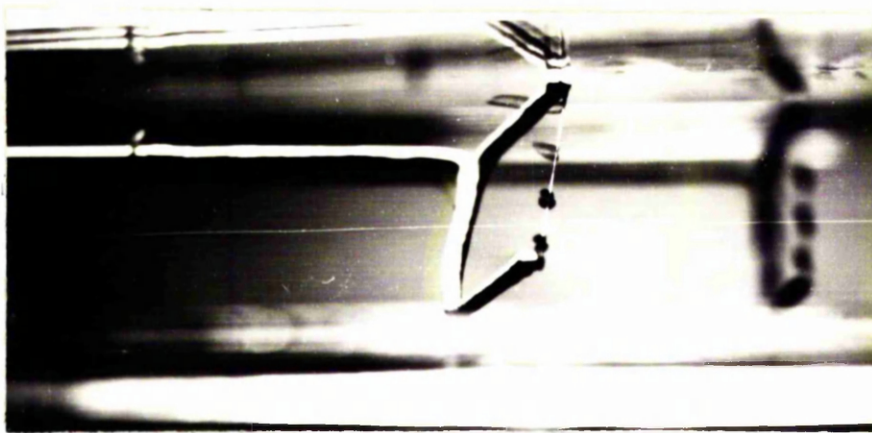
line No.3



Pair 4

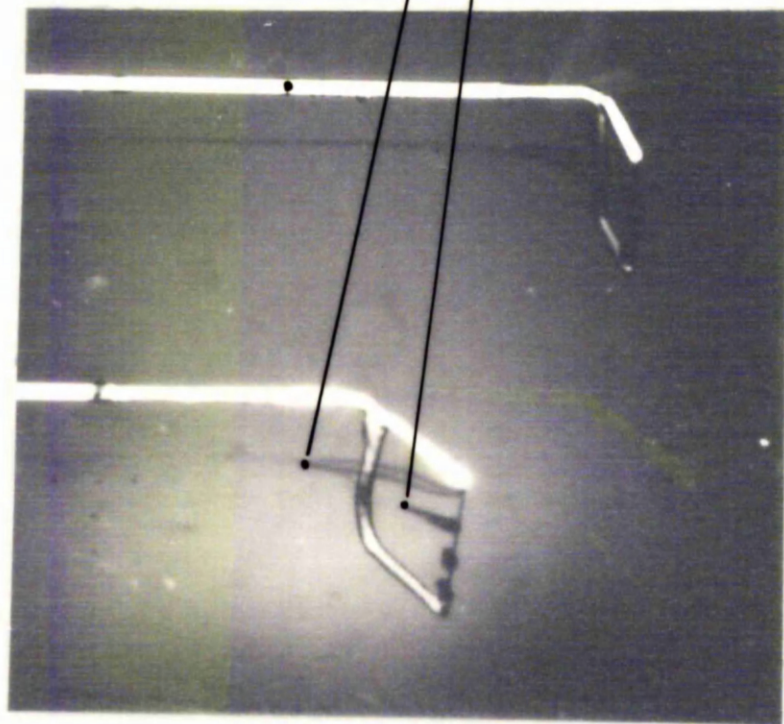


Ph. 17  
From camera 2 - 2350 s  
Simulator in operation



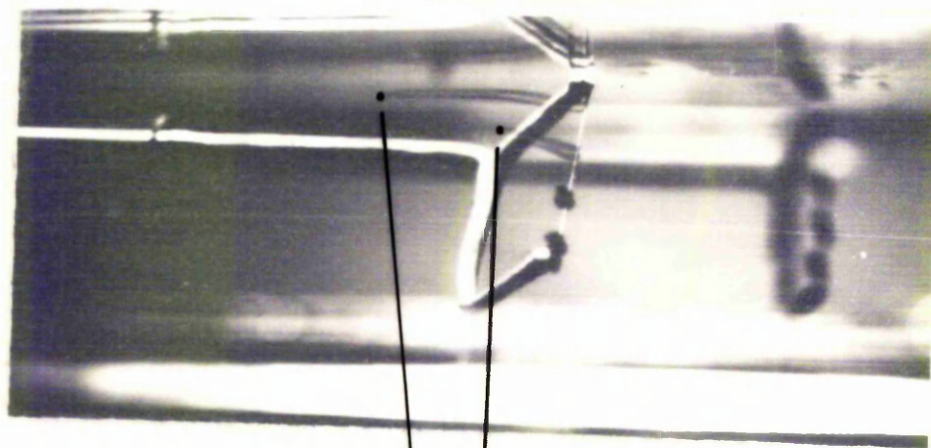
Ph. 18  
From camera 1 - 2350 s  
Simulator in operation

Pair 5



Ph. 19

From camera 2-2362 s  
Simulator in operation

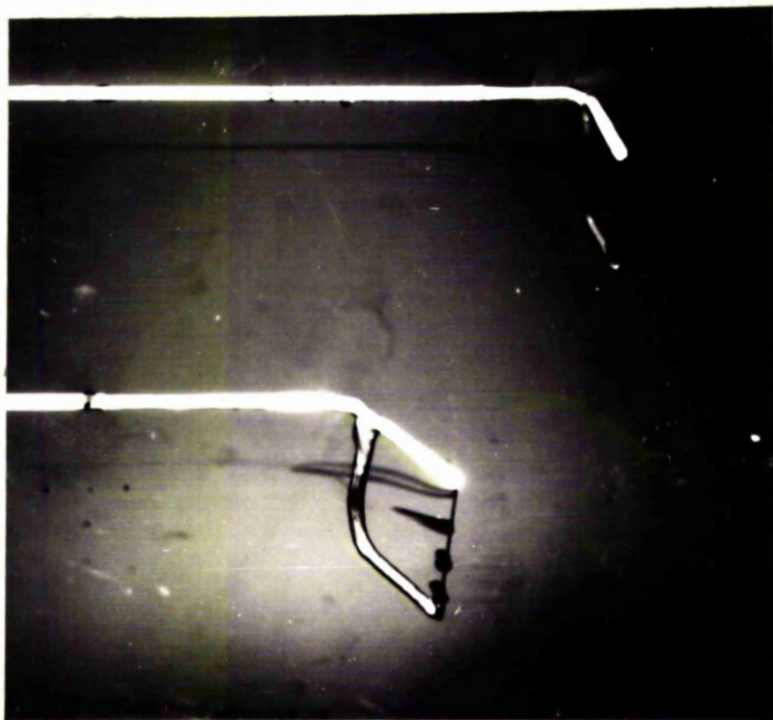


Ph. 20

From camera 1-2362 s  
Simulator in operation



Pair 5

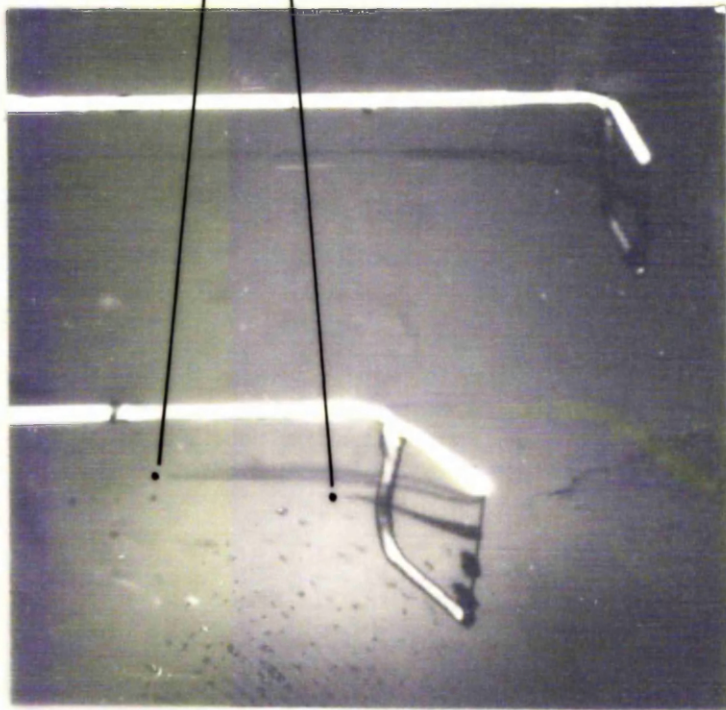


Ph. 19  
From camera 2- 2362 s  
Simulator in operation

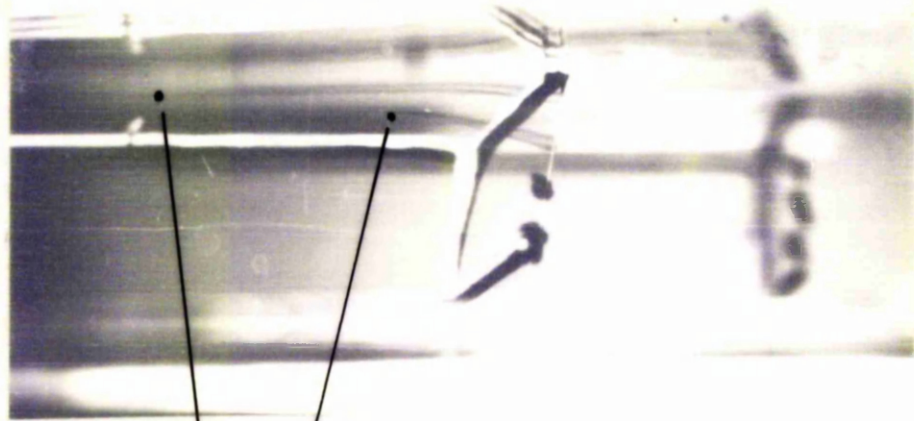


Ph. 20  
From camera 1- 2362 s  
Simulator in operation

Pair 6



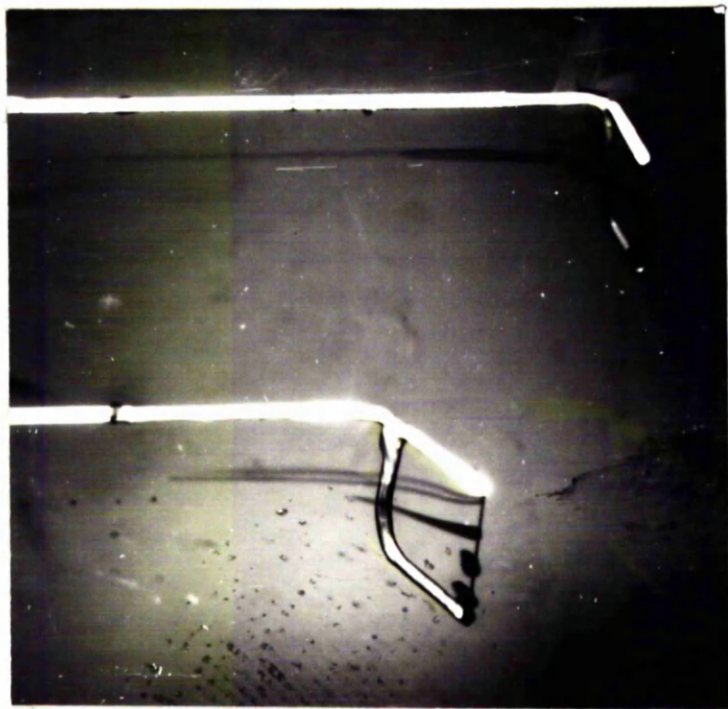
Ph. 21  
From camera 2 - 2375 s  
Simulator in operation



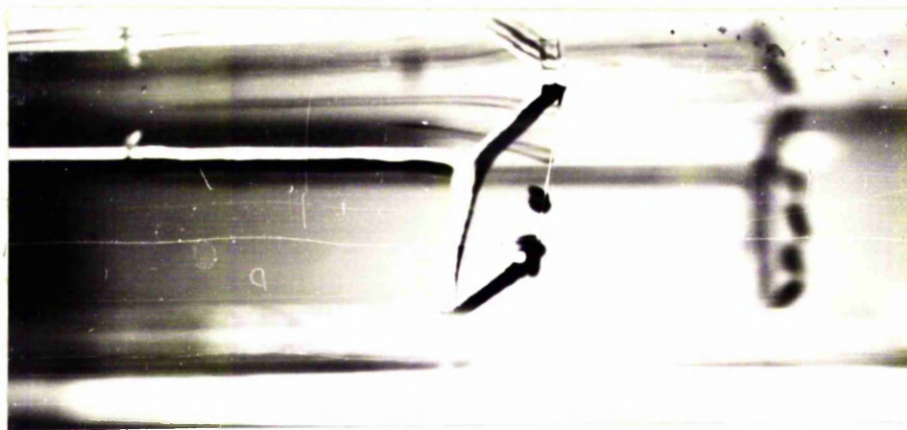
Ph. 22  
From camera 1 - 2375 s  
Simulator in operation

end points  
line No. 2  
line No. 3

Pair 6



Ph. 21  
From camera 2 - 2375 s  
Simulator in operation



Ph. 22  
From camera 1-2375s  
Simulator in operation

## Chapter 4

## CHAPTER 4

### FUTURE WORK

The experience gained in this programme of research suggests that the following aspects could usefully form further areas of research:

1. The computing program concerning the 3-dimensional laminar flow inside the transwall module should be refined to use less computing time and storage. This should include the following steps:
  - (a) the exclusion of step (vi) of the procedure solving the whole set of difference equations. This step means the repetition of a part of the procedure and its reason was to prevent any divergence of the whole set because of slow convergence of the sub-sets of momentum and "pressure correction" equations.
  - (b) further investigation of the convergence of the iterative solution of the "pressure correction" sub-set of equations. The direct method of solution has increased very much both storage and computing time requirements.
  - (c) adopting the Boussinesq approximation in which the density of the fluid is considered constant but the variation of density is taken into account in the buoyancy term of the momentum equations. The criteria for the applicability of the Boussinesq approximation are valid in the case of the transwall flow.
  - (d) examination of the importance of the temperature dependence of the other auxiliary variables of the liquid, e.g. the first coefficient of viscosity  $\mu$  and the thermal conductivity  $\lambda$ . The use of constant values of these variables at every time interval should be examined.

Any improvement in the computing program in respect to computer time requirements would allow a quantitative comparison between the two modes of the natural convection induced either by absorption of solar radiation or by temperature differences between the bulk of the liquid and the glass surfaces.

2. Further application of the numerical method is needed to establish easily usable relations of the effective conductivity of the transwall liquid with a few basic parameters, e.g. Rayleigh number, aspect ratio, etc. under various irradiance and temperature conditions. The application should also include the importance of the 3-dimensional radiation absorption of the transwall module, the surface radiation absorption of the boundary of the convection region and stratification effects.

The fitting of the experimental data collected from measurements of the temperature of a large number of points inside the transwall module of the test box would allow the calculation of the effective conductivity for this particular transwall module. A system of twenty thermocouples at four different and varying heights of the transwall module has already been constructed in M.E.R.A.

3. Experimental verification is required for the method of distributing the solar radiation among the internal surfaces of an enclosure. This could be obtained by measuring the incident radiation on the external surface of the semitransparent element of the enclosure, the radiation transmitted through this element and the radiation received by various points of the opaque surfaces.

4. Further verification of the analytical modelling of the transwall passive solar system by using the test-box is needed. This verification should include more complicated cases e.g. natural infiltration, ventilation, the inclusion of a controlled heater, etc. which have not been examined in this work. A number of uncertainties present in the verification of this work could be overcome by completing the measured climatological data and especially by measuring:

- (a) the temperatures of more nodes and surfaces than at present
- (b) the transmitted radiation through the transwall into the test-box after the first-strike.

The test-box can be used to model some other passive solar systems after some minor modifications. This allows the verification of the analytical modelling to be extended to these systems as well.

The experimental data collected from the test-box would be of additional use, because it would give important evidence of the thermal performance of an equivalent solar heated room with transwall under the climatological conditions of West-Scotland.

5. The 1-dimensional ray-tracing technique is much easier to use and less time consuming though less accurate than the 3-dimensional technique.

A systematic comparison between these techniques in the case of various transwall or other 3-dimensional solar systems is needed. This would allow the introduction of correction factors for the results obtained from the 1-dimensional technique.



6. Both techniques can be usefully applied to a variety of transwall modules with one or more outside glass (or plastic) plates with different optical properties. Although such variations are not expected to produce major difference from the results presented in sections 1.2 and 1.4, this would complete the assessment of the optical performance of the transwall system.
7. The discretization method concerning the diffuse solar radiation (section 1.3.2a) should be applied to a variety of commercial glazings and solar collector covers. This will complete the information about the equivalent angle of incidence of the isotropic sky and ground diffuse radiation at various tilts over the horizon given by Duffie et.al. (15). The method can easily examine factors, e.g. anisotropy and spectral composition of the incident radiation, spectral variation of the optical properties, etc., the importance of which has not yet been assessed.
8. When the method of distributing the solar radiation among the semitransparent elements and internal surfaces of an enclosure is verified, it should be applied to a number of common enclosures. Some of these common enclosures are given at the beginning of section 2.2. This distribution would be of use to a successive thermal analysis of the systems of which the enclosures are part.
9. The resulting analytical modelling of passive solar systems tested against experiment should be used to compare transwall systems with different features. For example, systems consisting of modules with and without some gel agents to stop circulation. Furthermore, it should be applied to some full size buildings and compared on that basis with rival passive solar systems, e.g. thermal storage wall.

## **Appendices**



## Appendix A

A closed-formula example of the 1-dimensional ray-tracing technique with infinite number of internal reflections.

The relations for the calculation of the total reflectance, transmittance and absorptance of the system of Fig. A1 are given for both directions of the incoming radiation.

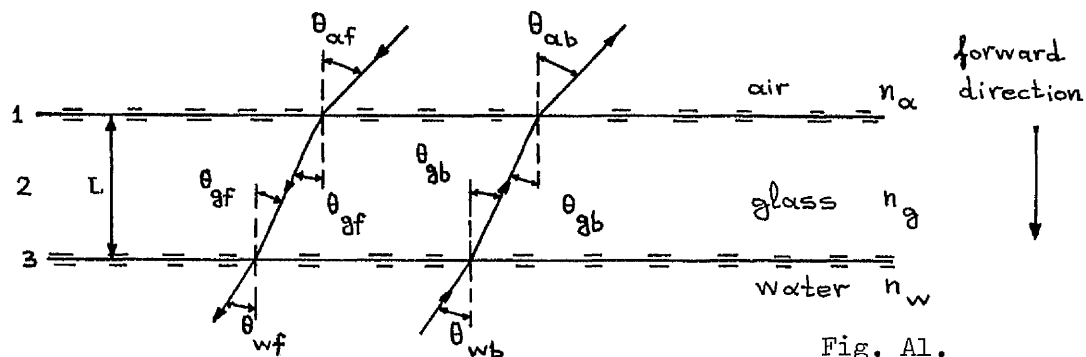


Fig. A1.

The system consists of three sub-systems:

1. the boundary surface between air and glass
2. the glass material
3. the boundary surface between glass and water.

The greek letter  $\theta$  denotes the angle of incidence or the angle of refraction.

The subscripts a, g and w are referred to the air, glass and water respectively.

The forward direction is defined as the direction from the air to the water. The subscripts f and b denote the forward and backward direction respectively.

The properties of the subsystems and the whole system are defined in the following tables

Table A.1

Properties →	Reflectivity		Transmissivity		Absorptivity	
	Forward	Backward	Forward	Backward	Forward	Backward
Sub-system ↓						
1	$F_f(1)$	$F_b(1)$	$Y_f(1)$	$Y_b(1)$	$A_f(1)$	$A_b(1)$
2	$F_f(2)$	$F_b(2)$	$Y_f(2)$	$Y_b(2)$	$A_f(2)$	$A_b(2)$
3	$F_f(3)$	$F_b(3)$	$Y_f(3)$	$Y_b(3)$	$A_f(3)$	$A_b(3)$

Table A.2

Properties of the system	Forward direction	Backward direction
Total reflectance	$F_{tf}$	$F_{tb}$
Total transmittance	$Y_{tf}$	$Y_{tb}$
Absorptance of sub-system 2	$A_{tf}$	$A_{tb}$

From the recurrence relations of section 1.1 we obtain the following relations:

$$F_{tf} = F_f(1) + \left( \left( F_f(2) * Y_f(1) * Y_b(1) \right) / \left( 1 - F_f(2) * F_b(1) \right) \right) + \\ \left( \left( F_f(3) * Y_f(1) * Y_f(2) * Y_b(1) * Y_b(2) \right) / \left( \left( 1 - F_f(2) * F_b(1) \right) * \right. \right. \\ \left. \left. \left( 1 - F_f(2) * F_b(1) - F_f(3) * F_b(2) + F_f(2) * F_f(3) * F_b(1) * F_b(2) + F_f(3) * F_b(1) * Y_f(2) * Y_b(2) \right) \right) \right) \quad (A.1)$$

$$F_{tb} = F_b(3) + \left( \left( F_b(2) * Y_f(3) * Y_b(3) \right) / \left( 1 - F_f(3) * F_b(2) \right) \right) + \\ \left( \left( F_b(1) * Y_f(2) * Y_f(3) * Y_b(2) * Y_b(3) \right) / \left( \left( 1 - F_f(3) * F_b(2) \right) * \right. \right. \\ \left. \left. \left( 1 - F_f(3) * F_b(2) - F_f(2) * F_b(1) + F_f(2) * F_f(3) * F_b(1) * F_b(2) + F_f(3) * F_b(1) * Y_f(2) * Y_b(2) \right) \right) \right) \quad (A.2)$$

$$Y_{tf} = \left( Y_f(1) * Y_f(2) * Y_f(3) \right) / \left( \left( 1 - F_f(2) * F_b(1) \right) * \right. \\ \left. \left( 1 - F_f(2) * F_b(1) - F_f(3) * F_b(2) + F_f(2) * F_f(3) * F_b(1) * F_b(2) + F_f(3) * F_b(1) * Y_f(2) * Y_b(2) \right) \right) \quad (A.3)$$

$$Y_{tb} = \left( Y_b(1) * Y_b(2) * Y_b(3) \right) / \left( \left( 1 - F_f(3) * F_b(2) \right) * \right. \\ \left. \left( 1 - F_f(3) * F_b(2) - F_f(2) * F_b(1) + F_f(2) * F_f(3) * F_b(1) * F_b(2) + F_f(3) * F_b(1) * Y_f(2) * Y_b(2) \right) \right) \quad (A.4)$$

$$A_{tf} = \left( \left( Y_f(1) - F_f(3) * F_b(2) * Y_f(1) - F_f(2) * Y_f(1) + F_f(2) * F_f(3) * F_b(2) * Y_f(1) - \right. \right. \\ \left. \left. F_f(3) * Y_f(1) * Y_f(2) * Y_b(2) - Y_f(1) * Y_f(2) * Y_f(3) \right) / \right. \\ \left. \left( 1 - F_f(3) * F_b(2) - F_f(2) * F_b(1) - F_f(3) * F_b(1) * Y_f(2) * Y_b(2) \right) \right) \\ - \left( \left( Y_f(1) * Y_f(2) - F_f(3) * Y_f(1) * Y_f(2) - Y_f(1) * Y_f(2) * Y_f(3) \right) / \right. \\ \left. \left( 1 - F_f(2) * F_b(1) - F_f(3) * F_b(2) + F_f(2) * F_f(3) * F_b(1) * F_b(2) - F_f(3) * F_b(1) * Y_f(2) * Y_b(2) \right) \right) \quad (A.5)$$

$$A_{tb} = \left( \left( Y_b(3) - F_f(2) * F_b(3) * Y_b(3) - F_b(2) * Y_b(3) + F_f(2) * F_b(1) * F_b(2) * Y_b(3) - \right. \right. \\ \left. \left. F_b(1) * Y_f(2) * Y_b(2) * Y_b(3) - Y_b(1) * Y_b(2) * Y_b(3) \right) / \right. \\ \left. \left( 1 - F_f(3) * F_b(2) - F_f(2) * F_b(1) - F_f(3) * F_b(1) * Y_f(2) * Y_b(2) \right) \right) \\ - \left( \left( Y_b(2) * Y_b(3) - F_b(1) * Y_b(2) * Y_b(3) - Y_b(1) * Y_b(2) * Y_b(3) \right) / \right. \\ \left. \left( 1 - F_f(2) * F_b(1) - F_f(3) * F_b(2) + F_f(2) * F_f(3) * F_b(1) * F_b(2) - F_f(3) * F_b(1) * Y_f(2) * Y_b(2) \right) \right) \quad (A.6)$$

The properties of the three subsystems are calculated from the following relations:

$$F_f(1) = \frac{\sin^2(\theta_{af} - \theta_{gf})}{\sin^2(\theta_{af} + \theta_{gf})} \quad (A.7) \quad \text{for the component of polarization perpendicular to the plane of incidence}$$

$$\text{or} \quad F_f(1) = \frac{\tan^2(\theta_{af} - \theta_{gf})}{\tan^2(\theta_{af} + \theta_{gf})} \quad (A.8) \quad \text{for the component of polarization parallel to the plane of incidence}$$

$$F_f(2) = 0 \quad (A.9) \quad \text{By definition}$$

$$F_f(3) = \frac{\sin^2(\theta_{gf} - \theta_{wf})}{\sin^2(\theta_{gf} + \theta_{wf})} \quad (A.10) \quad \text{for the component of polarization perpendicular to the plane of incidence and } \theta_{gf} < \theta_{gcf}$$

$$\text{or} \quad F_f(3) = \frac{\tan^2(\theta_{gf} - \theta_{wf})}{\tan^2(\theta_{gf} + \theta_{wf})} \quad (A.11) \quad \text{for the component of polarization perpendicular to the plane of incidence and } \theta_{gf} < \theta_{gcf}$$

$$F_f(3) = 1 \quad (A.12) \quad \text{for } \theta_{gf} > \theta_{gcf} \quad (\text{total reflection})$$

$$Y_f(1) = 1 - F_f(1) \quad (A.13) \quad A_f(1) = 0 \quad (A.16)$$

$$Y_f(2) = e^{-K \cdot t} \quad (\text{according to Bouguer's law}) \quad (A.14) \quad A_f(2) = 1 - Y_f(2) \quad (A.17)$$

$$Y_f(3) = 1 - F_f(3) \quad (A.15) \quad A_f(3) = 0 \quad (A.18)$$

Similarly

$$F_b(1) = \frac{\sin^2(\theta_{ab} - \theta_{gb})}{\sin^2(\theta_{ab} + \theta_{gb})} \quad (A.19) \quad \text{for the component of polarization perpendicular to the plane of incidence and } \theta_{gb} < \theta_{gcb}$$

$$\text{or} \quad F_b(1) = \frac{\tan^2(\theta_{ab} - \theta_{gb})}{\tan^2(\theta_{ab} + \theta_{gb})} \quad (A.20) \quad \text{for the component of polarization parallel to the plane of incidence and } \theta_{gb} < \theta_{gcb}$$

$$F_b(1) = 1 \quad (A.21) \quad \text{for } \theta_{gb} > \theta_{gcb} \quad (\text{total reflection})$$

$$F_b(2) = 0 \quad (A.22) \quad \text{By definition}$$

$$F_b(3) = \frac{\sin^2(\theta_{gb} - \theta_{wb})}{\sin^2(\theta_{gb} + \theta_{wb})} \quad (A.23) \quad \text{for the component of polarization perpendicular to the plane of incidence}$$

$$\text{or} \quad F_b(3) = \frac{\tan^2(\theta_{gb} - \theta_{wb})}{\tan^2(\theta_{gb} + \theta_{wb})} \quad (A.24) \quad \text{for the component of polarization parallel to the plane of incidence}$$

$$Y_b(1) = 1 - F_b(1) \quad (A.25) \quad A_b(1) = 0 \quad (A.28)$$

$$Y_b(2) = e^{-K \cdot t} \quad (\text{according to Bouguer's law}) \quad (A.26) \quad A_b(2) = 1 - Y_b(2) \quad (A.29)$$

$$Y_b(3) = 1 - F_b(3) \quad (A.27) \quad A_b(3) = 0 \quad (A.30)$$

According to Snell's law the relations which relate the angles

$\theta_a$ ,  $\theta_g$  and  $\theta_w$  for each direction of the radiation are:

$$\frac{\sin(\theta_a)}{\sin(\theta_g)} = \frac{n_g}{n_a}, \quad \frac{\sin(\theta_g)}{\sin(\theta_w)} = \frac{n_w}{n_g}$$

where  $n_a$ ,  $n_g$ ,  $n_w$  the refractive indices of air, glass and water, respectively.

Additionally,  $K$  is the extinction coefficient of glass

$t$  is the optical path of radiation inside the glass plate of thickness  $L$ ,  $t = L/\cos(\theta_g)$

$\theta_{gcf}$ ,  $\theta_{gcb}$  are the critical angles of incidence for forward and backward direction of the radiation, respectively.

$$\theta_{gcf} = \sin^{-1}[n_w/n_g] \quad \text{and}$$

$$\theta_{gcb} = \sin^{-1}[n_a/n_g]$$

It should be repeated here, that the values of  $n_a$ ,  $n_g$ ,  $n_w$  and  $K$  can be understood to be spectral or monochromatic values or they can be regarded as total gray values.

For the forward direction of the radiation total reflection never occurs because the angle of incidence  $\theta_{gf}$  at the glass-water interface is always smaller than the critical value  $\theta_{gcf}$ . Indeed the maximum value of the angle  $\theta_{gf}$  occurs for the maximum angle of incidence at the air-glass interface  $\theta_{af}$ . Thus, if  $\theta_{af} = 90^\circ \Rightarrow \text{maximum}\{\theta_{gf}\} = \sin^{-1}[(n_a/n_g) * \sin(90^\circ)]$

But, because  $n_g > n_w > n_a \Rightarrow$

$$\sin^{-1}[n_a/n_g] < \sin^{-1}[n_w/n_g] \Rightarrow$$

$$\text{maximum}\{\theta_{gf}\} < \theta_{gcf}$$

For the backward direction of the radiation total reflection occurs for angles of incidence  $\theta_{gb}$  at the glass-air interface larger than the critical angle  $\theta_{gcb}$ ,

For example, for  $n_a = 1.0$  and  $n_w = 1.33 \Rightarrow \theta_{gcb} = 48^\circ 45'$

This fact is quite significant because it implies that an optical system may behave differently for opposite direction incident radiation. This applies not only in respect to the total reflectance as is usually shown by the other (previously mentioned in section 1.1) techniques, but in respect to the total transmittance as well, when total reflection occurs.

Because of the relations

$$F_f(2) = 0$$

$$F_b(2) = 0$$

the relations A.1 to A.6 are simplified to the following forms:

$$F_{tf} = F_f(1) + \frac{F_f(3) * Y_f(1) * Y_f(2) * Y_b(1) * Y_b(2)}{1 - F_f(3) * F_b(1) * Y_f(2) * Y_b(2)} \quad (A.31)$$

$$F_{tb} = F_b(3) + \frac{F_b(1) * Y_f(2) * Y_f(3) * Y_b(2) * Y_b(3)}{1 - F_f(3) * F_b(1) * Y_f(2) * Y_b(2)} \quad (A.32)$$

$$Y_{tf} = \frac{Y_f(1) * Y_f(2) * Y_f(3)}{1 - F_f(3) * F_b(1) * Y_f(2) * Y_b(2)} \quad (A.33)$$

$$Y_{tb} = \frac{Y_b(1) * Y_b(2) * Y_b(3)}{1 - F_f(3) * F_b(1) * Y_f(2) * Y_b(2)} \quad (A.34)$$

$$A_{tf} = \frac{Y_f(1) - F_f(3) * Y_f(1) * Y_f(2) * Y_b(2) + F_f(3) * Y_f(1) * Y_f(2) - Y_f(1) * Y_f(2)}{1 - F_f(3) * F_b(1) * Y_f(2) * Y_b(2)} \quad (A.35)$$

$$A_{tb} = \frac{Y_b(3) - F_b(1) * Y_f(2) * Y_b(2) * Y_b(3) + F_b(1) * Y_b(2) * Y_b(3) - Y_b(2) * Y_b(3)}{1 - F_f(3) * F_b(1) * Y_f(2) * Y_b(2)} \quad (A.36)$$

## Appendix B

Exit point of a radiation vector from a control volume

Provided that the boundary of the control volume is a continuous function  $f(x,y,z)$ , the intersection point  $B(x,y,z)$  of the radiation vector  $a(a_1, a_2, a_3)$  and the boundary is given by the solution of the system of equations:

$$\frac{x - x_1}{a_1} = \frac{y - y_1}{a_2}$$

$$\frac{y - y_1}{a_2} = \frac{z - z_1}{a_3}$$

$$f(x,y,z) = 0$$

where  $A(x_1, y_1, z_1)$  is a known point through which the radiation vector passes.

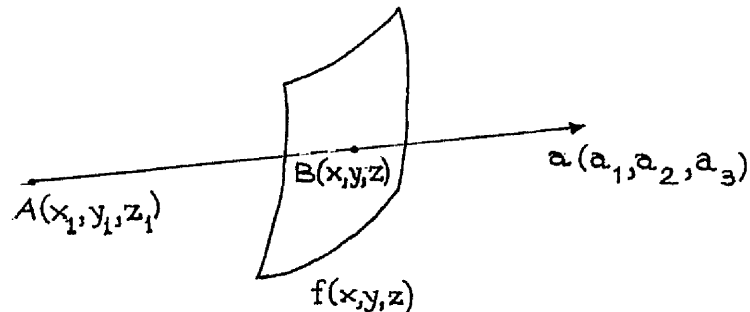


Fig. B.1

The boundary of the control volume is not usually a continuous function. This means that another procedure should be developed for the calculation of the exit point instead of the above mentioned solution of three equations.

The following flow-chart illustrates the procedure used to calculate the exit point in the case of a parallelepiped control volume. The known point  $A(x_1, y_1, z_1)$  is the entrance point to the control volume.

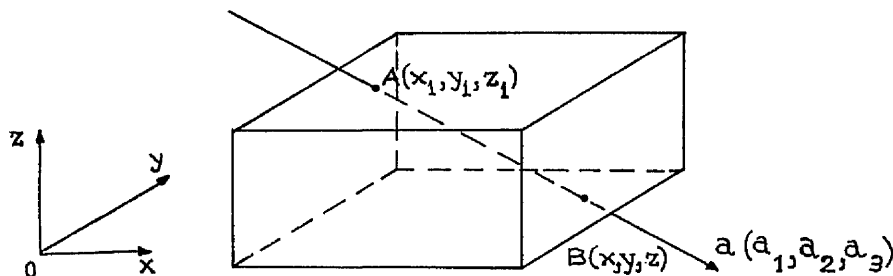


Fig. B.2

The three pairs of the opposite faces of the parallelepiped are parallel to three cartesian axes,  $Ox$ ,  $Oy$ ,  $Oz$ . Then the co-ordinates of the planes of the six faces are:

$(X10, 0, 0)$ ,  $(X20, 0, 0)$

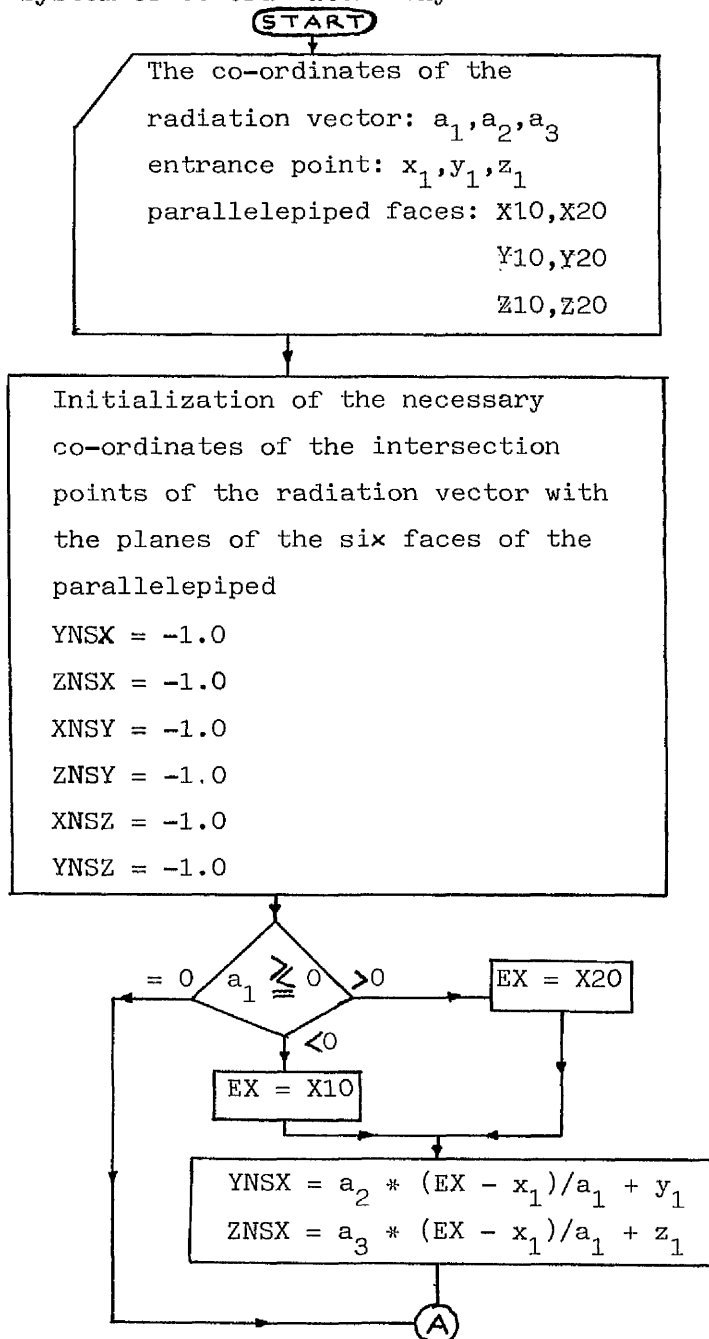
$(0, Y10, 0)$ ,  $(0, Y20, 0)$

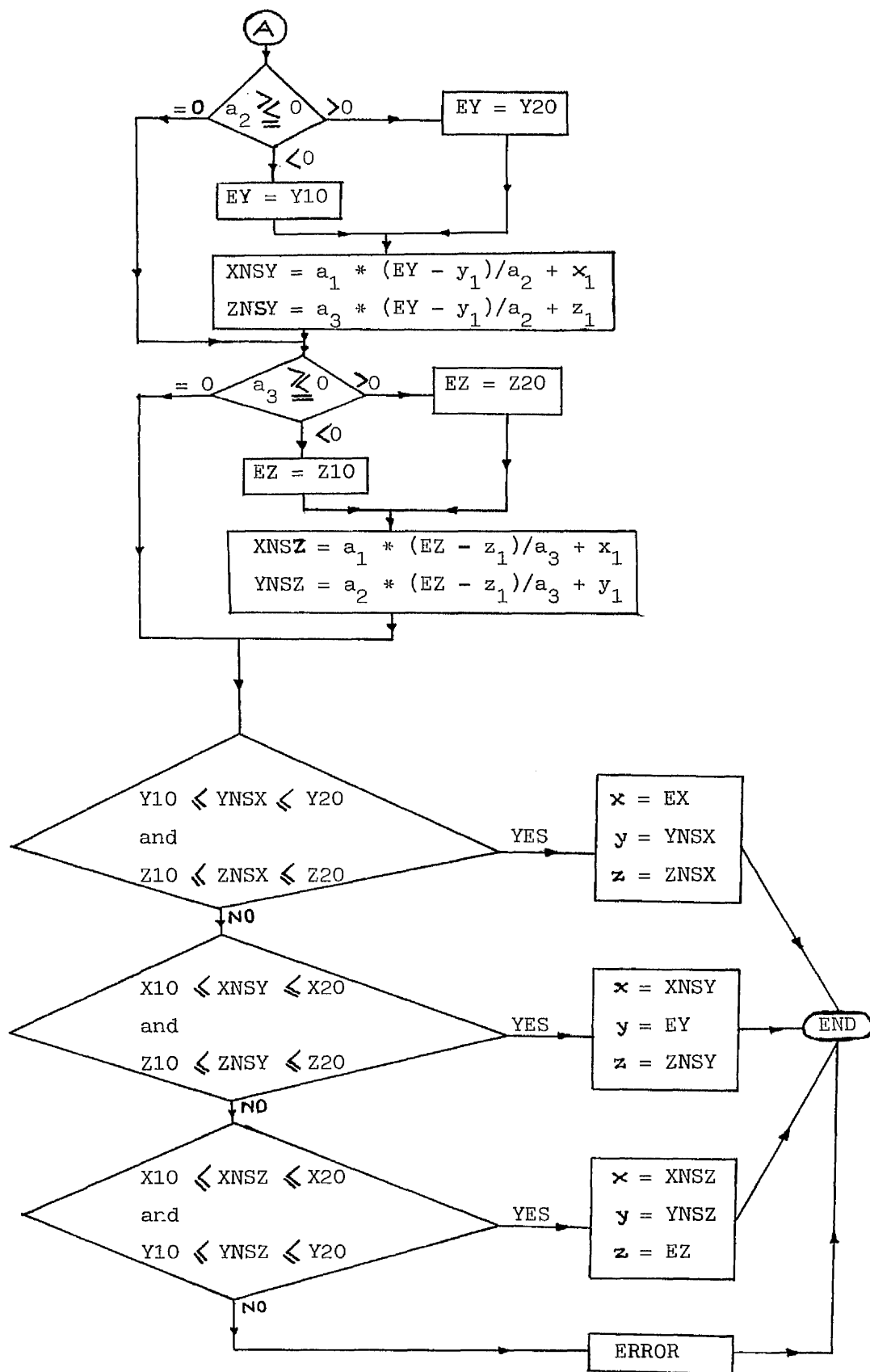
$(0, 0, Z10)$ ,  $(0, 0, Z20)$

By convention:

$X10 \gg 0$ ,  $X20 \gg 0$ ,  $Y10 \gg 0$ ,  $Y20 \gg 0$ ,  $Z10 \gg 0$ ,  $Z20 \gg 0$

The flow-chart gives the co-ordinates of the exit point  $x$ ,  $y$  and  $z$  in the system of co-ordinates  $O.xyz$ .







## Appendix C

Calculation of the vectors of the reflected and transmitted radiation in the case of specular reflection and refraction.

In Fig. C1 the radiation vector  $\vec{a}(a_1, a_2, a_3)$  coming from medium  $m_1$ , falls on point  $A(X, Y, Z)$  of the boundary  $\vec{p}(p_1, p_2, p_3)$  between the two dis-similar optical media  $m_1$  and  $m_2$ . In general, one fraction,  $ab$ , of the radiation vector absolute value,  $a$ , will be absorbed by the boundary, a second one,  $tr$ , will be transmitted to the second medium  $m_2$ , and a third fraction,  $re$ , will be reflected back to the medium  $m_2$ :

$$ab + tr + re = a$$

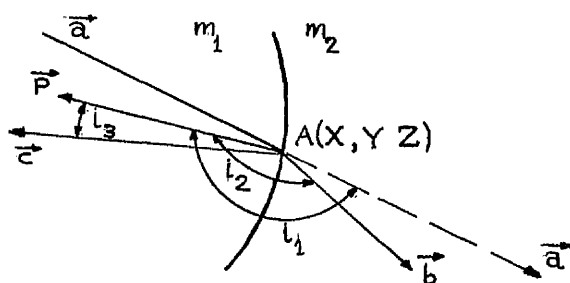


Fig. C1

In the ideal specular case, the transmitted and reflected fractions of radiation are the absolute values  $b$  and  $c$  of the vector  $\vec{b}(b_1, b_2, b_3)$  of the transmitted radiation and of the vector  $\vec{c}(c_1, c_2, c_3)$  of the reflected radiation, respectively.

$$b = tr$$

$$c = re$$

These two vectors can be calculated if the absolute value and the components of the vectors of the incident radiation  $\vec{a}$  and of the boundary surface  $\vec{p}$  are known.

Calculation of the angles of incidence, refraction and reflection.

The angle of incidence, that is the angle between the vectors  $\vec{a}$  and  $\vec{p}$  is  $i_1$  (Fig. C1).

$$i_1 = \cos^{-1} [ (a_1 p_1 + a_2 p_2 + a_3 p_3) / (a * p) ]$$

$$a = (a_1^2 + a_2^2 + a_3^2)^{0.5}$$

$$p = (p_1^2 + p_2^2 + p_3^2)^{0.5}$$

Because by convention the direction of the vector  $\vec{p}$  is taken to be from medium  $m_2$  to medium  $m_1$ :

$$i_1 \gg 90^\circ$$

The angle of refraction, that is the angle between the vectors  $\vec{b}$  and  $\vec{p}$  is  $i_2$  (Fig. C1).

There is no transmitted radiation if the optical medium  $m_2$  is opaque or total reflection occurs. In such a case the angle  $i_2$  does not exist and

$$tr = b = 0$$

The total reflection occurs if the refractive index  $n_1$  of the medium  $m_1$  from which the radiation vector  $\vec{a}$  comes is larger than the refractive index  $n_2$  of the medium  $m_2$  and the angle of incidence  $i_1$  is larger than a critical value  $i_{cr}$ :

$$n_1 > n_2$$

$$i_1 > i_{cr} = \sin^{-1}[(n_2/n_1)]$$

If there is transmitted radiation into the medium  $m_2$  the angle  $i_2$  is calculated from the relation:

$$i_2 = 180^\circ - \sin^{-1} \left[ \frac{n_1}{n_2} * \sin(180^\circ - i_1) \right]$$

This relation is another expression of the Snell's law.

The angle of reflection, that is the angle between the vectors  $\vec{a}$  and  $\vec{p}$  is  $i_3$  (Fig. C1).

From the definition of the specular reflection,  $i_3 = 180^\circ - i_1$

### Calculation of the reflected and transmitted fractions of radiation.

#### The reflected fraction

$$c = re = I_{\perp} * \rho_{\perp} + I_{\parallel} * \rho_{\parallel}$$

where  $I_{\perp}$  is the component of polarization of the incident radiation that is perpendicular to the plane of incidence

$I_{\parallel}$  is the component of polarization of the incident radiation that is parallel to the plane of incidence.

$\rho_{\perp}$ ,  $\rho_{\parallel}$  are the reflectivities of the boundary for the components of polarization  $I_{\perp}$  and  $I_{\parallel}$  respectively.

$$I_{\perp} + I_{\parallel} = a$$

For smooth surfaces,

$$\rho_{\perp} = \frac{\sin^2(i_1 - i_2)}{\sin^2(i_1 + i_2)}$$

$$\rho_{\parallel} = \frac{\tan^2(i_1 - i_2)}{\tan^2(i_1 + i_2)}$$

The transmitted fraction

If the optical medium  $m_2$  is opaque or total reflection occurs then

$$b = \text{tr} = 0$$

Otherwise,

$$b = 1 - c - ab$$

Calculation of the components of the vectors  $\vec{b}$  and  $\vec{c}$ .

In the ideal specular case, the vectors  $\vec{a}$ ,  $\vec{p}$ ,  $\vec{c}$  and  $\vec{b}$  are on the same plane. This means that the following two scalar triple products are zero:

$$\vec{a} \cdot (\vec{c} \times \vec{p}) = 0 \quad \Rightarrow \quad \begin{vmatrix} a_1 & a_2 & a_3 \\ c_1 & c_2 & c_3 \\ p_1 & p_2 & p_3 \end{vmatrix} = 0 \quad (\text{C1})$$

$$\vec{a} \cdot (\vec{b} \times \vec{p}) = 0 \quad \Rightarrow \quad \begin{vmatrix} a_1 & a_2 & a_3 \\ b_1 & b_2 & b_3 \\ p_1 & p_2 & p_3 \end{vmatrix} = 0 \quad (\text{C2})$$

For the vector  $\vec{c}$ ,

$$\vec{a} \cdot \vec{c} = -a * c * \cos(2 * i_3) \Rightarrow$$

$$a_1 * c_1 + a_2 * c_2 + a_3 * c_3 = -a * c * \cos(2 * i_3) \quad (\text{C3})$$

$$\vec{p} \cdot \vec{c} = p * c * \cos(i_3) \Rightarrow$$

$$p_1 * c_1 + p_2 * c_2 + p_3 * c_3 = p * c * \cos(i_3) \quad (\text{C4})$$

Similarly for the vector  $\vec{b}$

$$\vec{a} \cdot \vec{b} = a * b * \cos(i_1 - i_2) \Rightarrow$$

$$a_1 * b_1 + a_2 * b_2 + a_3 * b_3 = a * b * \cos(i_1 - i_2) \quad (\text{C5})$$

$$\vec{p} \cdot \vec{b} = p * b * \cos(i_2) \Rightarrow$$

$$p_1 * b_1 + p_2 * b_2 + p_3 * b_3 = p * b * \cos(i_2) \quad (\text{C6})$$

Each of the systems of equations

(C1), (C3), (C5)

(C2), (C4), (C6)

is a linear system of 3 equations with 3 unknowns. Their solution provides us with the values of the components of the vector  $\vec{c}$  and  $\vec{b}$ .

The subroutines EXAM, INRE and EXRE have been constructed in accordance with the above analysis. The solution of the system of the linear equations is obtained by the subroutine GAUSS based on the Gauss elimination method.

## Appendix D

Optical properties - refractive index and extinction coefficient -  
of clear float glass and Antisun glass, grey 41/60  
Clear float glass

Table D1 gives the refraction index and extinction coefficient of clear float glass made by Pilkington Brothers Limited. Transmittance data (23) was available for clear float glass samples of 3mm and 6mm thickness, produced by measurements at a large number of wavelengths and zero angle of incidence.

Using the basic equation of transmittance for one sheet of glass:

$$\tau_{\lambda} = \tau'_{\lambda} * ((1 - \rho'_{\lambda})^2 / (1 - \rho'^2_{\lambda} * \tau'^2_{\lambda})) \quad (D.1)$$

$$\text{where } \tau'_{\lambda} = e^{-K_{\lambda} * L} \quad (D.2)$$

the following system of two non-linear equations with two unknowns

$(K_{\lambda}, \rho'_{\lambda})$  had to be solved for each different wavelength  $\lambda$ :

$$\begin{aligned} ((e^{-L_1})^{K_{\lambda}} * (1 - \rho'_{\lambda})^2 / (1 - \rho'^2_{\lambda} * (e^{-L_1})^{2 * K_{\lambda}}) - \tau_{\lambda 1} &= 0 \\ ((e^{-L_2})^{K_{\lambda}} * (1 - \rho'_{\lambda})^2 / (1 - \rho'^2_{\lambda} * (e^{-L_2})^{2 * K_{\lambda}}) - \tau_{\lambda 2} &= 0 \end{aligned} \quad (D.3)$$

where  $L_1 = 3\text{mm}$  and  $L_2 = 6\text{mm}$

The NAG sub-routine C05NAF had to be used. The convergence of the method depended strongly on the first estimate  $(K_{\lambda_{\text{est}}}, \rho'_{\lambda_{\text{est}}})$  of the solution. The first estimate of the solution was given solving the following system of two non-linear equations with two unknowns  $(K_{\lambda_{\text{est}}}, \rho'_{\lambda_{\text{est}}})$

$$\begin{aligned} ((e^{-L_1})^{K_{\lambda_{\text{est}}}} * (1 - \rho'_{\lambda_{\text{est}}})^2 / (1 + \rho'^2_{\lambda_{\text{est}}}) - \tau_{\lambda 1} &= 0 \\ ((e^{-L_2})^{K_{\lambda_{\text{est}}}} * (1 - \rho'_{\lambda_{\text{est}}})^2 / (1 + \rho'^2_{\lambda_{\text{est}}}) - \tau_{\lambda 2} &= 0 \end{aligned} \quad (D.4)$$

Then, using the relation

$$\rho'_{\lambda} = (n_{\lambda} - 1)^2 / (n_{\lambda} + 1)^2 \quad (D.5) \quad \text{the refractive index}$$

of glass was obtained at the particular wavelength.

The whole procedure has been expressed in sub-routines:

ARGO.ROS36(13) and ARGO.AUXN36(2)

Antisun, grey 41/60 glass

Table D2 gives the extinction coefficient of Antisun glass, grey 41/60, which can be a candidate for a middle absorbing glass plate of a water filled transwall module. According to Lisley (24) the refraction index of the Antisun glass is expected to be the same as that of clear float glass. The extinction coefficient values have been obtained by digitization of transmittance curve of 6mm Antisun grey 41/60, from (25) and application of relations (D.1), (D.2) and (D.5). Average values of the extinction coefficient of the Antisun glass, grey 41/60 at 8 different wavelength bands are given in Table 1.1, pp.22.

Table D1

Optical properties of clear float glass

Wavelength $\lambda^*$	refraction index of clear float glass	extinction coefficient of clear float glass $m^{-1}$	Wavelength $\lambda^*$	refraction index of clear float glass	extinction coefficient of clear float glass $m^{-1}$
$\mu m$			$\mu m$		
0.300	1.510	1500.00	0.900	1.516	53.33
0.310	1.510	1000.00	0.950	1.509	55.63
0.320	1.510	520.00	1.000	1.513	55.72
0.330	1.510	290.00	1.050	1.511	56.31
0.340	1.510	120.00	1.100	1.513	55.72
0.350	1.516	44.11	1.150	1.506	54.99
0.360	1.509	25.51	1.200	1.518	52.76
0.370	1.516	17.61	1.250	1.506	50.79
0.380	1.511	21.04	1.300	1.512	47.40
0.390	1.516	11.82	1.350	1.511	44.59
0.400	1.518	9.83	1.400	1.506	41.27
0.410	1.518	10.62	1.450	1.510	37.65
0.420	1.512	11.81	1.500	1.514	34.14
0.430	1.512	12.21	1.550	1.512	30.70
0.440	1.512	11.41	1.600	1.516	28.35
0.450	1.512	10.22	1.650	1.514	27.39
0.460	1.518	9.43	1.700	1.515	26.93
0.470	1.519	8.65	1.750	1.515	26.93
0.480	1.519	7.48	1.800	1.509	27.36
0.490	1.518	7.48	1.850	1.509	27.36
0.500	1.511	7.01	1.900	1.514	27.39
0.510	1.507	7.07	1.950	1.518	27.43
0.520	1.512	6.68	2.000	1.513	27.86
0.530	1.507	7.07	2.050	1.517	27.89
0.540	1.511	7.08	2.100	1.517	27.89
0.550	1.507	7.46	2.200	1.510	27.89
0.560	1.515	7.86	2.300	1.510	30.00
0.570	1.519	8.26	2.400	1.510	29.00
0.580	1.519	9.04	2.500	1.510	35.00
0.590	1.513	10.21	2.600	1.510	40.00
0.600	1.513	11.01	2.700	1.510	50.00
0.610	1.516	12.22	2.800	1.510	290.00
0.620	1.511	13.83	2.900	1.510	330.00
0.630	1.509	15.07	3.000	1.510	350.00
0.640	1.508	16.73	3.100	1.510	350.00
0.650	1.511	18.01	3.200	1.510	350.00
0.660	1.514	18.88	3.300	1.510	350.00
0.670	1.507	21.02	3.400	1.510	350.00
0.680	1.509	22.36	3.500	1.510	350.00
0.690	1.512	23.71	3.600	1.510	350.00
0.700	1.509	25.51	3.700	1.510	350.00
0.710	1.516	26.48	3.800	1.510	350.00
0.720	1.516	28.35	3.900	1.510	350.00
0.730	1.517	30.26	4.000	1.510	350.00
0.740	1.504	32.57	4.100	1.510	400.00
0.750	1.505	34.06			
0.800	1.510	41.32			
0.850	1.517	48.62			

Table D2

Extinction coefficient of Antisun glass, grey 41/60

wavelength $\lambda$	Extinction coefficient of Antisun grey 41/60 glass	wavelength $\lambda$	Extinction coefficient of Antisun grey 41/60 glass
$\mu\text{m}$	$\text{m}^{-1}$	$\mu\text{m}$	$\text{m}^{-1}$
0.300	1000.00	0.712	82.14
0.331	1000.00	0.737	90.71
0.350	245.05	0.750	96.22
0.366	159.90	0.800	118.01
0.381	151.23	0.882	145.68
0.387	112.73	0.900	148.34
0.393	98.30	0.964	158.14
0.400	97.59	1.025	162.31
0.483	138.37	1.200	155.46
0.500	142.48	1.326	138.66
0.522	138.70	1.500	104.75
0.539	122.84	1.645	87.34
0.547	113.37	1.915	83.66
0.555	111.82	2.100	75.12
0.571	120.57		
0.589	139.41		
0.600	138.60		
0.621	134.17		
0.635	138.81		
0.650	137.03		
0.662	123.50		
0.665	101.54		
0.674	92.59		
0.694	83.85		

## Appendix E

Extinction coefficient of various dyes and gelling agents.

The extinction coefficient  $\epsilon(\lambda)$ , (Kg water/mol dye\*m) of various dyes has been calculated as a function of wavelength  $\lambda$ . The data was obtained with a Beckmann spectrophotometer from measurements of the absorption coefficients of a known strength solution  $W$  (Kg dye/Kg water) of dye in distilled water,  $A(\lambda)$ , and of distilled water,  $A_s(\lambda)$ , in a cell of thickness  $L$  (in m)

$$\epsilon(\lambda) * C = (A(\lambda) - A_s(\lambda)) / L \quad (E.1)$$

$$\text{where, } C = W / (M * 10^{-3}) \quad (E.2)$$

$C$  is the concentration of dye in water (mol dye/kg water) and  $M$  is the molecular weight of the particular dye (gr of dye/mol of dye). It is obvious from the right part of relation (E.1) that we assumed that the refractive index of the solution of dye remains the same as that of pure distilled water. This assumption is used everywhere in this thesis. It should be added that the relation (E.1) is another form of Beer-Lambert relation (1.15) of page 21. This Beer-Lambert relation is used with the known extinction coefficient of the dye  $\epsilon(\lambda)$ , its strength  $W$  and relation (E.2) to calculate the dye solution extinction coefficient  $K(\lambda, C)$  ( $m^{-1}$ ) at the particular concentration  $C$  (or strength  $W$ ).

Table E.1 gives the extinction coefficient  $\epsilon(\lambda)$  of the following dyes: acid green B, methyl orange, copper chloride. In Table E.1 are also included the extinction coefficients  $a_o(\lambda)$  over that of water  $a_s(\lambda)$ , of two solutions of the gelling agent Courlose F100G in water. In this case the extinction coefficient  $a_o(\lambda)$  is defined from the Beer-Lambert relation  $a_o(\lambda) = K(\lambda) - a_s(\lambda)$  where  $K(\lambda)$  the extinction coefficient of the solution.

Table E.2 gives the average extinction coefficients  $\epsilon(\lambda_b)$ ,  $a_o(\lambda_b)$  of the abovementioned three dyes and the two solutions of Courlose F100G in water respectively, at seven different wavelength bands. Average values of refraction index  $n(\lambda)$  and extinction coefficient  $K(\lambda)$  of water at 25°C at eight different wavelength bands have already been given in Table 1.1, page 22 (data from References (26), (27)).

Table E1

Extinction coefficient  $\epsilon(\lambda)$ , (Kg water/mol dye\*m) of acid green B (M = 1015.0), methyl orange (M = 327.3), copper chloride (M = 170.5) and  $a(\lambda)$ , ( $m^{-1}$ ) of the two solutions of the gelling agent Courlose Fl000G, with strength, W, of 0.0025 Kg gel/Kg water and of 0.005 Kg gel/Kg water.

M, molecular weight of dye in gr dye/mol dye.

wavelength $\lambda$ $\mu m$	$\epsilon(\lambda)*E-06$ acid green B	$\epsilon(\lambda)*E-06$ methyl orange	$\epsilon(\lambda)*E-03$ copper chloride	$a(\lambda)$ Courlose W=0.0025	$a(\lambda)$ Courlose W=0.005
0.300	2.6304	0.5504	0.5955	0.0	7.0
0.315	1.8870	0.4261	0.3026	0.1	6.4
0.330	1.7226	0.2853	0.1729	0.7	6.6
0.350	1.6726	0.3237	0.1105	1.1	6.3
0.360	1.5940	0.4462	0.0865	1.2	6.5
0.375	1.5011	0.7187	0.0816	1.3	6.5
0.390	1.3295	1.0533	0.0768	1.6	6.6
0.400	1.1437	1.2783	0.0768	1.7	6.7
0.420	0.9507	1.6605	0.0624	1.9	6.6
0.435	0.8077	1.9037	0.0624	2.1	6.6
0.450	0.6362	2.1085	0.0624	2.3	6.8
0.465	0.4503	2.1670	0.0480	2.2	6.7
0.480	0.3503	1.9970	0.0480	2.1	6.6
0.495	0.2931	1.5544	0.0528	2.1	6.5
0.510	0.2573	1.0259	0.0528	2.2	6.3
0.525	0.2216	0.5431	0.0576	2.3	6.4
0.540	0.2073	0.2322	0.0576	2.2	6.2
0.555	0.2144	0.0823	0.0672	2.2	6.2
0.570	0.2716	0.0293	0.0816	2.4	6.4
0.585	0.3645	0.0183	0.1104	2.4	6.4
0.600	0.4932	0.0165	0.1345	2.3	6.3
0.615	0.6576	0.0165	0.1729	2.4	6.3
0.630	0.8220	0.0128	0.2257	2.4	6.3
0.645	0.9721	0.0128	0.3074	2.5	6.3
0.660	1.0866	0.0146	0.4034	2.6	6.4
0.675	1.1508	0.0128	0.4995	2.5	6.3
0.690	1.1937	0.0128	0.6244	2.5	6.2
0.705	1.2366	0.0110	0.7444	2.4	6.2
0.720	1.2294	0.0128	0.8741	2.4	6.1
0.735	1.2080	0.0183	1.0038	2.5	6.0
0.750	1.1437	0.0201	1.1094	2.4	5.9
0.765	1.1294	0.0201	1.1959	2.3	5.8
0.780	0.9578	0.0183	1.2439	2.2	5.6
0.795	0.7864	0.0165	1.2727	2.0	5.0
0.800	0.8720	0.0	1.1190	4.0	7.9
0.840	0.5718	0.0	1.0998	4.5	7.8
0.900	0.2359	0.0	1.0134	5.0	9.4
0.960	0.0	0.0	1.0422	14.3	17.0
0.980	0.0	0.0457	0.9654	6.9	13.0
1.000	0.4432	0.0878	0.9942	6.1	11.5
1.040	0.3288	0.0841	0.7925	5.0	11.0
1.080	0.7863	0.0183	0.6244	6.8	10.7
1.120	0.3574	0.0	0.5667	26.3	11.8
1.160	0.2859	0.0	0.7492	20.0	22.7
1.200	0.4003	0.1079	0.6916	11.0	15.5
1.240	0.5718	0.1500	0.6484	8.6	14.0
1.280	0.3574	0.0914	0.5331	14.8	16.0
1.320	0.7148	0.0183	0.7156	41.0	32.0
1.330	0.7148	0.0	0.0	50.0	100.0



Table E2

Averaged, extinction coefficient  $\epsilon(\lambda_b^*)$  (Kg water/mol dye\*m) of acid green B (M = 1015.0), methyl orange (M = 327.3), copper chloride (M = 170.5) and  $a_o(\lambda_b^*)$ , ( $m^{-1}$ ) of the two solutions of the gelling agent Courlose F1000G, with strength, W; of 0.0025 Kg gel/Kg water and of 0.005 Kg gel/Kg water

M, molecular weight of dye in gr dye/mol dye

wavelength band, $\lambda_b^*$ $\mu m$	$\epsilon(\lambda_b^*) * E-06$ acid green B	$\epsilon(\lambda_b^*) * E-06$ methyl orange	$\epsilon(\lambda_b^*) * E-03$ copper chloride	$a_o(\lambda_b^*)$ Courlose W=0.0025	$a_o(\lambda_b^*)$ Courlose W=0.005
0.30 ÷ 0.35	1.898	0.375	0.263	0.5	6.5
0.35 ÷ 0.40	1.463	0.751	0.084	1.4	6.5
0.40 ÷ 0.65	0.464	1.084	0.067	2.2	6.5
0.65 ÷ 0.70	1.038	0.0143	0.547	2.5	6.2
0.70 ÷ 0.90	0.687	0.0059	1.121	3.8	7.4
0.90 ÷ 1.20	0.157	0.033	0.815	12.0	13.7
1.20 ÷ 1.33	0.636	0.094	0.608	18.7	21.6

## Appendix F

Calculation of the spectral composition of the components of solar radiation

The solar radiation received at each surface on earth is generally composed of three components

- 1) direct radiation
- 2) diffuse radiation from the sky
- 3) reflected radiation from the ground or other surfaces

Since, meteorological offices collect solar radiation measurements at only a few stations, mathematical models have been developed (14), (15), (28), (29), (30), (31) to calculate the three components of solar radiation under various climatic conditions on any surface. But both measurements and mathematical models (especially the first) give almost always average value of the intensity of the components of solar radiation over its whole spectrum. The data on the spectral composition of solar radiation is quite scarce.

As a first approximation, the spectral composition of the direct radiation can be adopted as that given by Thekaekara (32) for different air-masses, Mr. This spectral composition assumes certain atmospheric conditions (as turbidity parameter  $a = 0.66$  and  $b = 0.085$ , 20 mm H<sub>2</sub>O and 34mm of O<sub>3</sub>). All the columns of Table 1.2 and L3 have been constructed from Thekaekara's data (32), except of the column of air-mass 2, which is derived from Reference (33).

The attenuating effect of the earth's atmosphere is expressed as a function of the so-called air-mass (30). Assuming the atmosphere as a homogenous hollow sphere, the air-mass Mgr at sea level is given by the following relation :

$$M_{gr} = ((R/H)^2 * \cos^2(Z) + 2 * (R/H) + 1)^{0.5} - (R/H) * \cos(Z)$$

where Z is the zenith angle of sun

R is the radius of the earth

and  $H = P_0 / (g * \rho_0)$

where  $P_0$  = sea level atmospheric pressure

$\rho_0$  = sea level air density

At elevated sites the air-mass Mr may vary considerably from that at sea level and therefore is calculated from

$$M_r = M_{gr} * P / P_0$$

where P is the site barometric pressure.

If a more realistic spectral distribution of the direct radiation

on a clear day is needed the computational approach given by Cockroft (30) should be adopted. If  $I_{c\lambda}$  is the solar constant, that is the amount of energy per unit time falling on a unit area of plane normal to the sun's ray at the mean sun-earth distance, outside the earth's atmosphere, at the wavelength  $\lambda$  (see, for example, Reference (32)), then the amount of solar energy actually reaching the outside of the earth's atmosphere, due to the slightly elliptical orbit of the earth, is:

$$I_{o\lambda} = I_{c\lambda} * (1 + 0.0335 * \cos(2 * \pi * n/365))$$

where  $n$ , is the day number of the year, counted from January 1. The direct component of solar radiation reaching the earth's surface, at wavelength  $\lambda$  is given by the following relation:

$$I_{\lambda} = \tau_a * \tau_w * \tau_d * \tau_{wa} * \tau_{oz} * I_{o\lambda}$$

where the various transmission coefficients express the attenuating character of the atmosphere of the earth's surface particular site.

$$\tau_a = 10^{-0.00386 * (\lambda^{-4.05}) * Mr * P/1000}$$

to account for Mie scattering due to air molecules

$$\tau_w = 10^{-0.0075 * (\lambda^{-2}) * Mr * W/0.02}$$

to account for water scattering where  $W$ , the water content of the atmosphere expressed as metres of precipitable water

$$W = 0.0034 * P_o * c_o * (1 - \exp(-312.6/T_o))$$

where  $c_o$ , the atmospheric moisture content mixing ratio (Kg/Kg) at sea level

$T_o$ , sea level air temperature

$$\tau_d = 10^{-0.0353 * (\lambda^{-0.75}) * (\exp(-0.0005 * h)) * Mr * sc * (d/800)}$$

to account for dust particle scattering

where  $h$  is the site elevation (m).

$d$  is the dust particle concentration ( $\mu\text{g}/\text{m}^3$ ).

$$d = 96 + 62 * \cos\left(\frac{\text{mon} - 0.5}{6} * \pi\right) \quad (F1)$$

where  $\text{mon}$  is the month of the year, 1 to 12.

$sc$  is a scaling factor depending on site conditions

to correct the value of  $d$  and allow for atmospheric

concentrations not typical of a city environment, which

is actually represented by relation (F1).

$$\tau_{wa} = 10^{-a_w}$$

to account for water vapour absorption, carbon dioxide and oxygen

where  $a_w$  is the water vapour absorption coefficient given in Table F3 from empirical data as function of wavelength band

$\lambda_b$  and precipitable water depth,  $Mr.W$  (cm)

$$\tau_{oz} = 10^{-a \cdot X \cdot Mr}$$

to account for ozone absorption

where X, depth in cm NTP, given in Table F5, as function of mon (month of the year) and LAT, latitude of the site.

a, absorption coefficient, given in Table F4, as function of wavelength  $\lambda$ .

As far as the diffuse radiation from the sky is concerned, its spectral distribution according to (15) can be considered similar to the direct solar radiation for the particular air-mass Mr of site and time but with a slight shift towards the short-wave end of the spectrum. So, as a first approximation of the spectral distribution of diffuse sky radiation, that of direct solar radiation for the particular air-mass Mr of site and time can be used.

Hull (34) has presented another method of calculating the spectral composition of diffuse radiation under different weather types expressed by the clearness index KT, the ratio of total horizontal insolation at the earth's surface  $I_{h,tot}$  divided by the extraterrestrial horizontal insolation  $I_{h,ext}$

$$\text{But, } I_{h,ext} = \left( \int_0^\pi I_{o\lambda} \cdot d\lambda \right) \cdot \sin(a)$$

where  $a$  is the solar altitude angle

where  $a$  is the solar altitude angle. It is known that the solar altitude angle can be calculated from the following relation:

$$\sin(a) = \sin(LAT) \cdot \sin(\delta_s) + \cos(LAT) \cdot \cos(\delta_s) \cdot \cos(h_s) \quad (F2)$$

where,  $\delta_s$  is the declination of the sun, the angle between the sun's rays and the Zenith direction (directly overhead) at noon on the earth's equator.

$h_s$  is the solar hour angle,  $15^\circ$  times the number of hours from local solar noon. The declination of sun  $\delta_s$  as a function of  $n$  (day of the year) can be found in Reference (14)

Table F1 gives the colour temperature of sky  $T_w$ , from which the spectral distribution of the diffuse solar radiation from the sky is calculated as function of the clearness index KT, assuming that is a blackbody radiation of temperature  $T_w$  with a sharp total cut-off at  $0.3125$  (the radiation with wavelength shorter than  $0.3125 \mu m$  is neglected)

Table F1		
Equivalent blackbody temperature of sky $T_w$		
KT	$T_w(K)$	Weather type
$> 0.70$	13000	clear sky
$0.50 \div 0.70$	9000	haze
$0.25 \div 0.50$	7500	light overcast
$< 0.25$	6800	heavy overcast

If we adopt the methodology from Hull (34) Table F2 is constructed, that gives the fraction of solar radiation at 8 different wavelength bands over the total solar spectrum of the diffuse radiation from the sky for the four regions of clearness index.

Table F2

Sky diffuse radiation from Hull's method. Fraction of total diffuse radiation.

wavelength band, $\lambda_b$ $\mu\text{m}$		Clearness index, KT			
		>0.70	0.50+0.70	0.25+0.50	<0.25
0.3 + 0.35		0.159	0.102	0.068	0.055
	) ultraviolet				
0.35 + 0.4		0.167	0.122	0.098	0.083
	)				
0.4 + 0.6		0.377	0.362	0.333	0.314
	) visible				
0.6 + 0.75		0.120	0.149	0.162	0.165
	)				
0.75 + 0.9		0.065	0.088	0.104	0.111
	) near infrared				
0.9 + 1.2		0.058	0.089	0.113	0.127
	)				
1.2 + 2.1		0.045	0.070	0.094	0.112
	) infrared				
2.1 + 4.1		0.009	0.017	0.027	0.032
	)				

The comparison of values of Tables F2 and 1.2 (pp. 22) shows that Hull's method gives a quite large shift towards the short-wave end of the spectrum, especially for higher values of clearness index KT. This actually contradicts with measurements quoted in Reference (15). What is suggested is the adoption of Hull's method but with a more moderate shift towards the short-wave end of the spectrum. Anyway, more research is needed in this field, to establish the spectral distribution of diffuse solar radiation coming from the sky.

As far as the reflected radiation from the ground is concerned, the general knowledge, at present, is quite poor not only on the spectral composition of the reflected radiation but on the average value of the intensity and its directional character as well.

Table F3

Water vapour absorption coefficient $a_w$		precipitable water depth,							Mr.W,		(cm)	
Wavelength band, $\lambda_b$ $\mu m$		0.1	0.2	0.4	0.7	1.0	2.0	4.0	7.0	10.0	20.0	30.0
0.72 $\div$ 0.76	0.0005	0.001	0.002	0.002	0.005	0.008	0.017	0.033	0.056	0.072	0.12	0.14
0.76 $\div$ 0.80	0.002	0.003	0.0056	0.01	0.015	0.015	0.027	0.045	0.076	0.095	0.15	0.18
0.80 $\div$ 0.90	0.005	0.008	0.015	0.021	0.027	0.027	0.043	0.064	0.105	0.13	0.18	0.22
0.90 $\div$ 1.00	0.01	0.0135	0.022	0.031	0.040	0.040	0.060	0.092	0.125	0.16	0.22	0.26
1.00 $\div$ 1.25	0.017	0.023	0.033	0.047	0.058	0.058	0.087	0.129	0.177	0.21	0.272	0.315
1.25 $\div$ 1.5	0.097	0.143	0.203	0.260	0.302	0.302	0.388	0.483	0.567	0.62	0.720	0.780
1.5 $\div$ 2.0	0.066	0.092	0.120	0.144	0.160	0.160	0.191	0.223	0.249	0.266	0.295	0.315
2.0 $\div$ 3.0	0.190	0.256	0.328	0.402	0.435	0.435	0.566	0.683	0.786	0.863	1.00	1.09
3.0 $\div$ 5.0	0.21	0.285	0.365	0.465	0.52	0.52	0.67	0.81	0.98	1.1	1.25	1.35
5.0 $\div$ 7.0	0.23	0.300	0.39	0.49	0.56	0.56	0.70	0.88	1.05	1.18	1.38	1.50

Table F4

Ozone absorption coefficient, a

Wavelength band, $\lambda_b$ $\mu m$	a $cm^{-1}$	Wavelength band, $\lambda_b$ $\mu m$	a $cm^{-1}$	Wavelength band, $\lambda_b$ $\mu m$	a $cm^{-1}$
0.22 $\div$ 0.29	8.0	0.29 $\div$ 0.36	0.018	0.36 $\div$ 0.41	0.0
0.44 $\div$ 0.47	0.0002	0.47 $\div$ 0.50	0.001	0.50 $\div$ 0.53	0.002
0.56 $\div$ 0.59	0.005	0.59 $\div$ 0.63	0.0052	0.63 $\div$ 0.67	0.0023
0.72 $\div$ 0.76	0.0003	0.76 $\div$ 0.80	0.0	0.80 $\div$ 0.90	0.0
1.0 $\div$ 1.25	0.0	1.25 $\div$ 1.5	0.0	1.5 $\div$ 2.0	0.0
3.0 $\div$ 5.0	0.0	5.0 $\div$ 7.0	0.0	2.0 $\div$ 3.0	0.0

Table F5

Seasonal variation of atmospheric ozone in cm NTP

Latitude	Month											
	Jan.	Feb.	Mar.	Apr.	May	June	July	Aug.	Sept.	Oct.	Nov.	Dec.
90°N	0.33	0.39	0.46	0.42	0.39	0.34	0.32	0.30	0.27	0.26	0.28	0.30
80°N	0.34	0.40	0.46	0.43	0.40	0.36	0.33	0.30	0.28	0.27	0.29	0.31
70°N	0.34	0.40	0.45	0.42	0.40	0.36	0.34	0.31	0.29	0.28	0.29	0.31
60°N	0.33	0.39	0.42	0.40	0.39	0.36	0.34	0.32	0.30	0.28	0.31	0.31
50°N	0.32	0.36	0.38	0.38	0.37	0.35	0.33	0.31	0.30	0.28	0.29	0.30
40°N	0.30	0.32	0.33	0.34	0.34	0.33	0.31	0.30	0.28	0.27	0.28	0.29
30°N	0.27	0.28	0.29	0.30	0.30	0.30	0.29	0.28	0.27	0.26	0.26	0.27
20°N	0.24	0.26	0.27	0.28	0.27	0.26	0.26	0.26	0.26	0.25	0.25	0.25
10°N	0.23	0.24	0.24	0.25	0.26	0.25	0.25	0.24	0.24	0.23	0.23	0.23
0°	0.22	0.22	0.23	0.23	0.24	0.24	0.24	0.23	0.23	0.22	0.22	0.22
10°S	0.23	0.24	0.24	0.24	0.24	0.24	0.24	0.24	0.24	0.24	0.24	0.23
20°S	0.24	0.25	0.24	0.25	0.25	0.25	0.25	0.27	0.26	0.26	0.26	0.25
30°S	0.27	0.28	0.26	0.27	0.28	0.28	0.29	0.31	0.32	0.32	0.29	0.29
40°S	0.30	0.29	0.28	0.29	0.31	0.33	0.35	0.37	0.38	0.37	0.34	0.32
50°S	0.31	0.30	0.29	0.30	0.32	0.36	0.39	0.40	0.40	0.39	0.37	0.35
60°S	0.32	0.31	0.30	0.30	0.33	0.38	0.41	0.42	0.42	0.40	0.39	0.35
70°S	0.32	0.31	0.31	0.29	0.34	0.39	0.43	0.45	0.43	0.40	0.38	0.34
80°S	0.31	0.31	0.31	0.28	0.35	0.40	0.44	0.46	0.42	0.38	0.36	0.32
90°S	0.31	0.30	0.30	0.27	0.34	0.38	0.43	0.45	0.41	0.37	0.34	0.31

## Appendix G

Approximate calculation of the view factor of two polygons sited on two different planes.

The method is numerical and is an application of the relation (1G) that gives the view factor  $dF_{dA-dB}$  of the area element  $dA$  towards element area  $dB$ . The relation is based on the assumption that the intensity of radiation leaving the area  $dA$  is independent of direction.

$$dA * dF_{dA-dB} = \cos C_1 * \cos C_2 * dA * dB / (\pi * s^2) \quad (1G)$$

where the definition of the various quantities are given in Fig. G1.

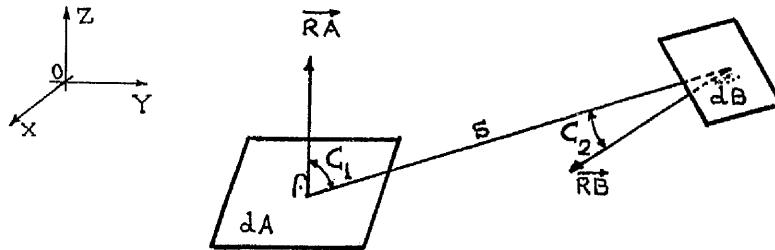


Fig. G1

The polygon A has  $n_A$  apexes and the polygon B,  $n_B$ , respectively. The co-ordinates of each apex are given:  $(a_{11}, a_{12}, a_{13}), (a_{21}, a_{22}, a_{23}), \dots, (a_{n_A 1}, a_{n_A 2}, a_{n_A 3}), (b_{11}, b_{12}, b_{13}), (b_{21}, b_{22}, b_{23}), \dots, (b_{n_B 1}, b_{n_B 2}, b_{n_B 3})$ , along the axes OX, OY, OZ, respectively.

The sequence of the apexes of each polygon should be such that the vector of the polygon plane be directed towards the same direction as the radiation leaving the polygon plane. The components of vectors of plane of polygon A and plane of polygon B along the axes OX, OY, OZ respectively are:

$$RA_x = (a_{22} - a_{12}) * (a_{33} - a_{13}) - (a_{32} - a_{12}) * (a_{23} - a_{13}) \quad (2G)$$

$$RA_y = (a_{23} - a_{13}) * (a_{31} - a_{11}) - (a_{33} - a_{13}) * (a_{21} - a_{11}) \quad (3G)$$

$$RA_z = (a_{21} - a_{11}) * (a_{32} - a_{12}) - (a_{31} - a_{11}) * (a_{22} - a_{12}) \quad (4G)$$

$$RB_x = (b_{22} - b_{12}) * (b_{33} - b_{13}) - (b_{32} - b_{12}) * (b_{23} - b_{13}) \quad (5G)$$

$$RB_y = (b_{23} - b_{13}) * (b_{31} - b_{11}) - (b_{33} - b_{13}) * (b_{21} - b_{11}) \quad (6G)$$

$$RB_z = (b_{21} - b_{11}) * (b_{32} - b_{12}) - (b_{31} - b_{11}) * (b_{22} - b_{12}) \quad (7G)$$

According to Fig.G1 if  $A_x, A_y, A_z$  are the co-ordinates of the centre of element area  $dA$  and  $B_x, B_y, B_z$ , the co-ordinates of the centre of element area  $dB$ , then, the co-ordinates of the straight line of the two centres are:

$$P_x = A_x - B_x \quad (8G)$$

$$P_y = A_y - B_y \quad (9G)$$

$$P_z = A_z - B_z \quad (10G) \text{ and}$$



$$\cos C_1 = (-R_{Ax} * P_x - R_{Ay} * P_y - R_{Az} * P_z) / ((P_x^2 + P_y^2 + P_z^2)^{0.5} * (R_{Ax}^2 + R_{Ay}^2 + R_{Az}^2)^{0.5}) \quad (11G)$$

$$\cos C_2 = (R_{Bx} * P_x + R_{By} * P_y + R_{Bz} * P_z) / ((P_x^2 + P_y^2 + P_z^2)^{0.5} * (R_{Bx}^2 + R_{By}^2 + R_{Bz}^2)^{0.5}) \quad (12G)$$

$$s^2 = P_x^2 + P_y^2 + P_z^2 \quad (13G)$$

$$\text{If } \cos C_1 \leq 0 \text{ or } \cos C_2 \leq 0 \quad (14G)$$

no radiation from one elemental area falls on the other. Each polygon (of  $n$  apexes) is separated into  $(n - 2)$  triangles according to Fig.G2

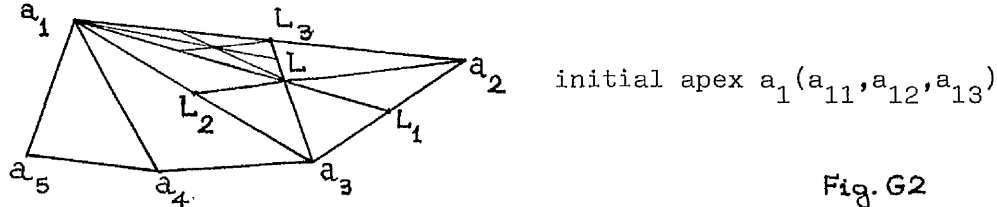


Fig.G2

Each triangle is subsequently separated into a further six triangles according to Fig.G2,

In turn each of these six triangles is similarly separated into a further six smaller triangles so that each initial triangle of the polygon is sub-divided into thirty-six smaller triangles.

The next step is the application of relations (1G) to (14G) between every pair of smaller triangles  $A_i$  and  $B_j$  with areas  $\Delta A_i$  and  $\Delta B_j$ , respectively. The straight line  $s$  of Fig.G1 joins now the centres  $L_{Ai}$  and  $L_{Bj}$  of the two smaller triangles. Thus, the view factor of the polygon  $A$  with area  $\Delta A$  towards the polygon  $B$ ,  $F_{A-B}$ , multiplied by the area  $\Delta A$ , is given approximately by the following relation:

$$\Delta A * F_{A-B} = \sum_{i=1}^{36*(n_A-2)} \sum_{j=1}^{36*(n_B-2)} \left( \frac{\cos C_{ij1} * \cos C_{ij2} * \Delta A_i * \Delta B_j}{\pi * s_{ij}^2} \right)$$

$$\text{where } \Delta A = \sum_{i=1}^{36*(n_A-2)} \Delta A_i$$

It can be shown numerically that more accurate results are obtained when the initial apexes  $a_1$  and  $b_1$  are chosen in such a way that they are not coincident for the case in which the polygons share a common side.

Two applications of the method follow:

The first application concerns the parallelepiped enclosure of the test box. The view factors are calculated between the six polygons of the enclosure dimensioned as shown in Fig. G3. In this figure

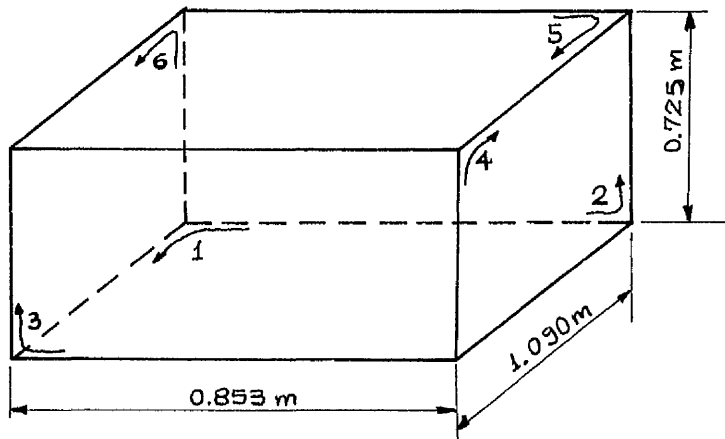


Fig. G3

each number and arrow determines the number of polygon, the initial apex of the polygon and the sequence of apexes. In Table G1 the view factors calculated with the present method are compared with accurate values. The accurate values are calculated from the relations given at the end of Table G1. These relations are from Reference (42). Values are also given in this table for the case in which the initial apex of polygon 6 co-incides with that of polygon 1. The comparison stresses the importance of not having the initial apexes of two polygons coincident. In Table G2 average values of the angle of incidence in each side of the parallelepiped are given for radiation coming from the other sides. This will be of value if the optical properties of the particular side are dependant on the angle of incidence of the incident radiation.

The second application is that of the enclosure of a typical horticultural glass-house. The view factors are calculated between the nine polygons dimensioned as shown in Fig. G4.

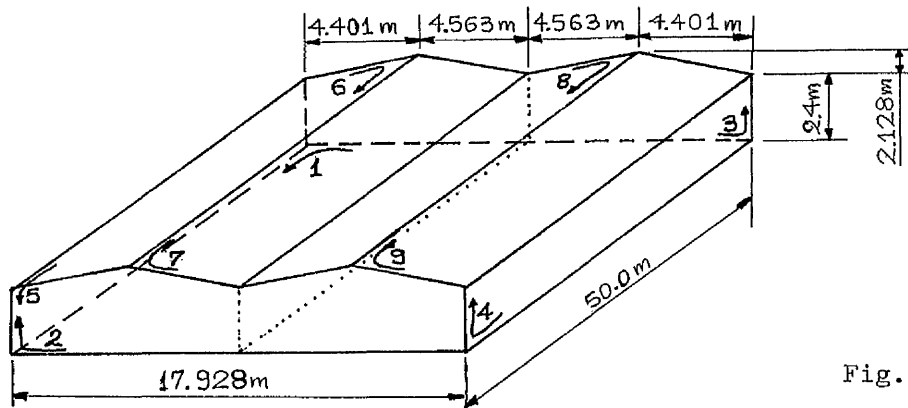


Fig. G4

Table G1

View factor  $F_{A-B}$  (the case of parallelepiped)Initial apex of polygon 1  $\neq$  initial apex of polygon 6  
approximate values

Polygon B	Polygon A					
	1	3	2	4	6	5
1	0.0	0.228	0.228	0.230	0.230	0.277
3	0.160	0.0	0.117	0.171	0.171	0.160
2	0.160	0.117	0.0	0.171	0.171	0.160
4	0.202	0.213	0.213	0.0	0.199	0.202
6	0.202	0.213	0.213	0.199	0.0	0.202
5	0.277	0.228	0.228	0.230	0.230	0.0

Accurate values  
Polygon A

	1	3	2	4	6	5
1	0.0	0.236	0.236	0.239	0.239	0.280
3	0.157	0.0	0.125	0.158	0.158	0.157
2	0.157	0.125	0.0	0.158	0.158	0.157
4	0.203	0.202	0.202	0.0	0.208	0.203
6	0.203	0.202	0.202	0.208	0.0	0.203
5	0.280	0.236	0.236	0.239	0.239	0.0

Initial apex of polygon 1 = initial apex of polygon 6

approximate values

Polygon A	1	3	2	4	6	5
1	0.0	0.232	0.232	0.230	0.264	0.264
3	0.152	0.0	0.119	0.171	0.195	0.152
2	0.152	0.119	0.0	0.171	0.145	0.152
4	0.192	0.217	0.217	0.0	0.182	0.192
6	0.240	0.201	0.201	0.199	0.0	0.240
5	0.263	0.232	0.232	0.230	0.264	0.0

For the calculation of the accurate values of  $F_{A-B}$ 

$$F_{A-B} = \frac{2}{\alpha \pi} * \left[ (\sqrt{h^2 + \alpha^2}) * \tan^{-1}[\sqrt{h^2 + \alpha^2}] - h * \tan^{-1}[b/h] \right] +$$

$$- \frac{2}{b \pi} * \left[ (\sqrt{h^2 + b^2}) * \tan^{-1}[\sqrt{h^2 + b^2}] - h * \tan^{-1}[\alpha/h] \right] -$$

$$\frac{h^2}{\alpha * b \pi} * \ln \left[ \frac{(h^2 + \alpha^2 + b^2) * h^2}{(\alpha^2 + h^2) * (b^2 + h^2)} \right]$$

$$F_{A-B} = \frac{\tan^{-1}[x^{-1}]}{\pi} + \frac{z * \tan^{-1}[z^{-1}]}{\pi * x} - \frac{(\sqrt{z^2 + x^2}) * \tan^{-1}[1/\sqrt{z^2 + x^2}]}{\pi * x} +$$

$$\frac{1}{4 * \pi * x} * \left[ \ln \left( \frac{(1 + z^2) * (1 + x^2)}{1 + z^2 + x^2} \right) + x^2 * \ln \left( \frac{x^2 * (1 + z^2 + x^2)}{(1 + x^2) * (z^2 + x^2)} \right) + \right.$$

$$\left. z^2 * \ln \left( \frac{z^2 * (1 + z^2 + x^2)}{(1 + z^2) * (z^2 + x^2)} \right) \right]$$

$$x = c/b$$

$$z = \alpha/b$$

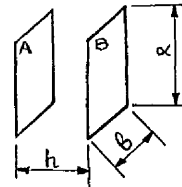
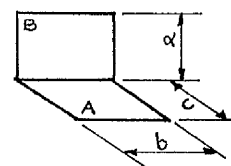
parallel  
parallelogramsvertical  
parallelograms

Table G2

Average angle of incidence on polygon plane B for incident radiation from A (initial apex of polygon 1  $\neq$  initial apex of polygon 6)

Polygon A	1	3	2	4	6	5
Polygon B						
1	-	59.4°	59.4°	58.1°	58.1°	32.8°
3	45.3°	-	19.9°	46.2°	46.2°	45.3°
2	45.3°	19.9°	-	46.2°	46.2°	45.3°
4	52.9°	55.1°	55.1°	-	27.6°	52.9°
6	52.9°	55.1°	55.1°	27.6	-	52.9°
5	32.8°	59.4°	59.4°	58.1	58.1°	-

In Fig. G4 each number and arrow determines the polygon number, the initial apex and the sequence of apexes. Table G3 gives the calculated values of view factors for each pair of internal surfaces,  $F_{A-B}$ . The subroutine ZEYS.SURNI has been developed for this purpose. The subroutine takes into account the "shading" effect imposed by the relative position of polygons 7 and 8. Each column of Table G3 has been calculated independently from the others. However, the non-deviation from the equality of the quantities  $\Delta A_i \cdot F_{A_i-B_j}$  and  $\Delta B_j \cdot F_{B_j-A_i}$  is a measure of the success of the described method.

Table G3

View factor  $F_{A-B}$  (the case of the glasshouse)

Polygon A →		1	2	3	4	5	6	7	8	9
Polygon B ↓	Area $\Delta A_i$ m <sup>2</sup>	896.4	81.2	81.2	120.0	120.0	244.4	251.7	251.7	244.4
1		0.0	0.403	0.403	0.380	0.380	0.653	0.772	0.772	0.653
2		0.022	0.0	0.008	0.020	0.020	0.021	0.022	0.022	0.021
3		0.022	0.008	0.0	0.020	0.020	0.021	0.022	0.022	0.021
4		0.068	0.066	0.066	0.0	0.036	0.011	0.0	0.099	0.219
5		0.068	0.066	0.066	0.036	0.0	0.219	0.099	0.0	0.011
6		0.199	0.117	0.117	0.019	0.373	0.0	0.084	0.0	0.0
7		0.212	0.111	0.111	0.000	0.152	0.076	0.0	0.0	0.0
8		0.212	0.111	0.111	0.152	0.000	0.0	0.0	0.0	0.076
9		0.199	0.117	0.117	0.373	0.019	0.0	0.0	0.084	0.0

## Appendix H

Calculation of the projection point on a plane.

The point  $S(S_x, S_y, S_z)$  is projected along the vector  $\vec{V}(V_x, V_y, V_z)$  on a plane  $P$ .

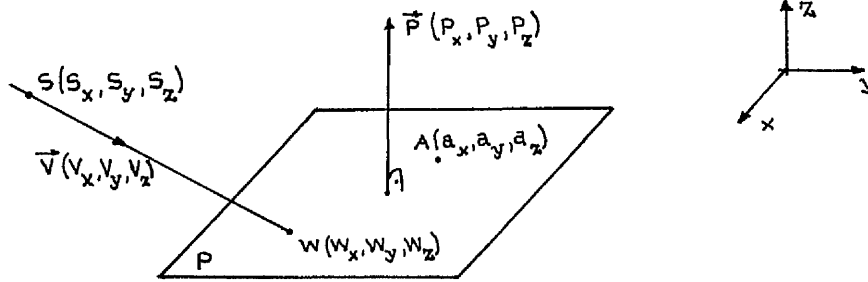


Fig. H1

The co-ordinates of the projection point  $W(W_x, W_y, W_z)$  being on a straight line that is parallel to the vector  $\vec{V}(V_x, V_y, V_z)$  and passes through the point  $S(S_x, S_y, S_z)$  obey the following relations:

$$\frac{W_x - S_x}{V_x} = \frac{W_y - S_y}{V_y} \quad (H1)$$

$$\frac{W_y - S_y}{V_y} = \frac{W_z - S_z}{V_z} \quad (H2)$$

Relations H1 and H2 can be written as relations H3 and H4 respectively:

$$W_x * V_y - W_y * V_x + (S_y * V_x - S_x * V_y) = 0 \quad (H3)$$

$$W_y * V_z - W_z * V_y + (S_z * V_y - S_y * V_z) = 0 \quad (H4)$$

If the plane is described by a vector  $\vec{P}(P_x, P_y, P_z)$  perpendicular to it and a point  $A(a_x, a_y, a_z)$ , then the co-ordinates of the projection point obey the following relation as well:

$$(W_x - a_x) * P_x + (W_y - a_y) * P_y + (W_z - a_z) * P_z = 0 \quad (H5)$$

This relation can be written into the following form,

$$W_x * P_x + W_y * P_y + W_z * P_z - (a_x * P_x + a_y * P_y + a_z * P_z) = 0 \quad (H6)$$

Solving the system of the three linear equations (H3), (H4) and (H6)

the co-ordinates of the point  $W(W_x, W_y, W_z)$  are calculated.

If the plane is described by three points  $A(a_x, a_y, a_z)$ ,  $B(b_x, b_y, b_z)$  and  $C(c_x, c_y, c_z)$  the components of vector  $\vec{P}(P_x, P_y, P_z)$  are first calculated from the co-ordinates of these three points:

$$P_x = (b_y - a_y) * (c_z - a_z) - (c_y - a_y) * (b_z - a_z) \quad (H7)$$

$$P_y = (b_z - a_z) * (c_x - a_x) - (b_x - a_x) * (c_z - a_z) \quad (H8)$$

$$P_z = (b_x - a_x) * (c_y - a_y) - (c_x - a_x) * (b_y - a_y) \quad (H9)$$

The subroutine PROJ has been developed according to the above analysis. The subroutine first examines the possibility the projection point W to be in infinity, which means that the vectors  $\vec{V}$  and  $\vec{P}$  are perpendicular to each other:

$$V_x * P_x + V_y * P_y + V_z * P_z = 0$$

The cases with zero magnitude of one or two of the coordinates  $V_x$ ,  $V_y$  and  $V_z$  of vector  $\vec{V}$  are handled appropriately.

## Appendix I

Calculation of the intersection polygon of two coplanar convex polygons

Two coplanar convex polygons A and B with apexes  $n_A$  and  $n_B$ , respectively are given in Fig. I1. The co-ordinates of each apex are,  $(a_{1x}, a_{1y}), (a_{2x}, a_{2y}), \dots, (a_{n_A x}, a_{n_A y})$  and  $(b_{1x}, b_{1y}), (b_{2x}, b_{2y}), \dots, (b_{n_B x}, b_{n_B y})$ .

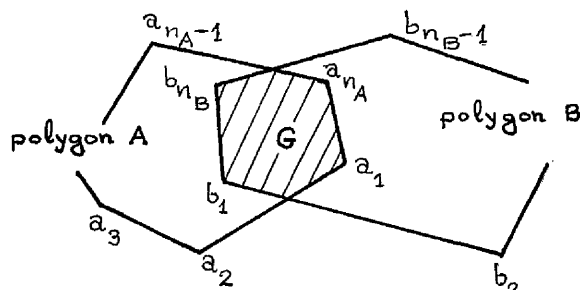


Fig. I1

The shaded area of Fig. I1 gives the intersection polygon G, with  $n_G$  apexes ( $n_G = 6$ , in the example of Fig. I1). The co-ordinates of these  $n_G$  apexes  $(c_{1x}, c_{1y}), (c_{2x}, c_{2y}), \dots, (c_{n_G x}, c_{n_G y})$  should be calculated from the co-ordinates of apexes of polygon A and B.

The relative position of point S ( $X_S, Y_S$ ) on the plane XOY in respect to the straight line  $y = d_1 * x + e_1$  can be expressed by one of the three relations:

$$Y_S - d_1 * X_S - e_1 > 0 \quad (1I)$$

when the point S belongs to the positive semi-plane in respect to the line

$$y = d_1 * x + e_1$$

$$Y_S - d_1 * X_S - e_1 = 0 \quad (2I)$$

when the point is on the line  $y = d_1 * x + e_1$

$$Y_S - d_1 * X_S - e_1 < 0 \quad (3I)$$

when the point S belongs to the negative semi-plane in respect to the line

$$y = d_1 * x + e_1$$

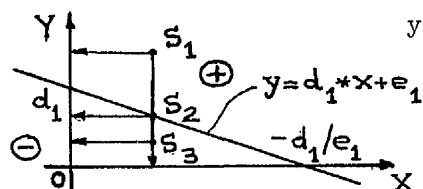


Fig. I2

Point  $S_1 (X_{s_1}, Y_{s_1})$ ,  $Y_{s_1} > d_1 * X_{s_1} + e_1$

Point  $S_2 (X_{s_2}, Y_{s_2})$ ,  $Y_{s_2} = d_1 * X_{s_2} + e_1$

Point  $S_3 (X_{s_3}, Y_{s_3})$ ,  $Y_{s_3} < d_1 * X_{s_3} + e_1$

So, each internal point of a polygon or a point on its sides  $(X, Y)$  is subject to a set of  $n$  inequalities of the following form:

$$l_{1i} * X + l_{2i} * Y + l_{3i} \leq 0 \quad (4I), i = 1, \dots, n$$

where,  $n$  the number of apexes of the polygon. The parameters  $l_{1i}$ ,  $l_{2i}$ ,  $l_{3i}$ ,  $i = 1, \dots, n$  correspond to the straight line  $Y = d_i * X + e_i$ , that passes through the  $i^{\text{th}}$  and  $(i+1)^{\text{th}}$  apexes of the polygon. So, finally, each internal point of the intersection polygon  $G$  and every point on its sides  $(X_G, Y_G)$  is subject to a set of  $(n_A + n_B)$  inequalities of the form:

$$l_{1i} * X_G + l_{2i} * Y_G + l_{3i} \leq 0 \quad i = 1, \dots, (n_A + n_B) \quad (5I)$$

that derive from the two sets of the inequalities (4I) that correspond to the two polygons A and B. The apexes of the two polygons and the intersection points of all the pairs of sides of the two polygons that have such co-ordinates  $(X_G, Y_G)$  which are subject to the set of the inequalities (5I) are actually apexes of the intersection polygon G. The sub-routines CAL and EUR3 have been developed for the calculation of the co-ordinates of the  $n_G$  apexes  $(c_{ix}, c_{iy})$  of the intersection polygon G from the co-ordinates of apexes of polygon A and B. The coincidence of two or more apexes of polygons A and B and intersection points of the pairs of sides of the two polygons is handled appropriately.



## Appendix J

Calculation of mass-flux  $(Gx)_{x+}$  and water vapour  
mass concentration  $m_{w,p}$ .

We consider that there is mass-flux  $(Gx)_{x+}$  across n different parts of the interface of the control volume P. The mass flux of each part  $(Gx)_{x+,j}$ ,  $j = 1$  to  $n$  and the vapour mass concentration  $m_{w,p}$  at the node of the control volume (section 2.4) are calculated from the simultaneous equations (J1) to (J5). It has been assumed that the control volume is filled with moist-air and the mass-flux is due only to convection and not to mass concentration gradients. These could arise, for example, from condensation or evaporation from the internal surfaces of the control volume.

$$m_{w,p} + m_{a,p} = 1 \quad (J1)$$

$$(Gx)_{x+,j} = f_j(P_p) \quad , \quad j = 1 \text{ to } n \quad (J2)$$

$$P_p = (-c_{v,p} * (\gamma_p - 1) * T_p * \Delta t / \Delta V) * \left( \sum_{j=1}^n (Gx)_{x+,j} * A_{xj} \right) + \rho_p^o * c_{v,p} * (\gamma_p - 1) * T_p \quad (J3)$$

$$\rho_p = P_p / (c_{v,p} * (\gamma_p - 1) * T_p) \quad (J4)$$

$$(\rho_p * m_{w,p} - \rho_p^o * m_{w,p}^o) * \Delta V / \Delta t + \sum_{j=1}^n (Gx)_{x+,j} * A_{xj} * m_{wx+,j} = (\dot{m}'_w + \dot{m}^o_w) * \Delta V / 2 \quad (J5)$$

where,  $T_p$  is the temperature at the node P.

$\rho_p$  is the density of the moist air at the node P.

$P_p$  is the pressure at the node P.

$c_{v,p}$  is the constant volume specific heat of the moist air at the node P.

$\gamma_p = c_{p,p} / c_{v,p}$  is the specific heat ratio of moist air.

$m_{wx+,j}$  is the mass concentration of the water vapour at the part of the control volume interface  $x+$ . (Kg of water / Kg of moist air).

$\dot{m}'_w$  is the mass creation rate of the water vapour. This creation could be due a humidifier or dehumidifier.

$m_{a,p}$  is the mass concentration of the dry air in the mixture of the moist air at the node P. (Kg of dry air / Kg of moist air).

$\Delta V$  is the volume of the control volume

$A_{xj}$  is the area of the part of the control volume interface.

$\Delta t$  is the time interval.

The superscript o denotes values at time t. Its absence implies values at time  $t + \Delta t$ . Finally, the symbol f means function.

Equation (J1) is derived from the definition of quantities  $m_{w,p}$  and  $m_{a,p}$ .

Equations (J2) give the mass-fluxes  $(Gx)_{x+,j}$  as functions of the pressure  $P_p$ . These may be functions of other variables, e.g. temperature, as well. These equations are usually semi-empirical relations produced from fitting experimental data. Extensive coverage for both infiltration and ventilation cases are given in the ASHRAE Handbook of Fundamentals, chapter 21 (18) and in Cockroft's thesis (30). The thermocirculation in a Trombe-wall system is given by Duffie et.al. (15).

Equation (J3) is derived from equation (J4) and the finite-difference representation of the continuity equation (J6):

$$(\rho_p - \rho_p^o) * \Delta V / \Delta t + \sum_{j=1}^n (Gx)_{x+,j} * A_{xj} = 0 \quad (J6)$$

Equation (J4) is an expression of the equation of state of the moist air. It is assumed that the moist air behaves as a perfect gas.

Equation (J5) is the finite difference representation of the mass-diffusion equation for the water vapour mass concentration.

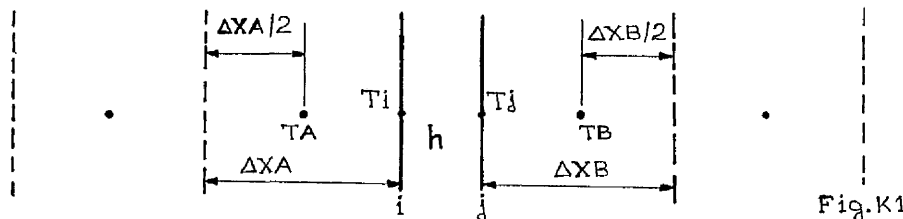
The solution of the system of equations (J1), (J2), (J3), (J4), and (J5) which provides the values of pressure  $P_p$ , water vapour and dry air mass concentration  $m_{w,p}$ ,  $m_{a,p}$ , mixture density  $\rho_p$  and mass fluxes  $(Gx)_{x+,j}$  at the time  $t+\Delta t$ , proceeds by the cyclic repetition of the following steps:

- 1) Provide initial estimates of the values of temperature  $T_p$ .
- 2) Provide initial estimates of the values of pressure  $P_p$ , the water vapour mass concentration  $m_{w,p}$  and mixture density  $\rho_p$ .
- 3) Calculate from equation (J1) the mass concentration of dry air.
- 4) Calculate from appropriate auxiliary equations, the properties  $c_{v,p}$ ,  $\gamma_p$  and  $c_{p,p}$ .
- 5) From equations (J2) calculate the values of  $(Gx)_{x+,j}$ .
- 6) From equation (J3) calculate the values of pressure  $P_p$ .
- 7) From equation (J4) calculate the density  $\rho_p$ .
- 8) From equation (J5) calculate the mass concentration  $m_{w,p}$ . The values of mass concentration of water vapour at the control volume interface  $m_{wx+,j}$  (equation (J5)) are calculated according to hybrid scheme.
- 9) Regard the new values of pressure  $P_p$ , and mass concentration of water vapour  $m_{w,p}$  as improved estimates and return to step 3. Repeat until convergence.

## Appendix K

Example of a closed air-gap discontinuity

The line-by-line solution of the algebraic equations derived from the discretization of the energy differential equations can be easily applied in a domain where a closed air-gap discontinuity exists, employing a similar analysis to that of section 3.1.4. So, the valuable information concerning the heat transfer between two parallel surfaces can be easily incorporated into the whole computational procedure. Only, the heat capacity effect of the air of the gap is neglected. The total heat transfer coefficient,  $h$ , between the surfaces  $i$  and  $j$  consists of two parts; a radiative,  $h_r$ , and a convective-conductive part,  $h_c$ :  $h = h_r + h_c$



The calculation of the radiative heat transfer coefficient,  $h_r$ , is given by Duffie et. al. (15). For example, assuming diffuse surfaces of equal area:

$$h_r = \epsilon * (T_i + T_j) * (T_i^2 + T_j^2) / ((1 - \epsilon_i) / \epsilon_i + (1 - \epsilon_j) / \epsilon_j + 1 / F_{ij})$$

where  $\epsilon = 5.6697 \times 10^{-8} \text{ W/m}^2 \text{ K}^4$

$\epsilon_i, \epsilon_j$  is the emissivity of surface  $i$  and surface  $j$  respectively

$F_{ij}$  is the view factor of surface  $i$  towards surface  $j$ .

The calculation of the convective-conductive heat transfer coefficient,  $h_c$ , for free convection between two parallel surfaces is given at the end of this appendix. It is based on References (47) and (48).

The analysis gives the following relations for the heat fluxes  $\overline{QA}$  and  $\overline{QB}$  at the interfaces  $i$  and  $j$  respectively:

$$\overline{QA} = (h_{Ai} * h_{Bj} * \Delta x * (T_A - T_B)) / (h_{Ai} + h_{Bj} * (1 + h_{Ai} / h))$$

$$\overline{QB} = (h_{Ai} * h_{Bj} * \Delta x * (T_B - T_A)) / (h_{Ai} * (1 + h_{Bj} / h) + h_{Bj})$$

where  $h_{Ai} = 2 * \lambda_{Ai} / \Delta x_A$  and  $h_{Bj} = 2 * \lambda_{Bj} / \Delta x_B$

and  $\lambda_{Ai}$  is the thermal conductivity of material of control volume A at the temperature of surface  $i$ .

$\lambda_{Bj}$  is the thermal conductivity of material of control volume B at the temperature of surface  $j$ .

The temperatures of the surfaces  $i$  and  $j$  are given by the following expressions:

$$T_i = (h_{Ai} * T_A + h_{Bj} * T_B + h_{Ai} * T_A * (h_{Bj} / h)) / (h_{Bj} + h_{Ai} + (h_{Ai} * h_{Bj} / h))$$

$$T_j = (h_{Bj} * T_B + h_{Ai} * T_A + h_{Bj} * T_B * (h_{Ai} / h)) / (h_{Bj} + h_{Ai} + (h_{Ai} * h_{Bj} / h))$$

Calculation of heat transfer coefficient  $h_c$  between two parallel surfaces of a closed air-gap.

The heat transfer coefficient  $h_c$  is given by the following expression:

$$h_c = Nu * \lambda / L \quad (K1)$$

where  $\lambda$  is the conductivity of the gas filling the gap, calculated at the arithmetic mean of the temperatures of the two surfaces,

$$(T_i + T_j)/2 \quad (K2)$$

The Nusselt number  $Nu$  is function of the Rayleigh number,  $Ra_L$ , given by the following definition:

$$Ra_L = (2 * g * (T_i - T_j) * L^3 * Pr) / (\nu^2 * (T_i + T_j))$$

where both Prandtl number  $Pr$  and kinematic viscosity  $\nu$  are calculated at the arithmetic mean of the temperatures of the two surfaces,

$$(T_i + T_j)/2 .$$

a) If the inclination angle  $\beta^\circ$  is between  $0^\circ$  and  $75^\circ$  the Nusselt number is given by the following relation,

$$Nu = 1 + 1.44 * \left(1 - \frac{1708}{Ra_L * \cos \beta^\circ}\right)^* \left(1 - \frac{1708 * (\sin(1.8 * \beta^\circ))^{1.6}}{Ra_L * \cos \beta^\circ}\right) + \left(\left(\frac{Ra_L * \cos \beta^\circ}{5830}\right)^{0.333} - 1\right)^*$$

$$\text{where, } (x)^* = (|x| + x)/2 \quad (K4)$$

b) If  $\beta^\circ$  is between  $75^\circ$  and  $90^\circ$ , then,

$$Nu = \text{MAX} \left( 1, 0.288 * ((L * Ra_L * \sin \beta^\circ) / H)^{0.25}, 0.039 * (Ra_L * \sin \beta^\circ)^{0.33} \right) \quad (K5)$$

where MAX indicates that, at any given value of  $Ra_L$ , the largest of the three quantities separated by commas should be used.

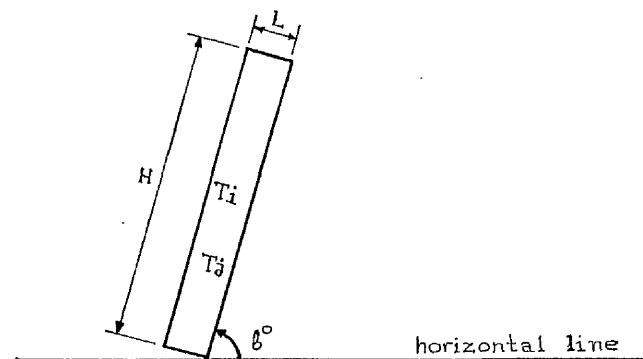


Fig. K2

## Appendix L

Application of the method of distribution of solar radiation among the surfaces of a typical glasshouse enclosure.

This is a characteristic example of application of the method to a quite complicated solar system, a glasshouse of the shape and dimensions of Fig.L1. The glasshouse is orientated East-West. Both surfaces 4 and 5 are the internal surfaces of transwall modules with one glass plate in front of them, exactly as that described in section 1.4. Each other internal surface of the enclosure of Fig.L1 apart from surface 1 (floor) is the internal surface of a 4mm clear float glass.

The assumptions about solar radiation composition, spectrum, type of sky diffuse radiation, type of reflected radiation from the ground, ground reflectivity and so on, are as before for the test box parallelepiped enclosure and Tables 2.3, 2.5 and 2.6 have been used. Surface 1 (floor) has been assigned a reflectance of 0.050 for every angle of incidence apart from  $80^\circ$  and  $90^\circ$ . The assigned reflectance for these two angles of incidence are 0.100 and 1.000 respectively. The specularly reflected portion of radiation has been taken as 1.0 for every surface apart from surface 1, taken as zero.

Because of the non-convex character of the glasshouse enclosure, the glasshouse is separated into three parts, each making its convex sub-enclosure, to each of which the method is applied successively.

The first part consists of the two inclined rectangular glass plates, the internal surfaces of which are the surfaces 7 and 8 of the total glasshouse enclosure. This first sub-enclosure is the one shown in Fig. 2.3 of section 2.2. The second and third part of the glasshouse is the half south and half north glasshouse respectively. Their sub-enclosures are actually symmetrical in respect to the imaginary vertical plane passing through the middle of the glasshouse and parallel to surfaces 4 and 5 (dotted plane in Fig.L1).

The method is first applied to the first sub-enclosure and some of the results are given in Table L1. Direct radiation is only transmitted through the north glass plate by three polygons a, b and c. These exit polygons a, b and c for the first sub-enclosure are the entrance polygons of the third sub-enclosure. The method is then applied successively to the second and third part of the glasshouse. These two last applications are repeated to take into account reflected radiation from the other small part of the glasshouse, initially neglected.

With the assumption that radiation that escapes from the second and third part of the glasshouse through the surfaces 7 and 8 of Fig. L1, respectively, escapes from the whole glasshouse once and for all, Table L2 gives the final distribution of the total solar radiation falling on the whole glasshouse, for 9 a.m. solar time on the 1st of January. A 99.6% of the area of each surface shown in Fig. L1 has been considered as net glass area for the calculation of values of Tables L1 and L2, to take into account the frame of each side although the frame and the rest structure has really much greater effect than this.

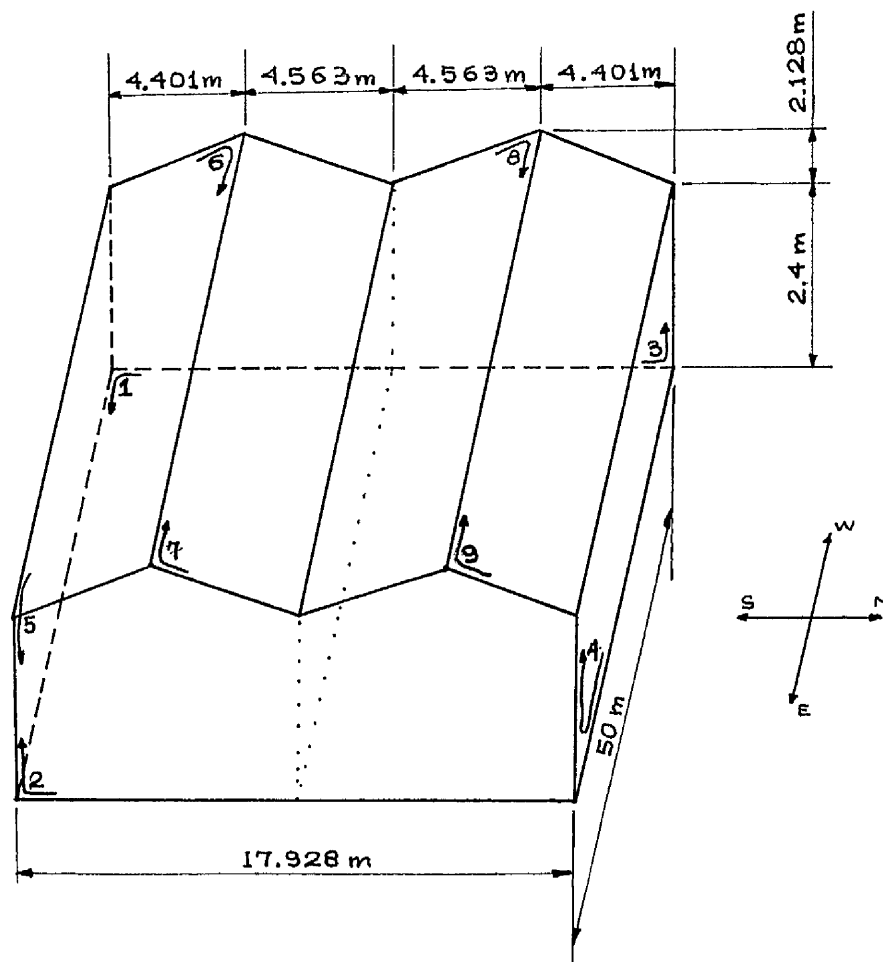


Fig. L1.

Table L1

Example of two inclined glass plates of a glasshouse.  
1st January - Assumption of Air-mass 2 spectrum

Solar time	Direct radiation % total	Diffuse radiation % total	Predicted Air-mass of direct radiation	Reflected radiation back % total	Absorbed radiation by north glass % total		Absorbed radiation by south glass % total		Transmitted radiation through north glass-diffuse % total	Transmitted radiation through south glass-diffuse % total	Transmitted radiation through north glass-direct % total	Transmitted radiation through south glass-direct % total	Absolute value and components of transmitted direct solar radiation				Direct radiation transmitted (watts) through polygons		
					V(W/m <sup>2</sup> )		V(W/m <sup>2</sup> )						V(W/m <sup>2</sup> )		a	b	c		
					V <sub>x</sub>	V <sub>y</sub>	V <sub>x</sub>	V <sub>y</sub>					V <sub>x</sub>	V <sub>y</sub>				V <sub>z</sub>	
9	36.1	63.9	19.6	40.1	9.4	4.4	12.5	12.5	21.1	0.0	82.9	-0.758	-0.651	-0.039	646	724	523		
10	52.5	47.5	3.0	32.1	10.7	3.2	9.2	9.2	35.6	0.0	186.7	-0.880	-0.460	-0.121	4788	5115	832		
11	59.9	40.1	5.7	27.2	11.3	2.7	7.7	7.7	43.3	0.0	264.4	-0.956	-0.238	-0.172	10051	10369	610		
12	65.7	34.3	5.2	23.9	11.8	2.3	6.6	6.5	48.9	0.0	371.8	-0.982	-0.0	-0.190	16080	16080	0		
13	62.4	37.6	5.7	26.4	11.4	2.5	7.3	7.2	45.1	0.0	305.5	-0.956	-0.238	-0.172	11994	11501	705		
14	54.7	45.3	8.0	31.4	10.9	3.1	8.8	8.8	37.1	0.0	218.9	-0.880	-0.460	-0.121	6028	5584	976		
15	46.8	53.2	19.8	38.1	10.2	3.6	10.4	10.4	27.3	0.0	107.9	-0.758	-0.651	-0.039	959	824	884		

Table L2

Example of a glasshouse with transwalls at the south and north facing sides - Distribution of solar radiation - Assumption of Air-Mass 2 spectrum. 1st January, 9 am solar time.

	Absorbed in KW	Radiation % of total		Absorbed in KW	Radiation % of total
Reflected radiation	23.6	42.2	South transwall total absorbed radiation (5)	7.8	14.0
Glasshouse floor (1)	14.0	25.0	South transwall outside glass	2.0	3.6
Glasshouse floor, south half (1S)	3.7	6.7	South transwall front glass	1.9	3.4
Glasshouse floor, north half (1N)	10.2	18.3	South transwall <u>1st</u> liquid layer	1.9	3.4
East side (2)	1.0	1.7	South transwall <u>2nd</u> liquid layer	0.9	1.6
East side south half (2S)	0.4	0.8	South transwall <u>3rd</u> liquid layer	0.2	0.4
East side north half (2N)	0.5	0.9	South transwall inside glass	0.9	1.6
West side (3)	0.7	1.3	North transwall total absorbed radiation (4)	2.9	5.1
West side south half (3S)	0.5	0.9	North transwall outside glass	0.3	0.6
West side north half (3N)	0.2	0.4	North transwall front glass	0.4	0.8
Ceiling south part (6)	2.3	4.1	North transwall <u>1st</u> liquid layer	0.2	0.4
Ceiling south middle part (7)	1.3	2.4	North transwall <u>2nd</u> liquid layer	0.4	0.7
Ceiling north middle part (8)	1.3	2.3	North transwall <u>3rd</u> liquid layer	0.7	1.2
Ceiling North part (9)	1.1	1.9	North transwall inside glass	0.8	1.5

Note: 1st liquid layer = 1.2cm  
 2nd liquid layer = 12.6 cm  
 3rd liquid layer = 1.2cm



Table L3

Fractional average solar radiation (Total radiation = 1.0)

wavelength band	Air-Mass , Mr				
$\mu\text{m}$	1	2	4	7	10
0.3 ÷ 0.315	0.000	0.000	0.000	0.000	0.000
0.315 ÷ 0.4	0.048	0.028	0.011	0.003	0.001
0.4 ÷ 0.51	0.161	0.130	0.107	0.066	0.040
0.51 ÷ 0.61	0.152	0.148	0.142	0.117	0.091
0.61 ÷ 0.7	0.125	0.138	0.142	0.143	0.137
0.7 ÷ 0.8	0.118	0.119	0.150	0.171	0.184
0.8 ÷ 2.1	0.360	0.397	0.403	0.447	0.484
2.1 ÷ 4.1	0.036	0.040	0.045	0.053	0.063

Table L4

Average optical properties of water and clear float glass

wavelength band	refractive index of water	extinction coeff. of water	refractive index of clear float glass	extinction coeff. of clear float glass <sub>-1</sub>
$\mu\text{m}$		$\text{m}^{-1}$		$\text{m}^{-1}$
0.3 ÷ 0.315	1.348	0.5546E-01	1.500	1126.7
0.315 ÷ 0.4	1.343	0.2669E-01	1.513	131.2
0.4 ÷ 0.51	1.337	0.6549E-02	1.515	9.6
0.51 ÷ 0.61	1.333	0.4688E-01	1.513	8.4
0.61 ÷ 0.7	1.331	0.1627E+00	1.510	18.7
0.7 ÷ 0.8	1.330	0.1130E+01	1.510	33.6
0.8 ÷ 2.1	1.318	0.4942E+04	1.513	39.6
2.1 ÷ 4.1	1.332	0.2005E+07	1.510	244.8

## Appendix M

A numerical example of the importance of the relative magnitude of all the coefficients APC, APi, BPC of the set of the discretization equations,  $APC*\phi_p = \sum_i (APi*\phi_i) + BPC$  on the convergence of the line-by-line iterative solution.

The example is referred to two dimensions. Equation (3.31)

of page 154 has the following form:

$$APC(I,J)*\phi(I,J) = AP1(I,J)*\phi(I+1,J) + AP2(I,J)*\phi(I-1,J) + \\ AP3(I,J)*\phi(I,J+1) + AP4(I,J)*\phi(I,J-1) + \\ BPC(I,J)$$

where  $I=1$  to  $NI$  and  $J=1$  to  $NJ$

These are NIS equations ( $NIS = NI*NJ$ ) with NIS unknowns. They can represent the NIS equations of NIS nodes of a rectangular grid written for a particular dependent variable  $\phi$ . The rectangular grid has  $NI$  columns and  $NJ$  rows. If a direct method has to be employed to solve this system of NIS equation with NIS unknowns, the solution  $\phi$  ( $K=1$  to  $NIS$ ) is given by the following matrix form  $[\phi] = [A]^{-1} [B]$  where the dimensions of the matrices are  $(NIS,1)$  for  $[\phi]$ ,  $(NIS, NIS)$  for  $[A]$  and  $(NIS,1)$  for  $[B]$ . The node  $K$  of the direct solution correspond to node  $(J-1) * NI + J$  of the iterative method. The following Figure M1 shows a rectangular grid with  $NI=3$  columns,  $NJ=3$  rows and  $NIS=9$  nodes. The present example concerns this grid:

	I = 1	I = 2	I = 3
J = 1	K $\overset{\circ}{=}$ 1	K $\overset{\circ}{=}$ 2	K $\overset{\circ}{=}$ 3
J = 2	K $\overset{\circ}{=}$ 4	K $\overset{\circ}{=}$ 5	K $\overset{\circ}{=}$ 6
J = 3	K $\overset{\circ}{=}$ 7	K $\overset{\circ}{=}$ 8	K $\overset{\circ}{=}$ 9

Fig. M1

Table M1 gives the values of the coefficients AP1, AP2, AP3, AP4 used in every case.

Table M1

Values of coefficients AP1, AP2, AP3, AP4.

J=	1			2			3		
I=	1	2	3	1	2	3	1	2	3
AP1(I,J)	-1.0	-0.7	0.0	-0.6	-0.4	0.0	-1.6	-1.0	0.0
AP2(I,J)	0.0	-0.8	-0.9	0.0	-1.4	-1.2	0.0	-1.4	-1.2
AP3(I,J)	-0.9	-1.1	-1.3	-1.4	-0.4	-0.7	0.0	0.0	0.0
AP4(I,J)	0.0	0.0	0.0	-1.0	-1.3	-0.8	-1.1	-1.4	-0.9

Table M2 gives three different sets of values of coefficients APC. The three sets differ from each other only for values of nodes (I=1, J=1) and (I=1, J=3).

Table M2

Values of coefficients APC

J	1			2			3		
I	1	2	3	1	2	3	1	2	3
set 1	2.0	5.0	4.0	4.0	2.0	6.0	1.0	3.0	3.0
set 2	5.0	5.0	4.0	4.0	2.0	6.0	3.0	3.0	3.0
set 3	10.0	5.0	4.0	4.0	2.0	6.0	10.0	3.0	3.0

Table M3 gives two different sets of values of coefficients BPC. These two sets differ from each other by a constant value.

Table M3

Values of coefficients BPC

J	1			2			3		
I	1	2	3	1	2	3	1	2	3
set 1	-0.2	-0.3	-0.4	-0.4	-0.4	-0.5	-0.2	-0.8	-0.4
set 2	-55.2	-55.3	-55.4	-55.4	-55.4	-55.5	-55.2	-55.8	-55.4

Table M4 gives the solution of the set of NIS=9 equations using a direct method (Gauss elimination method) and the line-by-line iterative method, for six different pairs of sets of values of APC and BPC coefficients. The first estimate of the solution of the iterative method was always zero for every node.

Table M4

Direct method and line-by-line iterative method results for the 9 nodes of Fig.M1 (K=1 to 9)									
APC → BPC →	K=1 2 3 4 5 6 7 8 9	set 1		set 2		set 3		set 4	
		set 1	set 2	set 1	set 2	set 1	set 2	set 1	set 2
Direct Method	1	-0.128446038E+00	-0.106243846E+02	+0.161797311E-01	-0.131350780E+02	-0.628024637E-02	-0.424094997E+01		
	2	+0.262923090E-01	-0.988769868E+01	-0.844593912E-01	+0.260096432E+01	-0.422596439E-01	-0.489295423E+01		
	3	-0.102972630E+00	-0.843438588E+01	-0.439490116E-01	-0.160725945E+02	-0.687635998E-01	-0.120153028E+02		
	4	+0.339997409E-01	-0.267372579E+02	-0.218265849E+00	+0.874936187E+01	-0.105486547E+00	-0.877505111E+01		
	5	-0.233294430E+00	+0.776551926E+01	+0.127379527E+00	-0.423144937E+02	-0.323118761E-01	-0.173015972E+02		
	6	-0.905581356E-02	-0.981809822E+01	-0.113992693E+00	+0.503808463E+01	-0.668553240E-01	-0.225779242E+01		
	7	-0.191125905E+00	+0.410815033E+02	+0.271754250E+00	-0.370526238E+02	+0.340096862E-01	-0.405563375E+01		
	8	-0.289211310E-01	-0.417940748E+02	-0.484481446E+00	+0.289584833E+02	-0.265038538E+00	-0.311944144E+01		
	9	-0.119048137E+00	+0.119639270E+01	+0.946570534E-01	-0.315614854E+02	-0.726132106E-02	-0.165415523E+02		
10th iteration of the line-by-line method	1	divergence	divergence	+0.147054214E-01	-0.129577510E+02	-0.628024880E-02	-0.424094980E+01		
	2			-0.824815079E-01	+0.236306853E+01	-0.422596390E-01	-0.489295458E+01		
	3			-0.450222339E-01	-0.159435095E+02	-0.687636022E-01	-0.120153026E+02		
	4			-0.213789319E+00	+0.821093395E+01	-0.105486539E+00	-0.877505168E+01		
	5			+0.120680147E+00	-0.415087060E+02	-0.323118899E-01	-0.173015962E+02		
	6			-0.112059775E+00	+0.480559714E+01	-0.668553202E-01	-0.225779269E+01		
	7			+0.264561091E+00	-0.361874453E+02	+0.340096814E-01	-0.405563340E+01		
	8			-0.476289430E+00	+0.279731643E+02	-0.265038524E+00	-0.311944238E+01		
	9			+0.908003713E-01	-0.310976115E+02	-0.726132749E-02	-0.165415519E+02		

## Appendix N

Comparison of 1-dimensional ray-tracing techniques with infinite and finite number of internal reflections.

Table N1 gives a comparison of different 1-dimensional techniques for  $0^\circ$  angle of incidence for the transwall system element (section 1.3). The one reflection technique is for reflection at the inside interface of the outside glass plate. An amount of energy (8.91% for the no internal reflections case and 5.43% for the one internal reflection case, of the total incident radiation) is not taken into account at all, if the infinite number of internal reflections technique is not employed (round off errors cause the 0.1% deviation from the true value in its case).

Table N1

Optical properties of transwall element, calculated with different 1-dimensional techniques. (Incident radiation = 100.0), Air-mass 1.

$0^\circ$  angle of incidence.

	infinite number of internal reflections	no internal reflections	one internal reflection
total reflectance	11.3	4.166	7.12
total transmittance	38.8	38.41	38.41
absorptance of outside glass plate	13.5	12.68	13.20
absorptance of front glass plate	12.0	11.79	11.79
absorptance of liquid	19.8	19.74	19.74
absorptance of back glass plate	4.5	4.31	4.31
	99.9	91.09	94.57

## Appendix 0

## The computer listing of the tridiagonal algorithm.

```

C THE SYSTEM OF EQUATIONS B(I)*W(I)=A(I)*W(I+1)+C(I)*W(I-1)+D(I)
C IS SOLVED, I=1 TO MD (MD=NUMBER OF EQUATIONS=NUMBER OF UNKNOWN)
C FOR, I=1, B(1)*W(1)=A(1)*W(2)+D(1) (NO NEED TO DEFINE C(1))
C I=MD, B(MD)*W(MD)=C(MD)*W(MD-1)+D(MD) (NO NEED TO DEFINE A(MD))
C THE SOLUTION IS: W(I), I=1 TO MD
C MD=6+3
C NMX=6+MD
C FOR LEAST ROUND OFF ERROR IS SUGGESTED: A(I).GT.0.0
C C(I).GT.0.0
C B(I).GT.0.0
C (B(I)-A(I)-C(I)).GT.0.0
C (I=2 TO MD-1)
C L(MD),F(MD), AUXILIARY ARRAYS
C SUBROUTINE TPIG(A,B,C,D,MD,E,F,W,NMX)
C DIMENSION A(NMX),B(NMX),C(NMX),D(NMX),E(NMX),F(NMX),W(NMX)
C E(1)=A(1)/B(1)
C F(1)=D(1)/B(1)
C MM=MD-1
C DO 16 N=2,MM
C DENA=B(N)-C(N)*E.(N-1)
C A(N)=A(N)/DENA
C F(N)=(D(N)+C(N)*F(N-1))/DENA
C THE FOLLOWING EXPRESSION SIMPLY IMPLIES C(MD).EQ.0.0
C SO, TAKE CARE OF THE RELATIVE MAGNITUDES OF THE REST COEFFICIENTS,
C E(MD),D(MD), IN ORDER TO PUT THE APPROPRIATE VALUE OF LIMIT
C IF(ABS(C(MD)).LT.1.0E-07) W(MD)=D(MD)/E(MD)
C IF(ABS(C(MD)).GT.1.0E-07) W(MD)=(F(MD)+D(MD)/C(MD))/(B(MD)/C(MD)
C * -E(MD))
C DO 17 MK=1,MM
C W(MD)=L(P)*W(MK+1)+F(W)
C RETURN
C END

```

## Appendix P

### OPTIMIZATION OF SOLAR SIMULATORS

G. Paparsénos

Mech. Eng. Dept., University of Glasgow,  
Glasgow G12 8QQ, U.K.

#### ABSTRACT

The individual lamps of a solar simulator have differing outputs which may be a function of time. The uneven flux produced can be corrected by varying the lamp output or by changing the position of the lamps. The former method can be difficult and expensive depending on the type of lamp. This method examines the latter alternative.

The tedium of trial and error lamp arrangement can be eliminated by applying the methods of operational research to optimize the relative outputs of the lamps, the position of the lamps, divergence of beam, etc. The method is verified to a low cost 12 lamp 3.5 kW solar simulator for air mass 2.

#### KEYWORDS

Solar simulator; optimization; integer programming; irradiance uniformity; volume uniformity; subtense angle.

#### INTRODUCTION

A solar simulator of direct radiation usually consists of an array of  $N$  light sources (lamps) that are positioned at  $N$  different positions on a mounting plane, that is at distance  $d$  from the test plane. The following considerations are essential: 1. the average total irradiance on the test plane; 2. the uniformity of total irradiance; 3. the volume uniformity; 4. the subtense angle; and 5. the spectral distribution of the produced radiation. The work deals directly with considerations 2,3 and 4, but takes into account the remaining two.

#### THE THEORETICAL ANALYSIS

##### Optimization of the Uniformity of Total Irradiance over a Specified Area of the Test Plane

$K$  points are specified on this area of the test plane. If  $I_k$ , ( $k = 1$  to  $K$ ) is the irradiance at the point  $k$  then the aim is to find what position  $\mu$  ( $\mu = 1$  to  $N$ ) on the mounting plane the light source  $\nu$  ( $\nu = 1$  to  $N$ ) should take in order to minimize

$[I_{k*}-I_{k**}]$ , where  $I_{k*}$  is the maximum irradiance (at point  $k^*$ ) and  $I_{k**}$  is the minimum irradiance (at point  $k^{**}$ ). That is,  $I_{k*} > I_{k**}$ ,  $k=1$  to  $K$ .

The requirements are: 1. Relative radiant output of each lamp,  $R_v$ ,  $v=1$  to  $N$ .

2. Distribution of irradiance in the test plane from each light source  $v$ ,  $f_v(x)$ , ( $v=1$  to  $N$ ) and  $x$  the distance from the point  $x=0$ , that is the projection of the centre light source  $v$  on the test plane. This distribution normalized at  $x=0$ , gives  $F_v(x)$ . If  $q_{k\mu}$  is the distance of the point  $k$  from the projection of the position  $\mu$  of the mounting plane on the test plane, then,  $S_{k\mu v} = F_v(q_{k\mu})$ ,  $k=1$  to  $K$ ,  $\mu=1$  to  $N$ ,  $v=1$  to  $N$ . The quantity  $G_{v\mu}$  is defined in the following way:

$G_{v\mu}=1$ , if the light source  $v$  takes the position  $\mu$

$G_{v\mu}=0$ , if the light source  $v$  does not take the position  $\mu$ , for  $v=1$  to  $N$ ,  $\mu=1$  to  $N$  (1)

Because each light source  $v$  takes only one position  $\mu$ ,  $\sum_{\mu=1}^N G_{v\mu} = 1$ ,  $v=1$  to  $N$  (2)

Because each position  $\mu$  is taken by only one light source  $v$ ,  $\sum_{v=1}^N G_{v\mu} = 1$ ,  $\mu=1$  to  $N$  (3)

Then, the irradiance of the point  $k$  is:  $I_k = \sum_{\mu=1}^N \sum_{v=1}^N G_{v\mu} \cdot R_v \cdot S_{k\mu v}$ ,  $k=1$  to  $K$

If  $[G_{v\mu}]$ , ( $v=1$  to  $N$ ,  $\mu=1$  to  $N$ ), is an arbitrary position of the  $N$  light sources at the  $N$  positions on the mounting plane (a solution of the system of equations (1), (2), (3)), an upper bound  $B$  and a lower bound  $b$  of irradiance will occur:

$B = I_{k*} > I_{k**} = b$ , for  $k=1$  to  $K$ . An improved uniformity would occur if we could decrease the difference  $B-b$ . This can be done solving the two separate problems of (A1) lowering the upper bound  $B$  and (A2) raising up the lower bound  $b$ . A new difference  $B-b$  will be produced in each case. We compare these two differences and adopt that solution as an improvement which gives the smaller difference  $B-b$ . This is repeated until the upper bound cannot be further lowered and the lower bound cannot be further raised. Then, the optimum solution of minimizing the difference  $[I_{k*}-I_{k**}]$  has been achieved. Each of the problems (A1) and (A2) has the following expression:

(A1) minimize  $[I_{k*}]$ , under the constraints (1), (2), (3) and  $I_k \leq B$ , for  $k=1$  to  $k^*-1$ ,  $k=k^*+1$  to  $K$  (4)

(A2) maximize  $[I_{k**}]$ , under the constraints (1), (2), (3) and  $I_k \geq b$ , for  $k=1$  to  $k^{**}-1$ ,  $k=k^{**}+1$  to  $K$  (5)

Converting the equalities (2) and (3) into inequalities and using the relation  $G_{v\mu} = Y_\lambda$  where,  $v=1$  to  $N$ ,  $\mu=1$  to  $N$  and  $\lambda = N(v-1) + \mu$  ( $\lambda=1$  to  $N \cdot N$ ), the final mathematical expressions of (A1) and (A2) are formed that are the typical expression of integer programming problem.

(A1)  $\min \sum_{\lambda=1}^{N \cdot N} C_{k*\lambda} \cdot Y_\lambda$ ,  $(I_{k*} = \sum_{\lambda=1}^{N \cdot N} C_{k*\lambda} \cdot Y_\lambda)$ , under the constraints:

$$\sum_{\lambda=1}^{N \cdot N} E_{\delta\lambda} \cdot Y_\lambda \leq 1, \quad \delta=1 \text{ to } 2N; \quad \sum_{\lambda=1}^{N \cdot N} D_{\lambda} \cdot Y_\lambda \leq Q;$$

$$\sum_{\lambda=1}^{N \cdot N} C_{k\lambda} \cdot Y_\lambda \leq B, \quad k=1 \text{ to } k^*-1, k=k^*+1 \text{ to } K; \quad \text{and } Y_\lambda, \quad 0 \text{ or } 1$$

The solution of the problem (A1) is  $Y_\lambda$ ,  $\lambda=1$  to  $N \cdot N$ .

(A2)  $\min \sum_{\lambda=1}^{N \cdot N} C_{k**\lambda} \cdot Y_\lambda$ ,  $(I_{k**} = \sum_{\lambda=1}^{N \cdot N} C_{k**\lambda} \cdot Y_\lambda)$ , under the constraints:

$$\sum_{\lambda=1}^{N \cdot N} E_{\delta\lambda} \cdot Y_\lambda \leq N-1, \quad \delta=1 \text{ to } 2N; \quad \sum_{\lambda=1}^{N \cdot N} D_{\lambda} \cdot Y_\lambda \leq Q;$$

$$\sum_{\lambda=1}^{N \cdot N} C_{k\lambda} \cdot Y_\lambda \leq \sum_{\lambda=1}^{N \cdot N} C_{k\lambda} - b, \quad k=1 \text{ to } k^{**}-1, k=k^{**}+1 \text{ to } K; \quad \text{and } Y_\lambda, \quad 0 \text{ or } 1.$$



The solution of the problem (A2) is  $Y_\lambda = 1 - Y'_\lambda$ ,  $\lambda = 1$  to  $N \cdot N$   
 where  $E_{\delta\lambda} = 1$ , when  $\delta = 1$  to  $N$  and  $\lambda = (\delta - 1) \cdot N + 1$  to  $\delta \cdot N$   
 or  $\delta = N + 1$  to  $2N$  and  $\lambda = (\delta - N)$  or  $N + (\delta - N)$  or  $2N + (\delta - N)$ ... or  $(N \cdot N - 1) + (\delta - N)$   
 otherwise  $E_{\delta\lambda} = 0$  ;

$$D_\lambda = - \sum_{\delta=1}^{2N} E_{\delta\lambda}, \quad \lambda = 1 \text{ to } N \cdot N \Rightarrow D_\lambda = -2, \quad \text{for } \lambda = 1 \text{ to } N \cdot N ;$$

$$Q = - \sum_{\delta=1}^{2N} 1 \Rightarrow Q = -2 \cdot N ; \quad Q' = - \sum_{\delta=1}^{2N} (N - 1) = -2N(N - 1) ;$$

$$C_{k\lambda} = R_v \cdot S_{k\mu v}, \quad \text{for } k = 1 \text{ to } K, \quad \mu = 1 \text{ to } N, \quad \lambda = (\mu - 1)N + 1 \text{ to } \mu \cdot N \text{ and } v = \lambda \text{ to } N(\mu - 1).$$

For both cases, there are  $N \cdot N$  unknowns ( $: Y_\lambda, \lambda = 1$  to  $N \cdot N$ ) and  $2N + K$  constraints.

#### Sensitivity Analysis of the Uniformity of Total Irradiance over a Specified Area of the Test Plane

1. The change of the uniformity of the total irradiance over the specified area of the test plane, by replacing an existing lamp  $v$  by a new one of different output or by imposing a different voltage  $V$  across the existing lamp  $v$ , is examined by the sensitivity analysis.

The output of a lamp and the resulting spectrum are functions of the imposed voltage  $V$  ( $R_v = q_v(V)$ ). Limits are imposed on the range of the voltage  $V$  ( $V_{\min}, V_{\max}$ ) and also on the range of relative radiant output of each lamp ( $R_{\min}, R_{\max}$ ) by the requirements for the average total irradiance to be higher than a specific value and the resulting spectrum to match a specified spectrum (e.g. of air mass 2).

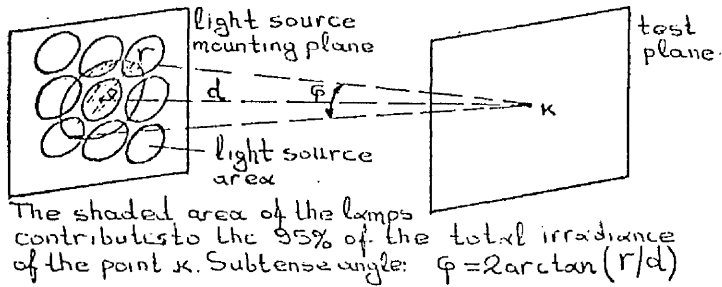
2. There are two main determinants of the irradiance distribution,  $f_v(x)$ . The divergence of the beam and the distance  $d$ , between the test plane and the mounting plane of the light sources. The first is determined by the design of the lamp (discharge length of the lamp, the spherical parabolic contour behind the lamp, etc.) and/or the distance  $l$  between the lamp and its lens in the case of a simulator that uses a combination of one lamp and one lens instead of one lamp only (in this case, the distance  $d$  is referred to the distance between the test plane and the lenses mounting plane). The sensitivity analysis using different distribution functions  $f_v(x)$ , gives information about the appropriate divergence of light (and so, the appropriate design of the whole system of a lamp and/or the combination of one lamp and one lens) and the appropriate distance  $d$  in order to have a specific uniformity over the specified area of the test plane (volume uniformity).

3. Finally, the sensitivity analysis gives information about the appropriate relative location of each of the  $N$  different positions on the mounting plane for a specified irradiance distribution function,  $f_v(x)$ .

The quantity  $S_{k\mu v}$  is a function of  $q_{k\mu}$ , which in its turn is a function of the relative location of each of the  $N$  positions on the mounting plane.

#### Subtense Angle of the Radiation

The subtense angle is defined as that angle of a cone centered on the normal to the test plane within which 95% of the incident radiation exists. The subtense angle is calculated for every point  $k$  of the test plane ( $k = 1$  to  $K$ ) for the various cases (e.g. arbitrary position of the  $N$  lamps, optimum position, etc.). A trial and



error approach allows the calculation of the radius r of the base circle of the subtense angle cone. Figure 1 gives details of this approach.

Fig. 1. Subtense angle calculation.

#### EXPERIMENTAL VERIFICATION

Computing programmes based on the theoretical analysis have been developed. The H02BAF NAG subroutine is used to solve the integer programming problem.

Some of the analytical results are verified on a small scale, air mass 2 solar simulator of lamp-lens combination of the same construction and details as that suggested by Grimmer and Bronisz (1979). The 12 Gen. El. ELH Quartzline projector lamps with dichroic reflectors are mounted on an aluminum sheet, with holes for the lamps, as Fig. 2 shows ( $N=12$ ). The 12 Fresnel lenses are mounted on a plywood sheet with hexagonal holes for the lenses as Fig. 3 shows. The distance l between lamps and lenses can be varied. Twenty-five points ( $k=25$ ) are specified on the test plane. The points are the projections of centres of the lamps and the centres of the triangles formed between the lamps on the test plane, that is parallel to the lamps and lenses mounting planes, as Fig. 1 shows.

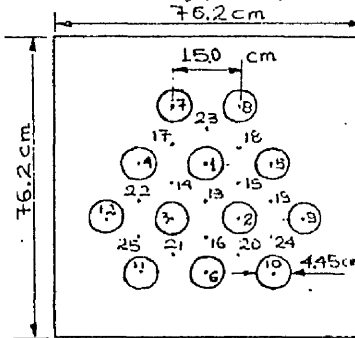


Fig. 2. Aluminum lamp-mounting sheet

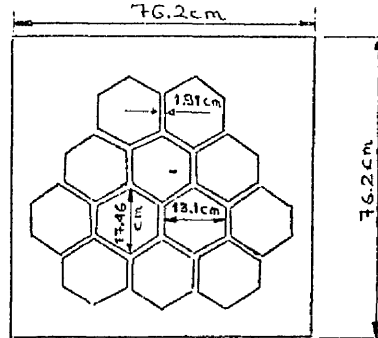


Fig. 3. Lens-mounting sheet.

The irradiance on the test plane was measured by a Moll-Gorczyński pyranometer.

#### Results

$V = 102.3$  Volts,  $l = 29$  cm,  $d = 340$  cm     $V = 102.3$  Volts,  $l = 35$  cm,  $d = 270$  cm  
 Uniformity: + 23.6%, - 24.9%,    + 15.1%, - 18.1% calc.  
                   + 26.1%, - 22.9%,    + 17.1%, - 20.0% meas.

#### Optimum position:

lamp	1	2	3	4	5	6	7	8	9	10	11	12	1	2	3	4	5	6	7	8	9	10	11	12
position	1	3	2	6	4	5	12	8	11	7	9	10	1	3	2	6	4	5	12	8	11	7	9	10

TABLE 1 Analytical Prediction of Total Irradiance  $I_k$  ( $\text{W/m}^2$ ) and Subtense Angle  $\phi$  (deg.) Measured Total Irradiance  $I_p$  ( $\text{W/m}^2$ )

V = 102.3 Volts, l = 29 cm, d = 340 cm						V = 102.3 Volts, l = 35 cm, d = 270 cm					
k	$I_k^m$	$I_k$	$\phi$	k	$I_k^m$	$I_k$	$\phi$	k	$I_k^m$	$I_k$	$\phi$
1	532	543	10.2	13	548	560	11.0	1	449	424	9.8
2	590	578	9.4	14	522	528	10.8	2	485	460	9.0
3	588	536	10.2	15	541	552	10.8	3	438	424	10.2
4	416	414	11.2	16	555	552	10.8	4	418	364	10.6
5	441	438	11.0	17	471	464	10.8	5	397	381	10.4
6	452	442	11.0	18	469	472	11.0	6	371	373	10.2
7	384	356	11.8	19	496	515	10.4	7	376	338	9.8
8	361	354	11.8	20	510	515	10.4	8	331	329	9.8
9	366	412	10.6	21	454	469	11.0	9	362	388	8.8
10	385	414	11.0	22	476	459	11.0	10	379	402	8.8
11	375	351	13.4	23	445	455	10.4	11	332	331	10.6
12	377	351	12.0	24	492	517	10.0	12	358	326	10.4
				25	455	451	10.8				
								25	396	393	10.0

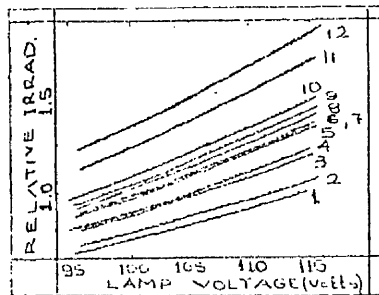


Fig. 4. Relative irradiance as function of lamps voltage.

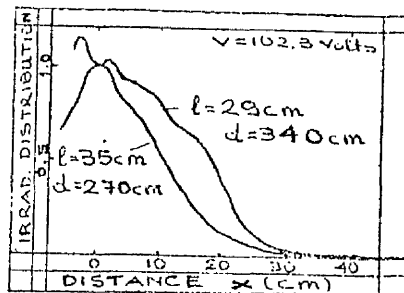


Fig. 5. Typical irradiance distribution  $f(x)$ , as function of the distance  $x$ , normalized at  $x=0$ .

#### ACKNOWLEDGMENTS

The author wishes to thank Dr S.K. Nisbet, Mech. Eng., Dept. for his advice, Dr P. Rosenberg, Comp. Serv., who assisted in the study of various integer programming subroutines, and Mr R. Kleiner for assistance in measurements.

#### REFERENCES

- Gillet, W.B. (1977). Solar simulators and indoor testing. Conference UK-ISES, 31.
- Grimmer, D.P. and L. Bronisz (1979). Small scale solar simulators for indoor testing of collector modules and materials. 1979 ISES Meeting, Atlanta, Georgia.
- Laidler, J.R. and G.R. Bainbridge (1979). The development and construction of a simulator for the proof testing of solar power devices. 1979 ILE Conference - Future Energy Concepts.
- Wagner, H.M. (1975). Principles of Operations Research. Prentice/Hall International, Inc., London.
- Yass, K. and H.B. Curtis (1974). Low cost, air mass 2 solar simulator. NASA Technical Memorandum, NASA TM X-3059.
- Yass, K. and H.B. Curtis (1975). Operational performance of a low cost air mass 2 solar simulator. NASA Technical Memorandum, NASA TM X-71662.

## References

REFERENCES

1. Fuchs, R. and McClelland, J.F. (1979). Passive solar heating of buildings using a transwall structure. Solar Energy, Vol. 23, pp. 123-128.
2. Hull, J.R. and McClelland, J.F. and Hodges, L. and Fuchs, R. and Block, D.A. (1980). Solar heating performance results for a transwall test-prototype. American section of I.S.E.S. conference, Phoenix, Arizona, June 2-6, 1980.
3. Hull, J.R. and McClelland, J.F. and Hodges, L. and Huang, J.L. and Fuchs, R. and Block, D.A. (1980). Effect of design parameter changes on the thermal performance of a transwall passive solar heating system. 5th National Passive Solar Conference, American Section of I.S.E.S., Amherst, October 19-26, 1980.
4. McClelland, J.F. and Mercer, R.W. and Hodges, L. and Szydlowski, R.F. and Sildes, P.H. and Struss, R.G. and Hull, J.R. and Block, D.A. (1981). Transwall-A modular visually transmitting thermal storage wall-Status report. Solar World Forum, Vol. 3, Brighton, England.
5. Mercer, R. and McClelland, J. and Hodges, L. and Szydlowski, R. Recent developments in the transwall system 6th National Passive Solar Conference of the American Section of I.S.E.S., Portland, Oregon, Sept. 8-12, 1981.
6. Hull, J.R. and McClelland, J.F. and Hodges, L. and Block, D.A. and Fuchs, R. Transwall-A modular visually transparent thermal storage wall system, Internal Report, A.M.E.S. Laboratory-USDOE, Iowa State University, WPAS-BD-01.
7. McClelland, J.F. and Mercer, R.W. and Hodges, L. and Szydlowski, R.F. Transwall Research, Internal Report, AMES laboratory - USDOE, Iowa State University, W-7405-Eng-82.
8. McClelland, J.F. (1982). Private Communication.

9. Burke, A.R. and Hudgens, C.R. and Wittenberg, L.J. (1979).  
Chemical and optical Studies of heat transfer fluids  
containing solar energy absorbers A.I.Ch.E. 86<sup>th</sup>  
National Meeting, Houston, Texas (April 1979).
10. Burke, A.R. and Etter, D.E. and Wiedenheft, C.J. and  
Wittenberg, L.J. (1979). Studies of directly absorbing  
fluids for mid-temperature solar thermal applications,  
American Section of I.S.E.S. Conference, Atlanta,  
U.S.A. (1979).
11. Stokes, G.G. (1862). On the intensity of the light reflected  
from or transmitted through a pile of plates.  
Proceedings of Royal Society, London, vol. 11,  
pp. 545-556.
12. Green, A.A. (1979). The influence of environmental parameters  
on flat plate solar collector performance. Proceed-  
ings of U.K. ISES/R. Met.Soc. Technical Meeting (C18)  
on meteorology for solar energy applications, London,  
pp. 95-107.
13. Hottel H.C. and Woertz, B.B. (1942). The Performance of  
flat-plate solar-heat Collectors. Transactions of  
the ASME, vol. 64, pp 91-104.
14. Kreith, F. and Kreider, J.F. (1978). Principles of Solar  
Engineering. Hemisphere Publishing Corporation  
and McGraw-Hill Book Company.
15. Duffie, J.A. and Beckman, W.A. (1980). Solar Engineering of  
Thermal Processes. John Wiley & Sons.
16. Belov, G.Y. (1974). Optical characteristics of a multi-  
layered coating and a semitransparent stack of  
absorbing and scattering materials with diffusely  
reflecting interfaces. High Temperature, vol. 12,  
part 6, pp. 1079-1084.
17. Siegel, R. (1973). Net radiation method for transmission  
through partially transparent plates. Solar Energy,  
vol. 15, pp. 273-276.
18. Shurcliff, W.A. (1974). Transmittance and reflection loss of  
multi-plate planar window of a solar-radiation  
collector; formulas and tabulations of results  
for the case  $n = 1.5$ . Solar Energy vol. 16,  
pp. 149-154.

19. Wijeyesundera, N.E. (1974). A net radiation method for the transmittance and absorptivity of a series of parallel regions. Solar Energy, vol. 17, pp. 75-77.
20. Edwards, D.K. (1977). Solar absorption by each element in an absorber-coverglass array. Solar Energy, vol. 19, pp. 401-402.
21. Gillette, R.B. and Deminet, C. and Beverly, W.D. (1975). Glass solar heat collector development. AIAA 10<sup>th</sup> thermophysics Conference, Denver, U.S.A.
22. Drotning, W.D. (1978). Optical properties of solar absorbing oxide particles suspended in a molten salt heat transfer fluid. Solar Energy, vol. 20, pp. 313-319.
23. Bamford, C.R. (1980). Pilkington Brothers Limited. Private communication.
24. Linsley, G.F. (1980). Pilkington Brothers Limited. Private communication.
25. Pilkington Brothers Limited (1977). Solar control glasses.
26. Hale, G.H. and Querry, M.R. (1973). Optical constants of water in the 200-nm to 200 m wavelength region. Applied Optics, vol. 12, No. 3, pp. 555-563.
27. Palmer, K.F. and Williams, D. (1974). Optical properties of water in the near infrared. Journal of the optical society of America, vol. 64, No. 8, pp. 1107-1110.
28. Ashrae (1977). Ashrae Handbook, Fundamentals
29. Ashrae (1978). Ashrae Handbook, Applications, ch. 58.
30. Cockroft, J. (1979). Heat transfer and air flow in buildings. Ph.D. thesis in Mechanical Engineering Dept., Glasgow University.
31. Rodgers, G.G. and Page, J.K. and Souster, C.G. (1979). Mathematical models for estimating the irradiance falling on inclined surfaces for clear, overcast and average conditions. Proceedings of U.K. ISES/ R. Met. Soc. Technical meeting (C18) meteorology for solar energy applications, London, pp. 95-107.

32. Thekaekara, M.P. (1974). The energy crisis and energy from the sun. Institute for environmental sciences.
33. Yass, K. and Curtis, H.B. (1974). Low cost, air mass 2 solar simulator. NASA Technical Memorandum, NASA TM X-3059.
34. Hull, J.R. (1980). Computer simulation of solar pond thermal behaviour. Solar Energy, vol. 25, pp. 33-40.
35. Canham, A.E. (1966). Artificial light in horticulture. Centrex Publishing Company, Eindhoven, Holland.
36. Kondratyev, K.Y. (1965). Actinometry. NASA TTF-9712.
37. Coulson, K.L. (1975). Solar and terrestrial Radiation. Academic Press.
38. Wehner, R. (1976). Polarized-light navigation of insects, Scientific American, vol. 235, pp. 106-115.
39. Lebens, R.M. (1980). Passive solar heating design. Applied Science Publishers Ltd., London.
40. Jones Jr., R.E. (1980). Effects of overhang shading of windows having arbitrary azimuth. Solar Energy, vol. 24, No. 3, pp. 305-311.
41. Klein, S.A. (1977). Calculation of monthly average insolation on tilted surfaces. Solar Energy, vol. 19, No. 4 pp. 325-329.
42. Eckert, E.R.G. and Drake Jr., R.M. (1972). Analysis of heat and mass transfer. McGraw-Hill Kogakusha Ltd.
43. Utzinger, D.M. and Klein, S.A. (1979). A method of estimating monthly average solar radiation on shaded receivers. Solar Energy, vol. 23, No. 5, pp. 368-378.
44. Eriksson, C. and Gay, B. and Rey, Y (1981). Mathematical modelisation of a direct gain-test cell. Solar World Forum, Brighton, England.
45. Johnson, T.E. (1977). Lightweight thermal storage for solar heated buildings. Solar Energy, vol. 19, pp. 669-675.



46. Min, T.C. and Schutrum, L.F. and Parmelee, G.V. and Vouris, J.D. (1956). Natural convection and radiation in a panel-heated room. Trans. ASHRAE, 62, pp. 337-358.
47. Hollands, K.G.T. and Konicek, L. and Unny, T.E. and Raithby, G.D. (1976). Free convection Heat Transfer Across Inclined Air Layers. Journal of Heat Transfer, vol. 98, pp. 189-193.
48. Buchberg, H. and Catton, I. and Edwards, D.K. (1976). Natural convection in enclosed spaces - A review of application to solar energy collection. Journal of Heat Transfer, May 1976, pp. 182-188.
49. Pacetti, M. and Principi, P. and Sabetta, F. (1981). Trombe wall channel modelling. Solar World Forum, Brighton, U.K. Aug. 1981, vol. 3, pp. 1876-1880.
50. Wray, W.O. (1980). A simple procedure for assessing thermal comfort in passive solar heated buildings. Solar Energy vol. 25, pp. 327-333.
51. Ohanessian, P. and Charters, W.W.S. (1978). Thermal simulation of a passive solar house using a Trombe-Michel wall structure. Solar Energy, vol. 20, pp. 275-281.
52. Grimmer, D.P. (1979). Theoretical considerations in the use of small passive-solar test-boxes to model the thermal performance of passively solar-heated building designs. Solar Energy, vol. 22, pp. 343-350.
53. Grimmer, D.P. and McFarland, R.D. and Balcomb, J.D. (1978). Initial experimental tests on the use of small passive-solar test-boxes to model the thermal performance of passively solar-heated building designs. Solar Energy, vol. 22, pp. 351-354.
54. Lee, K.S. and Oberdick, W.A. (1981). Development of a passive solar simulation technique using small-scale models. Solar World Forum, Brighton, U.K., August 1981, vol. 3, pp. 1803-1810.

55. Balcomb, J.D. and Hedstrom, J.G. and McFarland, R.D. (1978).  
Passive solar heating of buildings. Proceedings  
of CCMS/ISES international solar energy conference  
on the Performance of solar heating and cooling  
systems, Dusseldorf, W. Germany, April 1978,  
pp. 39-57.
56. Lewis, W.T. and Incropera, F.P. and Viskanta, R. (1982).  
Interferometric study of mixing layer development in  
a laboratory simulation of solar pond conditions.  
Solar Energy, Vol. 28, No. 5, pp. 389-401.
57. Snider, D.M. and Viskanta R. (1975). Radiation induced  
thermal stratification in surface layers of stagnant  
water. Journal of heat Transfer. Feb. 1975,  
pp. 35+ 40.
58. Rajvanshi, A.K. (1981). Effect of various dyes on solar  
distillation. Solar energy, Vol. 27, pp. 51-65.
59. Roache, P.J. (1972). Computational Fluid Dynamics. Hermosa  
Publishers, Albuquergue.
60. Torrance, K.E. and Rockett, J.A. (1969). Numerical study  
of natural convection in an enclosure with  
localised heating from below - creeping flow to  
the onset of laminar instability. Journal of Fluid  
Mechanics, Vol. 36, part 1, pp. 33-54.
61. Tritton, D.J. (1977). Physical Fluid Dynamics. Van Nostrand Reinhold.
62. Massie, A. (1968). Fluid Mechanics. Pergamon Press.
63. Kutateladze, S. and Borishanskii, V. (1966). A concise  
encyclopedia of heat transfer. Pergamon Press.
64. Kays, W.M. (1966). Convective heat and mass transfer.  
McGraw-Hill.
65. Larson, D. and Viskanta, R. (1976). Transient combined  
laminar free convection and radiation in a rect-  
angular enclosure. Journal of Fluid Mechanics,  
Vol. 78, part 1., pp. 65-85
66. Rosenhead, L. (1954). A discussion on the first and second  
viscosities of fluids. Proceedings of the Royal  
Society, London, Ser. A, Vol. 226, pp. 1-6
67. Launder, B.E. (1975), editor Studies in convection, theory,  
measurement and applications, volume 1. Academic  
Press.

68. Patankar, S.V. (1980). Numerical heat transfer and fluid flow. Hemisphere publishing corporation & McGraw-Hill Book Company.
69. Callen, H.B. (1960). Thermodynamics. John Wiley & Sons, Inc., New York, N.Y.
70. Weast, R.C. (1979), editor CRC Handbook of Chemistry and Physics, 59<sup>th</sup> edition.
71. Patankar, S.V. (1981). Procedure for elliptic situations. Numerical Heat Transfer, Vol. 4, No. 4, Dec. 1981.
72. Stoecker, W.F. (1971). Design of thermal systems. McGraw-Hill Book Company.
73. Yass, K. and Curtis H.B. (1975). Operational performance of a low cost air mass 2 solar simulator. NASA Technical Memorandum, NASA TM X-71662.
74. Grimmer, D.P. and Bronisz, L. (1979). Small scale solar simulators for indoor testing of collector modules and materials. 1979 ISES Meeting, Atlanta, Georgia.
75. Paparsenos, G.F. (1981). Optimization of Solar Simulators. 1981 ISES Solar World Forum, Brighton, England, Vol. 1.
76. Kucharczyk, J. (1972). Implicit enumeration algorithm for solving zero-one integer linear programs. Algorithm 16. Zastosowania Matematyki, Applicationes Mathematicae. Xiii, 1.
77. Merzkirch, W. (1974). Flow visualization. Academic Press, New York and London.
78. Buzyna, G. and Veronis, G. (1971). Spin up of a stratified fluid; Theory and experiment. Journal of Fluid Mechanics, 50, pp. 579-608
79. Plant, J.A. (1967). The climate of Glasgow. Climatological Memorandum No. 60. Meteorological Office. Climatological services (Met. 0.3).

